Cross-Subject Image Analysis in Diffusion Brain MRI

Marius de Groot

Cross-Subject Image Analysis in Diffusion Brain MRI

Marius de Groot

Cover 'the hidden wiring in our brain'

Cover design & thesis layout by Marius de Groot
Photo, page 239 by Ton Everaers
Printed by GVO drukkers & vormgevers

The work in this thesis was conducted at the departments of Radiology, Medical Informatics and Epidemiology of the Erasmus MC, Rotterdam, the Netherlands. The research was part of the 'Statistical analysis of 4D Diffusion Tensor MRI data' project, funded by the Netherlands organisation for scientific research (NWO), grant 612.065.821.

This work was carried out in the ASCI graduate school.
ASCI dissertation series number 310.

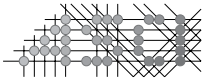

For financial support for the publication of this thesis, the following organizations are gratefully acknowledged: Alzheimer Nederland, the ASCI graduate school, the department of Radiology of the Erasmus MC, the Dutch Heart Foundation, and the Internationale Stichting Alzheimer Onderzoek (ISAO). Also the following companies are gratefully acknowledged for their financial support in the publication of this thesis: Bayer BV and Quantib BV.

ISBN 978-90-6464-814-4

Cross-Subject Image Analysis in Diffusion Brain MRI

Analyse van diffusie MRI hersenbeelden over meerdere personen

Proefschrift

ter verkrijging van de graad van doctor aan de
Erasmus Universiteit Rotterdam
op gezag van de rector magnificus

Prof.dr. H.A.P. Pols

en volgens besluit van het College voor Promoties.
De openbare verdediging zal plaatsvinden op

vrijdag 17 oktober 2014 om 13.30 uur

door

Marius de Groot
geboren te Delft

Promotiecommissie

Promotor:	Prof.dr. W.J. Niessen
Overige leden:	Prof.dr. F. Barkhof Prof.dr. P.J. Koudstaal Prof. S.M. Smith DPhil
Copromotor:	Dr. M.W. Vernooij

Contents

Chapter 1
General introduction

General introduction

We continue to live longer. Low-income countries currently gain about 10 hours in life-expectancy per day,[1] while global maximum life expectancy continues to increase linearly, as it has over the past 160 years.[2] As Alzheimer's disease occurs more frequently with higher age, the number of persons diagnosed will therefore rise dramatically.[3] This will affect quality of life for more patients and more relatives, but will also increase healthcare spending. Early diagnosis and, ideally, prevention of AD is therefore urgent. There is increasing evidence that, decades before the clinical diagnosis of Alzheimer's disease, early signs of the disease are present, and may be detectable. In this respect, neuroimaging techniques are promising, as they allow for non-invasive and sensitive assessment of subclinical tissue damage. However, in order to discriminate presymptomatic stages of neurodegenerative disease from a broad spectrum of age related changes, more insight in these 'normal' changes with age is essential.

Neuroimaging studies of the aging brain have for many years focused primarily on the role of grey matter anatomy, function and pathologies in the development and diagnosis of dementia. With the introduction of new technologies and increased understanding of neurodegenerative disorders, we have learned that white matter pathologies are more important in neurodegeneration than previously thought, leading to an increased interest to study different aspects of brain white matter in ageing and neurodegeneration. Initial studies focused on macrostructural white matter changes such as white matter atrophy and white matter lesion formation. These studies established associations between many vascular risk factors and these macrostructural white matter changes,[4,5] which in turn have been associated to increased risk of stroke, dementia and death.[6–8] Macrostructural brain changes however, are thought to occur later in disease than changes to tissue microstructure.[9,10] Diffusion imaging, which can be used to investigate tissue microstructure in vivo, therefore has the potential to provide insight in the early changes we are after.

Diffusion imaging of brain white matter

The axons that provide connectivity between brain regions are the main constituent of brain white matter. Signal transmission along these axons is sped up by myelin sheaths that wrap around and insulate the axons. These sheaths form gradually during neurodevelopment, with most myelin formed between birth and young adulthood with some (e.g. deep) regions myelinating earlier than others.[11,12] With increasing age there is gradual myelin breakdown and loss in myelinated fibers, processes which exacerbate in neurodegenerative diseases.[13–15]

Diffusion magnetic resonance imaging is a non-invasive MRI technique that is sensitive to the random movement of water molecules. Within the highly organized white matter, cell and myelin membranes, among other structures, affect this random motion. Diffusivity thereby depends on tissue properties such as myelination, axon diameter and axon count, but also on the measurement orientation with respect to the tissue. Diffusion MRI probes diffusion in specified directions by measuring signal attenuation relative to non-diffusion weighted images. In its simplest form, diffusion MRI allows quantification of the (non-directional) apparent diffusivity coefficient. When six or more directions are probed, a diffusion tensor that describes the orientational dependence of the local water diffusion can be estimated. In diffusion tensor imaging (DTI), this orientational dependence is reflected in the fractional anisotropy (FA). Additionally, DTI provides an estimate of the mean diffusivity (MD), and the directed diffusivities: axial diffusivity along the main fiber direction, and radial diffusivity perpendicular to the latter. The FA can be considered to reflect the degree of microstructural organization in case all axons inside a voxel are aligned and straight, and is often used in brain research. A decrease in FA could be caused by damage to the myelin sheaths, axonal loss or even changes in the size of the axons. The anatomy of the white matter is however much more complicated, with fibers e.g. crossing, bending or merging at resolutions beyond what can be resolved with diffusion MRI. The diffusion tensor model has therefore often been expanded to model more complex configurations, taking into account multiple fiber populations, or even directly estimating microstructural parameters such as axon diameter.[16–20] Besides for the characterization of tissue microstructure, diffusion MRI can also be used to reconstruct white matter pathways. These connections between brain regions and e.g. to the spinal cord, can be identified by following the estimated fiber directions using tractography.[21,22] Tractography can be performed on the estimated diffusion tensor, but also on more detailed models of diffusion.[20,23]

Diffusion image analysis: novel analytical approaches

The wealth of anatomical and microstructural information in diffusion MRI has been studied in relation to many diseases and conditions, including neurodevelopment and (age related) neurodegeneration. Traditionally, many studies analyzed diffusion measurements in anatomical regions by (manually) placing regions of interest (ROI). While simple and effective, ROI definition is often time-intensive and observer-dependent and thereby a limiting factor for larger sample sizes or when many regions are investigated. Voxel based analysis (VBA) similarly compares corresponding anatomical regions at the voxel level, but uses automated approaches to establish this correspondence. While straightforward to apply, VBA suffers from a conceptual complication that would require a-priory knowledge of the effect size,[24] but is also

especially prone to registration errors that may occur in the periphery of white matter tracts. Therefore, in 2006, tract-based spatial statistics (TBSS) was introduced to mitigate the drawbacks of VBA while simultaneously increasing power to detect differences in the centers of white matter tracts.[25,26] Voxel wise analyses, including TBSS, can however not yet incorporate anatomical knowledge of white matter pathways in a way that would allow aggregation of measurements over connections rather than spatial clustering For this type of analysis, tractography based methods have been developed that aggregate measurements over each tract or use a parameterization technique to incorporate anatomical information into the analysis.[27–29]

Diffusion imaging in population-based cohort studies

The Rotterdam study is a population-based study that investigates causes and consequences of diseases in the elderly. It was initiated in 1990, and prospectively follows nearly 15,000 inhabitants of Ommoord, a suburb of Rotterdam. In addition to rich phenotyping and close monitoring of health status, multi-sequence brain MRI is acquired in all participants to investigate brain aging. The multisequence imaging protocol includes measures of both macrostructural and microstructural tissue changes. Participants are scanned at regular intervals to investigate changes with age and in imaging markers over time, and well over 11 thousand imaging sessions have been acquired for over five thousand participants till date. Investigating this large population requires (fully) automated tools and analysis approaches that may not be readily available.

Aims and outline

The first aim of this thesis was to develop new analysis approaches for the investigation of white matter microstructure in elderly subjects. The second aim of this thesis was to provide new insights into microstructural changes of brain white matter with increasing age, which could be achieved by large-scale application of these methods to the diffusion data from the Rotterdam Study. These insights should contribute to a better understanding of the preclinical stages of dementia, which should ultimately enable early detection and with that enable disease modification.

In chapter 2, I describe new analysis approaches for diffusion imaging, focused on large-scale analyses. Chapter 2.1 explores an iterative tract-pruning approach aimed to investigate the cingulum. Further development of these automated tractography protocols is undertaken in chapter 2.2, to support a novel registration-evaluation framework in order to compare 639 registration settings. Longitudinal analysis of

structural images in relation to diffusion parameters is presented in chapter 2.3, in which I investigate normal-appearing white matter that later converts to a white matter lesion in a population of 689 persons.

Chapter 3.1 adopts the automated tractography approach presented in chapter 2.2 and focuses on tract microstructure in relation to age and cardiovascular risk factors. This chapter investigates various DTI measures in 4,532 non-demented participants from the Rotterdam Study. Chapter 3.2 integrates the symmetric intra-subject registration from chapter 2.3, with the optimized TBSS of chapter 2.2, and focuses on longitudinal analysis of microstructure in relation to age in a population of 501 participants that were scanned on two visits with an interval of 2.0 years.

Chapter 4 describes the application of diffusion imaging within studies on cerebral small vessel disease. In chapter 4.1, the relationship between small vessel disease, aging and microstructure is explored, focusing on white matter lesions and white matter atrophy as macrostructural manifestations of white matter change in 832 persons. Chapter 4.2 focuses on the relation between cerebral microbleeds as reflection of cerebral small vessel disease and systemic white matter microstructure in a population of 4,493 participants. Chapter 4.3 investigates white matter microstructure and cerebral small vessel disease, specifically in relation to mild cognitive impairment in a patient population of 74 persons.

Finally, in chapter 5, I discuss our findings in the context of existing research, and I discuss how future investigations could benefit from the work presented.

References

1. World Health Organization. World Health Statistics 2014. WHO press; 2014:1-180.
2. Oeppen J, Vaupel J. Broken limits to life expectancy. Science (80-). 2002;296:1029-1031.
3. Brookmeyer R, Johnson E, Ziegler-Graham K, Arrighi HM. Forecasting The Global Burden of Alzheimer's Disease. Alzheimer's Dement. 2007;3:186-191.
4. Pantoni L. Pathophysiology of age-related cerebral white matter changes. Cerebrovasc Dis. 2002;13 Suppl 2:7-10.
5. Appelman APA, Exalto LG, van der Graaf Y, Biessels GJ, Mali WPTM, Geerlings MI. White matter lesions and brain atrophy: more than shared risk factors? A systematic review. Cerebrovasc Dis. 2009;28(3):227-42.
6. Debette S, Markus HS. The clinical importance of white matter hyperintensities on brain magnetic resonance imaging: systematic review and meta-analysis. BMJ. 2010;341:c3666.
7. Carmichael O, Schwarz C, Drucker D, et al. Longitudinal changes in white matter disease and cognition in the first year of the Alzheimer disease neuroimaging initiative. Arch Neurol. 2010;67(11):1370-8.
8. Provenzano FA, Muraskin J, Tosto G, et al. White matter hyperintensities and cerebral amyloidosis: necessary and sufficient for clinical expression of Alzheimer disease? JAMA Neurol. 2013;70(4):455-61.
9. Oishi K, Mielke MM, Albert M, Lyketsos CG, Mori S. DTI analyses and clinical applications in Alzheimer's disease. J Alzheimers Dis. 2011;26 Suppl 3:287-96.

10. Ly M, Canu E, Xu G, et al. Midlife measurements of white matter microstructure predict subsequent regional white matter atrophy in healthy adults. Hum Brain Mapp. 2013;000:1-11.

11. Kinney H, Kloman A, Gilles F. Sequence of central nervous system myelination in human infancy. II. Patterns of myelination in autopsied infants. J Neuropathol Exp Neurol. 1988;47(3):217-234.

12. Deoni SCL, Mercure E, Blasi A, et al. Mapping infant brain myelination with magnetic resonance imaging. J Neurosci. 2011;31(2):784-91.

13. Meier-Ruge W, Ulrich J, Brühlmann M, Meier E. Age-related white matter atrophy in the human brain. Ann N Y Acad Sci. 1992;673:260-9.

14. Bartzokis G, Sultzer D, Lu PH, Nuechterlein KH, Mintz J, Cummings JL. Heterogeneous age-related breakdown of white matter structural integrity: implications for cortical "disconnection" in aging and Alzheimer's disease. Neurobiol Aging. 2004;25(7):843-51.

15. Haller S, Kövari E, Herrmann FR, et al. Do brain T2/FLAIR white matter hyperintensities correspond to myelin loss in normal aging? A radiologic-neuropathologic correlation study. Acta Neuropathol Commun. 2013;1(1):14.

16. Assaf Y, Basser PJ. Composite hindered and restricted model of diffusion (CHARMED) MR imaging of the human brain. Neuroimage. 2005;27(1):48-58.

17. Assaf Y, Blumenfeld-Katzir T, Yovel Y, Basser PJ. AxCaliber: a method for measuring axon diameter distribution from diffusion MRI. Magn Reson Med. 2008;59(6):1347-54.

18. Alexander DC, Hubbard PL, Hall MG, et al. Orientationally invariant indices of axon diameter and density from diffusion MRI. Neuroimage. 2010;52(4):1374-89.

19. Sotiropoulos SN, Behrens TEJ, Jbabdi S. Ball and rackets: Inferring fiber fanning from diffusion-weighted MRI. Neuroimage. 2012;60(2):1412-25.

20. Behrens TEJ, Woolrich MW, Jenkinson M, et al. Characterization and propagation of uncertainty in diffusion-weighted MR imaging. Magn Reson Med. 2003;50(5):1077-1088.

21. Conturo TE, Lori NF, Cull TS, et al. Tracking neuronal fiber pathways in the living human brain. Proc Natl Acad Sci U S A. 1999;96(18):10422-7.

22. Basser PJ, Pajevic S, Pierpaoli C, Duda J, Aldroubi A. In vivo fiber tractography using DT-MRI data. Magn Reson Med. 2000;44(4):625-632.

23. Parker GJM, Haroon HA, Wheeler-Kingshott CAM. A framework for a streamline-based probabilistic index of connectivity (PICo) using a structural interpretation of MRI diffusion measurements. J Magn Reson Imaging. 2003;18(2):242-254.

24. Jones DK, Symms MR, Cercignani M, Howard RJ. The effect of filter size on VBM analyses of DT-MRI data. Neuroimage. 2005;26(2):546-554.

25. Smith SM, Jenkinson M, Johansen-Berg H, et al. Tract-based spatial statistics: voxelwise analysis of multi-subject diffusion data. Neuroimage. 2006;31(4):1487-1505.

26. Smith SM, Johansen-Berg H, Jenkinson M, et al. Acquisition and voxelwise analysis of multi-subject diffusion data with tract-based spatial statistics. Nat Protoc. 2007;2(3):499-503.

27. Zhu H, Styner M, Tang N, Liu Z, Lin W, Gilmore J. FRATS: Functional Regression Analysis of DTI Tract Statistics. IEEE Trans Med Imaging. 2010.

28. Yushkevich PA, Zhang H, Simon TJ, Gee JC. Structure-specific statistical mapping of white matter tracts. Neuroimage. 2008;41(2):448-461.

29. Gong G, Jiang T, Zhu C, et al. Asymmetry analysis of cingulum based on scale-invariant parameterization by diffusion tensor imaging. Hum Brain Mapp. 2005;24(2):92-98.

Chapter 2
Improving cross-subject diffusion analysis

2.1

Asymmetry analysis along the entire cingulum in the general population

MICCAI 2009

Marius de Groot
Meike W. Vernooij
Stefan Klein
Alexander Leemans
Renske de Boer
Aad van der Lugt
Monique M.B. Breteler
Wiro J. Niessen

We present a method for the fully automated extraction of the cingulum using diffusion tensor imaging (DTI) data. We perform whole-brain tractography and initialize tract selection in the cingulum with a registered DTI atlas. Tracts are parameterized from which tract co-linearity is derived. The tract set, filtered on the basis of co-linearity with the cingulum shape, yields an improved segmentation of the cingulum and is subsequently optimized in an iterative fashion to further improve the tract selection. We evaluate the method using a large DTI database of 500 subjects from the general population and show robust extraction of tracts in the entire cingulate bundle in both hemispheres. We demonstrate the use of the extracted fiber-tracts to compare left and right cingulate bundles. Our asymmetry analysis shows a higher fractional anisotropy in the left anterior part of the cingulum compared to the right side, and the opposite effect in the posterior part.

Introduction

The use of diffusion tensor magnetic resonance imaging (DTI) for analyzing brain microstructure is well established.[1] The diffusion tensor, estimated from multiple diffusion weighted image volumes, captures the local organization of the brain. The fractional anisotropy (FA), derived from this tensor, describes the microstructural tissue organization in terms of the degree of diffusion directionality.[2] Comparing differences between neuroanatomical structures across subjects requires one to establish correspondence between these subjects. This may involve a common white matter skeleton,[3] or the identification of separating manifolds between white matter structures[4] for the projection of individual measures onto a reference frame. Compared to FA extraction, streamline tractography in the tensor field provides a richer description of the local white matter structure. Tractography based comparison between subjects will therefore be more sensitive to subtle differences, provided, of course, that the abundance of data in the tracts can be interpreted.

In this paper, we develop a method to automatically analyze the cingulum in a large cohort using streamline tractography.

The Cingulum

The cingulum is a tube-like structure that courses from the hippocampal formation and bends around the ventricles and the corpus callosum (cc) up to the genu of the cc. The anterior cingulate is thought to be primarily involved in executive functioning, whereas the posterior cingulate is assumed to play a role in memory processes. Its role in cognitive functioning has generated a large interest in the analysis of various aspects of the cingulum. Due to high curvature in its local anatomy, the cingulum is difficult to reconstruct with streamline tractography past the bending point around the splenium of the cc.[5] This may explain why most previous research focused on tracking only the anterior part of the cingulum. Research aiming to study the cingulum with the use of tractography in multiple subjects, has often relied on manual ROI definition to allow tract selection (e.g. [6–8]). O'Donnell et al. use a spectral embedding function to identify tracts similar to a template tract.[9] Their 'tract based morphometry' can robustly capture tracts in the anterior cingulate bundle, but has not been able to identify tracts when every tract only overlaps partly with the anatomical structure of interest. Depending on DTI data quality, the high curvature in the cingulum may pose a particular challenge for tractography. We propose an automated method that does not rely on individual tracts coinciding with the entire cingulum, but rather on extracting the parts of all tracts that describe at least some part of the cingulum. The complete filtered set of all (partial) tracts then has more power to capture the actual cingulum anatomy, in particular the posterior part.

Methods

In short, after performing whole-brain tractography, we propose to identify partial tracts that make up the cingulate bundle with the use of a registered anatomical atlas. We derive a parameterization, which allows for a more accurate selection of tracts that belong to the cingulum, and facilitates inter-subject comparison. The iterative approach, outlined in Figure 2.1.1, consists of the following steps: tract selection, derivation of the parameterization, projection of tracts and co-linearity filtering. In the method description, all parameters that need to be set are printed in italic.

Tractography and atlas registration

Deterministic streamline tractography is performed using the 'ExploreDTI' package (www.exploredti.com).[10] Tracts are described by cubic B-splines, and stored as equally spaced points. We adopted the neuroanatomical ICBM-DTI-81 atlas of Mori et al.[11] for the initial tract selection. This atlas is created by manual segmentation of 50 neuroanatomical structures. We nonrigidly registered the atlas' FA image towards

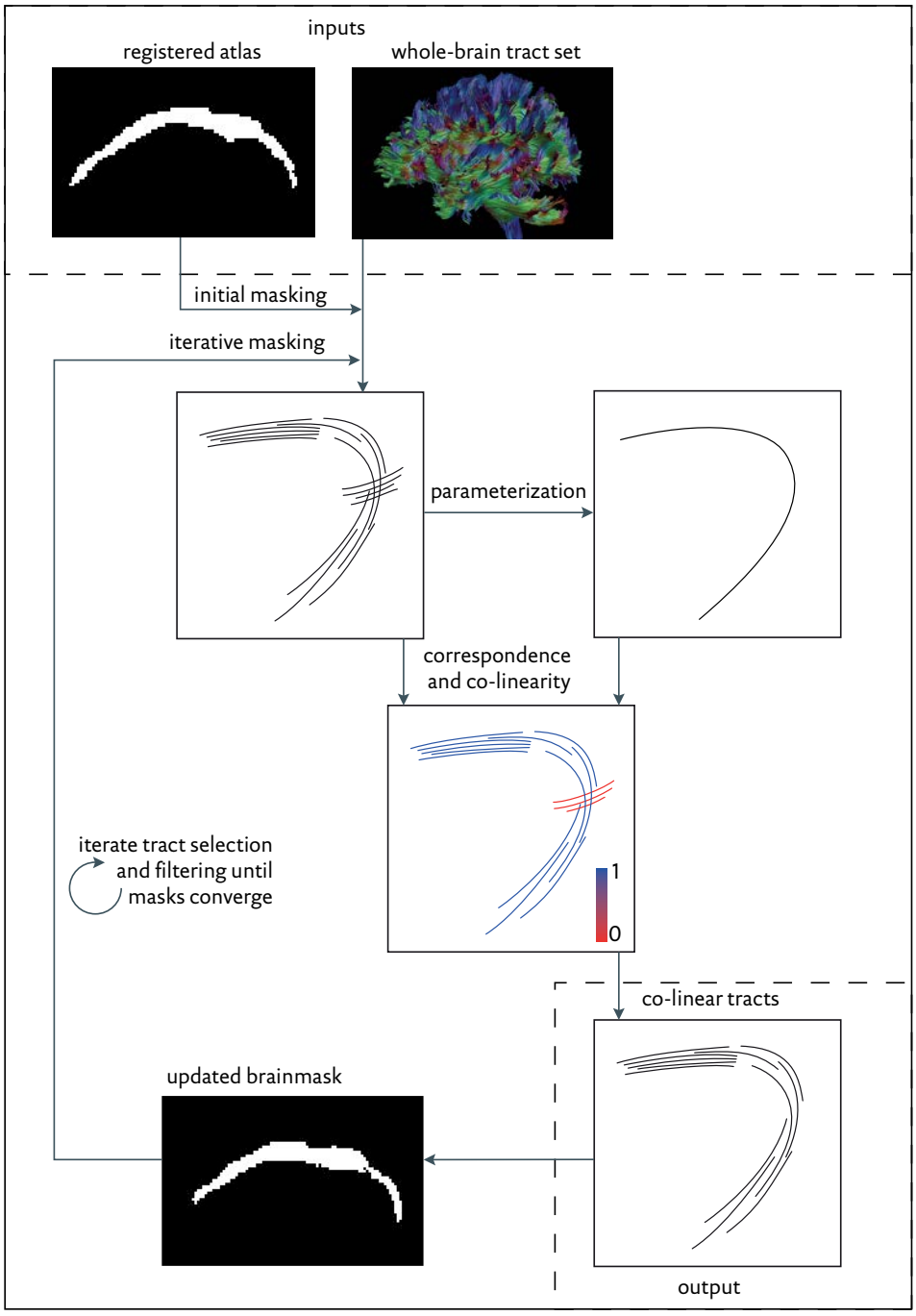

Figure 2.1.1. *Schematic overview of the tract selection procedure.*

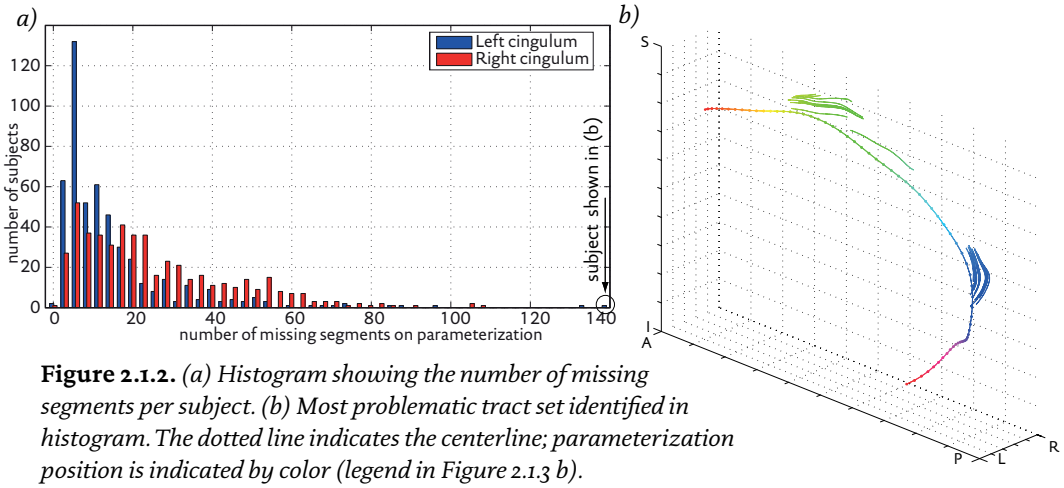

Figure 2.1.2. *(a) Histogram showing the number of missing segments per subject. (b) Most problematic tract set identified in histogram. The dotted line indicates the centerline; parameterization position is indicated by color (legend in Figure 2.1.3 b).*

all subjects' FA image using 'elastix', a publicly available software package that uses an efficient stochastic gradient descent optimization method.[12] The registration is used to transform the atlas' labels to each subject's native space, resulting in an initial three-dimensional segmentation of the cingulate bundle. In following iterations, an improved segmentation is used, which is derived after filtering for co-linearity.

Tract selection

The cingulate template is used to identify tracts running inside the cingulum. Owing to the absence of nearby co-linear structures, we assume that fiber tracts which are partially within the cingulum before they divert due to, e.g., partial voluming effects, can be included in the analysis.[9] Tracts are cut off when leaving the segmented region unless they reenter the segmentation within a maximum distance (*maxDist*). In this case they are considered part of the cingulum and included in the filtered tract set. A tract-density map is generated from the identified tracts at a 1mm cubic grid, indicating the number of cingulum tracts visiting each voxel.

Derivation of the centerline and projection of tracts

By extracting the centerline of the cingulum, we establish a parameterization axis for the tract set. We achieve this by treating the tract-density map as a reciprocal cost image, and find the minimum cost centerline from one end of the cingulum to the other. To bridge potential gaps in the tract sets, we allow background voxels to be part of the centerline, but only at high costs (*backgroundWeight*). The parameterization should permit direct inter-subject comparison and should therefore not depend on individual performance of the fiber tracking. Especially at the far ends of

the cingulum, tracts are often hard to reconstruct, leading to decreased tract density, which in turn could lead to problems in establishing correspondence across subjects. We therefore add the registered atlas mask to the tract density map with a fixed weight (*atlasWeight*), prior to converting it to the cost image. In dense regions, this has little effect, but in sparse regions, this allows to find the centerline aided by the registered atlas. The centerline is smoothed by fitting a Bspline with a fixed number of control points (*controlPoints*). The parameterization is then super sampled using *parSegments* equally spaced segments.

We then use the planes normal to the parameterized centerline to associate every tract segment to one of the parameterization segments.

Co-linearity filtering

Because of the linear structure of the cingulum, it is safe to assume tracts running inside the cingulum are to a certain extent co-linear. Therefore, for every tract segment, we use the local direction to calculate co-linearity defined as the absolute dot product of the tract and parameterization segment direction vectors. A filtering step is then applied to exclude tract segments that are not co-linear (less than *minColin*) with the parameterization for a prolonged segment length (*maxDist*). After filtering, we construct a binary segmentation of all voxels containing tract(s).

Iterative approach

The binary tract mask can be regarded as an improved segmentation of the cingulate bundle. It has been allowed to expand, by tracts locally exiting and re-entering the previous segmentation. And it has been allowed to shrink, by the local absence of co-linear tract segments. The mask is used as an updated segmentation for the entire procedure. The whole procedure is performed iteratively, until either follow-up iteration masks disagree on less than a fixed number of voxels (*maxVoxels*), or when a maximum number of iterations (*maxIt*) has been performed.

Statistical analysis

Measures describing tracts and tract locations, such as FA, tract curvature etc, are at this point associated with a single linear parameterization and can thus be compared across subjects. In our application study, we chose to study hemispheric asymmetry in FA of the cingulum. The FA is a well-established measure and allows comparison of our results with previously published findings.

Experiments and results

DTI data from the population based Rotterdam Scan Study is used.[13] From this prospective cohort study, a random subset of 500 datasets was selected. Mean age of participants was 54.9 years, with an SD of 5.52; 52 percent of participants was female. All subjects were scanned on a 1.5 tesla GE MRI system, with the following DTI acquisition parameters: 25 diffusion gradient directions, FOV= 210x210 mm^2, scan matrix= 96x64 (zero padded in k-space to 256x256), slice thickness 3.5 mm, 35 contiguous slices, TR= 8,000 ms, TE= 68.7 ms, b-value= 1000 s/mm^2 and 3 volumes acquired without diffusion weighting. Datasets were preprocessed using the FDT toolbox in FSL[14] to correct for head motion and Eddy currents and to calculate FA images for the atlas registration. Atlas registration was performed using a 10 mm B-spline control point spacing using mutual information for similarity and took 8 minutes per subject on a single standard CPU. Streamline tractography was performed seeding tracts in a 2 mm cubic grid; and ending tracts when FA dropped below 0.2, taking 2 minutes per subject to compute.

The applied setpoints have been determined empirically by visual inspection of resulting tract sets. The *maxDist* length of a tract part that is allowed outside the segmentation, as well as the maximum non-collinear length has been set to 3mm. The *backgroundWeight*, allowing the parameterization to cross over gaps, is set to 5 times the maximum costs encountered in the individual cost image. The *atlasWeight* is set to 1. The number of *controlPoints* of the parameterization is 15, later super sampled to 200 *parSegments*. Tract segments need to have a *minColin* of 0.8 to be considered co-linear with the parameterization. Iteration stops once the tract mask changes at most *maxVoxels*, 10, in a single iteration, or after reaching *maxIt*, 5, iterations. Iterative filtering took 9 minutes to compute; per subject per hemisphere.

The tract selection method does not require a tract to be mapped at every parameterization segment. Figure 2.1.2(a) shows a histogram of the number of associated parameterization segments per subject. Ideally, all subjects should have no missing segments, this is however not the case. For the worst performing subject, the rightmost element in Figure 2.1.2(a), the tract set is shown in Figure 2.1.2(b). The procedure identified a very limited number of tract segments; yet it did not make any apparent mistakes in corresponding the tract set. A typical tract set is shown in Figure 2.1.3(a).

The FA is compared between the left and right cingulum for every segment of the parameterization, using a two-tailed paired t-test. Data analysis is performed per parameterization segment. Subjects therefore need to have a mean FA value associated with a particular segment on both the left and the right side. Failure in either or both hemispheres leads to exclusion of that subject from the analysis at that particular pa-

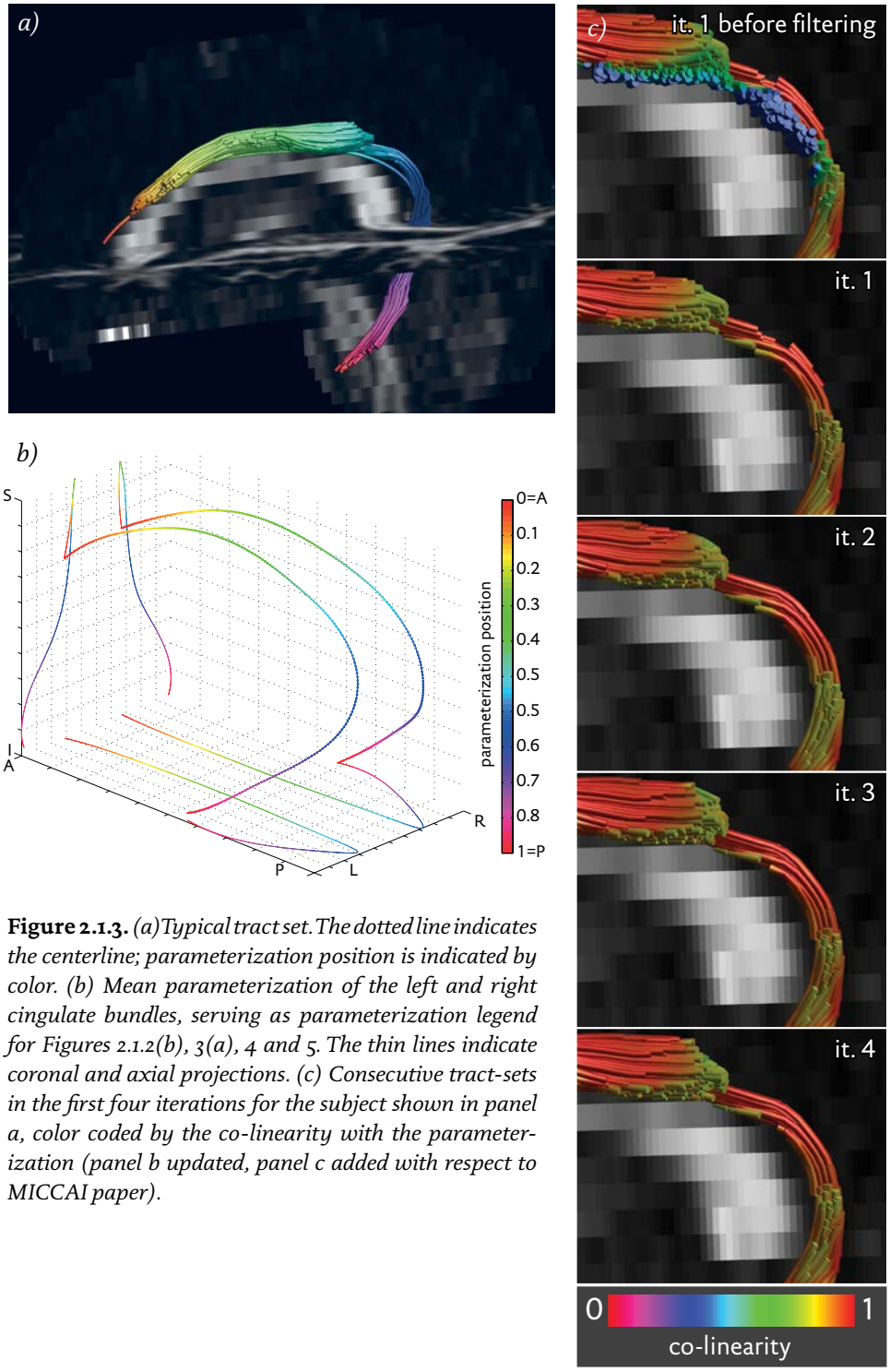

Figure 2.1.3. *(a) Typical tract set. The dotted line indicates the centerline; parameterization position is indicated by color. (b) Mean parameterization of the left and right cingulate bundles, serving as parameterization legend for Figures 2.1.2(b), 3(a), 4 and 5. The thin lines indicate coronal and axial projections. (c) Consecutive tract-sets in the first four iterations for the subject shown in panel a, color coded by the co-linearity with the parameterization (panel b updated, panel c added with respect to MICCAI paper).*

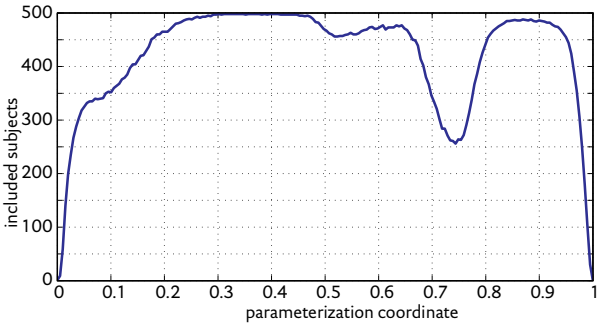

Figure 2.1.4. *(a) Number of complete cases, i.e. subjects with FA measurements in both left and right cingulate bundle, tested per parameterization segment.*

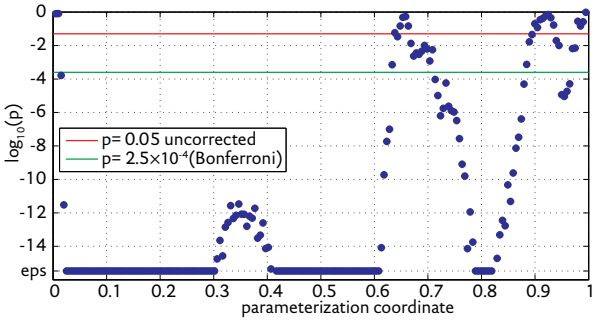

(b) Significance per tract segment, reported in log(p)-values.

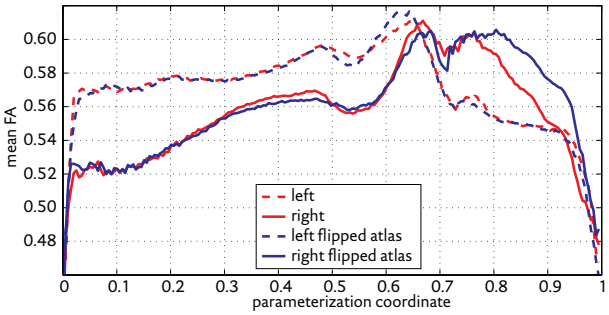

Figure 2.1.5. *(a) Mean FA in left and right cingulate bundles, compared to mean FA obtained using a flipped atlas.*

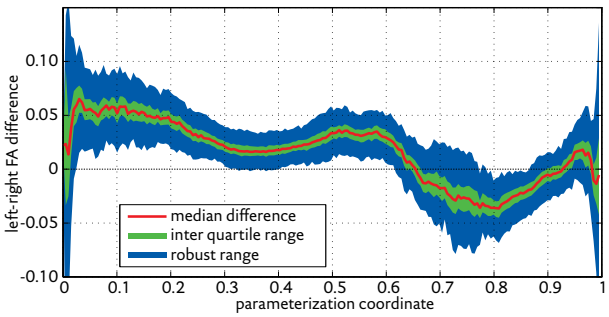

(b) Robustness of left-right FA difference, measured by 200 random draws of 50 subjects from the total set of 500 subjects.

rameterization segment. Figure 2.1.4(a) shows the number of subjects included for every tract segment. Resulting log(p)-values, shown in Figure 2.1.4(b), show highly significant differences in both the anterior and posterior part of the cingulum. Mean parameterization coordinates are presented in Figure 2.1.3(b) for reference, the mean FA along the left and right cingulate bundles is presented in Figure 2.1.5(a).

As we are studying hemispheric asymmetry, it is important to rule out asymmetric influence of the atlas. To verify our findings, we flipped the atlas over the sagittal plane and repeated the registrations to the subjects' FA images. These new registrations were used to again measure FA profiles in cingulate bundles for all subjects. The blue lines in Figure 2.1.5(a) present the mean FA profiles for left and right cingulate bundles, extracted with the flipped atlas, where left means subject-left. The profiles appear nearly identical to the original results, ruling out a bias by the atlas.

To investigate robustness of our findings, we evaluated the mean left – right FA in a subset of 50 subjects, repeatedly drawn random from the full set; shown in Figure 2.1.5(b).

Discussion

We have developed a novel method for selecting tracts of interest from a whole brain tract set. The approach is especially useful in large datasets and is aimed at investigating tracts that are difficult to follow with more conventional region of interest tract selection approaches. The present work allows tracking of tube-like structures such as the cingulate bundle or the fornix. We acknowledge that the method contains a number of thresholds, albeit most of them having a physical, intuitive meaning, which have to be predefined. These were determined by qualitative evaluation of the resulting tract selections. To validate our method we compared analysis results with published findings. To this extent we have studied inter-hemispheric differences in cingulate FA using a large sample of 500 subjects from the general population. We have shown that our findings are not caused by a bias in the initial atlas segmentation. In the anterior part of the cingulum, we observe a very significant difference with the FA being higher left than right. This is in agreement with results from other analyses that also used some form of tract selection.[6,7,9] Less is known, however, for the posterior cingulate. Malykhin et al.[7] selected tracts in this region in 24 healthy subjects. They found no significant difference between left and right tracts, possibly lacking statistical power. As the anterior and posterior cingulate are involved in different processes, the left/right difference in FA between the anterior and posterior cingulum might be hypothesized to reflect a difference in function between left and right hemispheric processes.

We tested for differences using a paired t-test on the parameterization-segment level, and reported p-values for every segment. To correct p-values for the number of tests performed (we tested on 200 segments), a permutation based correction method would be appropriate.[15] Applying a Bonferroni correction results in an overly conservative upper bound to the multiple comparison correction, but still leaves our findings highly significant, as indicated by the green threshold in Figure 2.1.4(b).

The method allows capturing the difficult connection between the posterior and anterior cingulate, but it does so with varying success along the pathway. For the most problematic segment, about half of the subjects give problems in either or both of the cingulate bundles, as shown in Figure 2.1.4(a).

Conclusion

We have developed a fully automated method for the robust extraction and parameterization of the cingulum including the posterior cingulate. As an example application, we studied asymmetry of FA in the cingulum. Our findings in the anterior part, where FA was found to be higher left than right, are in agreement with previous research. Our analysis also found right higher than left FA in the posterior part. This structural asymmetry might relate to functional differences between hemispheres.

References

1. Basser PJ, Mattiello J, LeBihan D. MR diffusion tensor spectroscopy and imaging. *Biophys J*. 1994;66(1):259-67.
2. Basser PJ, Jones DK. Diffusion-tensor MRI: theory, experimental design and data analysis - a technical review. *NMR Biomed*. 2002;15(7-8):456-467.
3. Smith SM, Jenkinson M, Johansen-Berg H, et al. Tract-based spatial statistics: voxelwise analysis of multi-subject diffusion data. *Neuroimage*. 2006;31(4):1487-1505.
4. Kindlmann G, Tricoche X, Westin C-F. Delineating white matter structure in diffusion tensor MRI with anisotropy creases. *Med Image Anal*. 2007;11(5):492-502.
5. Melonakos J, Mohan V, Niethammer M, Smith K, Kubicki M, Tannenbaum A. Finsler tractography for white matter connectivity analysis of the cingulum bundle. *Int Conf Med Image Comput Comput Assist Interv*. 2007;10(Pt 1):36-43.
6. Gong G, Jiang T, Zhu C, et al. Asymmetry analysis of cingulum based on scale-invariant parameterization by diffusion tensor imaging. *Hum Brain Mapp*. 2005;24(2):92-98.
7. Malykhin N, Concha L, Seres P, Beaulieu C, Coupland NJ. Diffusion tensor imaging tractography and reliability analysis for limbic and paralimbic white matter tracts. *Psychiatry Res*. 2008;164(2):132-142.
8. Nakata Y, Sato N, Nemoto K, et al. Diffusion abnormality in the posterior cingulum and hippocampal volume: correlation with disease progression in Alzheimer's disease. *Magn Reson Imaging*. 2009;27(3):347-354.
9. O'Donnell LJ, Westin C-F, Golby AJ. Tract-based morphometry for white matter group analysis. *Neuroimage*. 2009;45(3):832-844.
10. Leemans A, Jeurissen B, Sijbers J, Jones D. ExploreDTI: a graphical toolbox for processing, analyzing, and visualizing diffusion MR data. In: *Proceedings 17th Scientific Meeting International Society for Magnetic Resonance in Medicine*.Vol 17.; 2009:3537.

11. Mori S, Oishi K, Jiang H, et al. Stereotaxic white matter atlas based on diffusion tensor imaging in an ICBM template. *Neuroimage*. 2008;40(2):570-582.

12. Klein S, Staring M, Pluim JPW. Evaluation of optimization methods for nonrigid medical image registration using mutual information and B-splines. *IEEE Trans Image Process*. 2007;16(12):2879-90.

13. Hofman A, Breteler MMB, van Duijn CM, et al. The Rotterdam Study: objectives and design update. *Eur J Epidemiol*. 2007;22(11):819-829.

14. Smith SM, Jenkinson M, Woolrich MW, et al. Advances in functional and structural MR image analysis and implementation as FSL. *Neuroimage 23 S1*. 2004;23 Suppl 1:208-219.

15. Nichols TE, Holmes AP. Nonparametric permutation tests for functional neuroimaging: a primer with examples. *Hum Brain Mapp*. 2002;15(1):1-25.

2.2

Improving alignment in Tract-based spatial statistics: Evaluation and optimization of image registration

NeuroImage 2013

Marius de Groot
Meike W. Vernooij
Stefan Klein
M. Arfan Ikram
Frans M. Vos
Stephen M. Smith
Wiro J. Niessen
Jesper L.R. Andersson

Anatomical alignment in neuroimaging studies is of such importance that considerable effort is put into improving the registration used to establish spatial correspondence. Tract-based spatial statistics (TBSS) is a popular method for comparing diffusion characteristics across subjects. TBSS establishes spatial correspondence using a combination of nonlinear registration and a "skeleton projection" that may break topological consistency of the transformed brain images. We therefore investigated feasibility of replacing the two-stage registration-projection procedure in TBSS with a single, regularized, high-dimensional registration.

To optimize registration parameters and to evaluate registration performance in diffusion MRI, we designed an evaluation framework that uses native space probabilistic tractography for 23 white matter tracts, and quantifies tract similarity across subjects in standard space. We optimized parameters for two registration algorithms on two diffusion datasets of different quality. We investigated reproducibility of the evaluation framework, and of the optimized registration algorithms. Next, we compared registration performance of the regularized registration methods and TBSS. Finally, feasibility and effect of incorporating the improved registration in TBSS were evaluated in an example study.

The evaluation framework was highly reproducible for both algorithms (R^2 0.993; 0.931). The optimal registration parameters depended on the quality of the dataset in a graded and predictable manner. At optimal parameters, both algorithms outperformed the registration of TBSS, showing feasibility of adopting such approaches in TBSS. This was further confirmed in the example experiment.

Introduction

Diffusion imaging of the brain provides insight into architectural properties, and developmental and degenerative processes of the white matter.[1–3] Quantitative features derived from diffusion imaging, such as fractional anisotropy (FA) and mean diffusivity (MD), allow for comparison of diffusion properties across different subjects.[4] This can be achieved in a number of ways, for example region of interest-based or voxel-based.

Voxel-based analyses offer a fast and automated means of analyzing diffusion data.[5–7] They do however require the images to be in a common space in which anatomical correspondence across subjects is assured. Establishing correspondence by bringing images into a common space is a non-trivial task, for which image registration techniques are commonly employed. However, image registration approaches in general do not achieve perfect anatomical correspondence due to anatomical variability. In an attempt to account for the residual misalignment, increase sensitivity and to satisfy the assumptions of parametric tests (if applied), voxel-based analyses often rely on smoothing. The extent of this smoothing ideally needs to be matched to the expected effect size, which can be spatially varying and not known a-priori.[8] In 2006, an alternative approach for anatomical alignment of diffusion data was proposed. Tract-based spatial statistics (TBSS)[9,10] was introduced to mitigate the influence of residual misalignment in registration of diffusion data, and to overcome the need to set smoothing extent in voxel-based analyses. In TBSS, following an initial nonlinear registration step (of "medium" dimensionality), voxels that are local maxima for FA are mapped onto a skeleton composed of sheets of maximum FA voxels, and statistical analysis is performed on skeleton voxels. Constraining the analysis to the white matter skeleton results in a dimensionality reduction, ameliorating the issue of multiple testing. Over the past years, TBSS has been widely adopted, aided by its availability within FSL[11,12] and ease of use. The projection stage in TBSS however, is a spatially local operation, with the voxels containing locally maximal FA projected onto the skeleton independently; therefore it does not enforce spatial consistency of the warped images. This may result in an undesirable loss of anatomical topology of tracts in the projection stage. The main aim of this work is to investigate if it is feasible to replace the two registration + projection stages by a single regularized high-dimensional registration approach inside the TBSS method (while still aiming to carry out cross-subject voxelwise testing on the skeleton, to help minimize correspondence errors).

Since even small errors in correspondence may substantially influence results,[9] considerable effort has been put in improving the registration of diffusion data.[13–18] In registration, a spatial transformation is determined by optimizing a similarity metric. For evaluating registration performance across algorithms, such as performed for diffusion imaging by Wang et al.,[19] or to optimize different registration parameters, a similarity metric must be employed as well. This is necessary since we do not know the ground truth anatomical correspondence of two images. To objectively measure registration performance however, we cannot use the same similarity metric that was optimized in the registration process, since this would bias the evaluation.

Similarity metrics in diffusion image registration can be based on scalar images such as FA or structural images. Metrics can, alternatively, be based on higher dimensional image features, e.g., on the full diffusion tensor or a number of its compo-

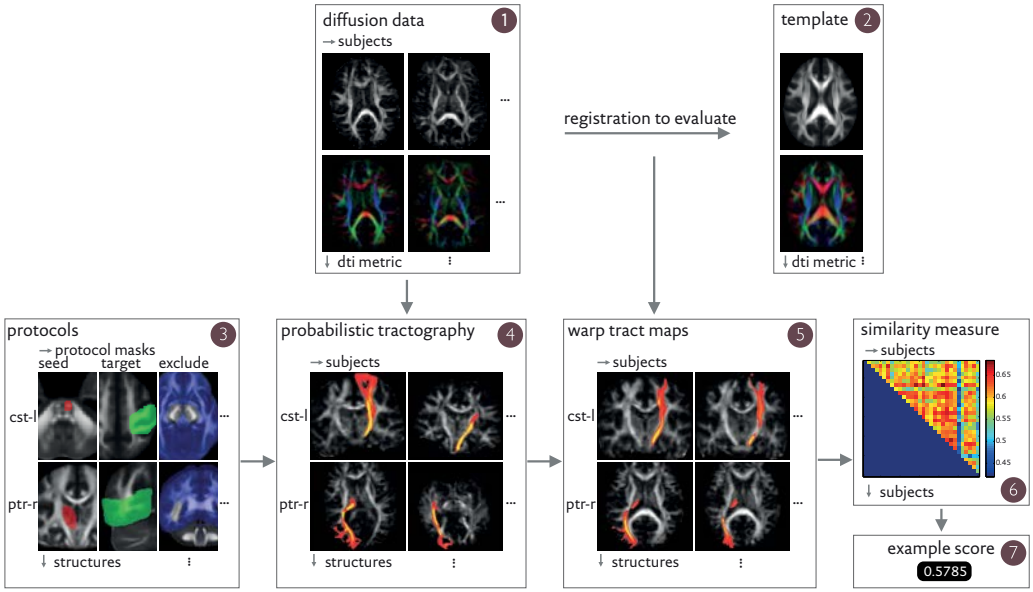

Figure 2.2.1. *Schematic overview of the evaluation framework. Diffusion data in subject-native space (box 1) for N subjects are registered to an appropriate template image (box 2). This registration can be based on FA images, the full tensor, or on any other DTI metric. This set of N registrations obtained with a particular registration algorithm is the registration under evaluation. Separately, standard space seed, target, stop and exclusion masks (box 3) that initialize the probabilistic tractography are transformed to subject native space using a conservative nonlinear registration. Tractography for the total set of 23 structures is performed in subject native space (box 4). The registration under evaluation is used to warp the tract-density images to standard space for all N subjects (box 5). The similarity of the warped tract-density images in standard space is quantified via spatial correlation, for each structure and for each pair of subjects (NxN). The similarity is averaged over all structures (box 6), and then averaged over all subject pairs to yield the registration performance for the particular registration under evaluation (box 7).*

nents. A third category of similarity metrics is defined on the results of white matter tractography. These three classes of similarity metrics have all been used in the objective functions of image registration approaches for diffusion images.[14,17,18,20–22] Analogously, similarity metrics in all three categories have been employed in order to evaluate registration performance.[14,16,17,19,23,24]

An important advantage of a performance measure based on similarity of tractography results is that it is independent of any particular similarity metric, defined on a scalar or higher order image, which is employed in most registration approaches. Also, optimal white matter tract alignment is most closely linked to the eventual registration aim of obtaining anatomical correspondence in white matter.[25] We therefore developed a framework to evaluate scalar or higher-order similarity met-

ric based registrations using tractography. Previous work using white matter tractography for this purpose was based either on whole brain tractography[14] or only on a small selection of tracts.[16,18,24,26,27] Furthermore, all previous work depended on deterministic tractography, which has more difficulty in coping with complex fiber architecture (e.g., crossing fibers) and signal noise than probabilistic tractography.[28]

In this work, we extended the use of tractography for image registration evaluation to a broader range of white matter tracts, and we used a probabilistic model for tractography. Parameters for two nonlinear registration algorithms were optimized using similarity of different subjects' warped tracts as the registration performance measure. The optimization was performed on two datasets acquired at different institutions with different spatial resolution. Registration performance for these optimized approaches was then compared to the registration performance of the TBSS method on a white matter skeleton. We show that the optimized registration reproducibly improved the alignment of white matter structures compared to TBSS.

Methods

The evaluation framework consists of an automated approach to perform probabilistic tractography and a tract-based evaluation metric. A schematic overview of the process is provided in Figure 2.2.1.

Tractography
Tractography was performed with PROBTRACKX,[28,29] a Bayesian approach to probabilistic tractography available in FSL.

Tractography was initialized by defining standard space "seed", "target", "stop" and "exclusion" ROIs (masks). These masks were based on the protocols described by Mori et al.,[30] Stieltjes et al.,[31] and Wakana et al.,[32,33] but had to be adapted to cope with the more dispersing nature of probabilistic tractography. Most importantly, exclusion masks were added, e.g., the mid-sagittal slice was added in all but the commissural tracts. All masks were transferred to subject native space using nonlinear registrations obtained with FNIRT[34] with default settings for FA images as available in FSL.

Tracts that could robustly be identified and which would lead to a reasonably uniform sampling across brain regions were selected. These tracts are listed in Table 2.2.1. Two tracts, the posterior thalamic radiation and the inferior fronto-occipital fasciculus, were excluded from the final set because of considerable overlap with other tracts. Exclusion of these tracts prevented uneven weighting of different regions in the registration evaluation. The final set therefore consisted of 23 tracts.

Table 2.2.1
Overview of tracking protocols for different tracts in the evaluation framework. Tracts with left/right homologues are listed under 'l/r'. If a stop mask is used, its relative location to the tract is given under the 'stop' column. The number of seed points per voxel is listed under 'seed #'. Tracts that were generated twice with inverted target-seed regions are listed under 'invert'. References ('refs') translate to a: Stieltjes et al.,[31] b: Wakana et al.,[32] c: Mori et al.,[30] d: Wakana et al.[33]

	l/r	stop	seed # (×1000)	inv.	refs
Tracts in brainstem					
Middle cerebellar peduncle	-		2	+	a,b
Medial lemniscus	+	sup.	4	-	a,b
Projection fibers					
Corticospinal tract	+		10	-	a,b,d
Acoustic radiation	+	med.	10	+	
Anterior thalamic radiation	+	post.	2	-	b,c,d
Superior thalamic radiation	+	inf.	2	-	b
Posterior thalamic radiation	+		30	-	b,c
Association fibers					
Superior longitudinal fasciculus	+		2	+	b,c,d
Inferior longitudinal fasciculus	+	ant.	2	-	b,c,d
Inferior fronto-occipital fasciculus	+		4	-	b,c,d
Uncinate fasciculus	+		4	-	b,c,d
Limbic system fibers					
Cingulate gyrus part of cingulum	+	ant. & post.	30	-	b,d
Parahippocampal part of cingulum	+	sup. & inf.	4	-	b,d
Callosal fibers					
Forceps minor	-		2	+	b,d
Forceps major	-		2	+	b,d

Tractography was performed in subject native space while recording tract density at a 1 mm^3 resolution and using between 2,000 and 30,000 samples per seed ROI voxel to account for differences in the number of seed voxels and tract geometry. These parameter settings were selected to aim for robust extraction of the tracts, and were based on the observed number of fiber-particles that were included in the tract together with visual inspection of tractography outputs. Commissural tracts and the middle cerebellar peduncle were tracked a second time (adding both runs) with inverted seed-target ROIs to ensure symmetry of the resulting tract. The acoustic radiations and the superior longitudinal fasciculus were also tracked in both directions to increase robustness. After tracking, the tract density image was normalized by dividing with the total number of particles.

An example of an individual subject's tracking result, thresholded for the purpose of visualization, for all tracts is shown in Figure 2.2.2. Tractography was performed for each subject and for each structure. The resulting maps of white matter structures reside in subject native space, and were used for all evaluations.

Tract-based evaluation metric
The registration performance measurement was based on cross-subject similarity of the warped tract maps. Non-thresholded tract density images in subject native space were warped to common space, and then tract similarity was assessed.

To avoid differences in image characteristics between individual and group mean tract maps influencing the results, tract similarity was evaluated on a subject-to-subject basis. Tract similarity was assessed for each structure individually, and then averaged for all structures in each pair of subjects. In order to provide an even weighting over tracts in this averaging, similarity of left–right homologue structures was jointly given an equal weight as that of the commissural tracts and the middle cerebellar peduncle. If a particular tract could not be identified in one of the subjects with the automated tractography approach (i.e. no particles fulfilled the criteria imposed by the protocol masks), the tract was omitted in the aggregation of the subject–subject similarity score.

Similarity was assessed with the spatial correlation similarity metric,

$$C = \frac{\sum_i \mathbf{J}_i \mathbf{K}_i}{\sqrt{\sum_i \mathbf{J}_i^2} \sqrt{\sum_i \mathbf{K}_i^2}}$$

which is similar to the Pearson correlation coefficient, and provides a measure of voxelwise similarity of the continuous tract density image intensities ($\mathbf{J}$ and $\mathbf{K}$) for two subjects, computed over all voxels (i), and is bound on a 0 – 1 scale. Similarity was calculated on the tract density images.

The probabilistic nature of tractography means that the intensity in the tract map varies; more support for the tract will translate into higher intensity. Increased uncertainty will conversely translate into lower tract-density. The information that is thereby encoded in the tract-density image is related to the anatomy of the tract. The similarity, as measured by the spatial correlation similarity metric, across two subjects therefore provides valuable feedback on alignment of the tracts in those subjects.

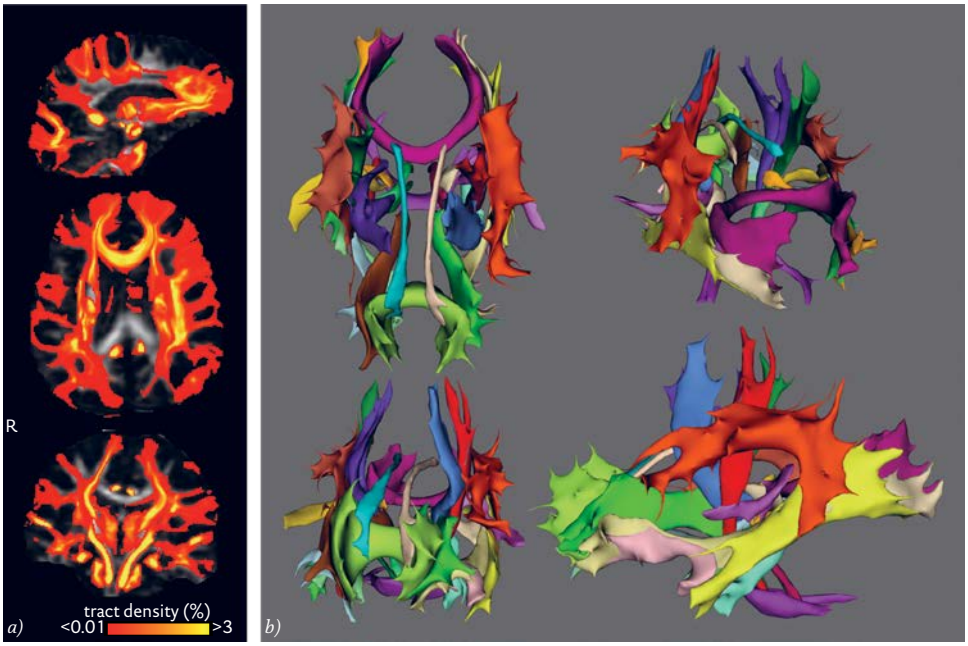

Figure 2.2.2. *Automated tractography result for one individual in the Rotterdam dataset. The same subject is shown in seven different views. (a). Continuous probabilistic tractography output used in the evaluation for all structures combined. (b). Probabilistic tractography output thresholded for visualization purposes only. The threshold was applied on the normalized tract-density images, rejecting voxels containing less than 0.5% of the total number of tracts per structure.*

Evaluation on the skeleton

To investigate the feasibility of replacing the registration-projection in TBSS with a regularized, high-dimensional registration, we compared registration performance for both registration algorithms with the standard TBSS approach. The registration evaluation framework described above was therefore further tailored for both approaches to enable this comparison.

First, for the high-dimensional registrations, the registration performance measurement had to be constrained to the TBSS skeleton. Hence, the warped continuous tract-density images that resulted from the regularized high-dimensional registration were masked using the TBSS white matter skeleton mask, producing skeletonized tract density images for each structure, for each subject, which were used to evaluate registration performance.

Next, for assessing registration performance of TBSS, the measurement also needed to be constrained to the skeleton. Hence, the continuous tract density images for all structures were (separately) projected onto the white matter skeleton using the

non-FA-image pipeline available within TBSS[9]; this allows the initial registration and the skeleton projection, both derived from the FA data, to be applied to other scalar images starting in the same space as the FA data. This produced skeletonized tract density images for each structure, for each subject, which were used to evaluate registration performance.

Optimization experiments

Diffusion MRI data

Two sets of scans from two different MRI centers were used in the experiments. The first dataset represents a "low-end" diffusion acquisition; the second dataset is representative of a state-of-the-art, though still relatively "off-the-shelf", high resolution, high signal-to-noise diffusion acquisition.

Lower resolution: Rotterdam data
The first dataset was derived from the Rotterdam Scan Study,[35] a neuroimaging study embedded in the larger, prospective population-based Rotterdam Study[36] composed of middle aged and elderly subjects. The diffusion data is part of a multi-sequence MRI protocol on a 1.5 tesla GE Signa Excite scanner. For DTI, single shot, diffusion-weighted spin echo-planar imaging data were acquired (repetition time (TR) = 8,575 ms, echo time (TE) = 82.6 ms, field-of-view (FOV) = 210 × 210 mm, matrix = 96 × 64 (phase encoding) (zero-padded in k-space to 256 × 256) slice thickness = 3.5 mm, 35 contiguous slices). b-value was 1000 s/mm2 in 25 non-collinear directions (number of excitations (NEX) = 1), and three volumes with no diffusion weighting were acquired. Acquisition time was 5 min. A sample of 30 subjects from the study population was rescanned on average 19.5 (SD 10.0) days after the baseline scan. These subjects were on average 76.7 years old (SD 4.8); 15 were female. The set of 30 baseline scans was used in the registration optimization experiments; the set of rescanned data (30 scans) was used to evaluate reproducibility of the evaluation framework. This dataset will be referred to as the Rotterdam data, with the timepoints being labeled as "baseline" and "rescan".

Higher resolution: Oxford data
The second dataset was acquired in healthy adults, described in Jbabdi et al.[37] Scanning was performed on a 1.5 tesla Siemens Sonata scanner. As described in Tomassini et al.,[38] diffusion-weighted data were acquired using echo planar imaging (72 × 2-mm-thick axial slices; matrix size, 128 × 104 (phase encoding); field of view, 256 × 208 mm; giving a voxel size of 2 × 2 × 2 mm). Diffusion weighting was isotropically distributed along 60 directions using a b-value of 1000 s/mm2. For each set of diffusion-weighted data, five volumes with no diffusion weighting were acquired at evenly spaced points throughout the acquisition. Three sets of diffusion-weighted

data were acquired for later averaging to improve the signal-to-noise ratio. The total scan time for the diffusion-weighted imaging protocol was 45 min. Data from 30 subjects were used. Mean age for this group was 32.0 years (SD 8.5); 12 were female. This dataset will be referred to as the Oxford data.

Diffusion data preprocessing

Diffusion data was preprocessed using the FDT toolbox included in FSL. Preprocessing included affine co-registration of all acquired volumes in order to compensate for subject motion and eddy currents. Non-brain tissues were removed with the Brain Extraction Tool. A tensor was fitted to log-transformed data using a linear least squares approach. The tensor image was then upsampled to 1 mm3 resolution, using cubic spline interpolation of the tensor components; note that upsampling of the tensor image is not currently done in TBSS. A high resolution FA image was then derived from the upsampled tensor image. Interpolating the tensor instead of the FA values allows the resulting FA image to contain more spatial detail that could aid the FA based registration algorithms, as visible in Figure 1b and e in Kindlmann et al.[39] Higher registration accuracy (as measured with the evaluation framework) for the tensor-upsampled FA images was confirmed in preliminary experiments.

Separately, following the motion and eddy current correction, a probabilistic model of fiber orientations was fitted for each voxel using BEDPOSTX.[28] BEDPOSTX was run with default parameters, as a preprocessing step for the probabilistic tractography.

Registration algorithms

For two registration algorithms, FNIRT[34] and Elastix,[40] the evaluation framework was used for parameter optimization and performance comparison.

FNIRT,[34] the nonlinear image registration algorithm in FSL, optimizes a B-spline deformation field,[41] and is specifically developed for brain imaging. The objective function is minimization of the sum of squared differences, and incorporates an intensity modulation term to compensate for intensity differences between the moving and reference images. FNIRT uses a multi-resolution strategy to increase robustness against local minima in the optimization. Following each resolution level, diffeomorphic warps are enforced. By concatenating multiple (each itself being multi-resolution) calls to FNIRT in a cascade, registration parameters can be varied over the course of the optimization. For evaluation, warp fields obtained with FNIRT were used to warp tract density images using the Applywarp utility in FSL. Tract density images were warped using cubic spline interpolation.

Table 2.2.2
Settings varied in the registration optimization of FNIRT. FNIRT is run as a cascade of three sets of parameters. Parameters are varied in one or two of these stages, as indicated. Stage 1 in itself contains a series of 4 substages, in which an initial regularization relaxation is performed. Warp field resolution is jointly varied in stages 2 and 3, and the final regularization level is varied in stage 3 alone

Parameter	Stage 1	Stage 2	Stage 3
Number of substages	4	1	1
Warp field resolution (cubic)	10 mm	varied in stages 2 and 3: 4; 2; 1 mm	
Regularization at each substage	varied: steep = 600,125,80,40 medium = 300,75,50,40 flat = 150,60,50,40	fixed (100)	varied: 70-10 (steps of 10)

Elastix[40] (version 4.5) also includes B-spline based nonlinear deformations, and is based on the open source ITK platform. Elastix is designed to run in a cascade of resolutions, and offers the choice between multiple objective functions and multiple optimizers including an efficient adaptive stochastic gradient descent optimizer.[42] When using the sum of squared differences (SSD) similarity metric, the intensity distributions of the moving and reference image are assumed to be equal. While FNIRT incorporates rescaling of the image intensities to compensate for differences, Elastix does not. In order to apply the SSD, we performed a linear intensity transformation as a preprocessing step. Based on the observed FA intensity histograms

Table 2.2.3
Settings varied in the registration optimization of Elastix. Elastix is run as a single cascade of substages

Parameter	Setting
Warp field resolution (cubic)	15 mm / 10 mm / 5 mm / 3 mm
Similarity metric	– normalized cross correlation
	– mutual information
	– sum of squared differences
Multiresolution strategy (of the image data)	– none
	– pyramidal downsampling moving image
	– pyramidal downsampling both images
Regularization weight	none / 1 / 10 / 100
Optimizer	– stochastic gradient descent
	– adaptive stochastic gradient descent
Localized metric	yes / no

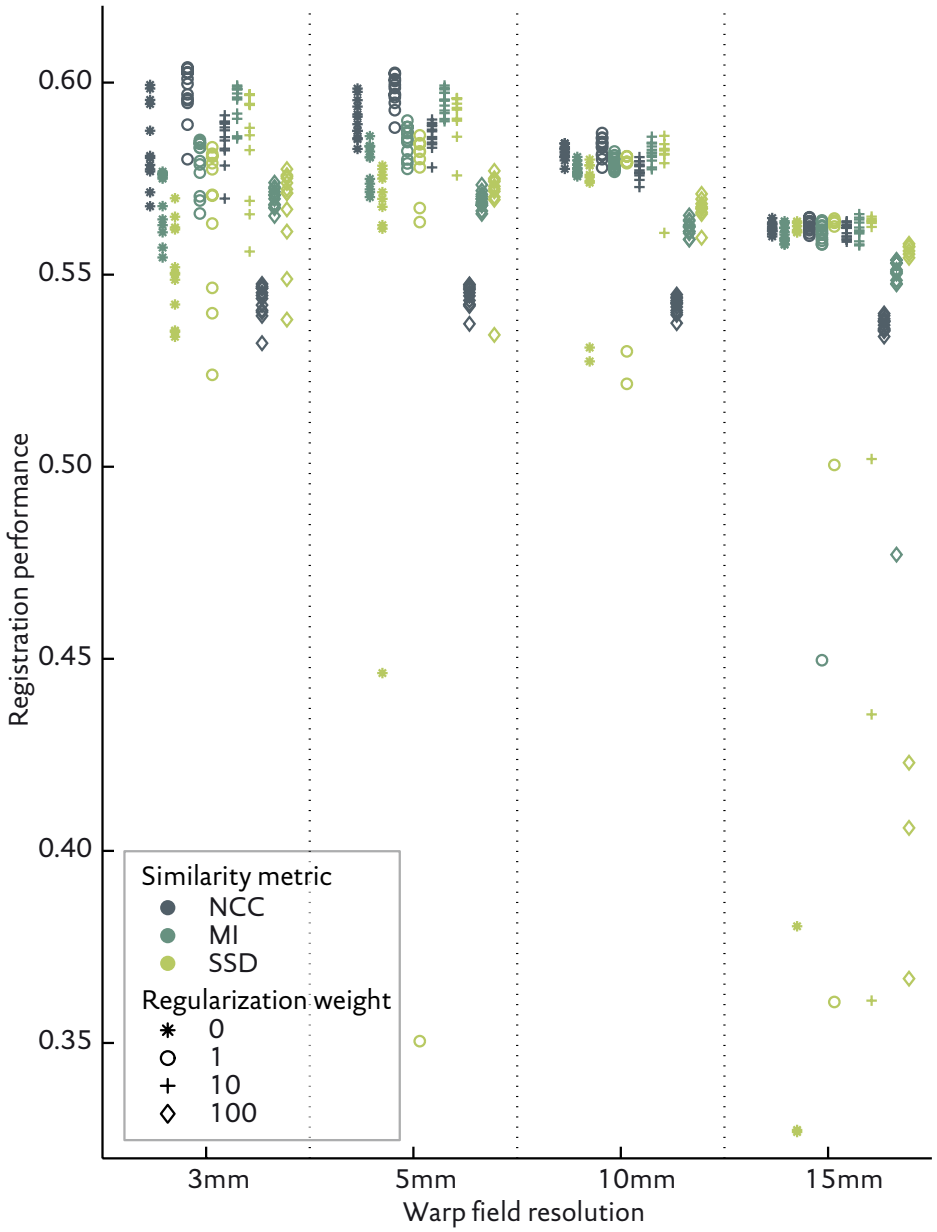

Figure 2.2.3. *Scatterplot of registration performances for all settings evaluated on the Oxford data with the Elastix registration algorithm. Each point represents registration performance (vertical axis) on the entire Oxford dataset as a function of the most influential parameters: warp field resolution (horizontal axis), regularization weight (symbol) and similarity metric (color). Repeated appearance of the same symbol and color corresponds to variations in multi-resolution strategy, optimizer and localization of the similarity metric. Abbreviations: NCC = normalized cross correlation, MI = mutual information, SSD = sum of squared differences.*

for each 30-subject dataset, we matched the 25 and 75 percentile points with those of the template image. Elastix furthermore offers the option to localize the behavior of the similarity metric by employing a regional sampling technique.[43] Spatial transformations obtained with Elastix were applied to the tract density images with Transformix, which is distributed with Elastix. As with FNIRT, we used a cubic spline interpolation.

Optimization experiments

All registrations were performed with the subject FA images as moving image and with the FMRIB-58 FA template as reference image.

For both registration algorithms, the parameters to be optimized were varied in an exhaustive fashion. For FNIRT, the parameters varied in the optimization strategy are listed in Table 2.2.2; fixed parameters are listed in the parameter supplement, which is available online*. All registrations with FNIRT contained some degree of regularization at all stages. The parameter space selected for the optimization resulted in a total of 63 settings of the algorithm.

For the Elastix optimization, parameters and settings that were varied are listed in Table 2.2.3; again, a parameter supplement is available online. This parameter space resulted in a total of 576 settings of the algorithm.

All trials were performed on both datasets. Registration performance, as measured by the tract based similarity measure, was compared between the optimized registration settings for both registration algorithms. To statistically examine the difference between two different sets of registrations, we computed, for each subject, the average similarity to all other subjects in the dataset as defined in the Tract-based evaluation metric section. We then performed paired t-tests, pairing subjects across both algorithms (30 pairs).

To be able to interpret the registration performance measure, we investigated the relationship between warp distance and this measure. Hereto, we applied the (optimum) nonlinear transformation obtained with FNIRT, but scaled it by a fraction between 0.8 and 0.995, and computed the resulting impact on the registration performance. For each subject in the Rotterdam and Oxford datasets, the spline coefficients of the warp field were multiplied by the warp fraction, leaving the affine component of the transformation unchanged. All tract density images were transformed with these fractional warps. Then, for each subject, tract similarity was computed between the partially and fully warped tracts.

* *http://dx.doi.org/10.1016/j.neuroimage.2013.03.015*

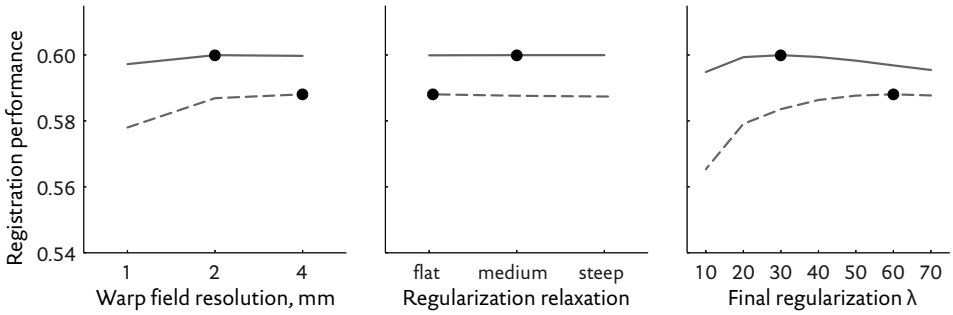

Figure 2.2.4. *Registration performance (vertical axis) of FNIRT, for each of the parameters around the optimum parameter setting. Shown for the Rotterdam data (dashed) and the Oxford data (solid). The optimum points are indicated with dots. Registration performance is separately shown as a function of warp field resolution, regularization relaxation speed and final regularization (higher means more regularization).*

We also compared deformation fields obtained with both registration algorithms operating at optimal parameters. This was done to investigate the difference between the algorithms.

Reproducibility of the performance measurement

As optimization introduces the risk of overfitting to the specific data used in the optimization, we used the unseen rescan data, available for 30 subjects in the Rotterdam data, to test reproducibility of the evaluation framework. This evaluation involved running the pre-processing, the tractography, and the registrations for all settings of both algorithms, and all evaluations on this set of scans. Two tests were performed on these reproducibility measurements. First, for both algorithms we measured the correlation between the performance measurements on the two sets of scans. Second, we focused on the optimal settings for both registration algorithms, and compared the performance with the performance obtained on the rescan data.

Comparison with TBSS

To test feasibility and effect of replacing the registration-projection approach in TBSS (v1.2) with a regularized high-dimensional registration method, we performed three experiments. First we determined whether constraining the performance measurement to the white matter skeleton (as described in Evaluation on the skeleton) altered the behavior of the performance measure for the two registration approaches. Second, we compared the skeletonized registration performance to the

TBSS performance on both datasets (Rotterdam and Oxford), and also between the registration algorithms. Third, we conducted an example analysis to investigate the influence of replacing the registration and projection stages with the improved registration, in a real-life study setting. For this experiment, we used MRI data of 50 female subjects from the Rotterdam Scan Study, aged 68–80 (mean 74.8, SD 2.9). These data were acquired and processed in a manner identical to the Rotterdam data that was used for the registration optimization but the subjects used for this example application were not included in the optimization experiment. We investigated the established[44,45] association between age and FA, with head size as a confound regressor, with both TBSS and TBSS using the improved registration using FNIRT. Further details are provided in the caption Figure 2.2.10.

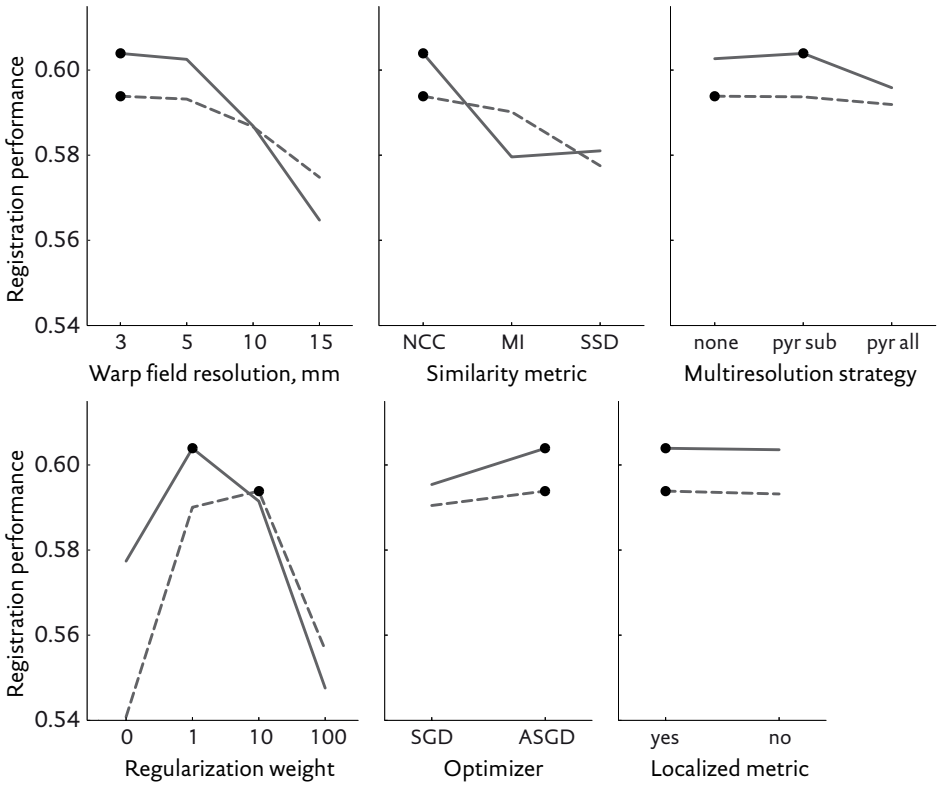

Figure 2.2.5. *Registration performance (vertical axis) of Elastix, for each of the parameters around the optimum parameter setting. Shown for the Rotterdam data (dashed) and the Oxford data (solid). The optimum points are indicated with dots. Registration performance is separately shown as a function of warp field resolution, similarity metric, multiresolution strategy, regularization weight, optimizer, and localization of the similarity metric. Abbreviations: NCC = normalized cross correlation, MI = mutual information, SSD = sum of squared differences, pyr = pyramidal downsampling, sub = subject (moving) image, all = both images.*

Results

Optimization experiments

For optimization of the two registration algorithms, 639 registration settings (63 for FNIRT, 576 for Elastix) on both the Rotterdam data and Oxford data were performed and evaluated, adding up to a total of 639 sets of 60 registrations each. For Elastix, some combinations of parameters resulted in aborted registrations due to non-convergence for one or more subject images. In this case, the particular setting of the registration algorithm (30 for the Rotterdam data, 34 for the Oxford data) was completely excluded from the analysis. The resulting 1,214 performance measurements therefore contained no cases of non-convergence, and are presented in three ways.

To illustrate the results of the optimization procedure for one of the four combinations of registration algorithm and dataset, the optimization of Elastix on the Oxford data, performance as a function of the most influential parameters is shown in Figure 2.2.3. This graph shows all performance measurements for the combination of algorithm and dataset, as a function of the parameters that influenced registration performance most (three parameters are not discernible in this figure). Warp field resolution is presented on the horizontal axis, regularization is indicated with a symbol, and registration similarity metric is indicated by color. The graph shows that the optimal amount of regularization depended on the similarity metric. The graph also shows that robustness with respect to the indiscernible parameters (multiresolution strategy, optimizer and localization of the similarity metric) depended on warp field resolution, as indicated by the distribution of similar marks general-

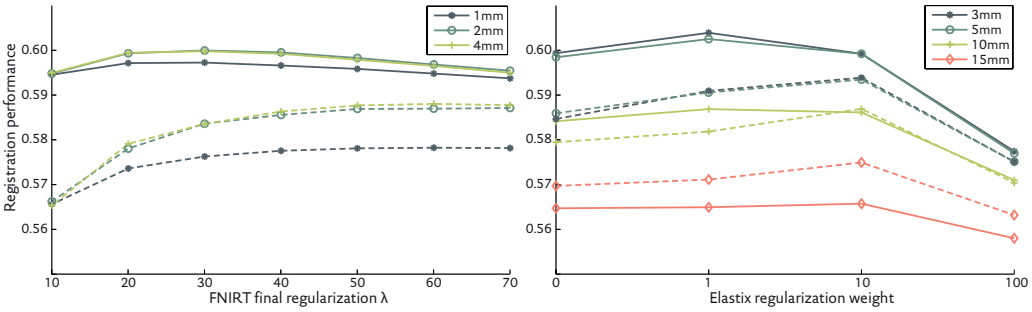

Figure 2.2.6. *Maximum registration performance (vertical axis) for both algorithms and both datasets, as a function of regularization (horizontal axis) and warp field resolution (color). For each point on the graph, the maximum performance as a function of the other parameters is plotted. Performance for FNIRT is shown on the left, Elastix on the right. The dashed lines indicate Rotterdam data, the solid lines Oxford data.*

ly fanning out for increasing resolution. For conciseness, graphs for the other three combinations of registration algorithm and dataset are omitted and summarized results are presented in Figs. 2.2.4 and 2.2.5. To visualize parameter dependence, the marginal variation of the performance measurement when varying parameters around the optimum point is shown in Figs. 2.2.4 and 2.2.5. Based on the optimal registration parameters, these graphs show the influence of each of the parameters under investigation. These figures show that the warp field resolution, regularization, and, for Elastix, similarity metric were the most influential parameters in the optimization.

Optimal registration parameters for FNIRT depended on the resolution of the data that was being registered (Figure 2.2.4), even though the optimum settings for both datasets are located in relatively flat segments of the parameter-performance curves and the dependence is therefore fairly weak. For the Rotterdam data, optimal resolution for the final B-spline grid was 4 mm, compared to 2 mm for the higher-resolution Oxford data, although in both cases either choice would not result in a large change in performance. The optimal regularization at the last cascade of the registration was 60 for the Rotterdam data, compared to 30 for the Oxford data. The relaxation speed for the regularization was the least influential parameter, but was different for both datasets nonetheless; flat for the Rotterdam data compared to medium steep for the Oxford data.

Optimal registration parameters for Elastix also depended on the dataset being optimized. Two of the most influential parameters were the same for both datasets; warp field resolution was optimal at 3 mm and normalized cross correlation (NCC) was the optimal similarity metric. Optimal regularization weight depended on the dataset; for the Rotterdam data a weight of 10 was optimal, and for the Oxford data a weight of 1. Of the least influential parameters, two parameters had the same optimum for both datasets; the optimal optimizer (adaptive stochastic gradient descent), and localization of the similarity metric (yes). One parameter differed; for the Rotterdam data, the optimal multiresolution strategy was to not smooth any of the images, and for the Oxford data, decreasing smoothing for the subject image, with no smoothing of the template image, was the optimal strategy.

To center on the aforementioned optimization results, Figure 2.2.6 shows the maximum performance as a function of the two most influential parameters (warp field resolution and regularization) for both datasets and both algorithms. Each point on these graphs represents the maximum performance across a set of 36 settings for Elastix, or three settings for FNIRT.

The performances with optimal parameter settings are listed in Table 2.2.4. The table shows that optimal registration performance for Elastix was slightly higher than for FNIRT with a difference in performance of 0.004–0.006. Although the differences were very small, they were statistically significant (Table 2.2.4; p-values for all datasets $< 10^{-4}$).

To be able to interpret these differences, the relationship between registration *performance* and deformation distance is shown in Figure 2.2.7. A difference in performance of 0.01 translates to an *average deformation difference* of about 0.2 mm; this is twice the difference in registration performance between FNIRT and Elastix.

For both algorithms operating at the optimal parameters for both datasets, the mean deformation distance is shown in Figure 2.2.8. For each dataset, the figure also shows the Euclidean difference between the optimal deformations of FNIRT and Elastix, including group wise differences in registration along white matter structures. The median difference for the Rotterdam data was 1.19 mm (IQR 0.91–1.71) and for the Oxford data 1.70 mm (IQR 1.14–2.52). Confined to the TBSS skeleton this corresponded to 1.10 mm (IQR 0.91–1.39) and 1.48 mm (IQR 1.03–1.98).

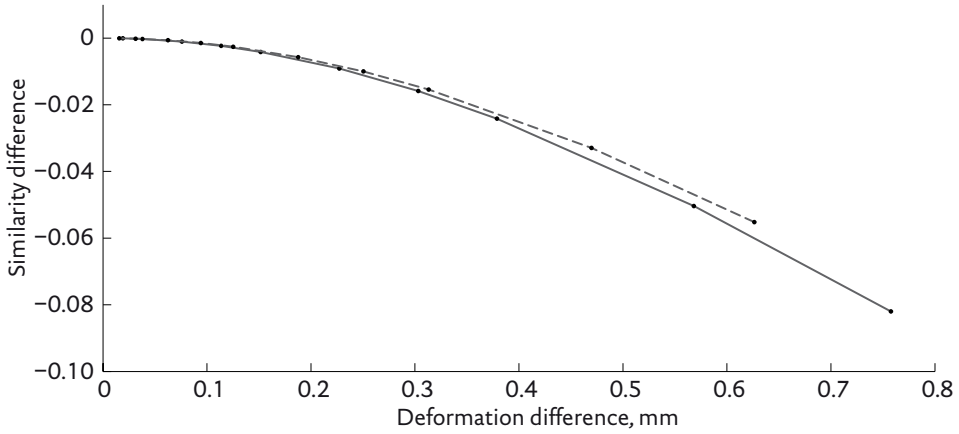

Figure 2.2.7. *The relationship between tract similarity difference (based on spatial correlation between two aligned tract density images) and warp deformation difference for the Rotterdam data (dashed) and the Oxford data (solid), computed for FNIRT operating at optimum parameters for each dataset. The largest difference is obtained when scaling the warp with a factor of 0.8. This translates into a similarity drop between fully and partially warped tracts. Deformation difference is computed by taking the deformation difference (vector) image for each subject, comparing the full and partial warps. The deformation difference in the graph is then the median Euclidean deformation difference distance (vector length), averaged over all subjects in each dataset.*

Table 2.2.4
Registration performance for all datasets at the optimal registration parameters for both FNIRT and Elastix. Performance on the Rotterdam rescan data is computed using the registration settings determined to be optimal based on the Rotterdam baseline data. p-values listed are computed for paired t-tests, comparing the registration performance for all 30 subjects across both registration algorithms

Algorithm	Rotterdam baseline	Rotterdam rescan	Oxford data
FNIRT	0.588	0.577	0.600
Elastix	0.594	0.583	0.604
FNIRT - Elastix (p-value)	-0.006 ($< 10^{-4}$)	-0.006 ($< 10^{-4}$)	-0.004 ($< 10^{-5}$)

Reproducibility of the performance measurement

The optimization experiment was repeated on the rescan data. This resulted in a second, independent performance-measurement for each of the registration parameter settings of FNIRT and Elastix, calculated on a different set of scans of the same subjects. Scatterplots of performance measurements for both datasets are shown in Figure 2.2.9. For FNIRT the scatterplot shows that the absolute performance on the rescan data was slightly reduced (mean difference 0.0105), but this difference was very consistent (SD 6.4×10^{-4}), indicating a slightly lower data quality in the rescan data. Both measures showed an excellent correlation, which is reflected in the R^2 value of the OLS regression of 0.993. For Elastix the scatterplot shows that a similar performance difference was obtained (mean difference 0.0099), but at an increased variability (SD 8.9×10^{-3}) which is reflected in a lower R^2 value of 0.931.

For the rescan data, registration performance was also measured for the optimal parameters determined on the baseline data. Performance measurements are listed in Table 2.2.4, showing that the small FNIRT – Elastix difference was exactly reproduced, albeit that the absolute performance measures for both algorithms were again slightly reduced.

Comparison with TBSS

Constraining the evaluation to the TBSS skeleton had little influence on the optimal parameters, especially around the optimal settings. While the optimal registration parameters evaluated on the whole tract did not exactly match the optimal parameters evaluated on the skeleton, this had very little influence on performance. The

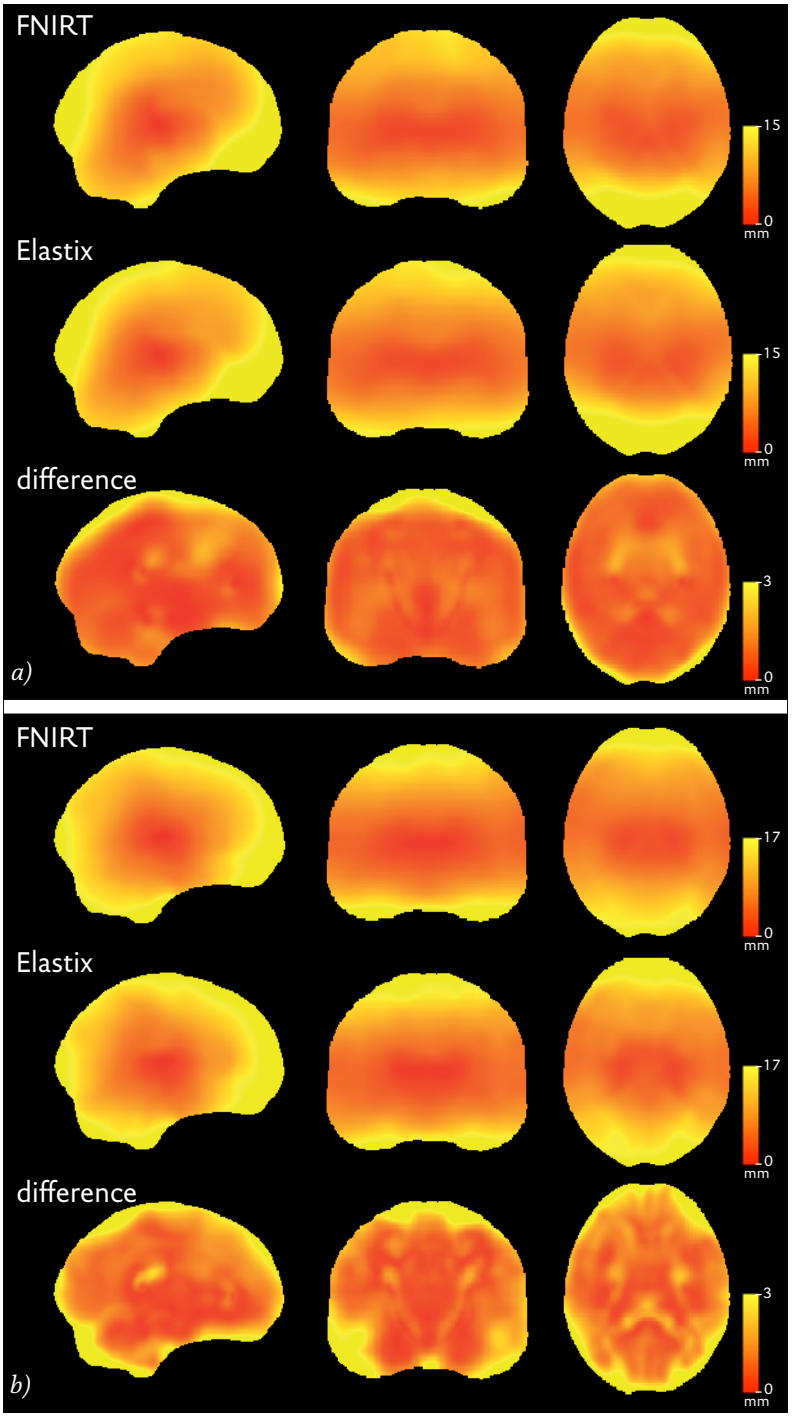

Figure 2.2.8. *Average Euclidean deformation distance for the Rotterdam data (a) and the Oxford data (b). For each algorithm operating at the →*

Table 2.2.5
Skeletonized performance at the optimum parameter settings for each dataset, compared to registration performance of TBSS. Performance on the Rotterdam rescan data is computed using the registration settings determined to be optimal based on the Rotterdam baseline data. p-values listed are computed for paired t-tests, comparing the registration performance for all 30 subjects across both registration algorithms and between registration algorithms and TBSS

Algorithm	Rotterdam baseline	Rotterdam rescan	Oxford data
FNIRT	0.685	0.674	0.690
Elastix	0.689	0.677	0.686
TBSS	0.643	0.636	0.647
FNIRT – Elastix (p-value)	-0.004 (0.002)	-0.003 (0.01)	0.005 ($< 10^{-6}$)
FNIRT – TBSS (p-value)	0.04 ($< 10^{-6}$)	0.04 ($< 10^{-6}$)	0.04 ($< 10^{-6}$)
Elastix – TBSS (p-value)	0.05 ($< 10^{-6}$)	0.04 ($< 10^{-6}$)	0.04 ($< 10^{-6}$)

difference in registration performance between parameters obtained in the registration optimization (Optimization experiments), and the optimal registration according to a skeletonized optimization was at maximum 2.6×10^{-3}.

To compare the performance of both FNIRT and Elastix to TBSS, Table 2.2.5 lists the registration performance for both DTI datasets restricted to the white matter skeleton. Performance differences between FNIRT or Elastix and TBSS were all significant and ranged from 0.038 to 0.046 (all p-values for paired t-tests between both nonlinear registration algorithms and TBSS were $<10^{-6}$). This indicates that registration performance was significantly better on the white matter skeleton for FNIRT and Elastix than for TBSS; the difference in performance between FNIRT and Elastix (in different directions in different datasets) was an order of magnitude smaller than the extent to which both performed better than TBSS.

Table 2.2.5 also contains a comparison between FNIRT and Elastix in the skeletonized evaluation. For the Rotterdam data, Elastix reproducibly outperformed FNIRT, but for the Oxford data, FNIRT was significantly better than Elastix.

← optimal parameters for each dataset, the individual deformation vector images are used to compute Euclidean deformation images, which are then averaged over all subjects to produce the images shown. For both algorithms we included the affine transformation in the deformation field, and then subtracted the mean displacement within the template image in order to account for differences in the coordinate definitions. The distance for both FNIRT and Elastix is shown in mm, the bottom panel in each graph shows the mean Euclidean deformation difference between both algorithms at their respective optimum settings.

Figure 2.2.10 shows the results of the association between age and FA in the 50 aging female subjects, comparing TBSS to TBSS with improved registration using FNIRT. Replacing the registration-projection approach in TBSS with the improved registration yielded more symmetry in the clusters of significant association between higher age and lower FA. Also, clusters were larger and more clusters were found (50% more voxels) when using the improved registration. Bland–Altman plots of the *t*-values and the cluster enhanced *t*-values for both approaches (Figure 2.2.10) further show that at the cluster level, TBSS with improved registration rendered on average higher *t*-values than TBSS.

Discussion

We developed a method to determine the accuracy of established anatomical correspondence of white matter tracts between different subjects. Using this method, we optimized parameters for two registration algorithms, and showed that alignment in TBSS can be improved by using a regularized high-dimensional nonlinear registration approach rather than the registration-projection procedure.

We reproducibly observed substantially better alignment of white matter structures on the white matter skeleton with the optimized registration algorithms than with the current approach in TBSS. This indicates feasibility of replacing the registration-projection approach in TBSS with a finely optimized nonlinear registration. This replacement would improve alignment, but also topological consistency

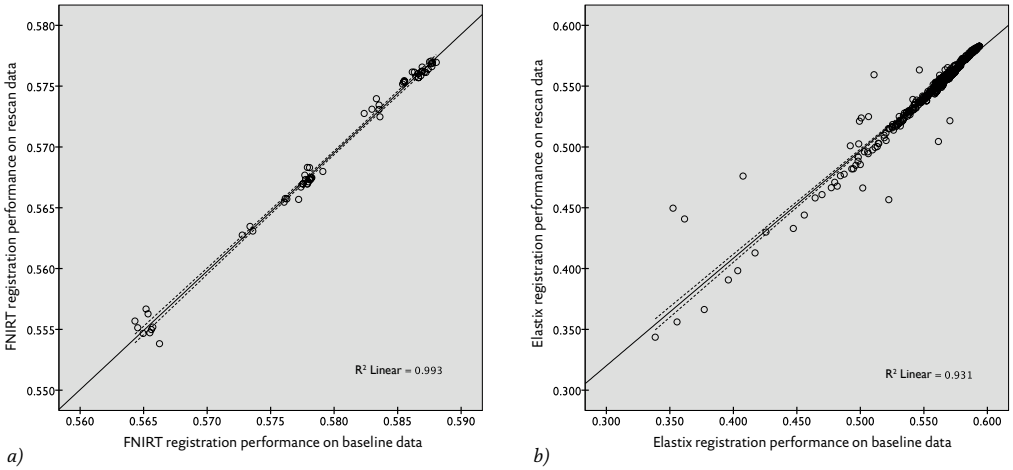

Figure 2.2.9. *Reproducibility of the registration performance measurements for FNIRT (a) and Elastix (b) experiments on the Rotterdam data. Each point represents the registration performance for one registration parameter setting, as measured on two different sets of scans of the same subjects.*

in white matter tracts, since this is explicitly preserved in the diffeomorphic registration of FNIRT, and almost always preserved by the regularized registration performed with Elastix.

The example analysis showed that TBSS with improved registration produced more symmetric, larger and more clusters of significant association between age and FA, and that clusters common to both approaches had smaller *p*-values using TBSS with improved registration. These observations do not prove that the improved registration yields higher sensitivity, as we do not know the ground-truth association in this experiment. However, the results are in line with the common notion of widespread degeneration of white matter with age,[44,45] and as such serve as an illustration of the potential benefit offered by the improved registration and maintained topological consistency, in the analysis of diffusion data in future studies.

There are several methodological considerations to be discussed. First, the optimization experiments showed that optimal registration parameters were different for both imaging datasets (low-end and high-resolution) used. Most notably the optimal regularization was different in both algorithms, for the Rotterdam data (low-end diffusion acquisition) this meant a higher final regularization of FNIRT and a larger regularization weight for Elastix compared to the Oxford data (high-resolution diffusion acquisition). For FNIRT this was coupled with a lower optimal warp field resolution for the Rotterdam data. With the quality of the Oxford data being higher than that of the Rotterdam data, this shows that there is a coherent relation between data quality and the optimal effective number of degrees of freedom of the registration, and that this relation can effectively be investigated with the registration evaluation framework presented here. The two datasets used for the optimization can be argued to encompass a large part of the range of diffusion data qualities commonly acquired. For a new dataset, interpolating optimal registration parameters with respect to e.g. acquisition time, allows making an informed decision on selecting optimal registration parameters. This allows future studies to benefit from improved registration accuracy without the need to redo the optimization for each new dataset.

The reproducibility of the registration, as measured with the evaluation on the rescan data shown in Figure 2.2.9, is influenced by the individual reproducibility of the tractography, the registration, and the optimization/evaluation framework itself. The observed dispersion of the difference between performances calculated on baseline and rescan data is therefore a combination of variances. Assuming independence of the registration evaluation variance from the registration algorithm means that the excellent reproducibility of the registration performance measures for FNIRT (Figure 2.2.9 a) provides a lower bound for the reproducibility of the registration evaluation framework. It should be noted that the performance ranges for the two registration algorithms across the parameter ranges are nearly one order of

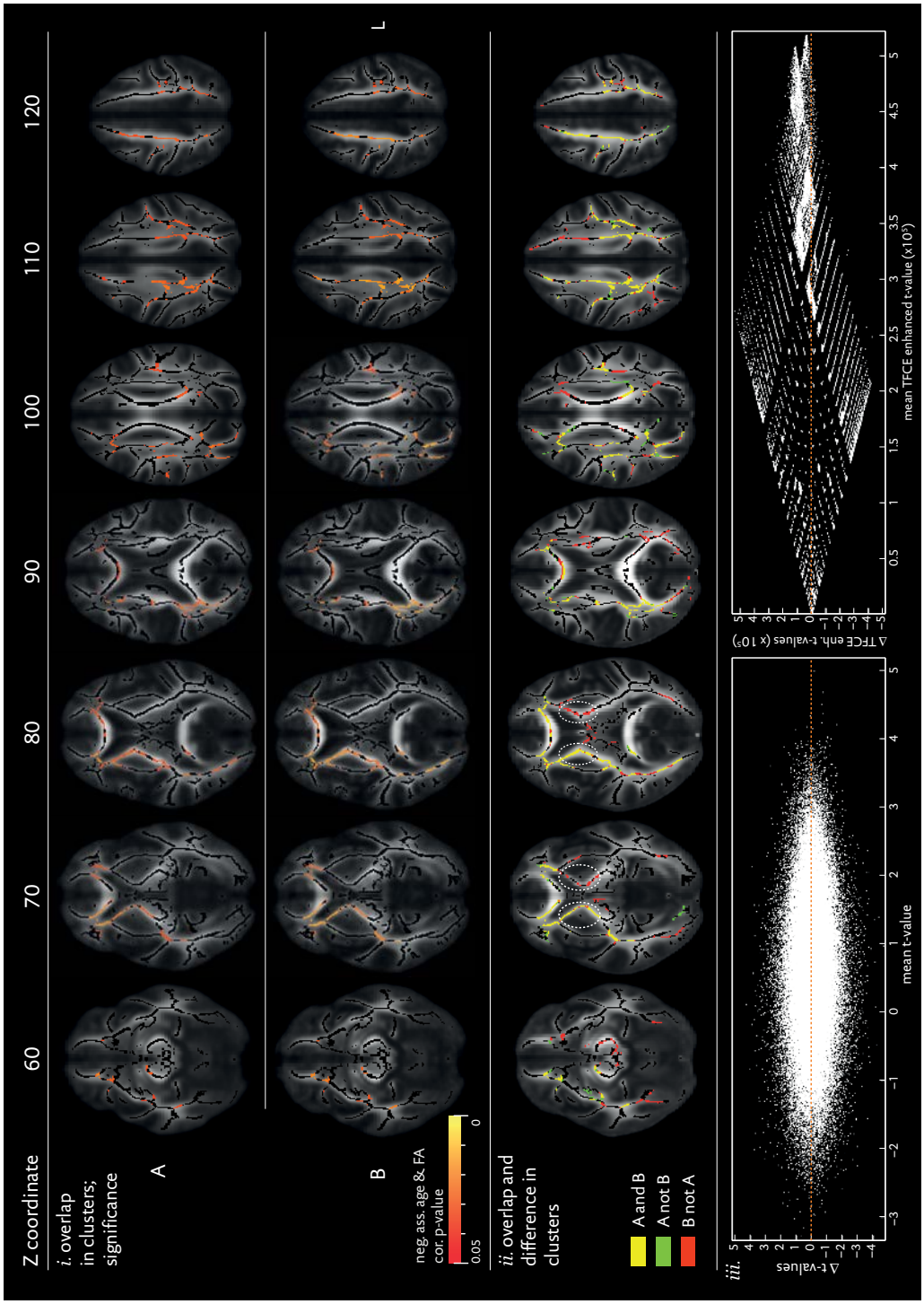

Figure 2.2.10. *Comparison of TBSS (A) with the proposed TBSS (B) with the improved →*

← registration using FNIRT. The top panel (i) shows overlapping clusters where FA was significantly lower with increase in age for both approaches (p-value 0.05), overlaid on the mean FA images obtained with each approach. The standard skeleton supplied with FSL was used with the default FA threshold of 0.2. Colors indicate the p-value for each voxel, adjusted for multiple comparisons using permutation testing (10k permutations), and using the TFCE clustering option available in the Randomise tool of FSL.[47,48] As shown, p-values were smaller for the TBSS method using the improved registration compared to the standard TBSS method. Analyses were performed with head size as confound regressor. Head size was computed by summation of cerebral tissue volumes (including cerebral spinal fluid) as determined by a standardized tissue segmentation procedure.[49]

The second panel (ii) shows which regions of significance were common to both approaches or unique to either of the two approaches, overlaid on the FA template supplied with FSL. Yellow voxels indicate the voxels significant for both approaches; Green voxels indicate significance only using TBSS with the registration-projection approach; Red voxels indicate significance only for TBSS using the proposed improved registration approach. For TBSS with improved registration, statistics were computed on the non-upsampled FA images for each subject, transformed to standard space using linear interpolation, identical to what is performed in standard TBSS. Results for TBSS with optimized registration were more symmetric, especially in the circled regions of slices Z=70 and 80. Also, TBSS with improved registration, in this experiment, showed 50% more significant voxels for the association between age and FA than TBSS with registration and projection. The opposite association (higher FA with increase in age) produced no significant voxels for either TBSS approach (not shown).

The third panel (iii) shows Bland-Altman plots for the skeletonized t-statistics comparing TBSS to TBSS with improved registration. The left plot shows voxelwise t-values, the right plot shows TFCE enhanced t-values. Each dot corresponds to a single skeleton voxel, presenting the average statistic for the two approaches on the x-axis, and the difference in statistic (TBSS with improved registration – TBSS) on the y-axis. For TFCE enhanced t-values, TBSS with improved registration produced on average larger cluster enhanced t-values than TBSS. For larger TFCE enhanced t-values, this is visualized in the figure by the cluster of voxels that have positive t-value differences (above the orange zero-difference line).

magnitude apart. With Elastix spanning a larger performance range, this also means that part of the range is covering registrations that are so far away from optimal that reproducibility is less informative. Even so, it seems that reproducibility for FNIRT was slightly better than for Elastix.

It is interesting to see that for Elastix, the sum-of-squared-differences (SSD) similarity metric, which is the similarity metric implemented in FNIRT, was consistently outperformed by the mutual information (MI) and normalized cross correlation (NCC) metrics. This might have been caused by nonlinear intensity differences between subjects across tracts. With different tracts having slightly different intensity across subjects, the assumptions of the SSD cannot be met. This might explain the difference in registration performance between Elastix and FNIRT observed on the full tract evaluation.

Registration performance on the skeleton for both registration algorithms showed heterogeneous behavior amongst the datasets, with Elastix performing slightly better on the worse data, and FNIRT performing slightly better on the better data. Comparison of both algorithms using the whole tract evaluation showed Elastix to perform slightly better than FNIRT with absolute deformation differences in the order of 1–2 mm. These differences will be a composition of deformation differences that do, and deformation differences that do not translate into registration performance differences (think e.g. of two sets of transformations, each with an equal amount of different random perturbations). By scaling the optimal deformations, we found that the obtained difference in registration performance between optimal warp fields of both algorithms would translate to deformation differences in the order of 0.1 mm, had all deformation differences translated into registration performance differences. While performing slightly worse, FNIRT is diffeomorphic and therefore produces invertible warps. Invertibility of the warp field is a desirable property in a neuroscience context such as TBSS as this allows back-projecting points in standard space to subject-native space and preserves topological consistency of the white matter through the transformation of native space to standard space.

The masks that initialize the probabilistic tractography (seed, target, exclusion, and stop) are defined in standard space, and transformed to subject space. The registration that is used for this transformation is obtained with a medium degree-of-freedom registration, i.e., the same registration that is used in the initial alignment of TBSS. This registration is inverted to obtain a standard space to subject transformation. The use of a registration inside a registration-evaluation framework can potentially bias the evaluation metric. However, this bias would favor trans- formations similar to the one used in the tractography initialization, i.e. conservative, medium degree-of-freedom transformations. It should also be noted that tractography is

only run in a preprocessing stage, and that the same tract-sets are used to evaluate all different registration parameter settings. We therefore consider bias due to this registration step not to be a major factor in our results.

In this evaluation we have included two nonlinear registration algorithms that were developed in the groups that contributed to this study and for which primary developers were involved in the project. Though not the aim of this study, the developed framework may lend itself to a comprehensive comparison of more registration algorithms. Such a comparison of registration algorithms could e.g. include a broad selection of algorithms out-of-the-box, such as carried out in Wang et al.,[19] or could include a full optimization in which case we recommend involvement of developers of each algorithm to design the algorithm-specific optimization scheme. Such an optimization would inherently be very computationally intensive. Computing the registration performance for a single registration parameter setting, for a group of 30 subjects, took on average around 50 CPU-hours. This included the actual registration, warping the tract maps, and computing the spatial correlation. Computations were performed on the LISA cluster in Amsterdam (www.sara.nl/systems/lisa) and on a local cluster in Rotterdam. The optimal registrations of the Rotterdam data required on average 51 min (FNIRT), and 68 min (Elastix) of CPU time on 2.1 Ghz AMD Magny Cours processors, compared to 12 min for the registration + projection of TBSS. For the Oxford data this was 71 min for FNIRT, 71 min for Elastix, and 12 min for TBSS.

We used probabilistic tractography for fiber tracking and evaluated registration performance using a spatial correlation similarity metric. This is different from previous work that used fiber tracts to quantitatively measure registration performance,[14,16,18,24,27] which were based on deterministic tractography. As a result, metrics for comparing similarity of warped tract maps in those methods were overlap-based, using similarity metrics such as the Dice, Jaccard and Cohen's Kappa metric,[31,46] or distance-based metrics, related to the Hausdorff distance or the mean absolute surface distance.[14,16,18,24] The near-continuous density information that results from probabilistic tractography is not so well suited for these similarity metrics. Most importantly, tract-density contains information about the tract, which would be lost if a thresholded, binary tract-mask was used. Secondly, setting a density threshold for binarization would introduce an- other parameter that requires setting. Spatial correlation as a similarity measure does not suffer from these drawbacks. Also, we have shown that when using the framework presented, based on multiple tracts identified with probabilistic tractography, using spatial correlation as similarity measurement allows for a precise and reproducible evaluation of registration quality. Investigating other evaluation metrics would be possible within this framework, but this is beyond the scope of the current research.

Registration performance measurements on the rescan data showed the difference between both nonlinear registration algorithms to be highly reproducible. Furthermore, performance measurements were highly reproducible themselves. This is an important observation, as it shows that using the tractography output to measure registration performance in the framework presented is not prone to overfitting registration parameters on the dataset that is used for training the registration parameters. This in turn allows one to train registration parameters without the explicit need to evaluate performance on a separate dataset that was not used in the optimization.

The optimized parameter sets that resulted from our experiments are available online for both registration algorithms. For Elastix, parameters can additionally be downloaded from the parameter file database on the Elastix wiki page (http://elastix.bigr.nl/wiki). For FNIRT, optimized parameter files will be distributed with FSL. Scripts and masks, developed for the automated tractography, will be made available for release with FSL.

Conclusions

In conclusion, firstly, we demonstrate that optimized nonlinear image registration algorithms produce better image alignment on the white matter skeleton than the registration-projection approach currently in TBSS.

Secondly, registration quality of diffusion imaging data can be assessed using probabilistic tractography and thus used for optimization of registration parameter settings and for comparison of registration algorithms. This evaluation is not in general biased towards any particular tensor or tensor metric based registration approach, and highly reproducible.

Thirdly, optimal registration parameters depend on the quality (resolution, number of averages etc.) of the diffusion dataset in a graded and predictable manner.

Future studies investigating cross-subject diffusion data with TBSS are expected to benefit from the improved anatomical alignment.

Supplementary data to this article can be found online at:
http://dx.doi.org/10.1016/j.neuroimage.2013.03.015.

References

1. 1. Basser PJ, Mattiello J, LeBihan D. Estimation of the effective self-diffusion tensor from the NMR spin echo. *J Magn Reson B*. 1994;103(3):247-54.
2. Beaulieu C. The basis of anisotropic water diffusion in the nervous system - a technical review. *NMR Biomed*. 2002;15(7-8):435-455.
3. Lebel C, Caverhill-Godkewitsch S, Beaulieu C. Age-related regional variations of the corpus callosum identified by diffusion tensor tractography. *Neuroimage*. 2010;52(1):20-31.
4. Basser PJ, Jones DK. Diffusion-tensor MRI: theory, experimental design and data analysis - a technical review. *NMR Biomed*. 2002;15(7-8):456-467.
5. Büchel C, Raedler T, Sommer M, Sach M, Weiller C, Koch MA. White Matter Asymmetry in the Human Brain: A Diffusion Tensor MRI Study. *Cereb Cortex*. 2004;14(9):1-7.
6. Buchsbaum MS, Tang CY, Peled S, et al. MRI white matter diffusion anisotropy and PET metabolic rate in schizophrenia. *Neuroreport*. 1998;9(3):425-430.
7. Van Hecke W, Leemans A, de Backer S, Jeurissen B, Parizel PM, Sijbers J. Comparing isotropic and anisotropic smoothing for voxel-based DTI analyses: A simulation study. *Hum Brain Mapp*. 2010;31(1):98-114.
8. Jones DK, Symms MR, Cercignani M, Howard RJ. The effect of filter size on VBM analyses of DT-MRI data. *Neuroimage*. 2005;26(2):546-554.
9. Smith SM, Jenkinson M, Johansen-Berg H, et al. Tract-based spatial statistics: voxelwise analysis of multi-subject diffusion data. *Neuroimage*. 2006;31(4):1487-1505.
10. Smith SM, Johansen-Berg H, Jenkinson M, et al. Acquisition and voxelwise analysis of multi-subject diffusion data with tract-based spatial statistics. *Nat Protoc*. 2007;2(3):499-503.
11. Smith SM, Jenkinson M, Woolrich MW, et al. Advances in functional and structural MR image analysis and implementation as FSL. *Neuroimage 23 S1*. 2004;23 Suppl 1:208-219.
12. Woolrich MW, Jbabdi S, Patenaude B, et al. Bayesian analysis of neuroimaging data in FSL. *Neuroimage*. 2009;45(1 Suppl):S173-186.
13. Jones DK, Griffin LD, Alexander DC, et al. Spatial normalization and averaging of diffusion tensor MRI data sets. *Neuroimage*. 2002;17(2):592-617.
14. Park H-J, Kubicki M, Shenton ME, et al. Spatial normalization of diffusion tensor MRI using multiple channels. *Neuroimage*. 2003;20(4):1995-2009.
15. Van Hecke W, Leemans A, D'Agostino E, et al. Nonrigid coregistration of diffusion tensor images using a viscous fluid model and mutual information. *IEEE Trans Med Imaging*. 2007;26(11):1598-1612.
16. Yap P-T, Wu G, Zhu H, Lin W, Shen D. TIMER: Tensor Image Morphing for Elastic Registration. *Neuroimage*. 2009;47(2):549-563.
17. Yeo BTT, Vercauteren T, Fillard P, et al. DT-REFinD: diffusion tensor registration with exact finite-strain differential. *IEEE Trans Med Imaging*. 2009;28(12):1914-1928.
18. Zhang H, Yushkevich PA, Alexander DC, Gee JC. Deformable registration of diffusion tensor MR images with explicit orientation optimization. *Med Image Anal*. 2006;10(5):764-785.
19. Wang Y, Gupta A, Liu Z, et al. DTI registration in atlas based fiber analysis of infantile Krabbe disease. *Neuroimage*. 2011;55(4):1577-1586.
20. Guimond A, Guttmann CRG, Warfield SK, Westin C-F. Deformable registration of DT-MRI data based on transformation invariant tensor characteristics. In: *ISBI 2002: IEEE International Symposium on Biomedical Imaging*.; 2002:761-764.
21. Xu D, Mori S, Shen D, van Zijl PCM, Davatzikos C. Spatial normalization of diffusion tensor fields. *Magn Reson Med*. 2003;50(1):175-182.
22. Zvitia O, Mayer A, Shadmi R, Miron S, Greenspan HK. Co-registration of white matter tractographies by adaptive-mean-shift and Gaussian mixture modeling. *IEEE Trans Med Imaging*. 2010;29(1):132-145.
23. Zhang H, Avants BB, Yushkevich PA, et al. High-dimensional spatial normalization of diffusion tensor images improves the detection of white matter differences: an example study using amyotrophic lateral sclerosis. *IEEE Trans Med Imaging*. 2007;26(11):1585-1597.

24. Zöllei L, Stevens A, Huber K, Kakunoori S, Fischl B. Improved tractography alignment using combined volumetric and surface registration. *Neuroimage*. 2010;51(1):206-213.

25. Lawes INC, Barrick TR, Murugam V, et al. Atlas-based segmentation of white matter tracts of the human brain using diffusion tensor tractography and comparison with classical dissection. *Neuroimage*. 2008;39(1):62-79.

26. Jia H, Yap P-T, Wu G, Wang Q, Shen D. Intermediate templates guided groupwise registration of diffusion tensor images. *Neuroimage*. 2011;54(2):928-39.

27. Xue Z, Li H, Guo L, Wong STC. A local fast marching-based diffusion tensor image registration algorithm by simultaneously considering spatial deformation and tensor orientation. *Neuroimage*. 2010;52(1):119-130.

28. Behrens TEJ, Johansen-Berg H, Jbabdi S, Rushworth MFS, Woolrich MW. Probabilistic diffusion tractography with multiple fibre orientations: What can we gain? *Neuroimage*. 2007;34(1):144-155.

29. Behrens TEJ, Woolrich MW, Jenkinson M, et al. Characterization and propagation of uncertainty in diffusion-weighted MR imaging. *Magn Reson Med*. 2003;50(5):1077-1088.

30. Mori S, Kaufmann WE, Davatzikos C, et al. Imaging cortical association tracts in the human brain using diffusion-tensor-based axonal tracking. *Magn Reson Med*. 2002;47(2):215-223.

31. Stieltjes B, Kaufmann WE, van Zijl PC, et al. Diffusion tensor imaging and axonal tracking in the human brainstem. *Neuroimage*. 2001;14(3):723-735.

32. Wakana S, Jiang H, Nagae-Poetscher LM, van Zijl PCM, Mori S, Zijl PCM Van. Fiber Tract–based Atlas of human white matter anatomy. *Radiology*. 2004;230(1):77-87.

33. Wakana S, Caprihan A, Panzenboeck MM, et al. Reproducibility of quantitative tractography methods applied to cerebral white matter. *Neuroimage*. 2007;36(3):630-644.

34. Andersson JL, Smith SM, Jenkinson M. FNIRT - FMRIB's Non-linear Image Registration Tool. In: *Fourteenth Annual Meeting of the Organization for Human Brain Mapping*. Melbourne; 2008.

35. Ikram MA, van der Lugt A, Niessen WJ, et al. The Rotterdam Scan Study: design and update up to 2012. *Eur J Epidemiol*. 2011;26(10):811-24.

36. Hofman A, van Duijn CM, Franco OH, et al. The Rotterdam Study: 2012 objectives and design update. *Eur J Epidemiol*. 2011;26(8):657-86.

37. Jbabdi S, Behrens TEJ, Smith SM. Crossing fibres in tract-based spatial statistics. *Neuroimage*. 2010;49(1):249-256.

38. Tomassini V, Jbabdi S, Klein JC, et al. Diffusion-weighted imaging tractography-based parcellation of the human lateral premotor cortex identifies dorsal and ventral subregions with anatomical and functional specializations. *J Neurosci*. 2007;27(38):10259-10269.

39. Kindlmann G, Tricoche X, Westin C-F. Delineating white matter structure in diffusion tensor MRI with anisotropy creases. *Med Image Anal*. 2007;11(5):492-502.

40. Klein S, Staring M, Murphy K, Viergever MA, Pluim JPW. elastix: a toolbox for intensity-based medical image registration. *IEEE Trans Med Imaging*. 2010;29(1):196-205.

41. Rueckert D, Sonoda LI, Hayes C, Hill DL, Leach MO, Hawkes DJ. Nonrigid registration using free-form deformations: application to breast MR images. *IEEE Trans Med Imaging*. 1999;18(8):712-721.

42. Klein S, Pluim JPW, Staring M, Viergever MA. Adaptive Stochastic Gradient Descent Optimisation for Image Registration. *Int J Comput Vis*. 2009;81(3):227-239.

43. Klein S, van der Heide UA, Lips IM, van Vulpen M, Staring M, Pluim JPW. Automatic segmentation of the prostate in 3D MR images by atlas matching using localized mutual information. *Med Phys*. 2008;35(4):1407.

44. Sullivan EV, Pfefferbaum A. Diffusion tensor imaging and aging. *Neurosci Biobehav Rev*. 2006;30(6):749-761.

45. Vernooij MW, de Groot M, van der Lugt A, et al. White matter atrophy and lesion formation explain the loss of structural integrity of white matter in aging. *Neuroimage*. 2008;43(3):470-477.

46. Zhang Y, Zhang J, Oishi K, et al. Atlas-guided tract reconstruction for automated and comprehensive examination of the white matter anatomy. *Neuroimage*. 2010;52(4):1289-1301.

47. Nichols TE, Holmes AP. Nonparametric permutation tests for functional neuroimaging: a primer with examples. *Hum Brain Mapp*. 2002;15(1):1-25.

48. Smith SM, Nichols TE. Threshold-free cluster enhancement: addressing problems of smoothing, threshold dependence and localisation in cluster inference. *Neuroimage.* 2009;44(1):83-98.

49. Vrooman HA, Cocosco CA, van der Lijn F, et al. Multi-spectral brain tissue segmentation using automatically trained k-Nearest-Neighbor classification. *Neuroimage.* 2007;37(1):71-81.

2.3

Changes in normal-appearing white matter precede development of white matter lesions

Stroke 2013

Marius de Groot*
Benjamin F. Verhaaren*
Renske de Boer
Stefan Klein
Albert Hofman
Aad van der Lugt
M. Arfan Ikram
Wiro J. Niessen
Meike W. Vernooij

* equal contribution

Background and Purpose – It is unknown whether white matter lesions (WML) develop abruptly in previously normal brain areas, or whether tissue changes are already present before WML become apparent on MRI. We therefore investigated whether development of WML is preceded by quantifiable changes in normal-appearing white matter (NAWM).

Methods – In 689 participants from the general population (mean age 67 years), we performed 2 MRI scans (including diffusion tensor imaging and Fluid Attenuation Inversion Recovery (FLAIR) sequences) 3.5 years apart using the same 1.5 T scanner. Using automated tissue segmentation, we identified NAWM at baseline. We assessed which NAWM regions converted into WML during follow-up and differentiated new WML into regions of WML growth and de novo WML. Fractional anisotropy, mean diffusivity, and FLAIR intensity of regions converting to WML and regions of persistent NAWM were compared using 3 approaches: a whole-brain analysis, a regionally matched approach, and a voxel-wise approach.

Results – All 3 approaches showed that low fractional anisotropy, high mean diffusivity, and relatively high FLAIR intensity at baseline were associated with WML development during follow-up. Compared with persistent NAWM regions, NAWM regions converting to WML had significantly lower fractional anisotropy (0.337 vs 0.387; $p < 0.001$), higher mean diffusivity (0.910×10^{-3} mm^2/s vs 0.729×10^{-3} mm^2/s; $p < 0.001$), and relatively higher normalized FLAIR intensity (1.233 vs −0.340; $p < 0.001$). This applied to both NAWM developing into growing and de novo WML.

Conclusions – White matter changes in NAWM are present and can be quantified on diffusion tensor imaging and FLAIR before WML develop. This suggests that WML develop gradually, and that visually appreciable WML are only the tip of the iceberg of white matter pathology.

Background and Purpose

Cerebral white matter lesions (WML) in the elderly are frequently seen on MRI. They are considered to reflect subclinical vascular brain disease and are associated with an increased risk of dementia and stroke.[1,2] Preventing or slowing down WML development may thus have the potential to decrease disease burden. To date, several potentially modifiable risk factors, such as smoking and high blood

pressure, have been associated with WML development.[1,3] Yet, the pathogenesis of WML is still poorly understood. Most important, it is unknown whether WML develop abruptly in previously normal brain regions or whether development of WML on MRI is a gradual process, in which tissue changes are already present before they become apparent on MRI as WML. This is especially important to identify in which persons and at what moment preventive measures should be installed.

On MRI, WML are best visualized by the Fluid Attenuation Inversion Recovery (FLAIR) sequence, on which WML appear as hyperintense regions in the white matter. WML can be quantified using visual rating scales or automated measurements. Both methods measure visually appreciable WML, that is, the macrostructural changes of the white matter that are clearly distinguished on a FLAIR scan. However, pathology studies suggest that these WML are only the tip of the iceberg of white matter pathology.[4] If WML development is indeed a gradual process, early stages of its development might be accompanied by subtly increased FLAIR intensities.

Diffusion tensor imaging (DTI) is a relatively recent MR imaging technique that allows in vivo study of tissue microstructure, and is often applied to study cerebral white matter. DTI provides multiple imaging metrics, such as fractional anisotropy (FA) and mean diffusivity (MD). These metrics have been shown to detect changes in white matter microstructure that are not distinguished on conventional MRI.[5] Performing DTI in longitudinal MR imaging studies enables investigation of normal-appearing white matter (NAWM) microstructure before WML develop.[6]

New WML form either as lesion growth (ie, adhering to already present WML) or as de novo WML. It is important to take this distinction into account. First, this allows investigation of potentially different pathogenecities. Second, around the border of existing WML, NAWM voxels can contain a fraction of WML tissue that affects measurements in that voxel (so-called partial volume effect). This introduces a potential bias, which is not present for de novo WML.

It is also important to take into account that DTI measurements vary considerably across brain regions because of neuronal tract-width and tract-geometry, and that WML preferentially occur in specific brain regions. These observations demand that longitudinal analyses of NAWM features and WML development take spatial location into account. Finally, to investigate the generic pathophysiology of WML development, this should preferably be studied in the general population.

Therefore, in 689 participants from the population-based Rotterdam Scan Study, we investigated whether DTI measures and the FLAIR intensity of NAWM at baseline are associated with growing WML and de novo WML over a period of 3.5 years. To take into account the lesion location of measurements in the white matter, we used regional matching and a voxel-based approach.

Methods

Study Population

This study is based on participants from a large, prospective, population-based cohort study in the Netherlands that investigates determinants of various chronic diseases in elderly people.[7] The original study population consisted of 7,983 people in the general population, aged ≥55 years and all residents of the Ommoord suburb of Rotterdam. In 2000 to 2001, the cohort was expanded with 3,011 people aged ≥55 years of age.[7] The institutional review board approved the study, and written informed consent was obtained from all participants.

In 2005, 1,073 from these 3,011 people were randomly selected for MRI scanning.[8] After exclusion of demented people (n=4) and people who had MRI contraindications (n=94), 975 were eligible, of whom 907 (93%) participated. Physical inabilities precluded image acquisition in 12 individuals. Imaging was incomplete for 3 subjects, leaving 892 people with complete MRI examinations. In 2008, these people were invited for a follow-up MRI scan. After exclusion of people who had died (n=21) or had new MRI contraindications (n=7), 864 people were eligible. From these, 770 (89%) were willing to participate, of whom 754 had complete MRI examinations. After exclusion of people with cortical infarcts at either baseline or follow-up (n= 32), 722 people were included in this study.

MRI Protocol

The MRI protocol performed at both time points was identical and was performed on the same 1.5T GE Signa Excite MR scanner in a standardized way. Details of this protocol have been described previously.[8] In short, structural imaging included a T1-weighted 3D Fast RF Spoiled Gradient Recalled Acquisition in Steady State with an inversion recovery prepulse sequence, a proton density weighted sequence, and a T2-weighted FLAIR sequence. For DTI, we performed a single shot, diffusion-weighted spin echo echo-planar imaging sequence. Maximum b-value was 1000 s/mm^2 in 25 noncollinear directions; 1 volume was acquired without diffusion weighting (b-value=0 s/mm^2).

Tissue Segmentation

Brain tissue was classified into NAWM, WML, grey matter, and cerebrospinal fluid. For classification of all tissues except WML, a multispectral tissue classification[9] was used, incorporating a multiatlas strategy with 6 manually labeled atlases for learning subject-specific tissue intensities. The FLAIR intensity was used to identify WML in an automated postprocessing step.[10] Tissue segmentations were visually inspected. Subjects with artifacts in the segmentation of either scan (eg, because of motion) were excluded (33), leaving 689 subjects for analysis.

Spatial and Intensity Normalization

Nonrigid image was used to align the T1w structural images of both time points. Registration was performed using FMRIB's Linear and Non-linear Image Registration Tools (FLIRT[11] and FNIRT[12]) part of the FMRIB Software Library (FSL).[13] To prevent biasing toward a particular time point,[14] both scans were transformed to the (subject-specific) intermediate space by inverting half the deformation fields of the transformations between both scans. For each subject, the mean intermediate T1w

Table 2.3.1
Population characteristics

	N = 689
Age, y	66.9 (5.0)
Female	52 % (355)
Baseline WML volume, ml*	3.4 (2.1 - 6.5)
New WML volume, ml*	1.4 (0.8 - 2.8)
De novo WML volume, ml*	0.2 (0.1 - 0.3)
Growing WML volume, ml*	1.1 (0.6 - 2.4)
Lost WML volume, ml*	0.8 (0.5 - 1.3)
Baseline NAWM volume, ml	397 (53)
NAWM FA	0.387 (0.017)
NAWM MD, 10^{-3} mm^2/s	0.730 (0.028)
NAWM FLAIR	-0.0332 (0.194)
Follow up time, y	3.5 (0.2)

*Values are means (standard deviation) or percentages (numbers). *median [interquartile range]. Abbreviations: WML = white matter lesion, NAWM = normal-appearing white matter, FLAIR = Fluid Attenuated Inversion-Recovery (normalized signal intensity).*

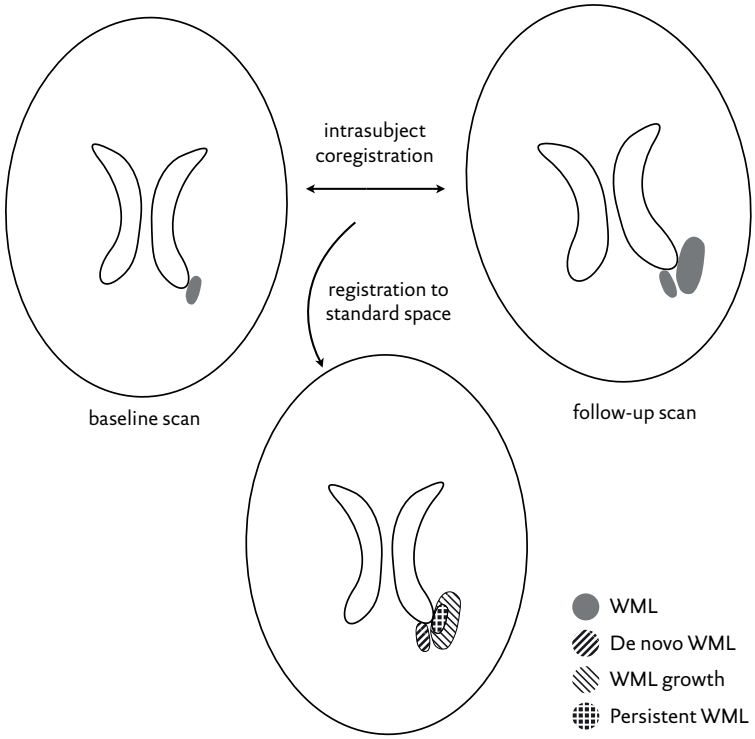

Figure 2.3.1. *Schematic overview of the spatial normalization procedure for two scans of the same subject. The baseline and follow-up scans are nonlinearly registered towards one another allowing creation of an intermediate image. This intermediate image is then non-linearly registered to standard space. WML segmentations for both scans, transformed to standard space, are automatically categorized into persistent WML and new WML. New WML are further distinguished into WML growth if the new lesion is connected to a baseline WML or de-novo WML if it is not. Abbreviation: WML = white matter lesion.*

images were registered to the 1-mm MNI_152 template, supplied with FSL using FNIRT. A schematic overview of the spatial normalization process is given in Figure 2.3.1. WML were masked to minimize their influence on the registration.

FLAIR intensities were normalized across subjects by matching grey matter intensity histograms for each subject (matching peak and full width at half maximum using linear transformations). This normalization was driven by grey matter intensities to avoid potential influence of subclinical white matter pathology. Nonuniformity correction (before normalization) and coregistration to the T1w image were performed as described by de Boer et al.[10]

Diffusion Data Processing

Diffusion data were corrected for motion and eddy currents by affine coregistration of the diffusion-weighted volumes to the b=0 volume. Registrations were performed with Elastix.[15] The rotation component of each transformation was used to realign each gradient vector to compensate for motion during the acquisition.[16] Transformed diffusion-weighted images were resampled at an isotropic resolution of 1.0 mm. The Brain Extraction Tool[17] from FSL was used to mask out nonbrain tissue. Tensor fits were performed with a Levenberg-Marquard nonlinear least squares optimization algorithm, available in ExploreDTI.[18] Data quality was examined by visual inspection of axial FA slices, every 4 mm, combined with 2 coronal and 2 sagittal slices around the center of the brain. Resampling of diffusion data in standard space was performed in 1 pass by concatenating an affine coregistration of the FA to the baseline T1w image, the nonlinear transformations of T1w space to mean structural space, and the transformation from that space to standard space. All registrations were checked by visually inspecting the warped structural and FA images in standard space. No unacceptable misregistrations were found.

Definition of New WMLs, Growing and De Novo WMLs

WMLs were defined as each group of voxels, classified as WMLs in the tissue segmentation, connected in a 3-dimensional 18-voxel-neighborhood (spherical kernel with a diameter of 3 voxels). In standard space, brain tissue segmentations for both time points were combined per subject to obtain voxelwise persistent NAWM, persistent WML, and new WML (ie, converting from NAWM to WML) tissue classes (Figure 2.3.1). Every WML in the follow-up image was then checked for overlap

Table 2.3.2
DTI and FLAIR parameters of persisting NAWM versus NAWM converting to WMLs; whole brain analysis

	Persisting NAWM	NAWM converting to WMLs		
		Total	Growing	De Novo
FA	0.387 (0.017) (Ref)	0.337 (0.030) p<0.001	0.335 (0.033) p<0.001	0.346 (0.038) p<0.001
MD	0.729 (0.027) (Ref)	0.910 (0.054) p<0.001	0.919 (0.055) p<0.001	0.866 (0.073) p<0.001
FLAIR	-0.340 (0.190) (Ref)	1.233 (0.150) p<0.001	1.295 (0.151) p<0.001	0.920 (0.191) p<0.001

Values are means (SD). p-Values are based on the paired-samples t-test results of the comparisons of mean FA, MD (× 10^{-3} mm^2/s)and FLAIR values of persisting NAWM versus the values of NAWM converting to WMLs. Abbreviations: WMLs = white matter lesions, NAWM= normal-appearing white matter, FA = fraction anisotropy, MD = mean diffusivity, FLAIR = Fluid Attenuated Inversion Recovery (normalized signal intensity).

driving subject in standard space defines objective ROI
De novo WML
WML growth
Persistent WML
Objective ROI
matched subject 1 e.g. full tissue match
matched subject 2 e.g. ventricle mis-registration
matched subject 3 e.g. full tissue match
matched subject 4 e.g. overlapping WML
Tissue matching
WML
NAWM
Ventricle
Driving subject tissue borders
Measurements
Matched ROI
measurements in case & control
measurements in case & control
measurements in case & control
measurements in case & control

with WML in the baseline image. The new WML voxels were subdivided into WML growth and de novo WML tissue, according to this overlap. New WML voxels were identified as WML growth, if they were part of a WML that overlapped with a WML at baseline. Accordingly, if not overlapping with a baseline WML, new WML voxels were classified as de novo WML.

Regional Matching

A schematic overview of the approach is given in Figure 2.3.2. To take into account that diffusion metrics and WML formation depend on anatomic location, we performed an analysis in which regions developing into WML were compared with anatomically corresponding regions of persistent NAWM. Regional matching was completed by confining measurements to the overlap between new WML in the driving subject and persistent NAWM in the matched subject to account for registration errors and potential (new) WML in the matched subject in those locations. In those regions in standard space, we averaged FLAIR and DTI metrics in the baseline scans. This process was repeated 4 times with different age- and sex-matched subjects for each driving subject for additional robustness.

← **Figure 2.3.2.** *Schematic overview of the regional matching procedure, illustrated with enlarged axial cutouts for 5 subjects. The left panel shows how the new WML in standard space for the driving subject are treated as objective region of interest (ROI). This objective ROI is distinguished into WML growth and de-novo WML (not shown). For age and gender matched subjects in the same population, the overlap between the matched subject NAWM and the objective ROI is determined. The matching is performed four times to increase robustness, e.g. to be robust against a situation where new lesions in the driving subject overlap with WML in the matched subject. The repetition also means that every subject is driving-subject once, and matched subject exactly four times in the analysis. In the graph, matched subjects 1 and 3 show a complete overlap between the objective ROI and the persistent NAWM. For subject 2, the enlarged ventricle is not perfectly registered, leading to part of the ventricle overlapping with the objective ROI. Subject 4 shows WML overlapping with the objective ROI. The unmatched regions are excluded from the objective ROI in calculating the average baseline DTI and FLAIR metrics. The four resulting measurement pairs for each metric are averaged across the pairs. Abbreviations: WML = white matter lesion, NAWM = normal-appearing white matter, ROI = region of interest, DTI = diffusion tensor imaging, FLAIR = fluid attenuated inversion recovery.*

Statistical Analyses

We investigated baseline tissue properties of NAWM developing into WMLs during follow-up using 3 approaches. First, we performed a whole-brain analysis without regional matching. We averaged FLAIR intensity and diffusion metrics in all persistent NAWM voxels and compared these with measures inside NAWM converting into WML, further partitioned into WML growth and de novo WMLs. Hereto, we used paired-samples *t* tests (2-sided; α-value=0.05) using SPSS statistical software (version 20).

Second, we used regional matching to compare baseline measurements in NAWM developing into WML with those in regionally matched persistent NAWM of age- and sex-matched controls. Persistent NAWM and WML measurements were averaged across the 4 repetitions to generate the measurement pairs to be used in paired-samples *t* tests. To test the added information of DTI metrics over FLAIR intensity and vice versa, we added measures from both modalities as independent variables and fitted a conditional logistic regression model with new lesion status as outcome measure, and DTI or FLAIR measurements in baseline NAWM as determinant.

Third, to investigate regional dependence of the associations, we tested for voxelwise differences in diffusion and FLAIR measurements between new WML and persistent NAWM. For each voxel, a regression was performed using the metric of interest as dependent variable, and age and lesion status as (voxelwise) independent variables provided that each tissue class was represented by at least 10 subjects. This constraint effectively limited the analysis to the periventricular watershed area. Analyses were performed using *t* tests in Randomise,[19] available in FSL, using 5,000 permutations to correct for multiple comparisons (α-value=0.05). Threshold-free

Table 2.3.3
Difference in DTI and FLAIR parameters between persisting NAWM and NAWM converting to WMLs; regionally matched analysis

	Persisting NAWM	NAWM converting to WMLs					
		Total		Growing		De Novo	
FA	(Ref)	-0.0327 (-0.0339, -0.0315)	p<0.001	-0.0340 (-0.0353, -0.0326)	p<0.001	-0.0233 (-0.0246, -0.0219)	p<0.001
MD	(Ref)	0.0646 (0.0625, 0.0668)	p<0.001	0.0678 (0.0656, 0.0700)	p<0.001	0.0435 (0.0413, 0.0456)	p<0.001
FLAIR	(Ref)	0.895 (0.884, 0.906)	p<0.001	0.942 (0.931, 0.953)	p<0.001	0.682 (0.671, 0.693)	p<0.001

Values are mean differences (95%-CI) of FA, MD ($\times 10^{-3}$ mm^2/s) or normalized FLAIR signal intensity of NAWM converting regions and NAWM persisting regions, matched on age, sex and anatomical region. p-values are based on paired-samples t-tests. NAWM = normal-appearing white matter, FA = fraction anisotropy, MD = mean diffusivity, FLAIR = Fluid Attenuated Inversion Recovery (normalized signal intensity).

cluster enhancement[20] was used to cluster significant results. We repeated the test for added information of diffusion metrics over FLAIR intensity and vice versa on a voxelwise level, by adding measures from both modalities as voxelwise-independent variable in the same model.

Results

Characteristics of the study population are presented in Table 2.3.1. The median WML volume at baseline was 3.4 ml. After an average of 3.5 years of follow-up, we observed a net increase in WML volume in 81% of the participants and a net decrease in WML volume in the remaining 19% of the participants (median increase 1.4 ml; loss 0.8 ml). Table 2.3.2 represents the DTI and FLAIR parameters of persisting NAWM versus NAWM converting to WML for the whole-brain analysis. Compared with persistent NAWM regions, NAWM regions converting to WML had significantly lower FA (0.337 [standard deviation: 0.030] vs 0.387 [standard deviation: 0.017]; p <0.001), higher MD (0.910×10^{-3} [0.054×10^{-3}] mm^2/s vs 0.729×10^{-3} [0.027×10^{-3}] mm^2/s; p <0.001) and relatively higher normalized FLAIR intensity (1.233 [0.150] vs –0.340 [0.190]; p <0.001). This applied to both NAWM regions of growing and de novo WML.

Table 2.3.4
Odds Ratios of WML development per SD increase in baseline DTI and FLAIR parameters of NAWM

	Total		Growth		De Novo	
Model I						
FA	0.31 (0.29, 0.34)	p<0.001	0.33 (0.30, 0.36)	p<0.001	0.42 (0.39, 0.46)	p<0.001
MD	3.99 (3.66, 4.35)	p<0.001	3.85 (3.54, 4.19)	p<0.001	2.83 (2.61, 3.08)	p<0.001
FLAIR	25.96 (19.37, 34.79)	p<0.001	25.45 (19.05, 34.01)	p<0.001	17.65 (14.36, 21.69)	p<0.001
Model II						
FA	0.84 (0.74, 0.95)	p=0.008	0.78 (0.69, 0.88)	p<0.001	0.81 (0.72, 0.92)	p<0.001
MD	1.19 (1.03, 1.39)	p=0.02	1.42 (1.22, 1.65)	p<0.001	1.04 (0.95, 1.15)	p=0.4
FLAIR*	23.99 (17.66, 32.58)	p<0.001	23.97 (17.48, 32.87)	p<0.001	16.75 (13.55, 20.69)	p<0.001

*Values are Odds Ratios (95%-CI) per SD increase in FA, MD or normalized FLAIR signal intensity. Model I: conditional logistic regression with age, sex and region matched converting and persisting NAWM regions, adjusted for time between scans. Model II: as Model I with additional adjustment for normalized FLAIR signal intensity. *adjusted for FA and MD. Abbreviations: NAWM = normal-appearing white matter, FA = fraction anisotropy, MD = mean diffusivity, FLAIR = Fluid Attenuated Inversion Recovery (normalized signal intensity)*

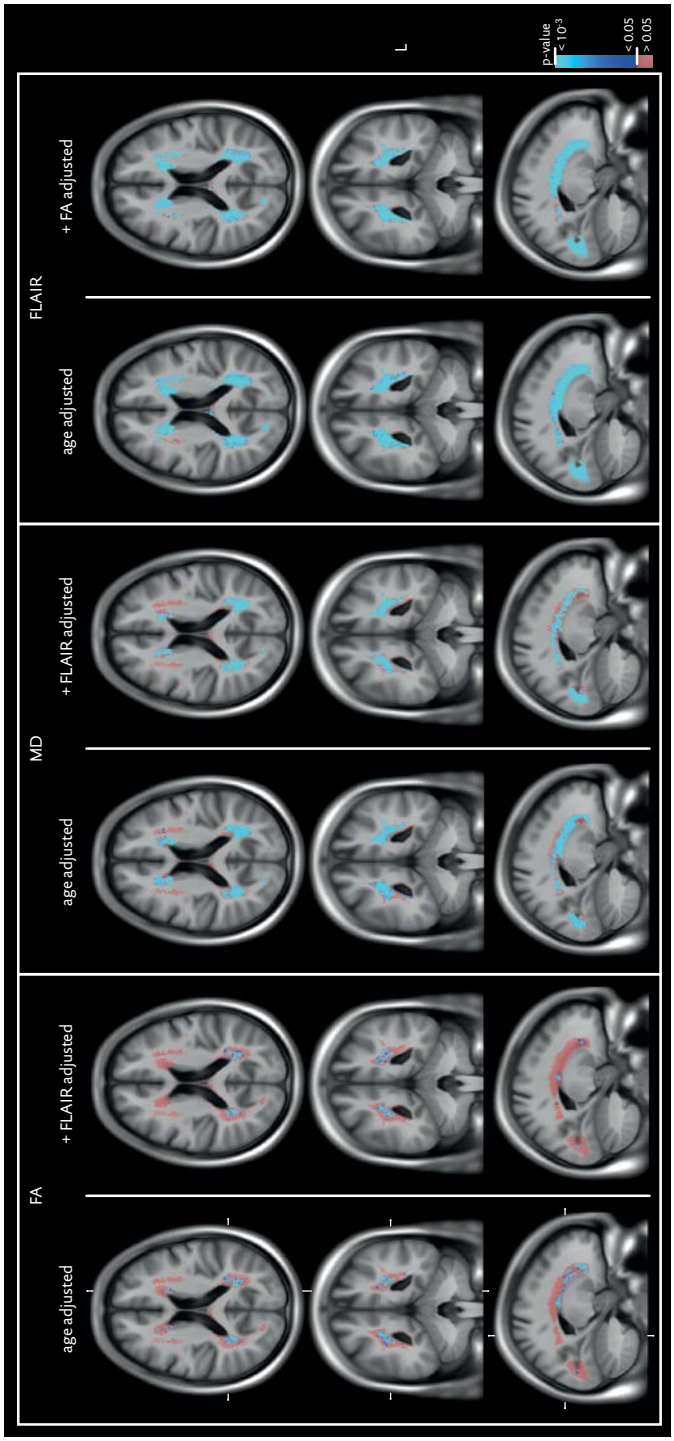

Figure 2.3.3. *Voxel-wise comparison of baseline DTI measures →*

In Table 2.3.3, the difference in DTI and FLAIR parameters is shown between converting NAWM versus persisting NAWM with respect to the regionally matched analyses, using 689 sets of matched subjects. Again, compared with persistent NAWM regions, NAWM regions converting to WML had lower FA (difference [95% confidence interval]: −0.0327 [−0.0339, −0.0315]; p <0.001), higher MD (0.0646 [0.0625, 0.0668]×$10^{-3}$$mm^2$/s; p <0.001), and relatively higher normalized FLAIR intensity (0.895 [0.884, 0.906]; p <0.001). This also applied to both NAWM regions of growing and de novo WML. In addition, we found that low FA and high normalized FLAIR intensity were associated with WML development (growing and de novo WML) after adjustment for one other (Table 2.3.4). MD was not significantly associated with WML development after adjustment for the normalized FLAIR intensity.

Results for the voxelwise analysis are displayed in Figure 2.3.3. All measures were indicative of deteriorated microstructure in the NAWM converting to WML compared with persistent NAWM. Differences were significant, bilaterally along the full span of the ventricles. However, using threshold-free cluster enhancement, cluster size of the associations did vary for the different measures. The cluster for higher MD was broader than that for lower FA. Relatively higher normalized FLAIR intensity was significant in almost the entire analyzed region. Adjusting for alternate measures only slightly reduced significance, mostly visible in the FA analysis corrected for FLAIR intensity (Figure 2.3.3).

Discussion

In this longitudinal MRI study over 3.5 years, we found that visually not appreciable but quantifiable changes of the white matter precede the development of WML. More specifically, we found that baseline DTI measures and FLAIR signal intensity

← and FLAIR intensity in NAWM converting to WML versus persisting NAWM. Only voxels in which there were at least 10 subjects in both categories were analyzed (shown in red and blue). This effectively constrained the analysis to the periventricular watershed area. Shown in blue are voxels in which DTI and/or FLAIR measures at baseline were significantly related to WML development during follow up. For the FA, the left panel shows regions of significantly lower FA, corrected for age. The right panel shows the same analysis, additionally corrected for voxel-wise FLAIR intensity. Left panels in MD and FLAIR show regions of significantly higher MD or relatively higher normalized FLAIR intensity related to WML development adjusted for age. The right panel for the MD is additionally adjusted for FLAIR intensity. The right panel for the FLAIR is additionally adjusted for FA values. FLAIR adjusted for MD showed similar results (not shown). Abbreviations: WML = white matter lesion, NAWM = normal-appearing white matter, FA = fractional anisotropy, MD = mean diffusivity, DTI = diffusion tensor imaging, FLAIR = fluid attenuated inversion recovery.

were associated with both growing WML (ie, new WML adhering to already present WML at baseline) and de novo WML (ie, new WML not adhering to an already present WML at baseline). Furthermore, we found that DTI measures and FLAIR signal intensity were associated with WML development independently from each other.

Strengths of this study are its longitudinal design, large sample size, population-based setting, and use of the same scanner and imaging protocol at baseline and follow-up. Additionally, we accounted for the spatial dependency of both WML and diffusion metrics in 2 ways: by using regional matching and a voxel-based approach. Furthermore, we distinguished between growing WML and de novo WML. This not only enabled us to study potential differences in pathogenicity, but also contributed to the validity of our study because analyses regarding de novo WML are less likely to suffer from biases. For example, the dichotomization of segmenting voxels into WML and NAWM based on FLAIR intensity leads to a so-called partial-voluming effect in the voxels on the interface between both tissues. For de novo WML, the absence of such an interface in the baseline NAWM avoids a potential partial-voluming bias for these lesions.

A limitation of our study is that although we know which voxels have developed into WML over 3.5 years of follow-up, we do not know at exactly which moment during follow-up these lesions developed; this may have been days, months, or years after the baseline scan. Nevertheless, this does not change our primary observation that NAWM changes precede the appearance of visually appreciable WML. Another consideration is that the WML burden in our study was relatively low because of the population-based setting. Yet, we expect that our conclusions also extend to a patient population with high WML burden because large WML have been reported to be surrounded by a penumbra of abnormal NAWM.[21]

We found an apparent net decrease of WML volume in 19% of our population, likely attributable to misclassification of tissues and measurement error at baseline or follow-up, which is in line with previous research.[22,23] Because we performed our analyses in standard space, the increase or decrease of WML could also be assessed at a voxel level. This not only showed new WML voxels in all subjects, but also a loss of one or more WML voxel in all subjects, which again is likely to result from misclassification or measurement error in either time point. Because these voxels did not qualify as new WML in our definition, they were not included in the analysis. Therefore, if anything, this misclassification will either not have influenced our results or may have led to a slight underestimation.

Only one other study reported on the relationship between changes of the NAWM at baseline and the development of WML in a longitudinal MR study, but it did not distinguish between growing and de novo WML.[6] In line with our findings, it found FA and FLAIR intensity to be independently associated with the development of

WML in a heterogeneous population of 119 people with Alzheimer disease, mild cognitive impairment, and normal cognitive function. Together with our findings, this further corroborates that WML are the result of a gradual process because we now assess that this also applies to the general population, and that it holds for both growing as well as de novo WML. In addition, using the voxelwise analysis, we found no evidence that this process is spatially varying along the ventricles.

WML in the elderly are considered to be mainly vascular in origin. This is based on numerous epidemiological studies that found vascular risk factors, such as high blood pressure, to be associated with WML, and pathology studies that found damage of the cerebral small vessels, signs of blood–brain barrier dysfunction, and ischemic pathology in WML.[1,24,25] Previous longitudinal studies have shown that baseline WML load is strongly associated with WML progression,[26,27] and cross-sectional studies found abnormalities in the NAWM to be related to WML burden.[4,21,28] Yet, it was unknown whether the disease process develops gradually or abruptly. This information is essential because if WML would develop abruptly, other causes would be more likely (eg, acute ischemia) than when WML develop over a longer period (eg, chronic ischemia). In addition, it was unknown whether WML growth and de novo WML development have a similar pathophysiology. Our findings suggest that both growing and de novo WML develop gradually. Therefore, a shared pathophysiological process is likely. Our results also suggest that DTI measures and FLAIR signal intensity provide some information independently from each other, implying that both measures partially capture different elements of tissue pathology. Furthermore, our findings confirm that WML are the extremes, or the tip of the iceberg, of white matter pathology.[4,21,26,28]

Our findings may have clinical implications. A clinician should take into account that the true white matter pathology may be more extensive than what is visually appreciable on structural MRI. This could lead to an improved estimate of a patients' risk of stroke, dementia, and death.[2,29] However, further research is needed to confirm these hypotheses.

In summary, in this longitudinal MRI study, we found NAWM changes to be present before WML develop. This suggests that the pathophysiology of WML is a gradual process. Furthermore, our results suggest that WML are only the tip of the iceberg of white matter pathology.

References

1. Pantoni L. Pathophysiology of age-related cerebral white matter changes. *Cerebrovasc Dis*. 2002;13 Suppl 2:7-10.
2. Debette S, Markus HS. The clinical importance of white matter hyperintensities on brain magnetic resonance imaging: systematic review and meta-analysis. *BMJ*. 2010;341:c3666.
3. Van Dijk EJ, Prins ND, Vrooman HA, Hofman A, Koudstaal PJ, Breteler MMB. Progression of cerebral small vessel disease in relation to risk factors and cognitive consequences: Rotterdam Scan study. *Stroke*. 2008;39(10):2712-2719.
4. Simpson JE, Ince PG, Higham CE, et al. Microglial activation in white matter lesions and nonlesional white matter of ageing brains. *Neuropathol Appl Neurobiol*. 2007;33(6):670-683.
5. Vernooij MW, de Groot M, van der Lugt A, et al. White matter atrophy and lesion formation explain the loss of structural integrity of white matter in aging. *Neuroimage*. 2008;43(3):470-477.
6. Maillard P, Carmichael O, Harvey D, et al. FLAIR and Diffusion MRI Signals Are Independent Predictors of White Matter Hyperintensities. *AJNR*. 2012.
7. Hofman A, van Duijn CM, Franco OH, et al. The Rotterdam Study: 2012 objectives and design update. *Eur J Epidemiol*. 2011;26(8):657-86.
8. Ikram MA, van der Lugt A, Niessen WJ, et al. The Rotterdam Scan Study: design and update up to 2012. *Eur J Epidemiol*. 2011;26(10):811-24.
9. Vrooman HA, Cocosco CA, van der Lijn F, et al. Multi-spectral brain tissue segmentation using automatically trained k-Nearest-Neighbor classification. *Neuroimage*. 2007;37(1):71-81.
10. De Boer R, Vrooman HA, van der Lijn F, et al. White matter lesion extension to automatic brain tissue segmentation on MRI. *Neuroimage*. 2009;45(4):1151-1161.
11. Jenkinson M, Smith SM. A global optimisation method for robust affine registration of brain images. *Med Image Anal*. 2001;5(2):143-56.
12. Andersson JLR, Jenkinson M, Smith SM. Non-linear registration aka Spatial normalisation. *FMRIB Tech Rep TR07JA2*. 2007.
13. Woolrich MW, Jbabdi S, Patenaude B, et al. Bayesian analysis of neuroimaging data in FSL. *Neuroimage*. 2009;45(1 Suppl):S173-186.
14. Reuter M, Fischl B. Avoiding asymmetry-induced bias in longitudinal image processing. *Neuroimage*. 2011;57(1):19-21.
15. Klein S, Staring M, Murphy K, Viergever MA, Pluim JPW. elastix: a toolbox for intensity-based medical image registration. *IEEE Trans Med Imaging*. 2010;29(1):196-205.
16. Leemans A, Jones DK. The B-matrix must be rotated when correcting for subject motion in DTI data. *Magn Reson Med*. 2009;61(6):1336-1349.
17. Smith SM. Fast robust automated brain extraction. *Hum Brain Mapp*. 2002;17(3):143-55.
18. Leemans A, Jeurissen B, Sijbers J, Jones D. ExploreDTI: a graphical toolbox for processing, analyzing, and visualizing diffusion MR data. In: *Proceedings 17th Scientific Meeting International Society for Magnetic Resonance in Medicine*.Vol 17.; 2009:3537.
19. Nichols TE, Holmes AP. Nonparametric permutation tests for functional neuroimaging: a primer with examples. *Hum Brain Mapp*. 2002;15(1):1-25.
20. Smith SM, Nichols TE. Threshold-free cluster enhancement: addressing problems of smoothing, threshold dependence and localisation in cluster inference. *Neuroimage*. 2009;44(1):83-98.
21. Maillard P, Fletcher E, Harvey D, et al. White matter hyperintensity penumbra. *Stroke*. 2011;42(7):1917-1922.
22. Van den Heuvel DMJ, ten Dam VH, de Craen AJM, et al. Measuring longitudinal white matter changes: comparison of a visual rating scale with a volumetric measurement. *AJNR*. 2006;27(4):875-8.
23. Silbert LC, Nelson C, Howieson DB, Moore MM, Kaye JA. Impact of white matter hyperintensity volume progression on rate of cognitive and motor decline. *Neurology*. 2008;71(2):108-13.
24. Xiong YY, Mok V. Age-related white matter changes. *J Aging Res*. 2011;2011:617927.
25. Pantoni L. Cerebral small vessel disease: from pathogenesis and clinical characteristics to therapeutic challenges. *Lancet Neurol*. 2010;9(7):689-701.

26. Gouw AA, van der Flier WM, Fazekas F, et al. Progression of white matter hyperintensities and incidence of new lacunes over a 3-year period: the Leukoaraiosis and Disability study. *Stroke*. 2008;39(5):1414-20.

27. Schmidt R, Enzinger C, Ropele S, Schmidt H, Fazekas F. Progression of cerebral white matter lesions: 6-year results of the Austrian Stroke Prevention Study. *Lancet*. 2003;361(9374):2046-8.

28. Ropele S, Seewann A, Gouw AA, et al. Quantitation of brain tissue changes associated with white matter hyperintensities by diffusion-weighted and magnetization transfer imaging: the LADIS (Leukoaraiosis and Disability in the Elderly) study. *JMRI*. 2009;29(2):268-74.

29. Poels MMF, Steyerberg EW, Wieberdink RG, et al. Assessment of cerebral small vessel disease predicts individual stroke risk. *J Neurol Neurosurg Psychiatry*. 2012;83(12):1174-1179.

Chapter 3
Diffusion imaging in aging

3.1 Tract-specific white matter Degeneration in aging. The Rotterdam Study

Alzheimer's & Dementia, 2014

Marius de Groot
M. Arfan Ikram
Saloua Akoudad
Gabriel P. Krestin
Albert Hofman
Aad van der Lugt
Wiro J. Niessen
Meike W. Vernooij

Background – Loss of brain white matter microstructure is presumed to be an early sign of neurodegenerative disease. Yet, little is known on microstructural changes of various white matter tracts with normal aging.

Methods – In 4,532 non-demented elderly persons, we studied age-related changes in tract-specific diffusion characteristics for 25 tracts using probabilistic tractography. We studied how diffusion differs across tracts with aging, whether this depends on macrostructural white matter changes, and whether cardiovascular risk factors affect microstructure.

Results – With increasing age, loss of microstructural organization occurred in association, commissural and limbic tracts. White matter lesions and atrophy each partially explained this loss. We observed worse microstructure with severe hypertension, current smoking and diabetes mellitus, independent from age and macrostructural white matter changes.

Conclusions – Microstructure of white matter tracts changes with age, and may mark neurodegeneration more sensitively than white matter lesion load and atrophy. Cardiovascular factors relate to loss in microstructural organization.

Background

With population aging, neurodegenerative diseases will become more prevalent and will pose a higher burden on individuals and on society. Both for additional insight into the pathophysiology of neurodegenerative diseases, and for identification of persons at increased risk, a better understanding of the early brain changes in neurodegeneration is needed. Previous research has primarily focused on changes that occur in neuronal grey matter. With imaging studies, in particular magnetic resonance imaging (MRI), grey matter atrophy, and more specifically hippocampal atrophy has been studied extensively in relation to manifestations of neurodegeneration such as cognitive deterioration and Alzheimer's disease (AD).[1–4] More recently, the role of cerebral white matter in neurodegeneration has increasingly been acknowledged. Imaging studies investigating cerebral white matter changes have initially focused mainly on macrostructural changes, such as white matter atrophy or the formation of white matter lesions (WML), which have both been linked to cognitive decline and dementia (e.g., Brickman et al., 2008[5]). Howev-

er, these macrostructural changes are likely only the tip of the iceberg of the white matter pathology present,[6,7] and are thought to be preceded by microstructural changes.[8,9] Investigating tissue microstructure in a population-based setting of aging could thereby offer insight into earlier stages of neurodegeneration, potentially before irreversible damage has occurred.

Diffusion MRI is a non-invasive method that can quantitatively characterize tissue microstructure. Diffusion measurements in white matter have for example been shown to differ between patients with AD and controls.[10] Because the white matter is composed of distinct tracts, and tracts are thought to subserve particular brain functions, investigating individual tracts may highlight tract-specific differences in vulnerability to degeneration. Diffusion tractography,[11] which integrates directional diffusion information, can be used to identify and delineate these tracts.

Despite the evidence of loss of white matter microstructural organization in a variety of neurological diseases,[12–14] little is known on tract degeneration in normal aging. Previous studies on white matter changes in aging in asymptomatic individuals primarily included wide age ranges, spanning childhood until old age,[15–19] instead of persons in middle and old age who are at greatest risk for neurodegeneration. Additionally, although there is increasing insight into risk factors for macrostructural white matter pathology, very little is known on how these factors affect white matter microstructure.

Therefore, in 4,532 middle aged and elderly participants from the population-based Rotterdam Study, we investigated how tissue microstructure in 25 white matter tracts changes with age. Secondly, we studied how common (cardiovascular) risk factors relate to tract alteration. In both analyses we took macrostructural markers of white matter pathology (i.e. atrophy and WML) into account to study the independent contribution of aging and risk factors on microstructure.[19]

Methods

Study population

This study is based on participants from the Rotterdam Study, an ongoing, prospective, population-based cohort study investigating causes and consequences of age-related diseases among 14,926 persons.[20] From 2005, all participants have been invited for additional brain imaging.[21] Between 2006 and 2011, of the 5,430 non-demented participants who were eligible for scanning and had no contraindications for MRI (including claustrophobia) 4,841 underwent a multi-sequence MRI acqui-

sition of the brain. After excluding incomplete acquisitions (53), scans with artifacts hampering automated processing (112) and participants with MRI-defined cortical infarcts (144), 4,532 scans were available for analysis. The Rotterdam Study has been approved by the medical ethics committee according to the Population Study Act Rotterdam Study, executed by the Ministry of Health, Welfare and Sports of the Netherlands. Written informed consent was obtained from all participants.

MRI acquisition

Multi-sequence magnetic resonance imaging (MRI) was performed on a 1.5 tesla MRI scanner (GE Signa Excite). Throughout the study period, imaging was performed on the same scanner without major hardware or software updates.[21] In short, structural imaging included a T1-weighted 3D fast RF spoiled gradient recalled acquisition in steady state with an inversion recovery pre-pulse (FASTSPGR-IR) sequence, a proton density (PD) weighted sequence, and a T2-weighted fluid-attenuated inversion recovery (FLAIR) sequence.[21] For diffusion weighted imaging (DWI), we performed a single shot, diffusion-weighted spin echo echo-planar imaging sequence (repetition time (TR)=8,575 ms, echo time (TE)=82.6 ms, axial field-of-view (FOV)=210 × 210 mm, matrix=96 × 64 (phase encoding) (zero-padded in k-space to 256×256) slice thickness=3.5 mm, 35 contiguous slices). Maximum b-value was 1000 s/mm^2 in 25 non-collinear directions; three volumes were acquired without diffusion weighting (b-value = 0 s/mm^2). Between February 2007 and May 2008, a technical issue caused 1,398 participants to be scanned with the phase and frequency encoding directions swapped for the diffusion acquisition. This rotated acquisition scheme led to a mild ghost artifact in the phase encoding direction and was treated as a covariate in the analyses (see analysis section).

Brain tissue segmentation

Brain tissues were segmented into grey matter, white matter, cerebrospinal fluid (CSF) and background tissue using an automated segmentation approach.[22] An automated post-processing step identified WML based on the FLAIR image and the tissue segmentation.[23] After co-registration to the diffusion space this segmentation was combined with the tract segmentation described below to obtain tract-specific WML volumes. Intracranial, cerebral volume (ICV) (excluding the cerebellum and surrounding CSF) was estimated by summing total cerebral grey and white matter and CSF volumes.

Diffusion image processing

Diffusion data were pre-processed using a standardized pipeline.[24] In short, all diffusion-weighted volumes were co-registered to compensate for misalignment due to subject motion and eddy currents. The rotation component of the co-registration was used to realign each gradient vector to its effective direction.[25] Diffusion tensors were estimated using a non-linear Levenberg Marquardt estimator, available in ExploreDTI.[26] Diffusion tensor imaging (DTI) measures of tissue microstructure, fractional anisotropy (FA), mean diffusivity (MD), axial diffusivity, radial diffusivity (average of the two minor eigenvalues) and mode of anisotropy,[27] were computed from the estimated tensor images. Transformations were also used to resample the DWI data in a 2.5 mm cubic resolution for the ball and stick diffusion model required for the probabilistic tractography.

Probabilistic tractography

Tractography was performed using PROBTRACKX,[28] a probabilistic Bayesian framework for white matter tractography, available in FSL (version 4.1.4).[29] PROBTRACKX uses a diffusion model estimated using BEDPOSTX, also available in FSL. Protocols for identifying 14 white matter tracts, 11 of which were defined for left and right hemispheres were defined as previously described[30] and were made available as the AutoPTX plugin for FSL* (version 0.1.1). Tracts were categorized in association, commissural, limbic and sensorimotor tracts. The 25 tracts included for analysis are listed in Appendix Table A.3.1.1, which also lists the seed number parameter of the tractography plugin. The diffusion model estimation and tractography algorithm were run with default settings. The resulting tract-density (visitation count) images for each tract were normalized by division with the total number of particles (tracts) in the tractography run. To account for partial coverage of the medial lemniscus at the lower border of the scan, alternative seed masks were selected (increasingly more cranially positioned) until reasonable coverage was achieved (seed mask volume >0.7 ml). This variable position of seed masks was taken into account as confound regressor in analyses in which the medial lemniscus was studied.

* *http://fsl.fmrib.ox.ac.uk/fsl/fslwiki/AutoPtx*

White matter tract segmentation

White matter tract segmentation was achieved by thresholding the normalized tract density images. To account for differences in geometric complexity, tract-specific thresholds were selected by optimizing the reproducibility of FA measurements on a subset of 30 participants who had been scanned twice, with a mean interval of 19.5 days (mean age 76.7 years (standard deviation 10.0)).[30] Reproducibility and optimal thresholds are listed in Appendix Table A.3.1.1. Resulting tract volumes were computed to correct analyses for tract-specific atrophy and confounding by partial volume effects in the segmentations. Visual inspections were performed for tract segmentations with volumes most dissimilar from the mean tract volume. Segmentations that did not cover the majority of the mean tract anatomy, and segmentations that veered off into neighboring tracts were rejected and coded as missing. We inspected the 50 most dissimilar segmentations per tract, or more until less than one in 20 segmentations was rejected.

Table 3.1.1
Population characteristics

	N = 4532
Age	63.8 (11.1)
Female	2509 (55.4)
Hypertension	
No	1783 (39.5)
Mild	818 (18.1)
Severe	1915 (42.4)
Smoking	
Never	1394 (30.9)
Former	2147 (47.6)
Current	968 (21.5)
Hypercholesterolemia	1108 (24.8)
Diabetes mellitus	406 (9.1)
APOE ε4 carriership	1215 (28.7)
Intracranial volume (ml)	1126 (119)
WML volume (ml)*	2.9 (1.6, 6.1)

APOE indicates apolipoprotein E, WML white matter lesions. Data are presented as mean (standard deviation) for continuous variables and number (%) for categorical variables. * *WML volume is presented as median (interquartile range). The following variables had missing data: hypertension (n=16), smoking (n=23), hypercholesterolemia (n=62), diabetes (n=63), APOE ε4 carriership (n=297).*

Assessment of risk factors

The following cardiovascular risk factors, based on information derived from home interviews and physical examination were assessed.[20] Blood pressure was measured twice in sitting position using a random-zero sphygmomanometer. Hypertension was classified into mild (systolic blood pressure >= 140 mmHg and <160 mmHg, or diastolic blood pressure >= 90 and <100 mmHg) and severe (systolic blood pressure >=160, or diastolic blood pressure >=100, or the use of blood pressure lowering medication).[31] Smoking was assessed by interview and coded as never, former and current. Diabetes mellitus status was determined based on fasting serum glucose level (>= 7.0 mmol/l), or if unavailable non-fasting serum glucose level (>=11.1 mmol/l) or the use of anti-diabetic medication. Hypercholesterolemia was defined as serum total cholesterol level (> 5.17 mmol/l)[32] and/or the use of lipid lowering medication. *Apolipoprotein E (APOE)* ε4 allele carriership was assessed on coded genomic DNA samples. APOE genotype was in Hardy-Weinberg equilibrium. Measurements for the most recent visit to the research center, prior to imaging, were used.

Statistical analysis

Median measures of tract microstructure were computed for voxels inside the tract segmentations. We computed FA, MD, and the additional diffusion measures: axial diffusivity, radial diffusivity and the mode of anisotropy. White matter tracts that were left/right homologues were (volume wise) averaged if both segmentations were available. Next, diffusion measurements were standardized (zero mean, unit standard deviation) across participants to facilitate comparison of associations with age and risk factors across tracts.

For each tract, the relation between age and standardized diffusion measures was investigated using linear regression for four different models. In the first model, we adjusted for sex and ICV. Next, we additionally adjusted for tract-specific white matter volume (model 2) or tract-specific WML volume (model 3). In model 4 we adjusted for both tract-specific volume and tract-specific WML load.

We investigated the association between cardiovascular risk factors and white matter tract diffusion characteristics using analyses of variance, adjusting for age, sex, ICV and tract-specific volume and WML volume (corresponding to model 4). We computed estimated marginal means for the different risk factor groups, and computed the associated difference in standardized diffusion measurement for each tract. For hypercholesterolemia, we additionally corrected for the use of lipid lowering drugs and serum high-density lipoprotein cholesterol level. We also tested

Table 3.1.2
Average tract-specific volume and diffusion measurements. Tract volume represents the average volume for each tract obtained by the probabilistic tractography segmentation. For each individual, median FA and MD is computed inside the (segmented) tracts and then averaged over all participants

	Volume		FA		MD	
	Mean	SD	Mean	SD	Mean	SD
Association						
ATR	7.37	1.09	0.33	0.02	0.75	0.04
IFO	4.07	0.43	0.44	0.03	0.76	0.04
ILF	6.82	0.79	0.41	0.02	0.76	0.04
PTR	4.34	0.65	0.39	0.03	0.77	0.05
SLF	12.17	1.44	0.38	0.02	0.71	0.04
UNC	2.13	0.37	0.37	0.02	0.76	0.03
Commissural						
FMA	6.80	0.98	0.48	0.04	0.76	0.04
FMI	3.45	0.51	0.46	0.05	0.77	0.04
Limbic						
CGC	1.09	0.17	0.43	0.04	0.72	0.02
CGH	0.73	0.08	0.32	0.03	0.75	0.03
Sensorimotor						
CST	5.13	0.69	0.47	0.03	0.69	0.03
MCP	19.50	6.79	0.29	0.05	0.69	0.04
ML	1.99	0.22	0.42	0.02	0.71	0.02
STR	4.81	0.60	0.41	0.03	0.69	0.03

Volume in ml, MD × 10^{-3} mm^2/s. SD indicates standard deviation, FA fractional anisotropy, MD mean diffusivity, ATR anterior thalamic radiation, IFO inferior fronto-occipital fasciculus, ILF inferior longitudinal fasciculus, PTR posterior thalamic radiation, SLF superior longitudinal fasciculus, UNC uncinate fasciculus, FMA forceps major, FMI forceps minor, CGC cingulate gyrus part of cingulum, CGH parahippocampal part of cingulum, CST corticospinal tract, MCP middle cerebellar peduncle, ML medial lemniscus, STR superior thalamic radiation.

for potential differences between the two risk groups defined in the analyses with smoking and hypertension (i.e., former versus current smoking and severe versus mild hypertension). In post-hoc analyses we added an interaction term between risk factor and age to the analyses with cardiovascular risk factors, to test whether the association between age and the diffusion measurements was different among risk-groups.

All analyses were performed with the phase encoding direction of the diffusion scan as a covariate. In a sensitivity analysis we repeated all analyses excluding the 1,398 participants who had a swapped acquisition.

For all analyses, we used an alpha level of 0.05, while controlling the family wise error by applying a Bonferroni correction, taking into account the three eigenvalues tested in five compositions (FA, MD and three additional diffusion measures) (150 models, correcting for 450 tests, Bonferroni adjusted p-value 1.1×10^{-4}). All analyses were performed using IBM SPSS (version 20.0.0) and the accompanying Python integration package.

Results

Characteristics of the study population are presented in Table 3.1.1. Mean age of participants was 63.8 years with age range 45.7-100.0 years. Tract-specific average volumes and diffusion measures are presented in Table 3.1.2 (additional diffusion measurements in Appendix Table A.3.1.2). Due to tractography failures or (visually) rejected segmentations, measurements were missing for on average 6 participants (ranging from 0 to 23) per tract. Mean FA ranged from 0.29 to 0.48 and MD from 0.69 to 0.77 ($\times10^{-3}$ mm/s2).

Associations between age and tract-specific diffusion measurements are presented in Table 3.1.3 and Appendix Table A.3.1.3 (for additional diffusion measures). Associations are visually represented in Figure 3.1.1. For the association tracts, commissural tracts and limbic fibers, age was significantly associated with both FA (lower with increase in age) and MD (higher with increase in age) in all models. Sensorimotor tracts showed only weak associations between age and FA (some higher, some lower with increase in age). For MD, sensorimotor tracts showed associations that were more consistent with other tract categories (higher with increase in age). Adjusting for tract volume and tract-specific WML load led to slight attenuation in the associations except for the limbic fibers, which showed constant associations with age regardless of the model used. Directional diffusivities showed increases in radial diffusivity with age for all tract categories and all models, and consistent increases in axial diffusivity for association and sensorimotor tracts. For commissural and limbic tracts, axial diffusivity was less clearly associated with age in the first three models, and not associated with any tract in the fourth model. In most tracts, the mode of anisotropy was lower with increasing age, but not in the sensorimotor tracts, which generally showed higher mode with age (Appendix Table A.3.1.3). A full set of scatterplots correlating diffusion measurements with age is shown in Appendix Figures A.3.1.1 to A.3.1.5.

Table 3.1.4 shows the associations between cardiovascular risk factors and tract-specific measures of white matter diffusion characteristics. Persons with severe hypertension showed loss of microstructural organization, reflected in both lower FA and higher MD, in association tracts, commissural tracts and limbic fibers compared to persons without hypertension. In contrast, persons with mild hypertension showed no significant changes in FA or MD. While no differences in FA were found between current and never smokers, current smokers did show lower FA in the forceps minor and in the corticospinal tract when compared to former smokers. Current smokers furthermore had higher MD in the forceps minor, the corticospi-

Table 3.1.3

Age and tract-specific diffusion measurements. Values represent regression coefficients (β) for change in standardized FA or MD per year increase in age, adjusted for sex and ICV (and additionally for tract volume and WML load in other models). Significant associations (at Bonferroni corrected threshold 1.1×10^{-4}) are printed in bold instead of italic. Tracts are grouped by functional role

	Model 1		Model 2: 1 + wm volume / tract		Model 3: 1 + wml volume / tract		Model 4: 1 + wm + WML vol / tract	
	FA β	MD β	FA β	MD β	FA β	MD β	FA β	MD β
Association								
ATR	**-0.033**	**0.058**	**-0.025**	**0.054**	**-0.008**	**0.030**	*-0.003*	**0.028**
IFO	**-0.051**	**0.056**	**-0.048**	**0.056**	**-0.036**	**0.037**	**-0.033**	**0.037**
ILF	**-0.038**	**0.051**	**-0.039**	**0.051**	**-0.021**	**0.030**	**-0.021**	**0.030**
PTR	**-0.045**	**0.052**	**-0.043**	**0.053**	**-0.029**	**0.029**	**-0.024**	**0.028**
SLF	**-0.041**	**0.052**	**-0.041**	**0.052**	**-0.029**	**0.038**	**-0.029**	**0.038**
UNC	**-0.034**	**0.052**	**-0.027**	**0.050**	**-0.029**	**0.046**	**-0.023**	**0.044**
Commissural								
FMA	**-0.044**	**0.045**	**-0.029**	**0.039**	**-0.028**	**0.021**	**-0.011**	**0.014**
FMI	**-0.062**	**0.049**	**-0.056**	**0.048**	**-0.060**	**0.046**	**-0.054**	**0.045**
Limbic								
CGC	**-0.029**	**0.044**	**-0.029**	**0.044**	**-0.029**	**0.042**	**-0.028**	**0.042**
CGH	**-0.023**	**0.022**	**-0.023**	**0.022**	**-0.023**	**0.021**	**-0.023**	**0.021**
Sensorimotor								
CST	**-0.009**	**0.054**	*-0.003*	**0.050**	*-0.004*	**0.042**	*0.002*	**0.038**
MCP	**0.010**	**0.028**	*-0.001*	**0.020**	*	*	*	*
ML	*0.004*	**0.024**	**0.007**	**0.023**	*	*	*	*
STR	**-0.014**	**0.057**	**-0.008**	**0.055**	*-0.004*	**0.038**	*0.003*	**0.036**

** WML were not segmented infratentorially.*

FA indicates fractional anisotropy, MD mean diffusivity, ICV intracranial volume, WML white matter lesion; refer to Table 3.1.2 for tract abbreviations.

nal tract, the medial lemniscus and the superior thalamic radiation compared with either never or former smokers while no significant associations were found when comparing former to never smokers. Persons with diabetes mellitus displayed loss of microstructural organization in the association tracts and in the forceps minor, reflected in a decrease in FA. No changes in microstructure were found for persons with hypercholesterolemia or *APOE* ε4 allele carriers.

Appendix Tables A.3.1.5 and A.3.1.6 show interactions between the various risk factors and age, showing higher MD, axial and radial diffusivity with increasing age for some tracts in hypertensives versus non-hypertensives. Additionally, axial diffusivity was higher with increasing age in the superior and inferior longitudinal fasciculi in persons carrying the *APOE* ε4 allele compared with non-carriers.

Excluding participants who had the swapped phase-frequency diffusion MRI acquisition from the analyses did not change the results materially.

Discussion

In a large sample of middle aged and elderly persons we studied age-related changes in tract-specific microstructure and we observed widespread loss of microstructural organization with age. This loss of tract microstructure was present for association, commissural and limbic tracts. In all tracts, except in the limbic system, this loss of microstructure could be partially attributed to tract atrophy and increase in WML load. Sensorimotor tracts were relatively spared from age related deterioration. Independent from age and macrostructural white matter changes, we observed substantially worse tract-specific microstructural organization in persons with severe hypertension, in current smokers and in diabetics.

Strengths of our study are the large sample size and the population-based setting. In contrast to previous studies that spanned very wide age ranges,[15–19] the age range in this study was appropriate to specifically study neurodegeneration. Furthermore, we took macrostructural white matter changes into account and assessed an independent association between age, cardiovascular risk factors and microstructural organization. Finally, we performed tract-specific measurements of tissue microstructure using fully automated methods that we previously made publicly available,[30] ensuring that our results can be used as reference values for other investigations.

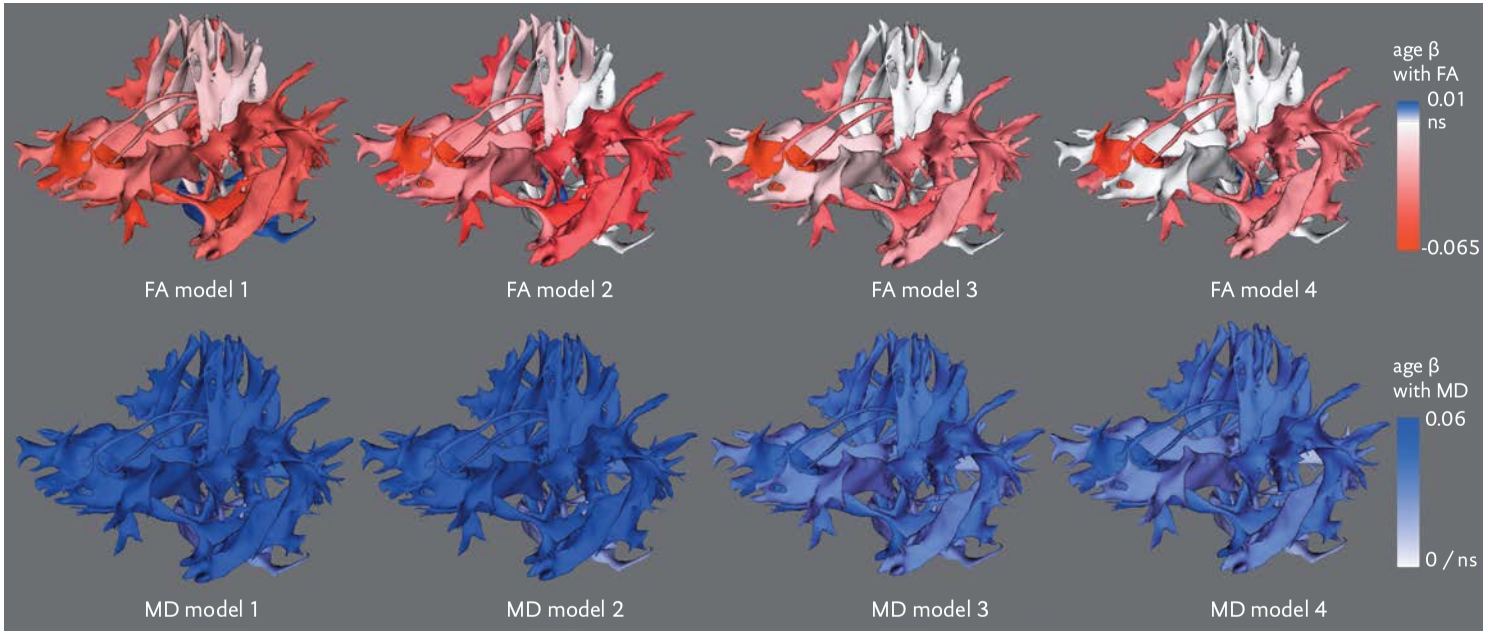

Figure 3.1.1. *Age and tract-specific FA and MD.*
Maps representing all 25 white matter tracts in the population, presented in a single subject's anatomy for visualization purpose. Colors reflect regression coefficients for change in standardized FA (row 1) or MD (row 2) per year increase in age, adjusted for sex and intracranial volume in model 1, and additionally for tract volume (model 2) and WML load (model 3), or both tract-specific volumes (model 4). Higher strength of association is depicted in red for negative associations, blue for positive, with non-significant (ns) associations displayed in white. FA indicates fractional anisotropy, MD mean diffusivity, WML white matter lesion.

Table 3.1.4
Risk factors and tract-specific diffusion measurements

	FA							MD						
	Mild HTN	Severe HTN	Former smoking	Current smoking	Hyper-chol	Diabetes	APOE ε4 carrier	Mild HTN	Severe HTN	Former smoking	Current smoking	Hyper-chol	Diabetes	APOE ε4 carrier
Association														
ATR	*-0.03*	*-0.07*	*0.04*	*-0.03*	*0.04*	*0.03*	*-0.01*	*0.00*	*0.07*	*0.00*	*0.09*	*0.00*	*0.04*	*0.02*
IFO	*-0.05*	**-0.13**	*0.02*	*-0.04*	*0.03*	**-0.19**	*0.00*	*0.03*	**0.12**	*-0.01*	*0.08*	*0.00*	*0.11*	*0.01*
ILF	*-0.04*	**-0.11**	*0.02*	*-0.03*	*0.04*	**-0.19**	*0.00*	*0.04*	**0.12**	*0.00*	*0.05*	*-0.02*	*0.12*	*0.03*
PTR	*-0.04*	**-0.12**	*0.01*	*-0.03*	*0.04*	**-0.18**	*-0.05*	*0.02*	*0.08*	*0.03*	*0.06*	*0.00*	*0.12*	*0.03*
SLF	*-0.03*	**-0.16**	*0.04*	*-0.05*	*0.03*	*-0.13*	*-0.01*	*0.04*	**0.18**	*0.00*	*0.09*	*-0.02*	*0.10*	*0.01*
UNC	*-0.01*	*-0.07*	*0.05*	*-0.04*	*0.03*	*-0.04*	*0.00*	*0.05*	**0.14**	*-0.02*	*0.08*	*0.02*	*0.04*	*0.01*
Commissural														
FMA	*0.00*	*-0.06*	*-0.02*	*-0.02*	*0.05*	*-0.09*	*-0.01*	*-0.01*	*0.04*	*0.02*	*0.05*	*-0.01*	*0.01*	*0.02*
FMI	*-0.03*	**-0.12**	*0.02*	*-0.10*	*0.03*	**-0.17**	*-0.02*	*0.03*	**0.15**	*-0.02*	**0.13**	*0.02*	*0.10*	*0.02*
Limbic														
CGC	*-0.01*	*-0.12*	*-0.01*	*-0.10*	*0.00*	*-0.17*	*-0.03*	*0.03*	**0.18**	*0.00*	*0.10*	*-0.01*	*0.10*	*0.04*
CGH	*-0.03*	*-0.04*	*0.01*	*-0.08*	*0.01*	*-0.09*	*0.02*	*0.02*	*-0.04*	*-0.02*	*0.03*	*0.04*	*0.11*	*0.02*
Sensorimotor														
CST	*0.09*	*0.10*	*0.03*	*-0.11*	*0.03*	*0.07*	*-0.02*	*0.01*	**0.13**	*0.01*	**0.15**	*-0.02*	*0.10*	*0.02*
MCP	*0.05*	*0.04*	*0.04*	*0.00*	*-0.01*	*-0.02*	*-0.03*	*-0.02*	*0.04*	*-0.01*	*0.07*	*-0.06*	*0.02*	*0.05*
ML	*0.05*	*0.01*	*0.01*	*-0.02*	*0.04*	*0.06*	*0.02*	*0.01*	*0.03*	*0.01*	**0.19**	*0.04*	*0.08*	*0.00*
STR	*0.11*	*0.08*	*0.04*	*-0.07*	*-0.04*	*0.08*	*-0.02*	*0.03*	**0.13**	*0.01*	**0.12**	*-0.01*	*0.10*	*0.02*

*Values represent difference in standardized FA or MD per tract for persons with specific risk factors compared to persons without. Participants with hypertension were compared to a normotensive reference group. Current or former smokers were compared to never smokers. Significant associations are printed in bold instead of italic. A significant difference between two different risk groups is indicated with an * (all tests with a Bonferroni corrected threshold of 1.1×10^{-4}). Tracts are grouped by functional role. FA indicates fractional anisotropy, MD mean diffusivity, HTN hypertension, hyperchol hypercholesterolemia, APOE apolipoprotein E; refer to Table 3.1.2 for tract abbreviations.*

There are a number of methodological considerations. For tract-specific diffusion measurements, we assessed median FA, MD and additional diffusion measures (axial and radial diffusivity and mode of diffusivity) over each entire tract. We chose to do so for reasons of specificity, which is lacking for global white matter measures,[33] and for efficiency, to reduce the number of multiple comparisons and to analyze tracts as functional entities. Analyzing complete tracts as functional entities has the advantage that damage along the entire tract is aggregated in the analysis, not requiring exact alignment across subjects.[34] Yet, aggregation over entire tracts may also discard some information (especially spatial information) compared to voxel-based analyses techniques. On the other hand, (conventional) voxel based techniques suffer from potential misregistration and require an a priori hypothesis on the expected spatial extent of the associations.[35,36] Further research needs to address whether a finer grained analysis or a different aggregation approach could improve sensitivity to detect cross-sectional differences.

Using our population-based sample, we investigated white matter microstructure in aging, community-dwelling subjects. While participants were non-demented at time of imaging, pre-clinical AD pathology according to recently published criteria,[37] may have been present in a proportion of our population. Though not all subjects with AD-related pathologic brain changes will eventually convert to AD, it may be hypothesized that our results are in part explained by these pathologies. Longitudinal investigations on the same population will eventually help to identify the contribution of incipient AD to our results.

Limitations of this study are the cross sectional design which precludes us to infer causality from the observed associations with age and cardiovascular risk factors. Due to limitations in the number of images that could be acquired in the diffusion sequence, the cerebellum could not be fully incorporated in the field of view (FOV) of the diffusion scan. We tried to take this into account in the tractography and in our analyses, but for both the medial lemniscus and the middle cerebellar peduncle, some variance in the diffusion measurements might still be attributable to the individual FOV. Tractography also has some general limitations, it is influenced by crossing fiber regions, and subject anatomy and physiology, which in turn influence the segmentation, and thereby the tract volumes. While this means that we cannot interpret tract volume as a pure indicator of tract atrophy, it is still the best estimate available for tract-specific atrophy. Regions of crossing fibers were dealt with in the model estimation for the probabilistic tractography; however, the descriptive measures used in our analyses were based on the tensor model, which assumes only a single fiber population. Although the tensor model is the most widely used model in diffusion image analysis, this does complicate the interpretation of the results in regions of crossing fibers. The DTI based mode of anisotropy[27] has been helpful in

investigating crossing fiber regions[38] and we therefore also included this measure in our analyses. Our approach, which does not model the free water component of the diffusion signal, did not allow analyzing the fornix as measurements in this tract would have been particularly affected by CSF contamination.[39]

With increasing age, we observed widespread and consistent decline in all but the sensorimotor tracts. Different patterns of degeneration in fiber tracts have been shown to lead to counter-intuitive findings (e.g., increases in both FA and MD) in regions where these tracts cross.[38,40] The observed weak associations of age with FA in the sensorimotor tracts, combined with consistent increases in MD in the same tracts may therefore well indicate relative sparing of the sensorimotor tracts in degeneration. This is further corroborated by the higher mode of anisotropy we found with increasing age only in the corticospinal tract and the superior thalamic radiation. This indicates the tendency of the tensors to become more needle-like in these regions, and less pancake-like (the prototypical shape in crossing fiber regions), i.e. what is expected in relative sparing of the sensorimotor tracts.

In the commissural tracts and the limbic fibers, we found more loss of microstructural organization with age in the (anterior) forceps minor and cingulate gyrus part of the cingulum, and less in the (posterior) forceps major, and parahippocampal part of the cingulum. This supports the hypothesis of an anterior-posterior gradient in neurodegeneration, in which white matter networks that develop later in life are most affected by neurodegeneration[41,42] possibly leading to functional compensation in tasks performed by the frontal lobes.[43]

We observed a linear decline in tract integrity with age, in contrast to previous studies that observed higher order associations of age and DTI measures.[15,16,18,19,44,45] Yet, those studies invariably included subjects of young age and in young adulthood, and therefore also modeled (proximity of) the inflection point between net development of white matter and the degeneration observed with aging. The loss in microstructural organization observed with age could partly be explained by WML load and tract volume decrease. However, unlike in a previous voxel-based analysis,[46] we still found a significant association with age and cardiovascular risk factors when correcting for these macroscopic manifestations of white matter degeneration. This differential portion of explained variance across tracts could highlight differences in susceptibility to vascular damage (predominantly association tracts) and other degenerative processes (e.g., in the cingulum). Furthermore, our data support the view that white matter microstructure may be a more sensitive or earlier marker of neurodegeneration than macrostructural changes.

The widespread changes in microstructure we observed with hypertension are in agreement with previous studies,[47] which found altered microstructure in frontal (including the genu of the corpus callosum), parietal and medial-temporal regions in hypertensives, which attenuated but persisted when additionally controlling for WML load. Loss of microstructure with hypertension in the splenium and the anterior body of the corpus callosum has also been reported,[48] with differences again attenuating but persisting when additionally controlling for macrostructural measures of neurodegeneration including WML volume.

We did not identify a direct association between *APOE* ε4 allele carriership and loss of white matter microstructure but we did identify a stronger association between increasing age and higher axial diffusivity (i.e., reduced microstructural organization) in ε4 carriers. Previous studies did identify direct associations in much smaller cohorts using region of interest[49] and voxelwise (TBSS) analyses.[50,51] Furthermore, there is growing evidence for systemic structural differences in the brain white matter of carriers of the risk allele.[52] We therefore had anticipated finding more widespread associations. Our unexpected findings might be caused by differences in the included populations across studies, or by variability in definitions of control and risk groups with respect to *APOE* genotype. Also, the previously suggested potential over-aggregation in analyzing whole tracts (including crossing fiber regions) versus smaller regions or voxels could contribute to these different results. Further research is needed to assess the individual impact of these differences.

A large study in persons with cerebral small vessel disease that related smoking status to changes in global FA and MD also found strong effects for current smokers, which were absent for persons who had quit smoking at least 20 years prior.[53] We also found higher diffusivity in several tracts in current smokers compared to never smokers, but not in former smokers. Additionally, the differences we directly observed between former and current smokers further corroborate the positive effect of smoking cessation.[53]

We found marked DTI measure changes, independent from age, for persons with diabetes mellitus reflected in reduced FA measurements in many association tracts. Similar results were found in a recent tractography analysis in a case control analysis focused on type 2 diabetes.[54] The changes we observed with diabetes translate to an effective age difference of between 3 and 9 years for white matter tract integrity. These results add to the growing body of evidence that diabetes affects the brain.[55]

In conclusion, in this general aging population, we identified widespread changes in white matter tissue microstructure with age, which could be partly attributed to tract atrophy and tract-specific WML load. We also found changes associated

to smoking, hypertension and diabetes mellitus when controlling for the effects of age and global measures of white matter degeneration. These data provide the groundwork for future studies on white matter deterioration in aging and neurodegeneration that will specifically focus on tract-specific patterns of degeneration and cognition.

Appendices

Appendix Table 3.1.1
Tractography parameters and reproducibility measures

	# seeds (× 1k)	max FA R^2	threshold at max R^2	Kappa	MASD (mm)
Association					
ATR	1.0	0.90	0.002	0.74	0.70
IFO	4.4	0.94	0.01	0.69	0.55
ILF	1.2	0.93	0.005	0.70	0.64
PTR	20.0	0.88	0.005	0.61	0.86
SLF	0.4	0.94	0.001	0.72	0.80
UNC	1.2	0.87	0.01	0.69	0.58
Commissural					
FMA	0.6	0.93	0.005	0.69	0.60
FMI	0.6	0.86	0.01	0.63	0.62
Limbic					
CGC	20.0	0.89	0.01	0.63	0.43
CGH	3.0	0.79	0.02	0.65	0.55
Sensorimotor					
CST	4.0	0.90	0.005	0.71	0.62
MCP	4.0	0.60	0.0001	0.67	1.12
ML	1.2	0.79	0.005	0.77	0.44
STR	0.8	0.92	0.005	0.67	0.64

 # seeds corresponds to the number of particles initialized per seed mask voxel. Reproducibility of the FA measurement was defined as the R^2 value for FA measurement in both scans, computed for each tract, while increasing the segmentation threshold. Max FA R^2 is the maximum reproducibility observed on the FA, obtained at the threshold on the tract density image specified in the next column. Additionally, we computed Cohen's Kappa statistic, and the mean absolute surface distance (MASD) for the selected thresholds after rigidly aligning the FA images to the halfway space in between both acquisitions which both reflect reproducibility of the tract segmentations. Abbreviations: FA, fractional anisotropy; MASD, mean absolute surface distance; refer to Table 3.1.2 for tract abbreviations.

Appendix Table 3.1.2
Average diffusion measurements for the directional diffusivities

	AxD		RD		MO	
	Mean	SD	Mean	SD	Mean	SD
Association						
ATR	1.04	0.05	0.61	0.04	0.57	0.05
IFO	1.16	0.05	0.57	0.05	0.70	0.06
ILF	1.12	0.04	0.58	0.04	0.63	0.06
PTR	1.14	0.07	0.60	0.05	0.58	0.08
SLF	1.01	0.04	0.56	0.04	0.41	0.07
UNC	1.08	0.04	0.59	0.03	0.70	0.05
Commissural						
FMA	1.28	0.06	0.53	0.05	0.86	0.05
FMI	1.21	0.05	0.55	0.05	0.80	0.07
Limbic						
CGC	1.08	0.04	0.53	0.03	0.73	0.10
CGH	1.04	0.04	0.61	0.04	0.66	0.09
Sensorimotor						
CST	1.09	0.05	0.49	0.03	0.71	0.07
MCP	0.99	0.10	0.58	0.04	0.47	0.13
ML	1.12	0.04	0.53	0.02	0.75	0.05
STR	1.03	0.05	0.52	0.03	0.58	0.09

For each individual, median axial diffusivity (AxD, × $10^{-3}$$mm^2$/s), radial diffusivity (RD, × $10^{-3}$$mm^2$/s) and mode of anisotropy (MO) is computed inside the (segmented) tracts, and then averaged over all participants. Abbreviations: SD, standard deviation; refer to Table 3.1.2 for tract abbreviations.

Appendix Table 3.1.3

Age and tract-specific diffusion measurements for directional diffusivities and tensor mode

	Model 1			Model 2: 1 + wm volume / tract			Model 3: 1 + WML volume / tract			Model 4: 1 + wm + WML vol / tract		
	AxD β	RD β	MO β	AxD β	RD β	MO β	AxD β	RD β	MO β	AxD β	RD β	MO β
Association												
ATR	**0.060**	**0.056**	*-0.003*	**0.056**	**0.051**	*0.005*	**0.033**	**0.027**	*-0.005*	**0.031**	**0.024**	*0.003*
IFO	**0.044**	**0.058**	**-0.030**	**0.046**	**0.057**	**-0.028**	**0.028**	**0.040**	**-0.026**	**0.030**	**0.038**	**-0.024**
ILF	**0.050**	**0.049**	*0.003*	**0.050**	**0.050**	*0.003*	**0.029**	**0.029**	*0.002*	**0.029**	**0.029**	*0.002*
PTR	**0.047**	**0.053**	**-0.024**	**0.048**	**0.052**	**-0.023**	**0.026**	**0.031**	**-0.024**	**0.027**	**0.028**	**-0.021**
SLF	**0.050**	**0.050**	**-0.007**	**0.050**	**0.050**	**-0.008**	**0.037**	**0.036**	**-0.006**	**0.037**	**0.036**	**-0.006**
UNC	**0.043**	**0.051**	**-0.015**	**0.045**	**0.047**	**-0.009**	**0.037**	**0.045**	**-0.014**	**0.040**	**0.041**	**-0.008**
Commissural												
FMA	**0.015**	**0.046**	**-0.030**	**0.024**	**0.035**	**-0.016**	**-0.008**	**0.024**	**-0.029**	*0.000*	**0.012**	**-0.014**
FMI	**-0.006**	**0.060**	**-0.035**	*0.001*	**0.056**	**-0.024**	**-0.008**	**0.057**	**-0.035**	*-0.001*	**0.053**	**-0.023**
Limbic												
CGC	*0.005*	**0.044**	**-0.050**	**0.006**	**0.044**	**-0.050**	*0.004*	**0.043**	**-0.049**	*0.005*	**0.042**	**-0.049**
CGH	**0.006**	**0.026**	*-0.004*	*0.006*	**0.026**	*-0.004*	*0.005*	**0.025**	*-0.004*	*0.005*	**0.025**	*-0.004*
Sensorimotor												
CST	**0.048**	**0.041**	**0.029**	**0.047**	**0.036**	**0.027**	**0.038**	**0.030**	**0.026**	**0.036**	**0.025**	**0.025**
MCP	**0.025**	**0.022**	**0.012**	**0.012**	**0.020**	*0.001*	*	*	*	*	*	*
ML	**0.014**	**0.017**	**-0.017**	**0.017**	**0.014**	**-0.013**	*	*	*	*	*	*
STR	**0.055**	**0.049**	**0.027**	**0.056**	**0.045**	**0.028**	**0.038**	**0.029**	**0.022**	**0.039**	**0.025**	**0.024**

*Values represent regression coefficients (β) for change in standardized axial diffusivity (AxD), radial diffusivity (RD) or mode of anisotropy (MO) per year increase in age, adjusted for sex and ICV (and additionally for tract volume and WML load in other models). Significant associations (at Bonferroni corrected threshold of 1.1×10^{-4}) are printed in bold instead of italic. Tracts are grouped by functional role. * WML were not segmented infratentorially. Abbreviations: ICV, intracranial volume; WML, white matter lesion; refer to Table 3.1.2 for tract abbreviations.*

Appendix Table 3.1.4

Risk factors and tract-specific diffusion measurements for directional diffusivities and tensor mode

	AxD							RD							MO						
	Mild HTN	Severe HTN	Former smoking	Current smoking	Hyper-chol	Diabetes	APOE ε4 carrier	Mild HTN	Severe HTN	Former smoking	Current smoking	Hyper-chol	Diabetes	APOE ε4 carrier	Mild HTN	Severe HTN	Former smoking	Current smoking	Hyper-chol	Diabetes	APOE ε4 carrier
Association																					
ATR	*-0.01*	*0.04*	*0.01*	**0.09**	*0.02*	*0.06*	*0.01*	*0.00*	*0.07*	*-0.01*	*0.08*	*-0.01*	*0.03*	*0.02*	*-0.01*	*-0.04*	*-0.02*	*0.05*	*0.05*	*0.05*	*-0.05*
IFO	*0.03*	*0.09*	*0.01*	*0.08*	*0.02*	*0.03*	*0.01*	*0.04*	**0.13**	*-0.01*	*0.07*	*-0.01*	**0.15**	*0.01*	*0.02*	*-0.05*	*-0.02*	*0.01*	*-0.01*	*-0.13*	*0.02*
ILF	*0.04*	**0.10**	*0.00*	*0.04*	*-0.01*	*0.05*	*0.04*	*0.04*	**0.13**	*0.00*	*0.05*	*-0.02*	**0.15**	*0.02*	*-0.03*	*-0.04*	*-0.01*	*0.03*	*0.03*	*-0.08*	*0.04*
PTR	*0.03*	*0.05*	*0.06*	*0.06*	*0.02*	*0.07*	*0.03*	*0.03*	**0.10**	*0.03*	*0.06*	*-0.01*	**0.15**	*0.03*	*-0.02*	*-0.09*	*-0.01*	*0.01*	*0.01*	**-0.22**	*0.00*
SLF	*0.04*	**0.17**	*0.03*	*0.10*	*-0.01*	*0.09*	*0.01*	*0.03*	**0.17**	*-0.01*	*0.08*	*-0.03*	*0.10*	*0.01*	*0.02*	*0.07*	*0.01*	*-0.01*	*0.06*	*0.16*	*-0.01*
UNC	*0.07*	**0.14**	*0.01*	*0.07*	*0.04*	*0.04*	*0.00*	*0.04*	**0.13**	*-0.03*	*0.08*	*0.01*	*0.05*	*0.00*	*0.04*	*0.06*	*0.03*	*0.02*	*0.04*	*0.03*	*0.00*
Commissural																					
FMA	*0.01*	*0.01*	*0.00*	*0.02*	*-0.01*	*-0.13*	*0.02*	*0.00*	*0.05*	*0.03*	*0.04*	*-0.03*	*0.05*	*0.02*	*0.01*	*0.04*	*-0.04*	*-0.03*	*0.03*	*-0.11*	*0.02*
FMI	*0.02*	*0.08*	*-0.01*	*0.07*	*0.06*	*-0.05*	*0.00*	*0.03*	**0.15**	*-0.02*	**0.12**	*0.00*	*0.14*	*0.02*	*0.05*	*-0.07*	*0.01*	*-0.01*	*0.01*	*-0.11*	*-0.01*
Limbic																					
CGC	*0.03*	*0.07*	*-0.02*	*-0.02*	*-0.01*	*-0.06*	*0.02*	*0.02*	**0.18**	*0.01*	*0.12*	*0.00*	*0.16*	*0.04*	*0.03*	*-0.08*	*-0.02*	*-0.09*	*0.00*	*-0.13*	*0.01*
CGH	*0.01*	*-0.05*	*-0.03*	*-0.04*	*0.04*	*0.06*	*0.03*	*0.04*	*-0.01*	*-0.02*	*0.05*	*0.02*	*0.12*	*0.02*	*0.04*	*0.05*	*-0.01*	*-0.04*	*-0.01*	*-0.01*	*0.00*
Sensorimotor																					
CST	*0.06*	**0.17**	*0.03*	*0.09*	*0.00*	**0.15**	*0.02*	*-0.05*	*0.02*	*-0.01*	**0.17**	*-0.03*	*0.03*	*0.03*	*0.12*	**0.17**	*0.03*	*-0.01*	*0.03*	*0.16*	*0.00*
MCP	*0.03*	*0.05*	*0.01*	*0.03*	*-0.05*	*0.00*	*0.03*	*-0.06*	*0.02*	*-0.03*	*0.07*	*-0.03*	*0.04*	*0.05*	*0.04*	*0.01*	*0.03*	*0.04*	*-0.01*	*-0.01*	*0.00*
ML	*0.07*	*-0.01*	*0.01*	*0.07*	*0.04*	*0.10*	*0.04*	*-0.02*	*0.03*	*-0.01*	*0.13*	*0.00*	*0.03*	*-0.01*	*0.04*	*-0.06*	*-0.01*	*-0.06*	*-0.02*	*-0.04*	*0.09*
STR	*0.09*	**0.17**	*0.04*	*0.09*	*-0.04*	**0.17**	*0.01*	*-0.03*	*0.06*	*0.00*	**0.11**	*0.00*	*0.03*	*0.02*	*0.12*	**0.14**	*0.04*	*0.05*	*-0.02*	**0.26**	*0.02*

*Values represent difference in standardized axial diffusivity (AxD), radial diffusivity (RD) or mode of anisotropy (MO) per tract for persons with specific risk factors compared to persons without. Participants with hypertension were compared to a normotensive reference group. Current or former smokers were compared to never smokers. Significant associations are printed in bold instead of italic. A significant difference between two different risk groups is indicated with an * (all tests with a Bonferroni corrected threshold of 1.1×10^{-4}). Tracts are grouped by functional role. Abbreviations: HTN, hypertension; hyperchol, hypercholesterolemia; APOE, apolipoprotein E; refer to Table 3.1.2 for tract abbreviations.*

Appendix Table 3.1.5

Interaction between age and risk factors for tract-specific diffusion measurements

	FA							MD						
	Mild HTN	Severe HTN	Former smoking	Current smoking	Hyper-chol	Diabetes	APOE ε4 carrier	Mild HTN	Severe HTN	Former smoking	Current smoking	Hyper-chol	Diabetes	APOE ε4 carrier
Association														
ATR	*0.001*	*-0.002*	*-0.003*	*-0.004*	*-0.004*	*0.001*	*-0.005*	*0.028*	*0.029*	*0.030*	*0.028*	*0.029*	*0.033*	*0.031*
IFO	*-0.030*	*-0.032*	*-0.033*	*-0.034*	*-0.033*	*-0.035*	*-0.035*	*0.035*	*0.037*	*0.039*	*0.036*	*0.038*	*0.039*	*0.040*
ILF	*-0.017*	*-0.019*	*-0.021*	*-0.022*	*-0.022*	*-0.018*	*-0.025*	*0.028*	*0.029*	*0.032*	*0.030*	*0.031*	*0.031*	*0.037*
PTR	*-0.022*	*-0.021*	*-0.025*	*-0.021*	*-0.025*	*-0.027*	*-0.027*	*0.025*	*0.028*	*0.030*	*0.024*	*0.029*	*0.032*	*0.033*
SLF	*-0.023*	*-0.027*	*-0.029*	*-0.030*	*-0.030*	*-0.027*	*-0.031*	*0.035*	*0.038*	*0.039*	*0.041*	*0.039*	*0.038*	*0.044*
UNC	*-0.019*	*-0.024*	*-0.024*	*-0.023*	*-0.023*	*-0.022*	*-0.023*	*0.043*	**0.046**	*0.046*	*0.044*	*0.046*	*0.047*	*0.049*
Commissural														
FMA	*-0.009*	*-0.013*	*-0.012*	*-0.009*	*-0.012*	*-0.016*	*-0.013*	*0.013*	*0.017*	*0.016*	*0.012*	*0.015*	*0.018*	*0.017*
FMI	*-0.048*	*-0.054*	*-0.055*	*-0.053*	*-0.054*	*-0.058*	*-0.054*	*0.043*	**0.046**	*0.046*	*0.047*	*0.045*	*0.047*	*0.047*
Limbic														
CGC	*-0.026*	*-0.030*	*-0.028*	*-0.027*	*-0.028*	*-0.034*	*-0.031*	*0.042*	*0.041*	*0.046*	*0.043*	*0.043*	*0.047*	*0.047*
CGH	*-0.028*	*-0.024*	*-0.023*	*-0.024*	*-0.025*	*-0.023*	*-0.025*	**0.035**	*0.022*	*0.022*	*0.020*	*0.023*	*0.030*	*0.024*
Sensorimotor														
CST	*0.003*	*0.001*	*0.003*	*0.000*	*0.002*	*0.003*	*0.001*	*0.036*	*0.039*	*0.040*	*0.041*	*0.039*	*0.043*	*0.042*
MCP	*-0.001*	*-0.001*	*-0.002*	*0.001*	*-0.001*	*-0.001*	*-0.002*	*0.021*	*0.019*	*0.021*	*0.022*	*0.021*	*0.021*	*0.024*
ML	*0.005*	*0.008*	*0.007*	*0.013*	*0.007*	*0.011*	*0.008*	*0.021*	**0.028**	*0.026*	*0.022*	*0.025*	*0.028*	*0.029*
STR	*0.003*	*0.002*	*0.003*	*0.001*	*0.004*	*0.007*	*0.001*	*0.034*	*0.036*	*0.038*	*0.040*	*0.037*	*0.039*	*0.042*

Values represent regression coefficients (β) for change in standardized fractional anisotropy (FA) or mean diffusivity (MD) per tract and per year increase in age for persons with specific risk factors compared to persons without. Participants with hypertension were compared to a normotensive reference group. Current or former smokers were compared to never smokers. Associations that differed significantly from the reference group are printed in bold instead of italic. No significant differences were found between two different risk groups (all tests with a Bonferroni corrected threshold of 1.1×10-4). Tracts are grouped by functional role. Abbreviations: HTN, hypertension; hyperchol, hypercholesterolemia, APOE, apolipoprotein E; refer to Table 3.1.2 for tract abbreviations.

Appendix Table 3.1.6

Interaction between age and risk factors for tract-specific diffusion measurements for AxD, RD and MO

	AxD							RD							MO						
	Mild HTN	Severe HTN	Former smoking	Current smoking	Hyper-chol	Diabetes	APOE ε4 carrier	Mild HTN	Severe HTN	Former smoking	Current smoking	Hyper-chol	Diabetes	APOE ε4 carrier	Mild HTN	Severe HTN	Former smoking	Current smoking	Hyper-chol	Diabetes	APOE ε4 carrier
Association																					
ATR	*0.032*	*0.033*	*0.034*	*0.031*	*0.032*	*0.037*	*0.033*	*0.024*	*0.025*	*0.026*	*0.024*	*0.025*	*0.028*	*0.027*	*0.000*	*0.004*	*0.003*	*0.009*	*0.003*	*-0.005*	*0.001*
IFO	*0.029*	*0.030*	*0.032*	*0.028*	*0.031*	*0.031*	*0.033*	*0.036*	*0.039*	*0.040*	*0.038*	*0.039*	*0.041*	*0.041*	*-0.025*	*-0.026*	*-0.025*	*-0.022*	*-0.024*	*-0.034*	*-0.023*
ILF	*0.029*	*0.029*	*0.031*	*0.029*	*0.031*	*0.034*	**0.036**	*0.026*	*0.028*	*0.031*	*0.029*	*0.030*	*0.029*	*0.035*	*0.003*	*0.002*	*0.001*	*0.001*	*0.003*	*0.004*	*0.004*
PTR	*0.025*	*0.027*	*0.028*	*0.024*	*0.028*	*0.030*	*0.032*	*0.026*	*0.028*	*0.030*	*0.025*	*0.030*	*0.033*	*0.034*	*-0.023*	*-0.022*	*-0.022*	*-0.017*	*-0.021*	*-0.026*	*-0.021*
SLF	*0.035*	*0.037*	*0.038*	*0.041*	*0.038*	*0.037*	**0.044**	*0.032*	*0.035*	*0.037*	*0.038*	*0.037*	*0.035*	*0.041*	*-0.010*	*-0.006*	*-0.007*	*-0.005*	*-0.006*	*-0.009*	*0.000*
UNC	*0.039*	**0.041**	*0.041*	*0.040*	*0.041*	*0.043*	*0.045*	*0.038*	**0.043**	*0.043*	*0.041*	*0.042*	*0.043*	*0.045*	*-0.005*	*-0.012*	*-0.010*	*-0.007*	*-0.008*	*-0.015*	*-0.007*
Commissural																					
FMA	*0.001*	*0.002*	*0.001*	*0.003*	*0.001*	*0.005*	*0.002*	*0.011*	*0.014*	*0.013*	*0.010*	*0.013*	*0.016*	*0.014*	*-0.013*	*-0.018*	*-0.015*	*-0.010*	*-0.014*	*-0.014*	*-0.013*
FMI	*0.004*	*-0.002*	*-0.001*	*0.004*	*0.000*	*-0.005*	*0.001*	*0.049*	*0.054*	*0.054*	*0.054*	*0.053*	*0.056*	*0.054*	*-0.016*	*-0.025*	*-0.025*	*-0.019*	*-0.022*	*-0.031*	*-0.022*
Limbic																					
CGC	*0.006*	*0.001*	*0.008*	*0.007*	*0.005*	*0.004*	*0.007*	*0.040*	*0.043*	*0.044*	*0.042*	*0.043*	*0.049*	*0.046*	*-0.048*	**-0.052**	*-0.048*	*-0.049*	*-0.049*	*-0.058*	*-0.050*
CGH	*0.014*	*0.005*	*0.007*	*0.003*	*0.005*	*0.014*	*0.007*	**0.037**	*0.026*	*0.026*	*0.025*	*0.027*	*0.033*	*0.028*	*-0.009*	*-0.004*	*-0.004*	*-0.004*	*-0.005*	*-0.006*	*-0.006*
Sensorimotor																					
CST	*0.035*	*0.036*	*0.039*	*0.038*	*0.038*	*0.044*	*0.040*	*0.024*	*0.026*	*0.025*	*0.029*	*0.025*	*0.027*	*0.028*	*0.023*	*0.022*	*0.027*	*0.021*	*0.026*	*0.031*	*0.028*
MCP	*0.015*	*0.011*	*0.012*	*0.015*	*0.013*	*0.013*	*0.014*	*0.021*	*0.020*	*0.022*	*0.022*	*0.022*	*0.021*	*0.024*	*0.000*	*0.003*	*0.001*	*0.000*	*0.001*	*0.002*	*0.000*
ML	*0.012*	*0.021*	*0.019*	*0.022*	*0.019*	*0.021*	*0.023*	*0.014*	*0.017*	*0.015*	*0.009*	*0.015*	*0.016*	*0.018*	*-0.017*	*-0.013*	*-0.014*	*-0.007*	*-0.012*	*-0.019*	*-0.010*
STR	*0.036*	*0.038*	*0.041*	*0.042*	*0.040*	*0.045*	*0.044*	*0.023*	*0.025*	*0.026*	*0.028*	*0.025*	*0.025*	*0.030*	*0.019*	*0.022*	*0.025*	*0.023*	*0.025*	*0.031*	*0.027*

Values represent regression coefficients (β) for change in standardized axial diffusivity (AxD), radial diffusivity (RD) or mode of anisotropy (MO) per tract and per year increase in age for persons with specific risk factors compared to persons without. Participants with hypertension were compared to a normotensive reference group. Current or former smokers were compared to never smokers. Associations that differed significantly from the reference group are printed in bold instead of italic. No significant differences were found between two different risk groups (all tests with a Bonferroni corrected threshold of 1.1×10-4). Tracts are grouped by functional role. Abbreviations: HTN, hypertension; hyperchol, hypercholesterolemia, APOE, apolipoprotein E; refer to Table 3.1.2 for tract abbreviations.

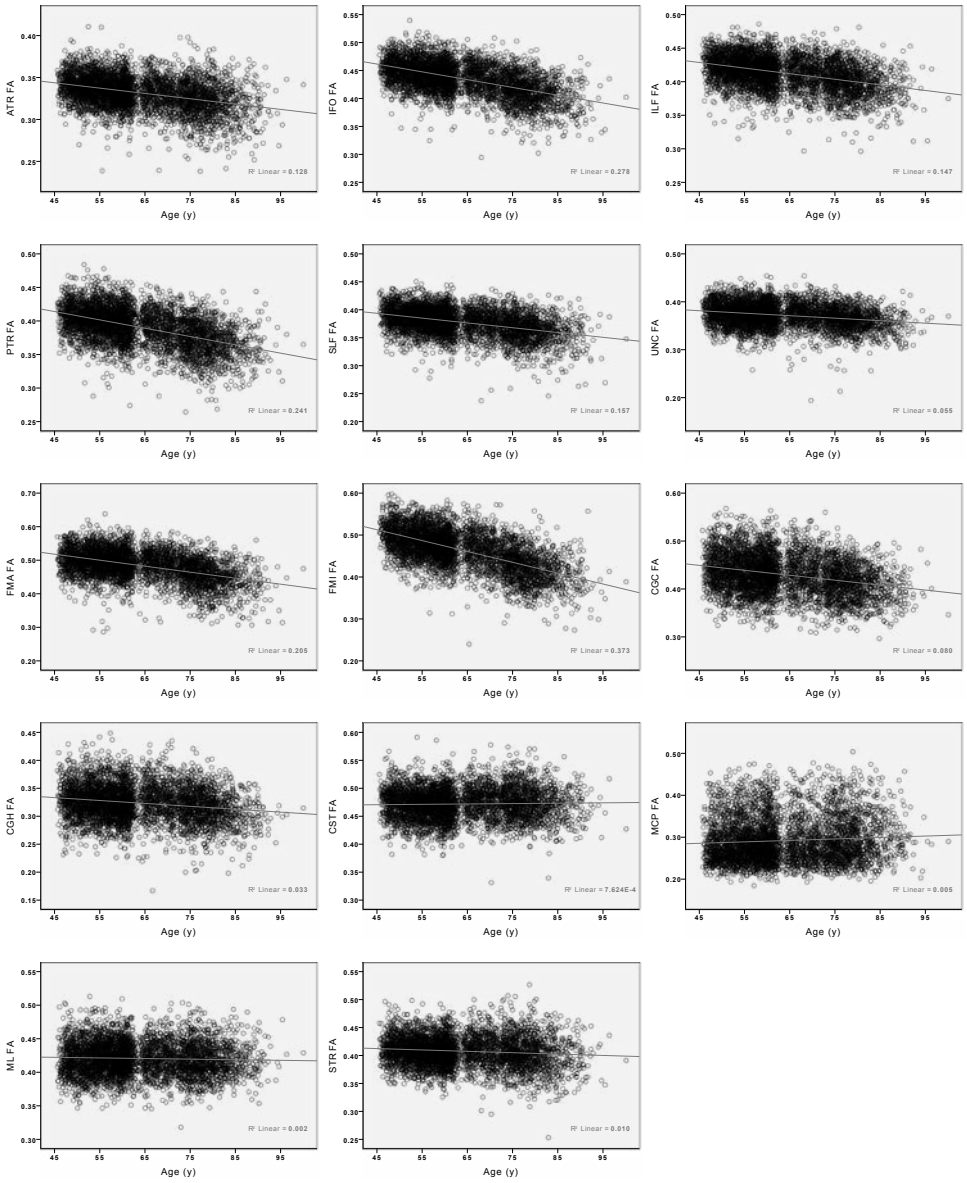

Appendix Figure 3.1.1. *Scatterplots of the relation between age and fractional anisotropy (FA) for all tracts. A linear regression line and the explained variance is added for each tract; refer to Table 3.1.2 for tract abbreviations.*

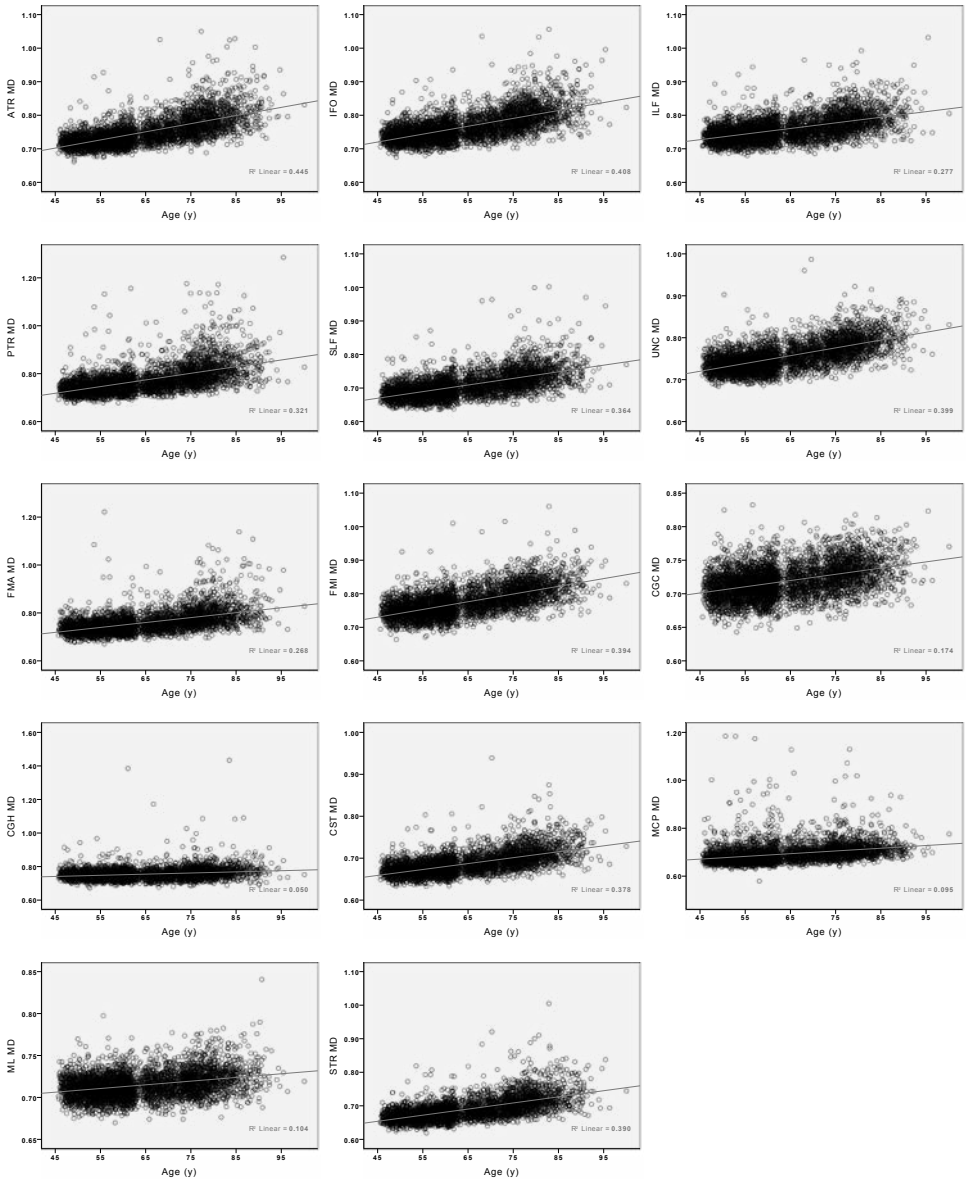

Appendix Figure 3.1.2. *Scatterplots of the relation between age and mean diffusivity (MD, × 10⁻³mm²/s) for all tracts. A linear regression line and the explained variance is added for each tract; refer to Table 3.1.2 for tract abbreviations.*

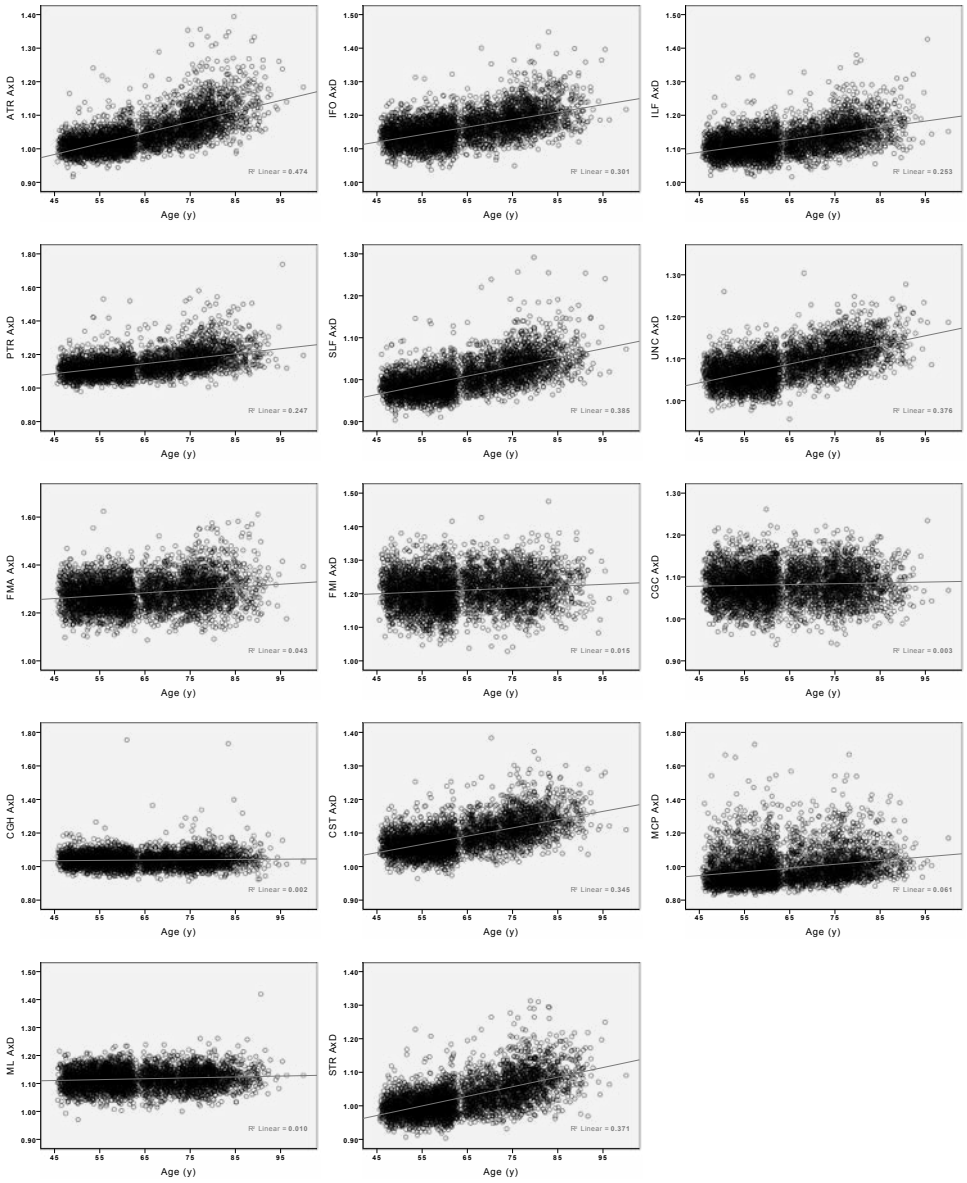

Appendix Figure 3.1.3. *Scatterplots of the relation between age and axial diffusivity (AxD, × 10⁻³mm²/s) for all tracts. A linear regression line and the explained variance is added for each tract; refer to Table 3.1.2 for tract abbreviations.*

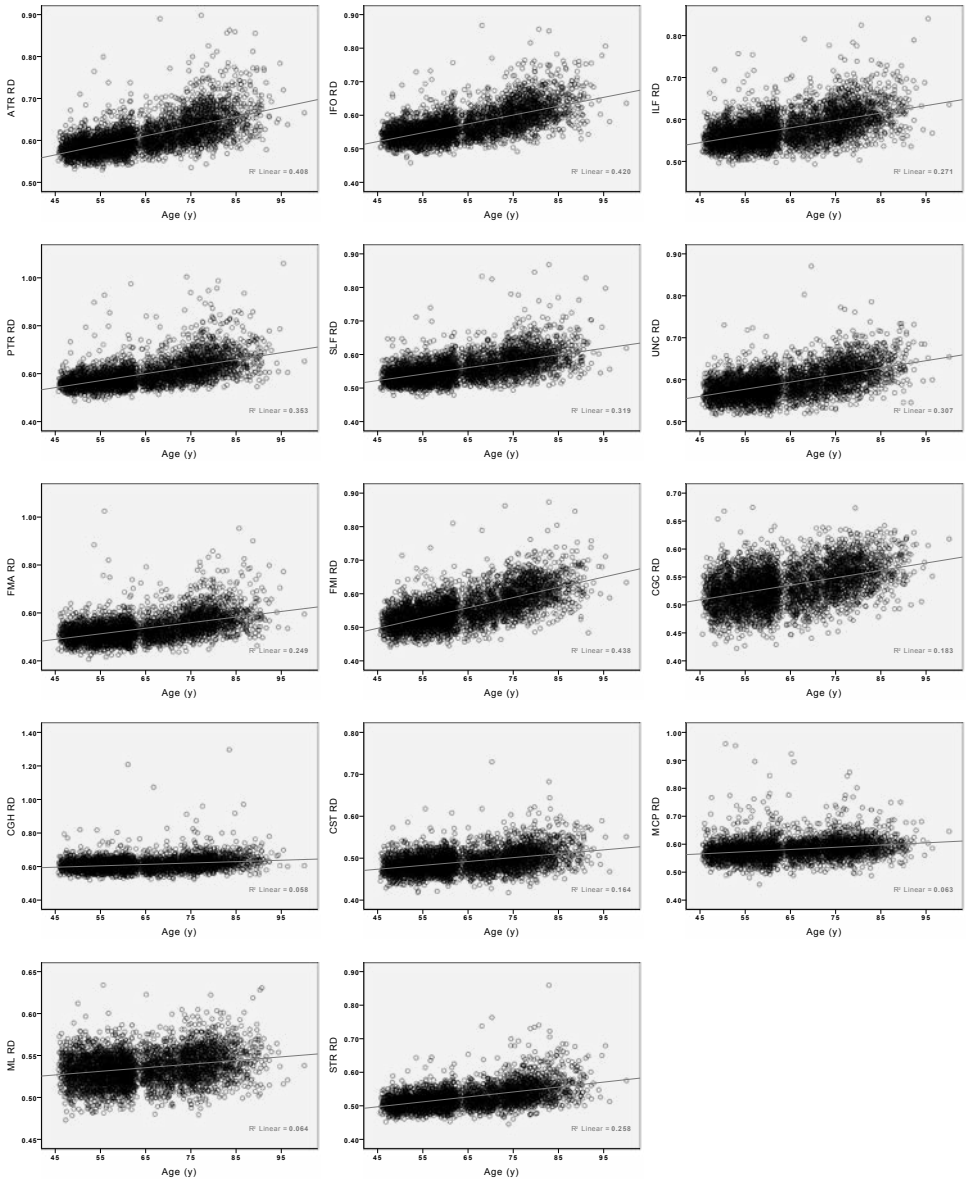

Appendix Figure 3.1.4. *Scatterplots of the relation between age and radial diffusivity (RD, × 10^{-3}mm^2/s) for all tracts. A linear regression line and the explained variance is added for each tract; refer to Table 3.1.2 for tract abbreviations.*

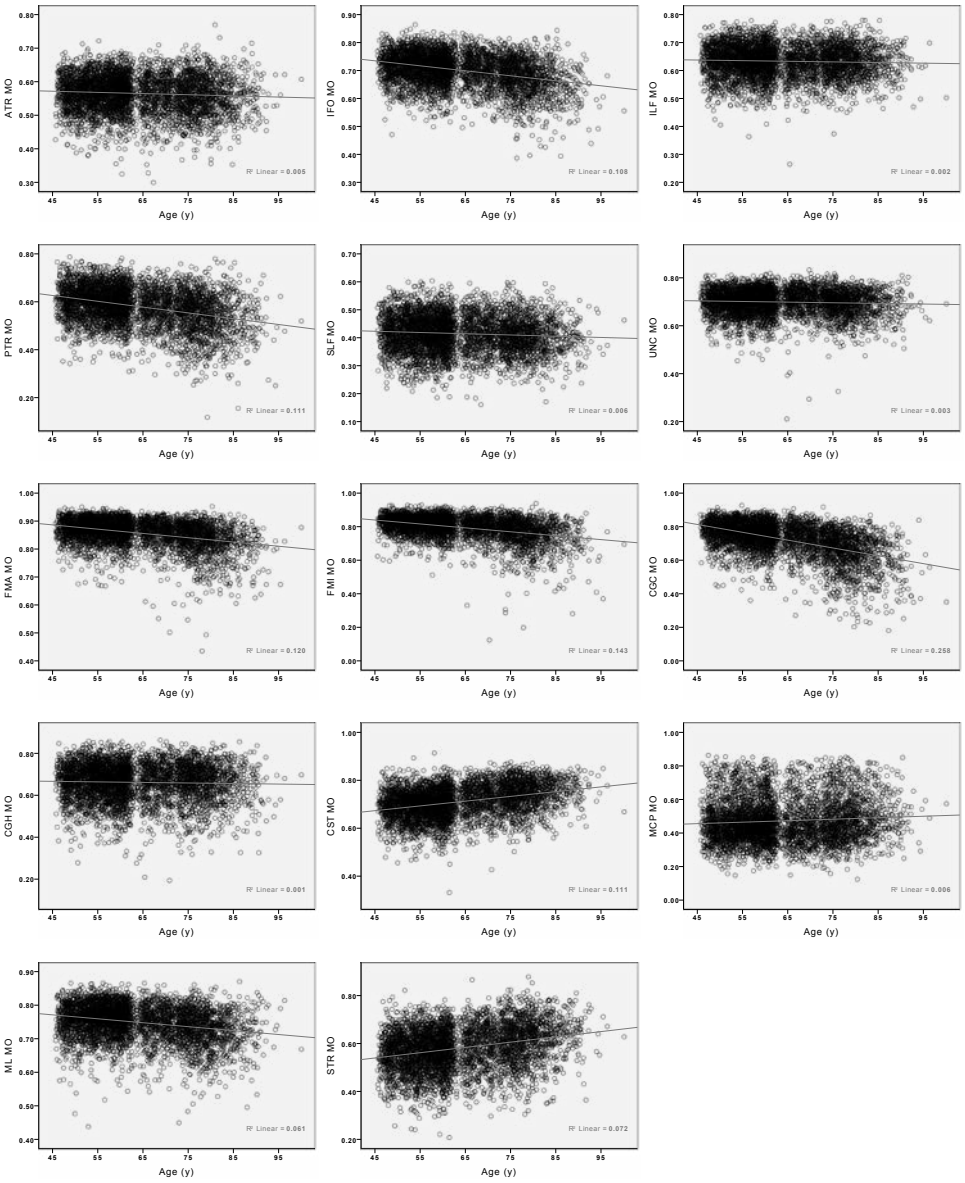

Appendix Figure 3.1.5. *Scatterplots of the relation between age and mode of anisotropy (MO) for all tracts. A linear regression line and the explained variance is added for each tract; refer to Table 3.1.2 for tract abbreviations.*

References

1. Spampinato M, Rumboldt Z, Hosker R, Mintzer J, Alzheimer's Disease Neuroimaging Initiative. Apolipoprotein E and gray matter volume loss in patients with mild cognitive impairment and Alzheimer disease. *Radiology*. 2011;258(3):843-852.
2. Prestia A, Caroli A, van der Flier WM, et al. Prediction of dementia in MCI patients based on core diagnostic markers for Alzheimer disease. *Neurology*. 2013;80(11):1048-56.
3. Frisoni G, Fox N, Jack C, Scheltens P, Thompson PM. The clinical use of structural MRI in Alzheimer disease. *Nat Rev Neurol*. 2010;6(2):67-77.
4. Achterberg HC, van der Lijn F, den Heijer T, et al. Hippocampal shape is predictive for the development of dementia in a normal, elderly population. *Hum Brain Mapp*. 2013;00:01-13.
5. Brickman AM, Honig LS, Scarmeas N, et al. Measuring cerebral atrophy and white matter hyperintensity burden to predict the rate of cognitive decline in Alzheimer disease. *Arch Neurol*. 2008;65(9):1202-8.
6. Maillard P, Fletcher E, Harvey D, et al. White matter hyperintensity penumbra. *Stroke*. 2011;42(7):1917-1922.
7. De Groot M, Verhaaren BFJ, de Boer R, et al. Changes in normal-appearing white matter precede development of white matter lesions. *Stroke*. 2013;44(4):1037-42.
8. Jack CR, Knopman DS, Jagust WJ, et al. Tracking pathophysiological processes in Alzheimer's disease: an updated hypothetical model of dynamic biomarkers. *Lancet Neurol*. 2013;12(2):207-16.
9. Ly M, Canu E, Xu G, et al. Midlife measurements of white matter microstructure predict subsequent regional white matter atrophy in healthy adults. *Hum Brain Mapp*. 2013;000:1-11.
10. Lee DY, Fletcher E, Martinez O, et al. Regional pattern of white matter microstructural changes in normal aging, MCI, and AD. *Neurology*. 2009;73(21):1722-8.
11. Conturo TE, Lori NF, Cull TS, et al. Tracking neuronal fiber pathways in the living human brain. *Proc Natl Acad Sci U S A*. 1999;96(18):10422-7.
12. Mielke MM, Kozauer NA, Chan KCG, et al. Regionally-specific diffusion tensor imaging in mild cognitive impairment and Alzheimer's disease. *Neuroimage*. 2009;46(1):47-55.
13. Werring DJ, Clark CA, Barker GJ, Thompson AJ, Miller DH. Diffusion tensor imaging of lesions and normal-appearing white matter in multiple sclerosis. *Neurology*. 1999;52(8):1626-32.
14. Douaud G, Filippini N, Knight S, Talbot K, Turner MR. Integration of structural and functional magnetic resonance imaging in amyotrophic lateral sclerosis. *Brain*. 2011;134(Pt 12):3470-9.
15. Lebel C, Gee M, Camicioli R, Wieler M, Martin W, Beaulieu C. Diffusion tensor imaging of white matter tract evolution over the lifespan. *Neuroimage*. 2012;60(1):340-52.
16. Westlye LT, Walhovd KB, Dale AM, et al. Life-span changes of the human brain white matter: diffusion tensor imaging (DTI) and volumetry. *Cereb Cortex*. 2010;20(9):2055-68.
17. Salat DH, Tuch DS, Greve DN, et al. Age-related alterations in white matter microstructure measured by diffusion tensor imaging. *Neurobiol Aging*. 2005;26(8):1215-27.
18. Michielse S, Coupland N, Camicioli R, et al. Selective effects of aging on brain white matter microstructure: a diffusion tensor imaging tractography study. *Neuroimage*. 2010;52(4):1190-201.
19. Kennedy KM, Raz N. Pattern of normal age-related regional differences in white matter microstructure is modified by vascular risk. *Brain Res*. 2009;1297:41-56.
20. Hofman A, Darwish Murad S, van Duijn CM, et al. The Rotterdam Study: 2014 objectives and design update. *Eur J Epidemiol*. 2013;28(11):889-926.
21. Ikram MA, van der Lugt A, Niessen WJ, et al. The Rotterdam Scan Study: design and update up to 2012. *Eur J Epidemiol*. 2011;26(10):811-24.
22. Vrooman HA, Cocosco CA, van der Lijn F, et al. Multi-spectral brain tissue segmentation using automatically trained k-Nearest-Neighbor classification. *Neuroimage*. 2007;37(1):71-81.

23. De Boer R, Vrooman HA, van der Lijn F, et al. White matter lesion extension to automatic brain tissue segmentation on MRI. *Neuroimage*. 2009;45(4):1151-1161.

24. Koppelmans V, de Groot M, de Ruiter MB, et al. Global and focal white matter integrity in breast cancer survivors 20 years after adjuvant chemotherapy. *Hum Brain Mapp*. 2014;35(3):889-99.

25. Leemans A, Jones DK. The B-matrix must be rotated when correcting for subject motion in DTI data. *Magn Reson Med*. 2009;61(6):1336-1349.

26. Leemans A, Jeurissen B, Sijbers J, Jones DK. ExploreDTI: a graphical toolbox for processing, analyzing, and visualizing diffusion MR data. In: *Proceedings 17th Scientific Meeting International Society for Magnetic Resonance in Medicine*.Vol 17.; 2009:3537.

27. Ennis DB, Kindlmann G. Orthogonal tensor invariants and the analysis of diffusion tensor magnetic resonance images. *Magn Reson Med*. 2006;55(1):136-146.

28. Behrens TEJ, Johansen-Berg H, Jbabdi S, Rushworth MFS, Woolrich MW. Probabilistic diffusion tractography with multiple fibre orientations: What can we gain? *Neuroimage*. 2007;34(1):144-155.

29. Jenkinson M, Beckmann CF, Behrens TEJ, Woolrich MW, Smith SM. FSL. *Neuroimage*. 2012;62(2):782-90.

30. De Groot M, Vernooij MW, Klein S, et al. Improving alignment in Tract-based spatial statistics: evaluation and optimization of image registration. *Neuroimage*. 2013;76:400-11.

31. Whitworth JA, World Health Organization International Society of Hypertension Writing Group. 2003 World Health Organization (WHO)/International Society of Hypertension (ISH) statement on management of hypertension. *J Hypertens*. 2003;21(11):1983-92.

32. National Cholesterol Education Panel. Third Report of the National Cholesterol Education Program (NCEP) Expert Panel on Detection, Evaluation, and Treatment of High Blood Cholesterol in Adults (Adult Treatment Panel III) final report. *Circulation*. 2002;106(25):3143-421.

33. Lövdén M, Laukka EJ, Rieckmann A, et al. The dimensionality of between-person differences in white matter microstructure in old age. *Hum Brain Mapp*. 2013;34(6):1386-98.

34. White T, Schmidt M, Karatekin C. White matter "potholes" in early-onset schizophrenia: a new approach to evaluate white matter microstructure using diffusion tensor imaging. *Psychiatry Res*. 2009;174(2):110-5.

35. Jones DK, Symms MR, Cercignani M, Howard RJ. The effect of filter size on VBM analyses of DT-MRI data. *Neuroimage*. 2005;26(2):546-554.

36. Smith SM, Jenkinson M, Johansen-Berg H, et al. Tract-based spatial statistics: voxelwise analysis of multi-subject diffusion data. *Neuroimage*. 2006;31(4):1487-1505.

37. Sperling RA, Aisen PS, Beckett LA, et al. Toward defining the preclinical stages of Alzheimer's disease: recommendations from the National Institute on Aging-Alzheimer's Association workgroups on diagnostic guidelines for Alzheimer's disease. *Alzheimers Dement*. 2011;7(3):280-92.

38. Douaud G, Jbabdi S, Behrens TEJ, et al. DTI measures in crossing-fibre areas: increased diffusion anisotropy reveals early white matter alteration in MCI and mild Alzheimer's disease. *Neuroimage*. 2011;55(3):880-90.

39. Berlot R, Metzler-Baddeley C, Jones DK, O'Sullivan MJ. CSF contamination contributes to apparent microstructural alterations in mild cognitive impairment. *Neuroimage*. 2014;92C:27-35.

40. Pierpaoli C, Barnett A, Pajevic S, et al. Water diffusion changes in Wallerian degeneration and their dependence on white matter architecture. *Neuroimage*. 2001;13(6 Pt 1):1174-1185.

41. Pfefferbaum A, Adalsteinsson E, Sullivan EV. Frontal circuitry degradation marks healthy adult aging: Evidence from diffusion tensor imaging. *Neuroimage*. 2005;26(3):891-9.

42. Kantarci K, Senjem ML, Avula R, et al. Diffusion tensor imaging and cognitive function in older adults with no dementia. *Neurology*. 2011;77(1):26-34.

43. Davis SW, Dennis NA, Daselaar SM, Fleck MS, Cabeza R. Que PASA? The posterior-anterior shift in aging. *Cereb Cortex*. 2008;18(5):1201-9.

44. Bartzokis G, Lu PH, Heydari P, et al. Multimodal magnetic resonance imaging assessment of white matter aging trajectories over the lifespan of healthy individuals. *Biol Psychiatry*. 2012;72(12):1026-34.

45. Inano S, Takao H, Hayashi N, Abe O, Ohtomo K. Effects of Age and Gender on White Matter Integrity. *Am J Neuroradiol*. 2011;32:2103-2109.

46. Vernooij MW, de Groot M, van der Lugt A, et al. White matter atrophy and lesion formation explain the loss of structural integrity of white matter in aging. *Neuroimage*. 2008;43(3):470-477.

47. Salat DH, Williams VJ, Leritz EC, et al. Inter-individual variation in blood pressure is associated with regional white matter integrity in generally healthy older adults. *Neuroimage*. 2012;59(1):181-92.

48. Gons RAR, van Oudheusden LJB, de Laat KF, et al. Hypertension is related to the microstructure of the corpus callosum: the RUN DMC study. *J Alzheimers Dis*. 2012;32(3):623-31.

49. Persson J, Lind J, Larsson A, et al. Altered brain white matter integrity in healthy carriers of the APOE epsilon4 allele: a risk for AD? *Neurology*. 2006;66(7):1029-33.

50. Honea RA, Vidoni E, Harsha A, Burns JM. Impact of APOE on the healthy aging brain: a voxel-based MRI and DTI study. *J Alzheimers Dis*. 2009;18(3):553-64.

51. Westlye LT, Reinvang I, Rootwelt H, Espeseth T. Effects of APOE on brain white matter microstructure in healthy adults. *Neurology*. 2012;79(19):1961-9.

52. Dean DC, Jerskey BA, Chen K, et al. Brain differences in infants at differential genetic risk for late-onset Alzheimer disease: a cross-sectional imaging study. *JAMA Neurol*. 2014;71(1):11-22.

53. Gons RAR, van Norden AGW, de Laat KF, et al. Cigarette smoking is associated with reduced microstructural integrity of cerebral white matter. *Brain*. 2011;134(Pt 7):2116-24.

54. Reijmer YD, Brundel M, de Bresser J, et al. Microstructural white matter abnormalities and cognitive functioning in type 2 diabetes: a diffusion tensor imaging study. *Diabetes Care*. 2013;36(1):137-44.

55. Mayor S. Time to add prevention of brain complications to heart and kidneys in diabetes? *Lancet Diabetes Endocrinol*. 2013;1(3):180-181.

3.2 White matter degeneration in aging, a longitudinal diffusion MRI analysis

Submitted

Marius de Groot
Lotte Cremers
M. Arfan Ikram
Albert Hofman
Gabriel P. Krestin
Aad van der Lugt
Wiro J. Niessen
Meike W. Vernooij

The risk of neurodegenerative diseases, including Alzheimer's disease (AD) increases with higher age. In neurodegenerative diseases and in brain aging, white matter deterioration plays an important role. Diffusion Tensor Imaging (DTI) is a magnetic resonance imaging (MRI) technique, that can detect subtle changes of white matter microstructure not visible on a structural MRI. Cross-sectional studies have shown that DTI parameters (fractional anisotropy (FA) and mean diffusivity (MD)) are altered in aging and AD. Yet, longitudinal data determining the rate of change in DTI parameters in aging are scarce and based on limited samples. We investigated, in a population of 501 non-demented community-dwelling elderly (mean age 69.9 years, range 64.1-91.1 years), changes of normal-appearing white matter DTI characteristics, over two-years of follow-up. Over this period, we found that global FA decreased by 0.0042 ($p < 10^{-6}$), while MD increased by $8.1 \times 10^{-6} mm^2/s$ ($p < 10^{-6}$) reflecting systemic loss of white matter microstructure. Voxelwise analysis showed a widespread decrease of FA in the brain, except in the sensorimotor pathway, which demonstrated increase of FA. MD values increased throughout the brain white matter. These changes suggest widespread deterioration of the normal-appearing white matter in aging, with relative sparing of sensorimotor fibers in regions of crossing fibers. Additionally, we found that this white matter degeneration was more pronounced in higher age. Cardiovascular risk factors were not associated with longitudinal changes in white matter microstructure.

Introduction

It has been recognized that not only grey matter loss, but also white matter (WM) deterioration plays an important role in brain aging and cognitive decline,[1,2] and often a vascular etiological pathway is hypothesized.[3,4] Diffusion Tensor Imaging (DTI) is a non-invasive magnetic resonance imaging (MRI) technique that measures diffusion of water, and that can quantify subtle changes of white matter tissue organization not visible on structural MRI. DTI provides multiple measures of diffusion, with fractional anisotropy (FA) and mean diffusivity (MD) most commonly used. FA describes the directionality of diffusion and a lower value typically reflects reduced microstructural organization in regions where white matter fibers are aligned. MD represents the overall magnitude of water diffusion and here a higher value reflects reduced microstructural organization more generally.[5,6]

Reduced microstructural white matter organization possibly impedes communication within and between neurocognitive networks which might result in cognitive impairment.[1,2,7] In order to identify persons at a higher risk of neurodegenerative disease, it is therefore important to quantify changes in brain tissue in an early stage.[8] This however also requires characterization of baseline age-related changes.

The quantitative nature of DTI makes it very suitable for longitudinal analyses, which are likely to be more sensitive to early detection of changes of the microstructure of the white matter. However, longitudinal data are still scarce and studies are mostly performed in small sample sizes and in patients with cognitive impairment or Alzheimer's disease.[2,9,10] The sparse longitudinal findings in 'normal' aging did however corroborate evidence from cross-sectional studies, which showed that during normal aging white matter demonstrates lower FA, with less uniform observations for regions with crossing fibers, combined with higher MD,[2,5,9–12] and that those aging effects differ across brain regions.[10,13,14] It is suggested that there is earlier or more rapid loss of white matter organization in anterior regions including the corpus callosum, superior longitudinal fasciculus, uncinate fasciculus, inferior fronto-occipital fasciculus and cingulate bundle, the so called anterior-posterior gradient.[2,9,10,15] Yet, these cross-sectional results need to be corroborated in longitudinal studies.

In the current study, we investigated in the large, population-based Rotterdam Scan Study, age-related changes in DTI parameters over two years of follow-up. We investigated changes both globally and locally, using an improved version of Tract-Based Spatial Statistics (TBSS).[16,17] Additionally, we investigated whether cardiovascular risk factors influence longitudinal change in white matter microstructure.[18]

Methods

Study population

This study is based on participants from the Rotterdam Study, a prospective, population-based cohort study that investigates causes and consequences of age-related diseases.[19] The original study population consisted of 7,983 participants aged 55 years and older within the Ommoord area, a suburb of Rotterdam. In 2000, the cohort was expanded with 3,011 persons (≥55 years) who were living in the study area and had not been included before.[19] Since 2005, brain MRI is incorporated in the core protocol of the Rotterdam Study. In 2005 and 2006, a group of 1,073 participants was randomly selected from this cohort expansion to participate in the Rotterdam

Scan Study.[20] Participants were scanned three times, in 2005-2006, 2008-2009 and in 2011-2012. The latter two time points included an upgraded (and identical) DTI acquisition that was used for the current analysis, defining the 2008-2009 scan as baseline, and the 2011-2012 scan as follow-up. We excluded individuals who (at either time point) were demented or had MRI contraindications (including claustrophobia). For the 2008-2009 scan, 899 out of the original 1,073 persons could be invited, of whom 810 were eligible and 741 participated. At follow up in 2011-2012, 649 out of 741 were re-invited, 625 were eligible and 548 participated. We excluded participants with an incomplete acquisition (n=5), persons with MRI-defined cortical infarcts (n=20), and scans with artifacts hampering automated processing (n=22), resulting in 501 participants with longitudinal DTI data available for analysis.

MRI acquisition

Multi-sequence MRI was performed with identical scan parameter settings at both time points on a 1.5T scanner (GE Signa Excite) dedicated to the study and maintained without major hardware or software updates.[20] In short, imaging included a T1-weighted 3D Fast RF Spoiled Gradient Recalled Acquisition in Steady State with an inversion recovery pre-pulse (FASTSPGR-IR) sequence, a proton density (PD) weighted sequence, and a T2-weighted fluid-attenuated inversion recovery (FLAIR) sequence.[20] For DTI, we performed a single shot, diffusion-weighted spin echo echo-planar imaging sequence (repetition time=8,575 ms, echo time=82.6 ms, field-of-view=210 × 210 mm, matrix=96 × 64 (phase encoding) (zero-padded in k-space to 256 × 256) slice thickness=3.5 mm, 35 contiguous slices). Maximum b-value was 1000 s/mm^2 in 25 non-collinear directions; three volumes were acquired without diffusion weighting (b-value=0 s/mm^2).

Tissue segmentation

Baseline scans were segmented into grey matter, white matter, cerebrospinal fluid (CSF) and background tissue using an automatic segmentation method.[21] An automatic post-processing step distinguished normal-appearing white matter from white matter lesions (WML), based on the FLAIR image and the tissue segmentation.[22] Intracranial volume (ICV) (excluding the cerebellum with surrounding CSF) was estimated by summing total grey and white matter and CSF volumes. The segmentation was mapped into DTI image space using boundary based registration[23] performed on the white matter segmentation, the b=0 and T1-weighted images.

DTI processing

Diffusion data was pre-processed using a standardized processing pipeline.[24] In short, DTI data was corrected for subject motion and eddy currents by affine co-registration of the diffusion-weighted volumes to the b=0 volumes, including correction of gradient vector directions. Diffusion tensors were estimated using a non-linear Levenberg-Marquardt estimator, available in ExploreDTI.[25] FA and MD, measures of tissue microstructure, were computed from the estimated tensor images.

Image registration

Intra-subject correspondence between the two time points, and between subjects was achieved by image registration, and analyses were performed in standard space (MNI152). Improved TBSS was used with optimized high degree-of-freedom registration in lieu of the two stage registration-projection approach followed by the original TBSS method.[16,17]

Firstly, for each subject, the baseline scan was registered to the follow-up scan, and vice versa. Secondly, each scan was transformed to the intermediate halfway space by inverting half the deformation fields of both registrations.[26] This procedure was followed to avoid asymmetry bias in longitudinal processing.[27] Image registration was performed using FMRIB's Linear and Non-linear Image Registration Tools (FLIRT[28] and FNIRT[29]) available in FMRIB's Software Library (FSL).[30] Intra-subject registration parameters were optimized based on tract-density image similarity[17] and are available online. Thirdly, similar to bringing subject FA images to standard space, as is done in the original TBSS approach,[16] the subject specific intermediate time points were brought to standard space using the previously determined registration parameters.[17] Fourthly, transformations were concatenated to allow direct transformation from the acquisition spaces to standard space, where change in diffusion measures could be computed on a voxel level by subtracting baseline from follow-up images.

Finally, a study specific white matter skeleton was constructed by using the TBSS skeletonization procedure on the average FA image composed of all subject images at both time points combined in standard space, thresholding the FA skeleton at a value of 0.25.

Assessment of risk factors

The following cardiovascular risk factors were assessed based on information derived from home interviews and physical examinations.[19] Blood pressure was measured twice in sitting position using a random-zero sphygmomanometer. Use of anti-hypertensive drugs was collected. Diabetes mellitus status was determined based on a fasting serum glucose level (>= 7.0 mmol/l), or a non-fasting serum glucose level (>=11.1 mmol/l) or the use of anti-diabetic medication. Smoking was assessed by interview and coded as never, former and current. Total and high-density lipoprotein (HDL) cholesterol were determined in blood serum, while recording the use of lipid lowering medication. *Apolipoprotein E (APOE)*-ε4 allele carriership was assessed on coded genomic DNA samples.[31] *APOE* genotype was in Hardy-Weinberg equilibrium. Assessment of risk factors was predating the baseline MRI on average 3 years.

Statistical analysis

Changes in diffusion characteristics were investigated in two ways: globally and locally. For both approaches, we focused on the white matter skeleton as determined by TBSS. For the global analysis, we investigated the average change in FA and MD over the entire skeleton for each subject, excluding voxels labeled as WML in the baseline scan. We assessed whether there was a global change in diffusion measures with multiple linear regression models using three models. In model 1, we adjusted for, age, sex, scan interval and ICV. In model 2, we additionally adjusted for measures of white matter macrostructure: white matter atrophy (by using normal-appearing white matter volume) and WML load (natural log-transformed to correct for the skewed volume distribution). In model 3, we added the different cardiovascular risk factors individually to model 1. For analyses with blood pressure and cholesterol, medication use was considered a confounder and added to the model. All global analyses were performed using SPSS (version 20), using an alpha value of 0.05; controlling the family wise error rate by using Bonferroni correction, correcting for 34 tests (number of tested parameters per model: 4, 6, 7 (×2 diffusion measures)) with threshold for significance of 0.0015.

For the localized TBSS analyses, we performed voxelwise multiple linear regressions for the same models as for the global analysis, also restricting the analyses to the (baseline) normal-appearing white matter. If significant associations were found, we additionally performed an analysis correcting for measures of macrostructural white matter degeneration (corresponding to model 2) to rule out confounding by white matter atrophy and WML. We used threshold free cluster enhancement[32]

with default settings for skeletonized data to promote spatially clustered findings and controlled the family wise error rate by using a permutation based approach (using 5,000 permutations).[33] All analyses were performed using a modified version of the Randomise tool available in FSL that discarded WML voxels in every permutation, effectively performing a voxelwise available-case analysis.

Table 3.2.1
Population characteristics

	N=501
Age, y	69.9 (4.3)
Female	253 (50.5)
Follow up time, y	2.0 (0.5)
NAWM baseline FA	0.322 (0.016)
NAWM baseline MD, $10^{-3}mm^2/s$	0.726 (0.022)
Brain volume, ml	1125 (114)
NAWM volume, ml	394 (58)
WML volume, ml*	3.74 (2.28, 7.39)
Systolic blood pressure, mmHg	142.3 (16.5)
Diastolic blood pressure, mmHg	81.0 (9.7)
Use of blood pressure lowering medication	168 (33.7)
Diabetes mellitus	34 (6.9)
Smoking	
never	162 (32.7)
former	270 (54.4)
current	64 (12.9)
Total serum cholesterol, mmol/l	5.73 (0.94)
Serum HDL cholesterol, mmol/l	1.45 (0.40)
Use of lipid lowering medication	107 (21.4)
APOE ε4 carriership	118 (23.1)

Data is presented as mean (SD) for continuous variables and number (%) for categorical variables. † White matter lesion volume presented as median (interquartile range). The following variables had missing data: cholesterol (n=3), blood pressure (n=2), APOE-ε4 carriership (n=15), diabetes (n=5), smoking (n=5). NAWM indicates normal-appearing white matter; FA fractional anisotropy; MD mean diffusivity, WML white matter lesion.

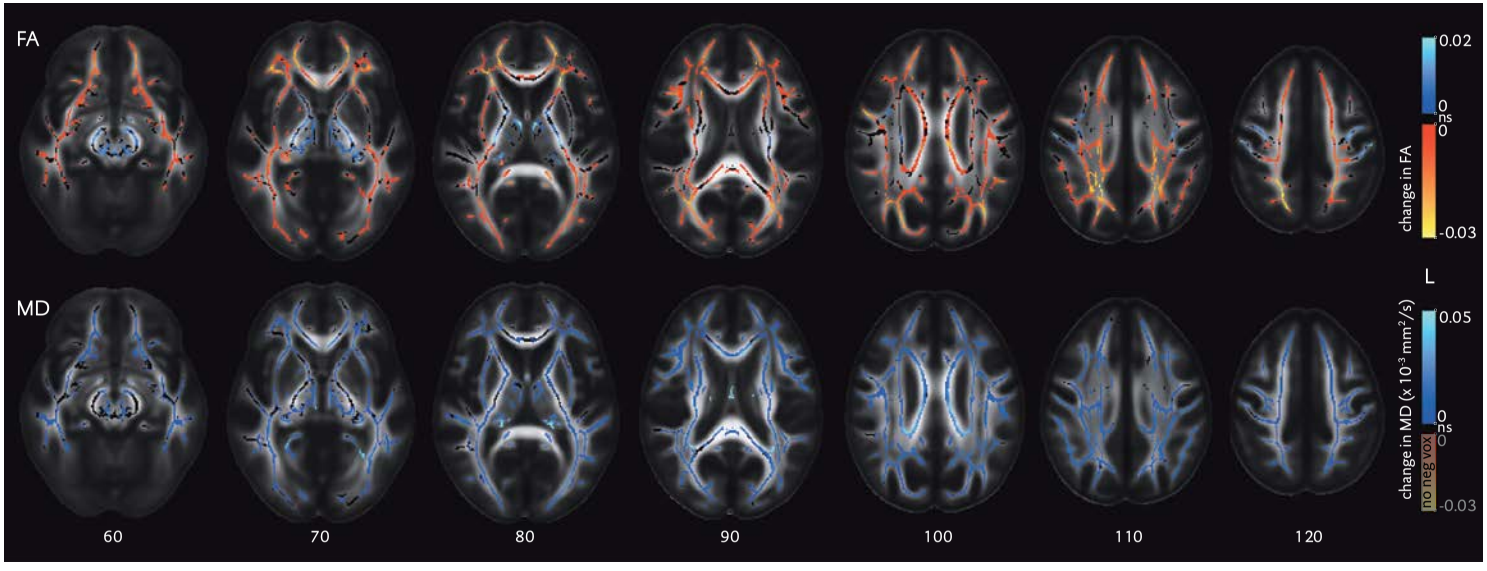

Figure 3.2.1. *Change in diffusion characteristics over two-years of follow-up. The top row shows regions of significant change in fractional anisotropy (FA) over time, color coded blue to indicate increase, and red and yellow to indicate decrease in FA. The bottom row shows regions of significant change in mean diffusivity (MD), color-coded blue for increase (no voxels showed a significant decrease in MD). The family wise error rate was controlled using a permutation approach. Results are overlaid on a population specific average-FA image in MNI coordinates, showing non-significant (ns) skeleton voxels in black.*

Results

Table 3.2.1 shows the population characteristics of the 501 participants. The mean age at the baseline MRI scan was 69.9 years (ranging from 64.1 to 91.1 years), and 253 (50.5%) participants were female. The global analyses, corrected for age, sex, scan interval and ICV, showed an average decrease of FA in normal-appearing white matter of 0.0042 ($p<10^{-6}$) and an average increase of MD of $8.1\times10^{-6}mm^2/s$ ($p<10^{-6}$) over the follow-up interval (model 1). The same changes were observed when additionally controlling for white matter atrophy and WML load (model 2). As can be seen in Table 3.2.2, these two additional confounding variables were also associated with changes in MD (a higher WML load resulted in increase in MD) but not with FA.

Voxelwise analyses, visualized in Figure 3.2.1 for model 2, showed decrease in FA over the two-years follow-up interval in the majority of the brain white matter, except in most of the sensorimotor tracts. Change over time for models 1 and 2 was not materially different. Increase in FA was found in the motor tracts extending from the brain stem, through the internal capsule (both the anterior and posterior limbs) and the corona radiata up into the motor cortex (Figure 3.2.1). The MD increased over the follow-up period throughout the brain, with most marked increase periventricularly and around the fornix. Constraining the voxelwise analysis to the normal-appearing white matter meant that the number of degrees-of-freedom of the analysis varied from voxel to voxel, but variation was smooth and the minimum number of subjects included per voxel was 293.

Table 3.2.2
Demographic characteristics and global change in white matter microstructure, corrected for scan interval and computed alongside the population mean change of -0.0042 in FA and $8.1\times10^{-6}mm^2/s$ in MD

	Change in FA $\times 10^{-3}$	p-value	Change in MD $\times 10^{-6}mm^2/s$	p-value
Age	*-0.12*	0.09	*0.20*	0.01
Sex	*0.37*	0.57	*-0.07*	0.93
Brain volume	*-0.18*	0.69	*0.91*	0.08
NAWM volume	*0.27*	0.51	*-1.43*	2×10^{-3}
ln WML volume	*-0.29*	0.31	***1.21***	2×10^{-4}

Significant result (at Bonferroni corrected threshold of 0.0015) is shown in bold instead of italic.

Table 3.2.3
Cardiovascular risk factors and global change in white matter microstructure computed with respect to the population mean change of -0.0042 in FA and 8.1×10^{-6}mm^2/s in MD

	change in FA × 10^{-3}	p-value	change in MD × 10^{-6}mm^2/s	p-value
Systolic blood pressure	*-0.46*	0.09	*0.33*	0.29
Diastolic blood pressure	*-0.01*	0.98	*0.10*	0.76
Diabetes mellitus	*0.08*	0.77	*0.46*	0.13
Smoking (never – current)	*-0.15*	0.86	*0.22*	0.83
Total serum cholesterol	*-0.42*	0.15	*-0.09*	0.78
Serum HDL cholesterol	*0.31*	0.28	*-0.23*	0.49
APOE ε4 carriership	*1.12*	0.07	*-1.51*	0.04

Values represent change in diffusion measure, per SD of change for continuous variables, or absolute for categorical variables. All associations shown are not significant (at Bonferroni corrected threshold of 0.0015).

Figures 3.2.2 and 3.2.3 show how changes in FA (Figure 3.2.2) and MD (Figure 3.2.3) depended on various parameters included in models 1 and 2. For the (minimal) model 1, we observed an association between age and FA (decrease) and MD (increase). This association was reduced both in strength and in extent, when additionally adding measures of macrostructural white matter changes (atrophy and WML load) in the model. The figures also show associations between white matter atrophy and WML load, and change in FA and MD in model 2. No difference in change in diffusion characteristics was observed for men and women.

Investigating cardiovascular risk factors in relation to longitudinal DTI changes, we only found associations for *APOE* ε4 carriership. Specifically, ε4 carriers showed localized decrease in FA to a lesser degree when compared to non-carriers, but no changes globally. These local differences were more prominent in the right than in the left hemisphere and primarily in the centrum semiovale and in the white matter adjacent to the trigone of the lateral ventricle. In contrast, we observed lower MD only in a small peritrigonal cluster in carriers compared to non-carriers. These observed associations became statistically non-significant when additionally correcting for macrostructural measures of white matter degeneration. Similarly, we observed that global increase in MD to a lesser degree associated with *APOE* ε4 carriership (Table 3.2.3), but this association became non-significant when correcting for multiple comparisons. Other cardiovascular risk factors were associated with neither global nor local changes in tissue microstructure. Results on global DTI characteristics are represented in Table 3.2.3.

Discussion

In this large, population based longitudinal sample of elderly persons, we found reduced microstructural tissue organization over a two-year follow-up interval. Loss of microstructure was globally reflected in decreases in FA and increases in MD, independent of severity of white matter atrophy and WML load.

Strengths of this study are the large sample size of elderly participants, the population based setting, and the longitudinal design. Additionally, all longitudinal imaging data were acquired using the same protocol and on the same MRI scanner which did not receive a major hardware or software update in the study period. Also, we restricted our analyses to the normal-appearing white matter, ignoring identifiable pathologies in the form of WML. Finally, we corrected for macroscopic imaging measures of white matter disease to identify deterioration of white matter microstructure not explained by WML load and white matter atrophy.

Limitations of our study are the relatively short follow-up interval, which may limit sensitivity to detect differences over time. Another limitation of our study is that the study protocol was defined in 2005-2006 and therefore the spatial resolution for the diffusion acquisition was relatively poor for current day standards.[17] We did nevertheless identify widespread deterioration of white matter microstructure within the studied time interval.

On a voxelwise level, we found regional differences in white matter degeneration, with a decreased FA in most of the brain, but on the contrary an increased FA in most of the sensorimotor pathway, running from the brainstem up to the motor cortex. In contrast, MD was found to increase throughout the white matter skeleton, without any significant decreases. The seemingly paradoxical increase of FA in the sensorimotor pathway may relate to partial voluming of multiple, crossing fiber tracts within certain voxels. Selective degeneration of one crossing fiber bundle and at the same time relative sparing of another bundle may lead to relative increase in FA (directionality of diffusion) in the voxel, with concomitant increase in MD (mean diffusivity). This effect was previously observed in a study on Wallerian degeneration,[34] and described in detail in a cross-sectional study on Alzheimer's disease.[35] This effect would attenuate changes in global FA measurements, making MD more sensitive to detect global changes than FA,[36] which is in agreement with our observations. Because in selective degeneration, FA change can occur in both directions, MD may also be more sensitive to detect changes locally. This again is in line with our observations.

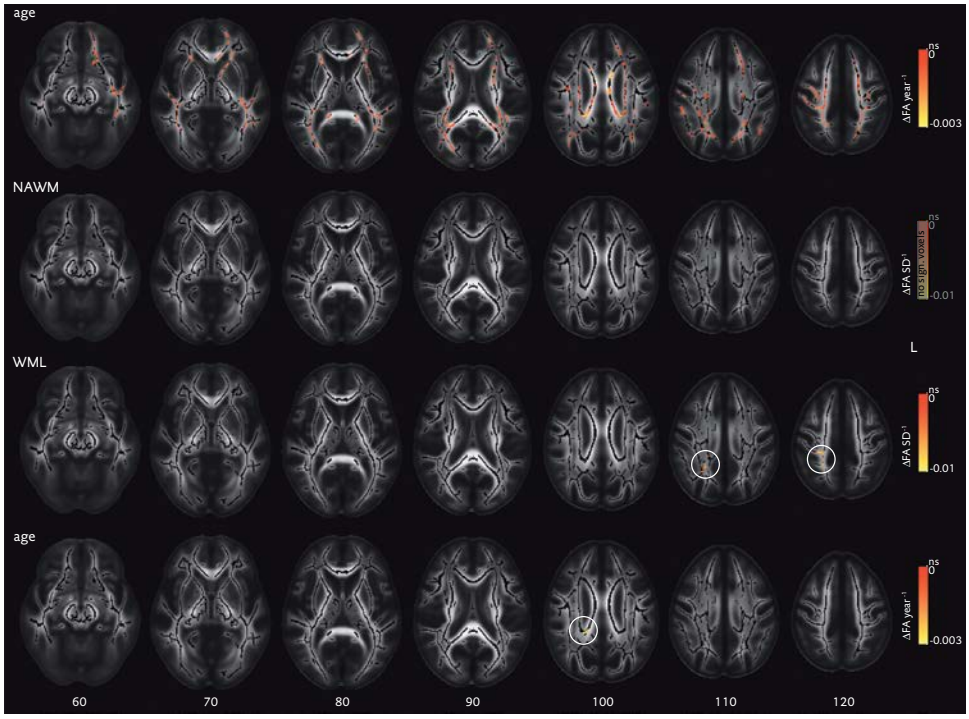

Figure 3.2.2. *Age and macrostructural white matter changes at baseline and change in fractional anisotropy (FA) over two-years of follow-up. The top row shows in yellow-to-red regions of decrease in FA that relate to higher age at baseline (adjusted for sex, scan interval and intracranial volume (ICV)). The second and third row show FA changes that are associated with respectively a decrease in normal-appearing white matter (NAWM) volume and an increase in white matter lesion (WML) volume (both adjusted for age, sex, scan interval, ICV). The final row shows regions of decrease in FA related to higher age, when additionally adjusted for NAWM volume and WML volume. Inverse directions of association showed no significant voxels (not shown). The family wise error rate was controlled using a permutation approach. Results are overlaid on a population specific average-FA image in MNI coordinates, showing non-significant (ns) NAWM skeleton voxels in black.*

We found the most distinct increase in MD over time in the fornix. This may reflect loss of microstructural organization in this limbic fiber, but we should note that this tract is rather small and close to CSF, so we cannot rule out partial volume effects with CSF in this tract.[37]

We found that white matter deterioration was locally more pronounced with higher age, indicating that older persons show more white matter degeneration over the same follow-up time than younger persons. This could partly be explained by

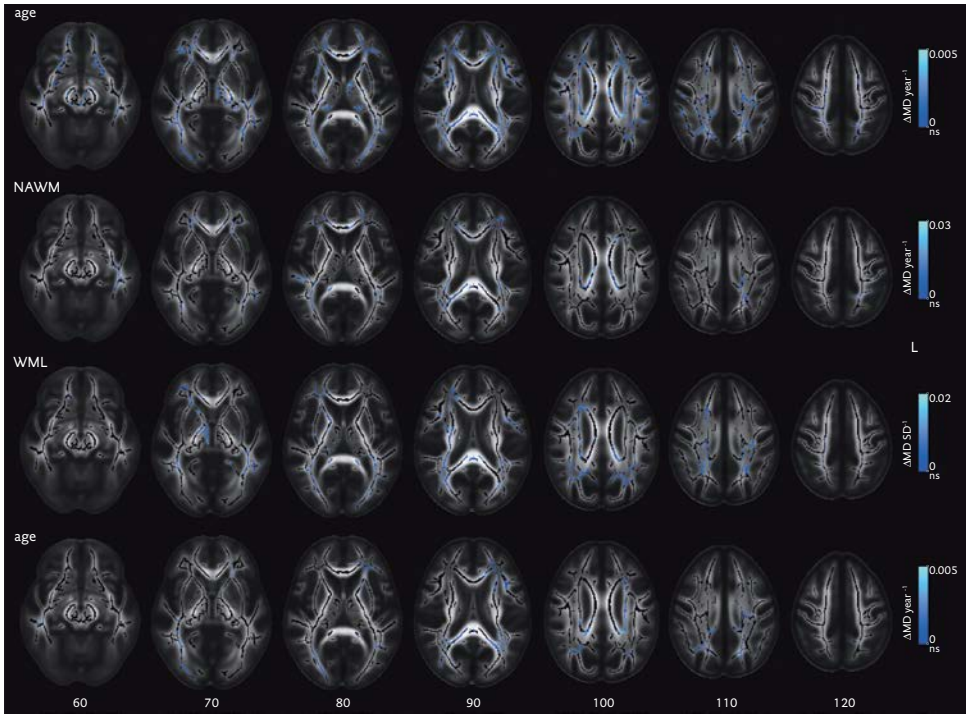

Figure 3.2.3. *Age and macrostructural white matter changes at baseline and change in mean diffusivity (MD) over two-years of follow-up. The top row shows in blue regions of increase in MD that relate to higher age at baseline (adjusted for sex, scan interval and intracranial volume (ICV)). The second and third row show MD changes that are associated with respectively a decrease in normal-appearing white matter (NAWM) volume and an increase in white matter lesion (WML) volume (both adjusted for age, sex, scan interval, ICV). The final row shows regions of decrease in MD related to higher age, when additionally adjusted for NAWM volume and WML volume. Inverse directions of association showed no significant voxels (not shown). The family wise error rate was controlled using a permutation approach. Results are overlaid on a population specific average-FA image in MNI coordinates, showing non-significant (ns) NAWM skeleton voxels in black.*

macroscopic measures of white matter degeneration, i.e. white matter atrophy and WML load, which also increase with age. In a cross-sectional analysis of an earlier time point for the same population we found a similar effect with age itself, i.e. most of the associations with age were driven by macroscopic measures of white matter degeneration.[1] Both results indicate that white matter degeneration with aging is not intrinsically due to aging alone or driven by macroscopic measures of white matter degeneration. In that respect it is also interesting that we did not identify associations between known (cardiovascular) determinants of white matter atrophy and

WML load and changes in diffusion characteristics over time, neither globally nor locally. Perhaps this suggests additional (unmeasured, e.g. genetic) determinants for change in diffusion characteristics.

We did not observe a significant association between global DTI changes and *APOE* ε4 carriership. Locally, we observed in *APOE* ε4 carriers counter-intuitive reduced decreases in FA comparison to non-carriers, in regions with a high prevalence of WML. These became non-significant when additionally correcting for WML and white matter atrophy. While non-significant, these observations are in contrast to cross-sectional studies with *APOE* genotype which have generally shown widespread deterioration of white matter microstructure associated with the ε4 allele.[38,39] When investigating other cardiovascular risk factors, we observed no associations with either global or local degeneration, which is in line with another longitudinal study [2] but in disagreement to cross-sectional observations.[3,40,41] These discrepancies, both for *APOE* and cardiovascular factors, might be due to the relatively short follow-up time, lacking power in the (clustered) voxelwise and global statistics. Another possibility is that changes induced by cardiovascular risk factors may be more prominent in the periphery of WM tracts, whereas the TBSS method we used focused on tract centers. Most importantly however, our longitudinal design only probes differential effects, and not the difference accumulated over the total exposure time. For accumulated exposure, this leads to reduced statistical power compared to a cross sectional design.

Cross-sectional studies of normal aging of white matter have shown lower FA and higher MD with higher age,[5,11,13] which is in line with our results. The anterior-posterior gradient in white matter degeneration, often described in cross-sectional studies, hypothesizes regional differences in degeneration with more rapid white matter deterioration in the later myelinating anterior regions compared to posterior regions.[42–44] In a previous longitudinal analysis, this gradient has not been identified,[2] and neither did our results show a clear gradient (age panels in Figures 3.2.2 and 3.2.3). In a cross-sectional study design, a causal effect of the observed association, and whether differences observed actually reflect change over time, can only be assumed. In contrast, longitudinal aging studies directly measure change over time, and are therefore less influenced by confounding effects of e.g. diet, education and lifestyle on brain microstructure measures correlated with age. Longitudinal studies are therefore closer to establishing causality than cross sectional studies. On the other hand, longitudinal imaging studies require consistency of the image acquisition pipeline, which is not trivial as most scanners in clinical settings receive regular updates. Combined with the additional time inherently required to collect longitudinal data, this might explain why so few longitudinal (DTI) studies have been performed.

In conclusion, in this large longitudinal analysis of brain white matter microstructure with normal aging, we found altered diffusion characteristics widespread in white matter consistent with loss of tissue microstructure. We found changes to be more prominent in older persons, which was partly explained by concomitant macroscopic white matter pathology. Cardiovascular risk factors did not relate to white matter degeneration. These insights into white matter degeneration in aging may help in understanding the pathophysiology of neurodegenerative diseases.

References

1. Vernooij MW, de Groot M, van der Lugt A, et al. White matter atrophy and lesion formation explain the loss of structural integrity of white matter in aging. *Neuroimage*. 2008;43(3):470-477.
2. Barrick TR, Charlton RA, Clark CA, Markus HS. White matter structural decline in normal ageing; a prospective longitudinal study using tract based spatial statistics. *Neuroimage*. 2010;51(2):565-77.
3. Gons RAR, van Oudheusden LJB, de Laat KF, et al. Hypertension is related to the microstructure of the corpus callosum: the RUN DMC study. *J Alzheimers Dis*. 2012;32(3):623-31.
4. Verdelho A, Madureira S, Ferro JM, et al. Differential impact of cerebral white matter changes, diabetes, hypertension and stroke on cognitive performance among non-disabled elderly. The LADIS study. *J Neurol Neurosurg Psychiatry*. 2007;78(12):1325-30.
5. Laukka EJ, Lövdén M, Kalpouzos G, et al. Associations between white matter microstructure and cognitive performance in old and very old age. *PLoS One*. 2013;8(11):e81419.
6. Sundgren PC, Dong Q, Gómez-Hassan D, Mukherji SK, Maly P, Welsh R. Diffusion tensor imaging of the brain: review of clinical applications. *Neuroradiology*. 2004;46(5):339-50.
7. Burzynska AZ, Garrett DD, Preuschhof C, et al. A scaffold for efficiency in the human brain. *J Neurosci*. 2013;33(43):17150-9.
8. Klimas A, Drzazga Z, Kluczewska E, Hartel M. Regional ADC measurements during normal brain aging in the clinical range of b values: a DWI study. *Clin Imaging*. 2013;37(4):637-44.
9. Teipel SJ, Meindl T, Wagner M, et al. Longitudinal changes in fiber tract integrity in healthy aging and mild cognitive impairment: a DTI follow-up study. *J Alzheimers Dis*. 2010;22(2):507-22.
10. Sullivan EV, Rohlfing T, Pfefferbaum A. Longitudinal study of callosal microstructure in the normal adult aging brain using quantitative DTI fiber tracking. *Dev Neuropsychol*. 2010;35(3):233-56.
11. Abe O, Aoki S, Hayashi N, et al. Normal aging in the central nervous system: quantitative MR diffusion-tensor analysis. *Neurobiol Aging*. 2002;23(3):433-441.
12. Madden DJ, Bennett IJ, Burzynska A, Potter GG, Chen N-K, Song AW. Diffusion tensor imaging of cerebral white matter integrity in cognitive aging. *Biochim Biophys Acta*. 2012;1822(3):386-400.
13. Burzynska AZ, Preuschhof C, Bäckman L, et al. Age-related differences in white matter microstructure: region-specific patterns of diffusivity. *Neuroimage*. 2010;49(3):2104-12.
14. Nusbaum AO, Tang CY, Buchsbaum MS, Wei TC, Atlas SW. Regional and global changes in cerebral diffusion with normal aging. *AJNR Am J Neuroradiol*. 2001;22(1):136-42.
15. Schulte T, Maddah M, Müller-Oehring EM, Rohlfing T, Pfefferbaum A, Sullivan EV. Fiber tract-driven topographical mapping (FTTM) reveals microstructural relevance for interhemispheric visuomotor function in the aging brain. *Neuroimage*. 2013;77:195-206.

16. Smith SM, Jenkinson M, Johansen-Berg H, et al. Tract-based spatial statistics: voxelwise analysis of multi-subject diffusion data. *Neuroimage*. 2006;31(4):1487-1505.

17. De Groot M, Vernooij MW, Klein S, et al. Improving alignment in Tract-based spatial statistics: evaluation and optimization of image registration. *Neuroimage*. 2013;76:400-11.

18. Bettcher BM, Walsh CM, Watson C, et al. Body mass and white matter integrity: the influence of vascular and inflammatory markers. *PLoS One*. 2013;8(10):e77741.

19. Hofman A, Darwish Murad S, van Duijn CM, et al. The Rotterdam Study: 2014 objectives and design update. *Eur J Epidemiol*. 2013;28(11):889-926.

20. Ikram MA, van der Lugt A, Niessen WJ, et al. The Rotterdam Scan Study: design and update up to 2012. *Eur J Epidemiol*. 2011;26(10):811-24.

21. Vrooman HA, Cocosco CA, van der Lijn F, et al. Multi-spectral brain tissue segmentation using automatically trained k-Nearest-Neighbor classification. *Neuroimage*. 2007;37(1):71-81.

22. De Boer R, Vrooman HA, van der Lijn F, et al. White matter lesion extension to automatic brain tissue segmentation on MRI. *Neuroimage*. 2009;45(4):1151-1161.

23. Greve DN, Fischl B. Accurate and robust brain image alignment using boundary-based registration. *Neuroimage*. 2009;48(1):63-72.

24. Koppelmans V, de Groot M, de Ruiter MB, et al. Global and focal white matter integrity in breast cancer survivors 20 years after adjuvant chemotherapy. *Hum Brain Mapp*. 2014;35(3):889-99.

25. Leemans A, Jeurissen B, Sijbers J, Jones DK. ExploreDTI: a graphical toolbox for processing, analyzing, and visualizing diffusion MR data. In: *Proceedings 17th Scientific Meeting International Society for Magnetic Resonance in Medicine*.Vol 17.; 2009:3537.

26. De Groot M, Verhaaren BFJ, de Boer R, et al. Changes in normal-appearing white matter precede development of white matter lesions. *Stroke*. 2013;44(4):1037-42.

27. Reuter M, Fischl B. Avoiding asymmetry-induced bias in longitudinal image processing. *Neuroimage*. 2011;57(1):19-21.

28. Jenkinson M, Smith SM. A global optimisation method for robust affine registration of brain images. *Med Image Anal*. 2001;5(2):143-56.

29. Andersson JLR, Jenkinson M, Smith SM. Non-linear registration aka Spatial normalisation. *FMRIB Tech Rep TR07JA2*. 2007.

30. Jenkinson M, Beckmann CF, Behrens TEJ, Woolrich MW, Smith SM. FSL. *Neuroimage*. 2012;62(2):782-90.

31. Wenham PR, Price WH, Blandell G. Apolipoprotein E genotyping by one-stage PCR. *Lancet*. 1991;337(8750):1158-9.

32. Smith SM, Nichols TE. Threshold-free cluster enhancement: addressing problems of smoothing, threshold dependence and localisation in cluster inference. *Neuroimage*. 2009;44(1):83-98.

33. Nichols TE, Holmes AP. Nonparametric permutation tests for functional neuroimaging: a primer with examples. *Hum Brain Mapp*. 2002;15(1):1-25.

34. Pierpaoli C, Barnett A, Pajevic S, et al. Water diffusion changes in Wallerian degeneration and their dependence on white matter architecture. *Neuroimage*. 2001;13(6 Pt 1):1174-1185.

35. Douaud G, Jbabdi S, Behrens TEJ, et al. DTI measures in crossing-fibre areas: increased diffusion anisotropy reveals early white matter alteration in MCI and mild Alzheimer's disease. *Neuroimage*. 2011;55(3):880-90.

36. Nir TM, Jahanshad N, Villalon-Reina JE, et al. Effectiveness of regional DTI measures in distinguishing Alzheimer's disease, MCI, and normal aging. *NeuroImage Clin*. 2013;3:180-95.

37. Metzler-Baddeley C, O'Sullivan MJ, Bells S, Pasternak O, Jones DK. How and how not to correct for CSF-contamination in diffusion MRI. *Neuroimage*. 2012.

38. Persson J, Lind J, Larsson A, et al. Altered brain white matter integrity in healthy carriers of the APOE epsilon4 allele: a risk for AD? *Neurology*. 2006;66(7):1029-33.

39. Westlye LT, Reinvang I, Rootwelt H, Espeseth T. Effects of APOE on brain white matter microstructure in healthy adults. *Neurology*. 2012;79(19):1961-9.

40. Kennedy KM, Raz N. Pattern of normal age-related regional differences in white matter microstructure is modified by vascular risk. *Brain Res*. 2009;1297:41-56.

41. Salat DH, Williams VJ, Leritz EC, et al. Inter-individual variation in blood pressure is associated with regional white matter integrity in generally healthy older adults. *Neuroimage*. 2012;59(1):181-92.

42. Pfefferbaum A, Adalsteinsson E, Sullivan EV. Frontal circuitry degradation marks healthy adult aging: Evidence from diffusion tensor imaging. *Neuroimage*. 2005;26(3):891-9.

43. Kantarci K, Senjem ML, Avula R, et al. Diffusion tensor imaging and cognitive function in older adults with no dementia. *Neurology*. 2011;77(1):26-34.

44. Davis SW, Dennis NA, Daselaar SM, Fleck MS, Cabeza R. Que PASA? The posterior-anterior shift in aging. *Cereb Cortex*. 2008;18(5):1201-9.

Chapter 4
Diffusion imaging in small vessel disease

4.1

White matter atrophy and lesion formation explain the loss of structural integrity of white matter in aging

NeuroImage 2008

Meike W. Vernooij*
Marius de Groot*
Aad van der Lugt
M. Arfan Ikram
Gabriel P. Krestin
Albert Hofman
Wiro J. Niessen
Monique M.B. Breteler

* equal contribution

The importance of macrostructural white matter changes, including white matter lesions and atrophy, in intact brain functioning is increasingly being recognized. Diffusion tensor imaging (DTI) enables measurement of the microstructural integrity of white matter. Loss of white matter integrity in aging has been reported, but whether this is inherent to the aging process itself or results from specific white matter pathology is unknown. In 832 persons aged 60 years and older from the population-based Rotterdam Study, we measured fractional anisotropy (FA) and directional diffusivities in normal-appearing white matter using DTI. All subjects' DTI measures were projected onto a common white matter skeleton to enable robust voxelwise comparison. With increasing age, multiple regions showed significant decreases in FA or increases in axial or radial diffusivity in normal-appearing white matter. However, nearly all of these regional changes were explained by either white matter atrophy or by white matter lesions; each of which related to changes in distinct brain regions. These results indicate that loss of white matter integrity in aging is primarily explained by atrophy and lesion formation and not by the aging process itself. Furthermore, white matter atrophy and white matter lesion formation relate to loss of integrity in distinct brain regions, indicating the two processes are pathophysiologically different.

Introduction

Intact white matter connections in the brain are important for the processing and integration of information generated by neural networks. Loss of integrity of these white matter pathways is thought to cause loss of "connectivity" and subsequent age-related cognitive decline.[1] There are two distinct macroscopic processes affecting the white matter that are commonly seen in aging and which are readily recognized in both radiologic and pathologic examinations. Firstly, atrophy of white matter dominates brain tissue loss in aging, rather than does loss of grey matter neurons.[2] Secondly, over 90% of elderly persons demonstrate on brain magnetic resonance imaging (MRI) so-called 'white matter lesions',[3] which pathologically represent signs of ischemic injury.[4] Although white matter atrophy and white matter lesion formation often coincide and have shared determinants,[5] it is still not understood whether these are part of the same pathophysiologic spectrum or whether these are independent processes. Furthermore, it is unknown whether and how these two macroscopic processes are related to loss of microstructural integrity of normal-appearing white matter. Diffusion tensor imaging (DTI)[6] enables non-invasive quantification of the microstructural integrity of white matter using

MRI.[7] DTI measures the amount and directional dependence of microscopic diffusion of water molecules in the brain. In white matter, diffusion is hindered by the high degree of structural organization, resulting in anisotropic movement of water molecules predominantly parallel to the orientation of the fiber tracts. A lower fractional anisotropy (FA) as measured by DTI signifies less anisotropic diffusion and thus lower microstructural integrity.[6] Furthermore, from animal studies, it has been suggested that analysis of directional diffusivities – axial diffusivity (AxD) and radial diffusivity (RD)– may provide additional information on the underlying mechanisms of loss of white matter integrity. Myelin breakdown has been associated with increased diffusivity perpendicular to the white matter tract (RD), whilst axonal damage is reflected in diffusivity changes parallel (AxD) to the primary fiber orientation.[8–10]

So far, FA in white matter has been shown to decrease with age,[11] but it is unknown to what extent this represents concurrent macroscopic changes in white matter, or whether aging itself causes white matter microstructural changes. Furthermore, analysis of regional patterns in FA changes has so far been limited to manually placed regions-of-interest[11] or to voxelwise measurement methods, both of which are prone to methodological constraints hindering interpretation and analysis of FA data.[12,13] Tract-based spatial statistics (TBSS) is a new technique for aligning FA images from multiple subjects and constructing a common skeleton of the white matter tracts, enabling robust voxelwise analysis of the microstructural integrity of white matter across subjects.[13] Using TBSS, we investigated in 832 persons aged 60 years and older from the general population whether white matter atrophy and white matter lesions relate to integrity of normal-appearing white matter independent from aging, and if so, in which brain regions these associations are strongest.

Materials and methods

Participants

This study is embedded within the Rotterdam Study, a large population-based cohort study in The Netherlands that started in 1990–1993 and is aimed at investigating determinants of various chronic diseases among elderly participants.[14] The original study population consisted of 7,983 participants aged 55 years and older within the Ommoord area, a suburb of Rotterdam. In 2000, the cohort was expanded with 3011 persons (≥55 years) who were living in the study area and had not been included before.[14] From August 2005 to May 2006, we randomly selected 1,073 members of this cohort expansion for the current MRI study, the Rotterdam Scan Study. We excluded individuals who were demented or had MRI contraindications (including claustrophobia). The institutional review board approved the study. A total of 975

persons were eligible, of whom 907 participated and gave written informed consent (response 93%). Due to physical inabilities (e.g. back pain), imaging could not be performed or completed in 12 individuals. A total of 895 MRI examinations were performed. Image quality was substandard due to motion artifacts or DTI artifacts in 63 scans, leaving a total of 832 scans in this analysis.

Image acquisition

We performed a multi-sequence MRI protocol on a 1.5 tesla MRI scanner (General Electric Healthcare, Milwaukee, WI, USA). For DTI, we performed a single shot, diffusion-weighted spin echo echo-planar imaging sequence (repetition time (TR)=8,000 ms, echo time (TE)= 68.7 ms, field-of-view (FOV)= 21 cm^2, matrix = 96 × 64 (interpolated to 256 × 256) slice thickness=3.5 mm, 36 contiguous slices, applying parallel imaging (array spatial sensitivity encoding technique) with acceleration factor = 2). Maximum b-value was 1000 s/mm^2 in 25 non-collinear directions (number of excitations (NEX)= 1), and one volume was acquired without diffusion weighting (b-value = 0 s/mm^2). Acquisition time was 3:44 min. We further performed three high-resolution axial MRI sequences, i.e. a T1-weighted 3D Fast RF Spoiled Gradient Recalled Acquisition in Steady State with an inversion re-

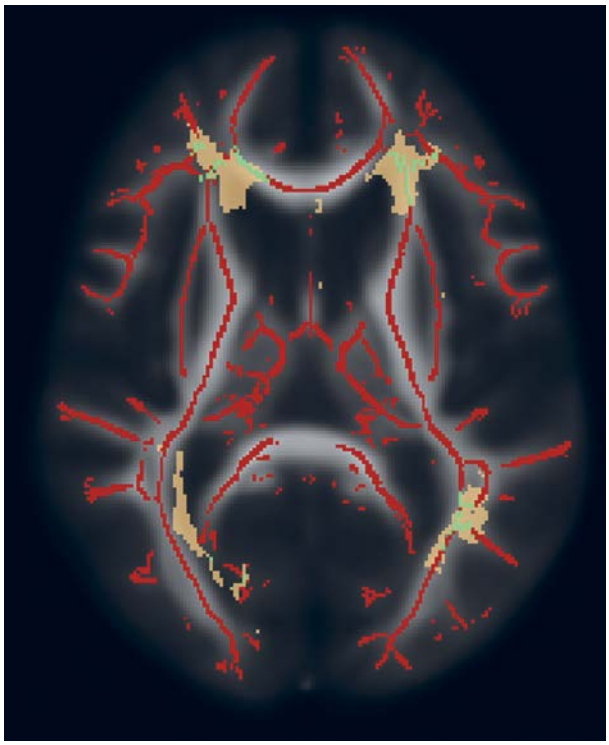

Figure 4.1.1. *Identification of voxels on the white matter skeleton originating in white matter lesions. Axial mean fractional anisotropy image with overprojection of the white matter skeleton (in red). Voxels that were segmented as white matter lesions in a single individual on structural MR images are depicted in brown. In green, the voxels on the white matter skeleton that originate in a white matter lesion are shown. These green voxels were then removed from the individual's skeleton in order to obtain a skeleton of the normal-appearing white matter.*

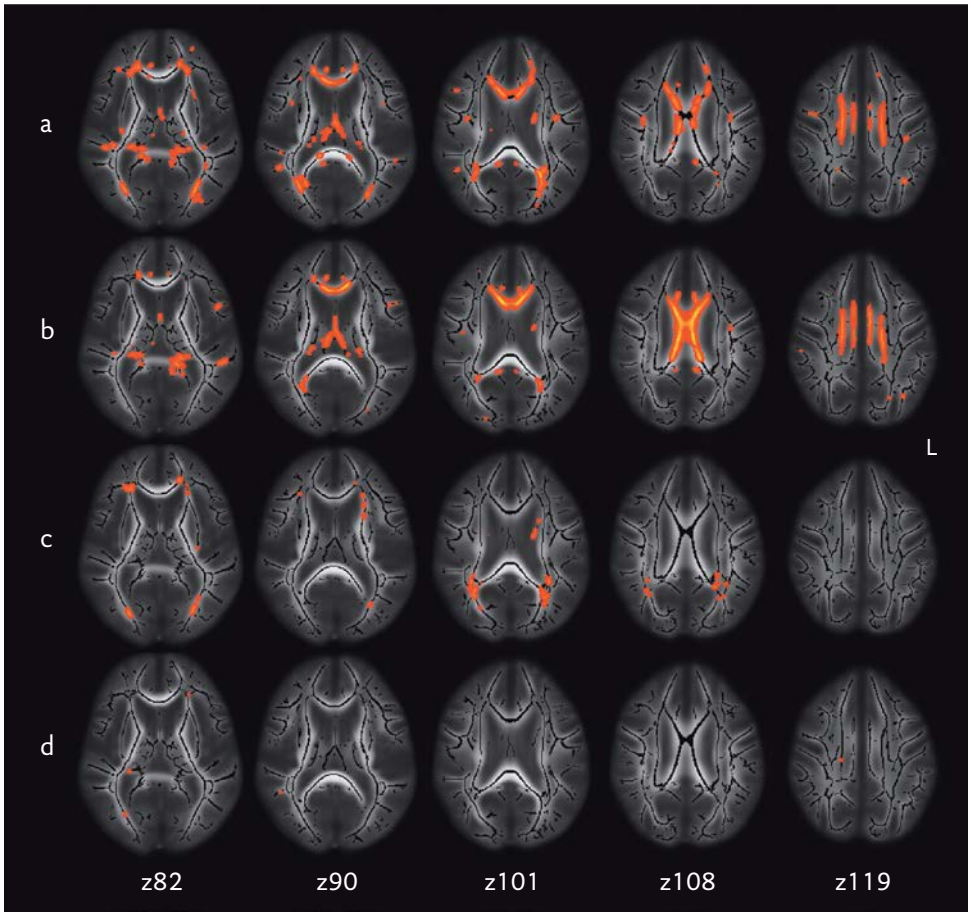

Figure 4.1.2. *Effects of age, global white matter atrophy and white matter lesions on fractional anisotropy values of normal-appearing white matter. Images are shown in the Montreal Neurological Institute (MNI) stereotactic space, with MNI coordinates for axial levels (z) depicted for each column. The white matter skeleton (black) is projected onto the axial MR images. Yellow-to-red colors represent normal-appearing white matter regions with reduced fractional anisotropy (FA) in relation to (a) increasing age, adjusted for sex only, (b) global white matter atrophy, adjusted for age, sex and white matter lesions, (c) white matter lesions, adjusted for age, sex and white matter atrophy and (d) increasing age, adjusted for sex, white matter atrophy and white matter lesions. With increasing age, multiple regions show significant decreases in FA (a). However, after adjustment for white matter atrophy and white matter lesions, only few regions remain (d). Global white matter atrophy (b) relates to decreases in FA in the hippocampal region (z82), fornix (z90), corpus callosum (z90 to z108) and along the cingulate bundle (z119). In contrast, white matter lesion burden (c) is associated with reduced periventricular FA (z82 to z108).*

covery pre-pulse (FASTSPGR-IR) sequence (TR = 13.8 ms, TE = 2.8 ms, inversion time (TI) = 400 ms, FOV = 25 m^2, matrix = 416 × 256 (interpolated to 512 × 512), flip angle=20°, NEX=1, bandwidth (BW)= 12.50 kHz, 96 slices with slice thickness 1.6 mm zero-padded in the frequency domain to 0.8 mm), a proton density (PD) weighted sequence (TR=12,300 ms, TE=17.3 ms, FOV=25 cm^2, matrix=416 × 256, NEX=1, BW=17.86 kHz, 90 slices with slice thickness 1.6 mm), and a fluid-attenuated inversion recovery (FLAIR) sequence (TR = 8,000 ms, TE=120 ms, TI=2,000 ms, FOV=25 cm^2, matrix=320 × 224, NEX=1, BW=31.25 kHz, 64 slices with slice thickness 2.5 mm). All slices were contiguous.

Normal-appearing white matter and white matter lesion segmentation

For the assessment of volumes of normal-appearing white matter and white matter lesions, the structural MRI scans (T1-weighted, PD-weighted, FLAIR) were transferred offline to a Linux workstation. Preprocessing steps and the classification algorithm have been described elsewhere.[15] In summary, preprocessing included co-registration, non-uniformity correction and variance scaling. We used a k-nearest neighbour classifier based on multi-spectral MRI intensities to label voxels into cerebrospinal fluid, grey matter, normal-appearing white matter and white matter lesions.[16] The feature space for the automated classification was created from manually segmented datasets, as described elsewhere.[5,15] In a postprocessing step, normal-appearing white matter was dilated with one voxel to assess overlap between voxels classified as white matter and those labelled as white matter lesion in order to remove voxels that were incorrectly classified as white matter lesion (e.g. in cortical grey matter). All segmentation results were visually inspected and, if needed, manually corrected. To remove non-cerebral tissue, e.g. eyes, skull, and cerebellum, we applied non-rigid registration[17] to register to each brain a template scan in which these tissues were manually masked. Global normal-appearing white matter and white matter lesion volumes were calculated by summing all voxels of the corresponding tissue class across the whole brain, to yield volumes in ml. To normalize for head size, these tissue volumes were expressed as percentage of total intracranial volume (which is the summation of all tissue classes, i.e. cerebrospinal fluid, grey matter, normal-appearing white matter and white matter lesions). As normal-appearing white matter volume was highly correlated with total white matter volume (i.e. the sum of normal-appearing white matter and white matter lesions) (Pearson's r = 0.991), we used relative normal-appearing white matter volume as a measure of white matter atrophy.

Global normal-appearing white matter volume was further subdivided into lobar volumes (frontal, occipital, parietal, temporal lobes and deep region) using a previously described protocol,[18] in which a template brain with labels for the various

lobes was non-rigidly registered to all scans. Lobar white matter atrophy was defined as normal-appearing white matter volume in the specific region relative to the total lobe volume (the summation of all tissue classes in the specific lobe).

Processing of raw DTI data

Processing of DTI data was performed with FSL[19] (http://www.fmrib.ox.ac.uk/fsl). Eddy current and head-motion correction were performed by means of an affine registration to the reference (b0) volume. The corrected data was skull-stripped by applying FSL's Brain Extraction Tool (BET) on both the b0 and the diffusion-weighted images.[20] Next, a tensor model was fitted to the diffusion data using FMRIB's Diffusion Toolbox (FDT) [19] to yield FA and both axial (λ_1) and radial [$(\lambda_2+\lambda_3)/2$] diffusivities.

Tract-based spatial statistics processing

Voxelwise statistical analysis of the DTI data was carried out using Tract-Based Spatial Statistics (TBSS 1.1),[13] part of FSL.[19] As the mean age of our study population differed greatly from the FMRIB cohort from which the TBSS template brain was derived,[13] we used the anatomically most representative subject from our dataset as study specific template brain. For computational reasons, a two-stage hierarchical search strategy was used to find this target. All 832 FA images were randomly split into 26 subgroups of 32 subjects each. Cross-wise nonlinear registration using the Image Registration Toolkit (IRTK)[17] was performed on the Erasmus Computing Grid (Rotterdam, The Netherlands). The 26 candidate targets from each subset identified by the lowest summed transformation cost were subsequently cross-wise registered to identify the subject closest to the group mean anatomy. In accordance with the standard TBSS pipeline, the remaining 831 subjects were then transformed to this study specific template subject in a stereotactic coordinate system (MNI space) using the ICBM152 template.[21] Subsequently, all FA images were averaged to produce a group mean FA image. Next, the mean FA image was thinned to create a mean FA skeleton, which represents the centres of all white matter tracts common to the group. This skeleton was thresholded at an FA value of 0.20,[13] to include the major white matter pathways but exclude pathways with large inter-subject variability. Each subject's aligned FA data was then projected onto this skeleton by searching perpendicular to the skeleton to find local maxima in FA. This step locally corrects for residual misalignment and lines up the centres of individual tracts. Next, values of AxD and RD were mapped onto the skeleton by using the projection vectors from each individual's FA-to-skeleton transformation.[13] Voxelwise analysis of FA and directional diffusivity data across the group of subjects was performed only on the data projected onto the skeleton template.

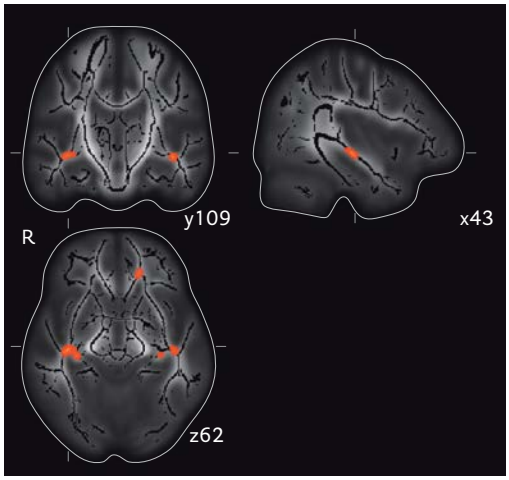

Figure 4.1.3. *Aging and reduced fractional anisotropy in inferior longitudinal fasciculus. Coronal, sagittal and axial projections of mean fractional anisotropy (FA) MRI image on which the white matter skeleton (black) is projected. MNI coordinates are depicted for each projection. Yellow-to-red colors represent normal-appearing white matter regions with reduced FA in relation to increasing age. When adjusted for global white matter atrophy and white matter lesion volume, only very few regions in the normal-appearing white matter show reduced FA with age, most notably a small region bilateral in the inferior longitudinal fasciculus.*

Figure 4.1.4. *Global white matter atrophy and reduced fractional anisotropy in cingulate bundle. Coronal, sagittal and axial projections of mean fractional anisotropy (FA) MRI image on which the white matter skeleton (black) is projected. MNI coordinates are depicted for each projection. Yellow-to-red colors represent normal-appearing white matter regions with reduced FA in relation to white matter atrophy. Arrows indicate the cingulate bundle on both sides.*

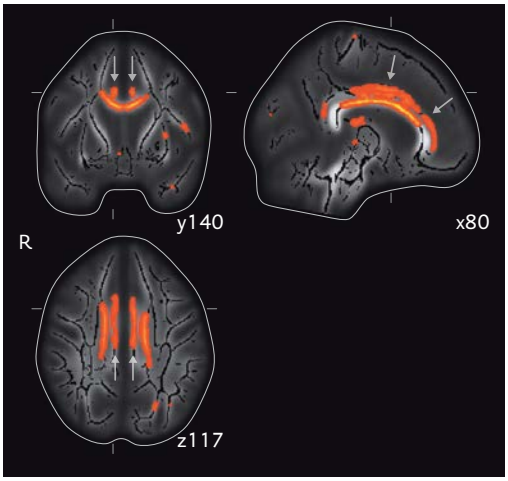

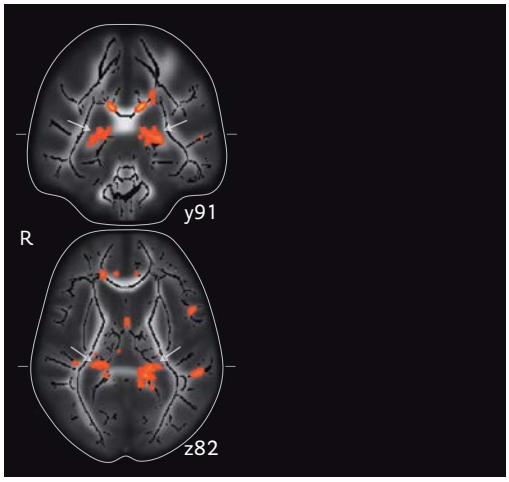

Figure 4.1.5. *Global white matter atrophy and reduced fractional anisotropy in hippocampal region. Coronal and axial projection of mean fractional anisotropy (FA) MRI image on which the white matter skeleton (black) is projected. MNI coordinates are depicted for both projections. Yellow-to-red colors represent normal-appearing white matter regions with reduced FA in relation to white matter atrophy. Arrows indicate the hippocampal region on both sides.*

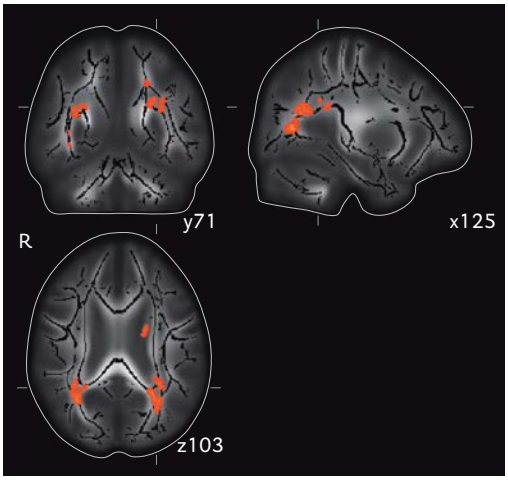

Figure 4.1.6. *White matter lesions and reduced fractional anisotropy in periventricular regions. Coronal, sagittal and axial projections of mean fractional anisotropy (FA) MRI image on which the white matter skeleton (black) is projected. MNI coordinates are depicted for each projection. Normal-appearing white matter with reduced FA in relation to white matter lesions is visible in posterior periventricular regions (yellow-to-red colors).*

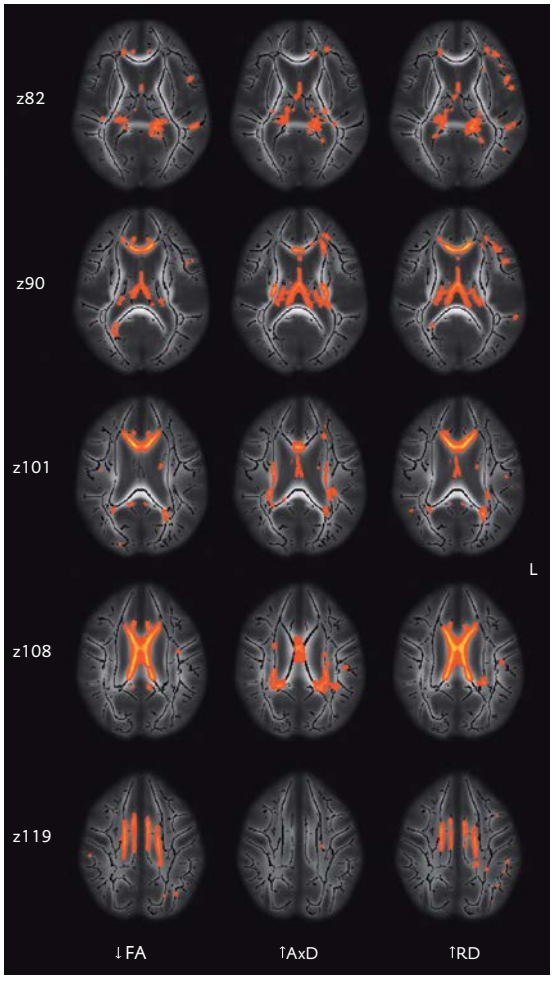

Figure 4.1.7. *Global white matter atrophy and increased directional diffusivity. Axial projections of mean fractional anisotropy (FA) MRI images on which the white matter skeleton (black) is projected. Columns show regions where global white matter atrophy is associated with decreases in FA or increases in axial (AxD) and radial (RD) diffusivity, respectively. Rows depict the same axial levels as Figure 4.1.2, in MNI coordinates (z). The first (z = 82) and second (z = 90) rows show decreases in FA in the hippocampal region and fornix associated with white matter atrophy, accompanied by increases of both AxD and RD (yellow-to-red colors) in these regions. The third (z=101) and fourth row (z=108) show that reductions of FA in the corpus callosum and cingulate bundle are almost fully explained by increases in RD in these regions, without accompanying changes in AxD. In contrast, AxD is increased in posterior periventricular regions (z=108), without a marked change in RD.*

Removal of white matter lesions

White matter lesion maps (automatically classified as described above) were resampled to the DTI image space and fed into the pipeline for non-FA data provided by TBSS.[13] By applying the FA-to-skeleton transformation on this lesion map, as was also done for the directional diffusivities, we created a lesion mask in skeleton space. This mask was used to identify voxels on the skeletons that originated in lesions (Figure 4.1.1). These voxels were then removed from the skeleton to obtain in each individual a skeleton of the normal-appearing white matter.

Voxelwise statistical analysis

Skeletonized FA images created by TBSS were analyzed using a generalized linear model implementation in Matlab's Statistical Toolbox (Version 6.1, Release 2007b, The MathWorks, Natick, MA, USA). In a voxelwise manner, a multiple linear regression model was fitted to identify those voxels on the white matter skeleton that showed significant decrease in FA associated with age, relative global normal-appearing white matter volume and relative white matter lesion volume. Because of skewness of the untransformed measure, relative white matter lesion volume was natural log-transformed. All analyses were adjusted for sex and furthermore, if appropriate, for each of the other variables in the model (age and relative volumes of global normal-appearing white matter and white matter lesions). We subsequently analyzed the relation between lobar white matter volumes and FA, for each lobe separately, adjusted for age, sex and white matter lesion volume. Finally, we investigated changes in AxD and RD associated with age, relative global normal-appearing white matter volume and relative white matter lesion volume. For all analyses, the null distributions of the *t*-values were estimated using a permutation-based method (10,000 permutations), in order to correct for multiple comparisons.[22] As a result, the displayed figures show t-statistics for each association thresholded at a multiple-comparison corrected *p*-value of 0.05. The skeletonized results were then thickened for better visibility.[13] Significant results are shown in red-to-yellow colorings of voxels on the skeleton, with yellow representing higher *t*-values and color intensities standardized between all figures.

Results

Mean age of the study population (n = 832) was 67.3 years and 419 (50.4%) participants were women. Mean volume percentage of global normal-appearing white matter was 34.4% (SD 3.7). Median volume percentage of white matter lesions was 0.3% (interquartile range 0.2–0.5%). A significant decrease in FA was seen in multi-

ple regions on the white matter skeleton with increasing age (Figure 4.1.2 A), reflecting a loss of microstructural integrity of normal-appearing white matter. However, nearly all of these regional decreases in FA were explained by either white matter atrophy (Figure 4.1.2 B) or by white matter lesions (Figure 4.1.2 C). When adjusted for both white matter atrophy and white matter lesions, only few regions in the normal-appearing white matter still displayed changes with age (Figure 4.1.2 D), most notably a small region bilateral in the inferior longitudinal fasciculus (Figure 4.1.3). The white matter regions that showed FA changes associated with either white matter atrophy or white matter lesions differed clearly. White matter atrophy was related to loss of microstructural integrity in the body of the corpus callosum, the fornix and in the cingulate bundle along its complete course from anterior up to its posterior connection to the hippocampal region (Figures 4.1.2 B, 4.1.4 and 4.1.5). In contrast, a larger relative volume of white matter lesions caused FA decreases in periventricular regions (Figures 4.1.2 C and 4.1.6). We did not find any increases in FA with age, white matter atrophy or white matter lesions.

When analyzing lobar white matter atrophy, we found that for each lobe, white matter atrophy in that region was associated with a similar pattern in FA decreases compared with global white matter atrophy (Figure 4.1.9). Also, there were no differences between left or right lobes in this respect (results not shown).

Similarly to FA changes, we found that changes in AxD and RD that occurred with increasing age were almost fully explained by white matter atrophy or by white matter lesions, apart from the region bilateral in the inferior longitudinal fasciculus. Also corresponding to FA changes, we found regional differences in AxD and RD between atrophy and lesions. White matter atrophy was associated with increases in both AxD and RD in fornix and hippocampal regions, the same regions where FA showed decreases with atrophy (Figure 4.1.7). AxD was increased in posterior periventricular regions with atrophy, without accompanying change in RD (Figure 4.1.7). In contrast, significant increases in RD almost fully explained the previously described FA decreases in the corpus callosum and cingulate bundle (Figure 4.1.7).

Regarding white matter lesions, we found with increasing lesion load significant increases in AxD lateral from the ventricles extending to the centrum semiovale and corona radiata, without an associated increase in RD (Figure 4.1.8) or change in FA. In contrast, RD was mainly increased in posterior periventricular regions with increasing white matter lesion load (Figure 4.1.8). We did not find any decreases in AxD or RD with age, white matter atrophy or white matter lesions.

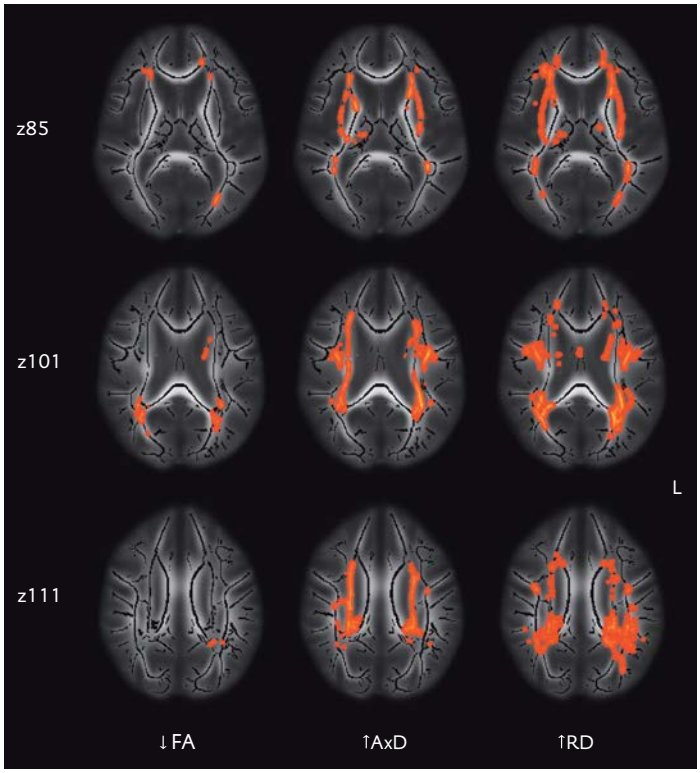

Figure 4.1.8. *White matter lesions and increased directional diffusivity. Axial projections of mean fractional anisotropy (FA) MRI images on which the white matter skeleton (black) is projected. Columns show regions where relative white matter lesion volume is associated with decreases in FA or increases in axial (AxD) and radial (RD) diffusivity, respectively. Rows depict axial levels in MNI coordinates (z). The first (z = 85) and second (z = 101) rows show in the anterior periventricular regions and bilateral in the extreme capsule increases in both AxD and RD (yellow-to-red colors) associated with white matter lesions, but no change in FA. The second (z = 101) and third row (z = 111) show increases in AxD lateral from the ventricles extending to the centrum semiovale and corona radiata, without accompanying increases of RD in these regions. In contrast, RD shows marked increases in posterior periventricular regions.*

Discussion

Using DTI, we found that independent of age, both white matter atrophy and white matter lesion burden are related to loss of integrity in multiple yet distinct regions of normal-appearing white matter.

Strengths of our study are the large sample of persons from a general elderly population in whom both structural MRI and DTI were performed, and our automated and validated techniques for quantification of white matter atrophy and white matter lesion volume. The voxelwise analysis technique we used, TBSS,[13] is an automated observer-independent method which has been shown to be more robust and accu-

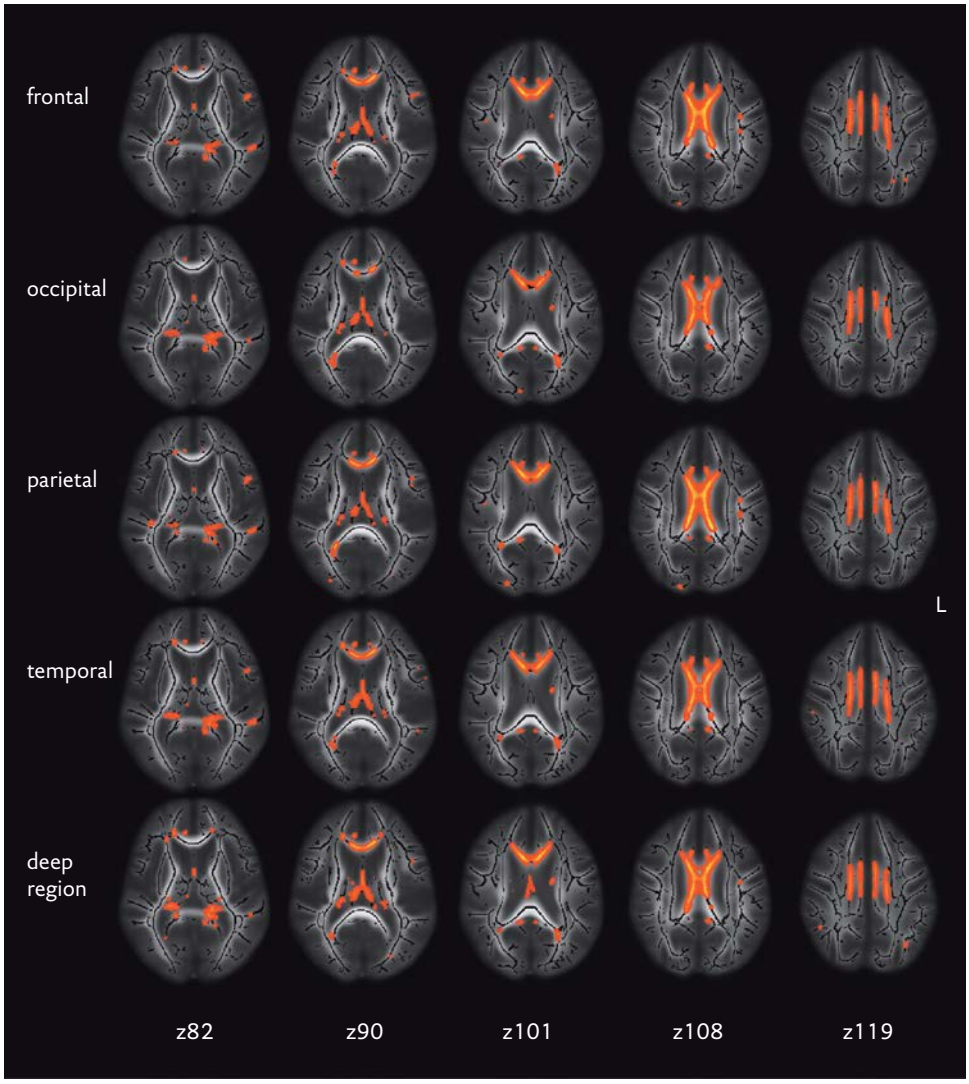

Figure 3.1.9. *Lobar white matter atrophy and reductions in fractional anisotropy. Axial projections of mean fractional anisotropy (FA) MRI images on which the white matter skeleton (black) is projected. Images are shown in the Montreal Neurological Institute (MNI) stereotactic space, with MNI coordinates for axial levels (z) depicted for each column. Axial levels correspond to the levels depicted in Figure 4.1.2. Yellow-to-red colors represent normal-appearing white matter regions with reduced fractional anisotropy (FA) in relation to lobar white matter atrophy (represented in rows; respectively frontal, occipital, parietal and temporal lobes and the deep region), adjusted for age, sex and relative white matter lesion volume. The regions that show significant reductions in FA associated with lobar white matter atrophy do not differ between the lobes and are furthermore similar to the regions that show FA reductions with global white matter atrophy (see Figure 4.1.2).*

rate than other voxelwise analysis techniques (such as statistical-parametrical mapping) which are prone to residual misalignment and in which the amount of spatial smoothing greatly affects the results.[23]

Our results have several major implications for the understanding of white matter changes in the aging brain. Firstly, they confirm that FA, and thus microstructural integrity, is reduced even in normal-appearing white matter, although no macroscopic alterations are visible on conventional MRI. Age-related changes in normal-appearing white matter microstructure have previously been described by studies measuring FA in manually placed regions-of-interest.[24–26] Also, in small case-control studies, FA reductions in normal-appearing white matter were found to be more pronounced in persons with signs of ischemic brain disease[7,27,28] and in persons with Alzheimer's Disease or mild cognitive impairment[29,30] in comparison with healthy controls. We now demonstrate in a large sample of the general population the predilection areas of age-related changes in the normal-appearing white matter, and we show that these changes are associated with both ischemic white matter lesions and with white matter atrophy.

Secondly, our data show that aging related loss of microstructural integrity of white matter is primarily explained by white matter atrophy and white matter lesion formation. White matter breakdown in aging and associated loss of "connectivity" is thought to be a major factor in cognitive decline.[31] Our results may therefore provide a better understanding of the pathophysiologic processes underlying cognitive deterioration in aging.

Thirdly, our results indicate that white matter atrophy and white matter lesion formation, which are very common in the aging brain, are related to FA reductions and increases in directional diffusivities in distinct brain regions. The regions that showed loss of microstructural integrity associated with white matter atrophy, namely the fornix, cingulate bundle and hippocampal region, are those that are part of the limbic system which is the anatomic substrate for memory, emotion and learning, and which since long has been related to development of cognitive decline and Alzheimer disease.[32] The normal-appearing white matter regions that showed reduced FA in relation to a larger burden of white matter lesions, the periventricular regions, are specifically known to be vulnerable to ischemic events.[33] Furthermore, we found that the regions where changes in AxD and RD occurred differed for white matter atrophy and white matter lesions, but also that increases in AxD and RD did not always overlap. Several animal studies have shown that the nature of the underlying white matter pathology may be reflected in changes in AxD and RD. Myelin degradation has been shown to primarily lead to increases in diffusivity perpendicular to the tracts (RD), whilst acute axonal injury in animal models led to (transient) decreases in parallel diffusivity (AxD).[8,10] In the present study, we did not find any decreases in diffusivity, but rather increases in AxD and RD, in line with other

reports in humans that studied aging[34–36] or trauma[37] or even preterm infants with diffuse white matter changes.[38] It has been suggested that increases in both AxD and RD reflect decreased packing within a voxel[36] or that apparent increases in AxD result from loss of fiber coherence in regions with fiber crossing.[38]

In summary, the regional distinction in loss of integrity of the normal-appearing white matter in relation to atrophy or white matter lesion formation indicates that the two processes are not sequential events but are rather independent and thus pathophysiologically potentially different. As such, our study provides new insight into white matter changes in aging and a starting point for further research into preventive measures.

References

1. O'Sullivan M, Jones DK, Summers PE, Morris RG, Williams SC, Markus HS. Evidence for cortical "disconnection" as a mechanism of age-related cognitive decline. *Neurology*. 2001;57(4):632-638.
2. Meier-Ruge W, Ulrich J, Brühlmann M, Meier E. Age-related white matter atrophy in the human brain. *Ann N Y Acad Sci*. 1992;673:260-9.
3. De Leeuw F-E, de Groot JC, Achten E, et al. Prevalence of cerebral white matter lesions in elderly people: a population based magnetic resonance imaging study. The Rotterdam Scan Study. *J Neurol Neurosurg Psychiatry*. 2001;70(1):9-14.
4. Englund E, Brun A, Alling C. White Matter Changes In Dementia Of Alzheimer's Type. *Brain*. 1988;111:1425-1439.
5. Ikram MA, Vrooman HA, Vernooij MW, et al. Brain tissue volumes in the general elderly population. The Rotterdam Scan Study. *Neurobiol Aging*. 2008;29(6):882-890.
6. Basser PJ, Jones DK. Diffusion-tensor MRI: theory, experimental design and data analysis - a technical review. *NMR Biomed*. 2002;15(7-8):456-467.
7. O'sullivan M, Summers PE, Jones DK, Jarosz JM, Williams SC., Markus H. Normal-appearing white matter in ischemic leukoaraiosis: A diffusion tensor MRI study. *Neurology*. 2001;57:2307-2310.
8. Song S-K, Sun S-W, Ju W-K, Lin S-J, Cross AH, Neufeld AH. Diffusion tensor imaging detects and differentiates axon and myelin degeneration in mouse optic nerve after retinal ischemia. *Neuroimage*. 2003;20(3):1714-1722.
9. Song S-K, Yoshino J, Le TQ, et al. Demyelination increases radial diffusivity in corpus callosum of mouse brain. *Neuroimage*. 2005;26(1):132-40.
10. Sun S-W, Liang H-F, Trinkaus K, Cross AH, Armstrong RC, Song S-K. Noninvasive detection of cuprizone induced axonal damage and demyelination in the mouse corpus callosum. *Magn Reson Med*. 2006;55(2):302-8.
11. Salat DH, Tuch DS, Greve DN, et al. Age-related alterations in white matter microstructure measured by diffusion tensor imaging. *Neurobiol Aging*. 2005;26(8):1215-27.
12. Bookstein FL. "Voxel-based morphometry" should not be used with imperfectly registered images. *Neuroimage*. 2001;14(6):1454-1462.
13. Smith SM, Jenkinson M, Johansen-Berg H, et al. Tract-based spatial statistics: voxelwise analysis of multi-subject diffusion data. *Neuroimage*. 2006;31(4):1487-1505.
14. Hofman A, Breteler MMB, van Duijn CM, et al. The Rotterdam Study: objectives and design update. *Eur J Epidemiol*. 2007;22(11):819-829.
15. Vrooman HA, Cocosco CA, van der Lijn F, et al. Multi-spectral brain tissue segmentation using automatically trained k-Nearest-Neighbor classification. *Neuroimage*. 2007;37(1):71-81.
16. Anbeek P, Vincken KL, van Bochove GS, van Osch MJP, van der Grond J. Probabilistic segmentation of brain tissue in MR imaging. *Neuroimage*. 2005;27(4):795-804.

17. Rueckert D, Sonoda LI, Hayes C, Hill DL, Leach MO, Hawkes DJ. Nonrigid registration using free-form deformations: application to breast MR images. *IEEE Trans Med Imaging*. 1999;18(8):712-721.

18. Ikram MA, Vrooman HA, Vernooij MW, et al. Brain tissue volumes in relation to cognitive function and risk of dementia. *Neurobiol Aging*. 2010;31(3):378-86.

19. Smith SM, Jenkinson M, Woolrich MW, et al. Advances in functional and structural MR image analysis and implementation as FSL. *Neuroimage 23 S1*. 2004;23 Suppl 1:208-219.

20. Smith SM. Fast robust automated brain extraction. *Hum Brain Mapp*. 2002;17(3):143-55.

21. Mazziotta J, Toga A, Evans A, et al. A probabilistic atlas and reference system for the human brain: International Consortium for Brain Mapping (ICBM). *Philos Trans R Soc L B Biol Sci*. 2001;356(1412):1293-1322.

22. Nichols TE, Holmes AP. Nonparametric permutation tests for functional neuroimaging: a primer with examples. *Hum Brain Mapp*. 2002;15(1):1-25.

23. Jones DK, Symms MR, Cercignani M, Howard RJ. The effect of filter size on VBM analyses of DT-MRI data. *Neuroimage*. 2005;26(2):546-554.

24. Abe O, Aoki S, Hayashi N, et al. Normal aging in the central nervous system: quantitative MR diffusion-tensor analysis. *Neurobiol Aging*. 2002;23(3):433-441.

25. Bartzokis G, Sultzer D, Lu PH, Nuechterlein KH, Mintz J, Cummings JL. Heterogeneous age-related breakdown of white matter structural integrity: implications for cortical "disconnection" in aging and Alzheimer's disease. *Neurobiol Aging*. 2004;25(7):843-51.

26. Helenius J, Soinne L, Perkiö J, et al. Diffusion-weighted MR imaging in normal human brains in various age groups. *AJNR Am J Neuroradiol*. 2002;23(2):194-9.

27. Chabriat H, Pappata S, Poupon C, et al. Clinical Severity in CADASIL Related to Ultrastructural Damage in White Matter : In Vivo Study With Diffusion Tensor MRI. *Stroke*. 1999;30(12):2637-2643.

28. Jones DK, Lythgoe D, Horsfield MA, Simmons A, Williams SCR, Markus HS. Characterization of White Matter Damage in Ischemic Leukoaraiosis with Diffusion Tensor MRI. *Stroke*. 1999;30(2):393-397.

29. Fellgiebel A, Müller MJ, Wille P, et al. Color-coded diffusion-tensor-imaging of posterior cingulate fiber tracts in mild cognitive impairment. *Neurobiol Aging*. 2005;26(8):1193-1198.

30. Kantarci K, Jack CR, Xu YC, et al. Mild cognitive impairment and Alzheimer disease: regional diffusivity of water. *Radiology*. 2001;(7):101-107.

31. Fazekas F, Schmidt R, Scheltens P. Pathophysiologic mechanisms in the development of age-related white matter changes of the brain. *Dement Geriatr Cogn Disord*. 1998;9 Suppl 1:2-5.

32. Hopper MW, Vogel FS. The limbic system in Alzheimer's disease. A neuropathologic investigation. *Am J Pathol*. 1976;85(1):1-20.

33. Chalela JA, Wolf RL, Maldjian JA, Kasner SE. MRI identification of early white matter injury in anoxic-ischemic encephalopathy. *Neurology*. 2001;56(4):481-5.

34. Bastin ME, Clayden JD, Pattie A, Gerrish IF, Wardlaw JM, Deary IJ. Diffusion tensor and magnetization transfer MRI measurements of periventricular white matter hyperintensities in old age. *Neurobiol Aging*. 2009;30(1):125-36.

35. Salat DH, Tuch DS, van der Kouwe AJW, et al. White matter pathology isolates the hippocampal formation in Alzheimer's disease. *Neurobiol Aging*. 2008.

36. Sullivan EV, Rohlfing T, Pfefferbaum A. Quantitative fiber tracking of lateral and interhemispheric white matter systems in normal aging: Relations to timed performance. *Neurobiol Aging*. 2008.

37. Kraus MF, Susmaras T, Caughlin BP, Walker CJ, Sweeney JA, Little DM. White matter integrity and cognition in chronic traumatic brain injury: a diffusion tensor imaging study. *Brain*. 2007;130(Pt 10):2508-2519.

38. Counsell SJ, Shen Y, Boardman JP, et al. Axial and radial diffusivity in preterm infants who have diffuse white matter changes on magnetic resonance imaging at term-equivalent age. *Pediatrics*. 2006;117(2):376-86.

4.2

Cerebral microbleeds are related to loss of white matter structural integrity

Neurology 2013

Saloua Akoudad
Marius de Groot
Peter J. Koudstaal
Aad van der Lugt
Wiro J. Niessen
Albert Hofman
M. Arfan Ikram
Meike W. Vernooij

Objective – To investigate whether the presence of cerebral microbleeds, which present as focal lesions on imaging, is associated with a diffuse loss of white matter microstructural integrity in the brain.

Methods – In the prospective, population-based Rotterdam Scan Study, a total of 4,493 participants underwent brain MRI to determine microbleed status. With diffusion tensor imaging, global fractional anisotropy (FA) and mean diffusivity (MD) were measured in normal-appearing white matter. Multiple linear regression models, adjusted for age, sex, cardiovascular risk factors, white matter lesions, and infarcts, were applied to investigate the independent association between microbleeds and organization of brain white matter. Analyses were repeated after stratification by APOE ε4 carriership.

Results – Presence of microbleeds was related to a lower mean FA and higher mean MD, in a dose-dependent manner, and was already apparent for a single microbleed (standardized FA: 20.13, 95% confidence interval 20.21 to 20.05; MD: 0.12, 95% confidence interval 0.05 to 0.19). For lobar microbleeds, alterations in diffusion tensor imaging measurements were solely driven by APOE ε4 carriers.

Conclusions – Presence of microbleeds relates to poorer microstructural integrity of brain white matter, even after adjusting for cardiovascular risk and other markers of cerebral small-vessel disease. Our data suggest that microbleeds reflect diffuse brain pathology, even when only a single microbleed is present.

Objective

As the elderly population is growing, cerebral small-vessel disease (CSVD) and its phenotypes are expected to put a larger psychosocial and economic burden on society.[1] CSVD is, despite its diffuse character, typically recognized by focal lesions such as white matter lesions (WMLs) and lacunes on conventional MRI.

Recent advances in noninvasive brain imaging techniques have expanded the possibilities to study brain changes that cannot be visually appreciated on conventional MRI. Diffusion tensor imaging (DTI) is an MRI technique that allows for quantifi-

cation of subtle pathology in the architecture of brain white matter.[2] Indeed, with DTI, it has been shown that people with WMLs or lacunes on brain MRI have diffuse loss of white matter integrity not seen on conventional MRI.[3]

In the past decade, cerebral microbleeds (CMBs) have emerged as a novel marker of CSVD. CMBs also appear as well-demarcated focal lesions on MRI.[4–6] It may be hypothesized that these microbleeds, like WMLs and lacunes, mark more widespread brain damage. Although there is some pathologic evidence linking CMBs to surrounding white matter damage,[7–10] large in vivo studies on this topic are lacking. DTI can provide us with new insights regarding global white matter structural deterioration in the presence of these focal microbleeds.

We investigated whether the presence of microbleeds is related to diffuse loss of microstructural integrity of brain white matter in a large sample of middle-aged and elderly people from the general population.

Methods

Participants

This study was conducted within the Rotterdam Scan Study, an ongoing prospective population-based imaging study designed to investigate preclinical brain changes in the elderly. The Rotterdam Scan Study is performed in the context of the population-based Rotterdam Study. Its rationale and study design for both studies have been described extensively elsewhere.[11,12] We have previously published the prevalence of CMBs in 3,979 Rotterdam Study participants who completed brain MRI scanning between 2005 and 2008.[13] Since then, additional participants were scanned, and until 2012, a total of 5,990 participants were invited to undergo brain MRI. Of 5,445 eligible participants (all without dementia and MRI contraindications), 4,843 (88.9%) gave written informed consent. After excluding participants with the inability to complete MRI (n = 71), scans of inadequate quality (n = 125), and subjects with cortical brain infarcts (n = 154), data on 4,493 participants were available for analyses.

Brain MRI and assessments of MRI markers

We performed a multisequence MRI protocol on a 1.5T scanner (GE Healthcare, Milwaukee, WI) in all participants.[11] All scans were reviewed by 1 of 5 trained research physicians, who recorded the presence, number, and location of microbleeds and infarcts using a protocol that was initiated at the beginning of the study in 2005

with good inter- and intraobserver agreement.[14] Raters were blinded to clinical data, including *APOE* genotyping. CMBs were rated as focal areas of signal loss on 3-dimensional T2* gradient recalled echo-weighted MRI. Presence of CMBs was categorized by location based on presumed differences in underlying etiology: deep or infratentorial microbleeds are thought to represent hypertensive arteriopathy whereas strictly lobar CMBs point toward cerebral amyloid angiopathy (CAA).[14] The presence of lacunes and cortical infarcts was rated on fluid-attenuated inversion recovery (FLAIR), proton density–weighted, and T1-weighted sequences. Lacunes of presumed vascular origin[15] were defined as focal lesions of ≥3 mm and <15 mm in size with the same signal intensity as CSF on all sequences and a hyperintense rim on the FLAIR (when located supratentorially). Infarcts larger than 15 mm were identified as subcortical infarcts, irrespective of their location in the brain (subcortical or striatocapsular).[14] Infarcts showing involvement of gray matter were classified as cortical infarcts. Brain tissue was segmented into gray matter, white matter, CSF, and background using a fully automated approach incorporating a multiatlas strategy with 6 manually labeled atlases for learning specific tissue intensities. WMLs were automatically segmented based on the FLAIR image using a postprocessing step.[16] This enabled identification of the normal-appearing white matter as white matter unaffected by WMLs. This segmentation approach was specifically developed for MRI data acquired in the Rotterdam Scan Study. The automated detection of WMLs was achieved with high similarity index (0.72) when compared with gold-standard manual segmentations, which is comparable to the interobserver variability for manual segmentation (similarity index 0.75).[16]

Processing of DTI data

Loss of white matter microstructural integrity is accompanied by changes in DTI-derived measurements. DTI measurements most frequently used are fractional anisotropy (FA) and mean diffusivity (MD). Higher values of FA and lower values of MD generally indicate better microstructural integrity. Moreover, directional diffusivity measurements (axial and radial diffusivity) are thought to provide more subtle insight into underlying pathophysiologic proceses, as myelin damage has been associated with increased radial diffusivity and axonal damage with increased axial diffusivity.[17]

Diffusion data were preprocessed using a standardized pipeline.[18] In summary, to compensate for subject motion and eddy currents, all acquired volumes were coregistered using affine registrations performed with Elastix.[19] Data were resampled at an isotropic resolution of 1 mm^3, and diffusion tensors were fitted using a Levenberg-Marquardt nonlinear least-squares algorithm available in ExploreDTI.[20] The diffusion data were then coregistered to the T1-weighted image using affine registration. The tensor image, resampled in the T1-weighted space, was used to ob-

tain FA, MD, and directional diffusivity images. These diffusion metrics were then combined with the tissue segmentation results to obtain global measurements in the normal-appearing white matter of the brain, which were used in the analyses. All FA images were visually inspected, and 61 subjects were excluded because of scanning artifacts or excessive motion.

Assessment of cardiovascular risk factors

Cardiovascular risk factors were assessed during study visits by interview and laboratory and physical examinations at regular visits of study participants to the research center.[12] Risk factors corrected for in our analyses included systolic and diastolic blood pressure (measured twice with a random-zero sphygmomanometer), total cholesterol (determined by using an automated enzymatic procedure, Hitachi analyzer, Roche Diagnostics), diabetes (fasting blood glucose of ≤7.0 mmol/L, and/or the use of any glucose-lowering medication), smoking (ever vs never smoked), and lipid-lowering and antihypertensive medication. Medication use was assessed during home visits. *APOE* genotyping was performed on coded genomic DNA samples.[21] Distribution of *APOE* genotype and allele frequencies in this population was in Hardy-Weinberg equilibrium.

History of cardiovascular disease

A history of symptomatic stroke and coronary heart disease was assessed by self-report, and by continuous monitoring of medical records through automatic linkage of general practitioners' files with the study database, as described previously.[22]

Data analysis

WML volume was natural log-transformed because of its skewed distribution. Diffusion measures were aver- aged inside the normal-appearing brain white matter for each subject. Subject-specific mean FA, MD, and axial and radial diffusivity were standardized to z scores. Microbleed status was investigated dichotomously (none vs one or more CMBs), categorically for microbleed count (none [reference category] vs 1, 2–4, and ≥5 CMBs), and by location (none vs strictly lobar CMBs, and none vs deep or infratentorial CMBs [with or without the presence of lobar CMBs]). We used linear regression to evaluate the association between microbleed status and integrity of brain white matter and evaluated 4 models. In the first model, analyses were age- and sex-adjusted. Model 2 was additionally adjusted for cardiovascular risk (systolic and diastolic blood pressure, total cholesterol, smoking, diabetes, and lipid-lowering and antihypertensive medication). We adjusted model 3 for age, sex,

intracranial volume, and for other markers of CSVD, namely, lacunes, white matter volume, and WML volume. A final fourth model was adjusted for both cardiovascular risk and other markers of CSVD. We also examined R^2 in the regression models to evaluate the proportion of total variance in FA and diffusivity measurements that was attributed to microbleeds after having corrected for the other variables in models 2, 3, and 4. We additionally investigated whether adjustments for age-squared would give a better adjustment for confounding by age.

Quantitative risk factors such as blood pressures and total cholesterol were modeled continuously per SD increase. Analyses were repeated after stratification by *APOE* ε4 carriership, and formal interaction tests were applied to determine significant differences in subgroups. Finally, apart from cortical infarcts, we additionally excluded persons with lacunes, subcortical infarcts, and a history of symptomatic stroke in sensitivity analyses. All analyses were performed using statistical software package SPSS 20.0 (IBM Corp., Armonk, NY), and an α value of 0.05. Additionally, we adjusted for multiple testing using Bonferroni correction (p-value threshold of 0.0028) based on 18 independent tests.

Standard protocol approvals, registrations, and patient consents

The institutional review board approved the study. We obtained consent for examinations from all participants. The study conforms to the Strengthening the Reporting of Observational Studies in Epidemiology (STROBE) statement guidelines.

Results

Table 4.2.1 provides characteristics of our study population. Mean age was 63.9 years (range, 45.7–100.1 years) and 2,493 of the participants were female. A total of 875 participants had at least one microbleed of whom 588 had strictly lobar and 287 deep or infratentorial microbleeds (with or without presence of lobar microbleeds). Mean brain normal-appearing white matter volume was 389.7 ml with a mean FA of 0.34, mean MD of 0.7×10^{-3} mm^2/s, mean axial diffusivity of 1.0×10^{-3} mm^2/s, and mean radial diffusivity of 0.6×10^{-3} mm^2/s.

The association between the presence of one or more CMBs and diffusion measurements of brain normal-appearing white matter is shown in Table 4.2.2. When adjusted for age and sex, there was a significantly lower mean FA and higher mean MD in brain white matter, reflecting loss of integrity of brain white matter in subjects with microbleeds compared with those who did not have any microbleeds. Additional adjustments for cardiovascular risk did not change the results meaningfully (model 2). The association also remained unchanged after adjustment for other

markers of CSVD (WML volume and presence of lacunes, model 3), and after adjusting for a full model of cardiovascular risk and imaging markers of CSVD (model 4). Both axial and radial diffusivity were higher in subjects with microbleeds compared with those who did not have microbleeds. A maximum of 1.1% of the variance in DTI measurements was explained by microbleeds in these models. All associations described above survived multiple comparison correction. When analyzing microbleed count, we found that the presence of a single microbleed was associated with a significantly lower mean FA and higher MD. These associations became more prominent with increasing microbleed count (Figure 4.2).

Table 4.2.1
Baseline characteristics of the study population (N= 4493)

	No CMBs (n=3618)	CMBs (n=875)
Age, y	62.4 (10.7)	69.9 (10.8)
Female	2027 (56.0)	466 (53.3)
NAWM volume, ml	391.2 (47.9)	383.9 (48.5)
FA in NAWM	0.34 (0.02)	0.33 (0.02)
MD in NAWM, $10^{-3}mm^2/s$	0.73 (0.02)	0.75 (0.03)
AxD in NAWM, $10^{-3}mm^2/s$	1.01 (0.03)	1.03 (0.03)
RD in NAWM, $10^{-3}mm^2/s$	0.59 (0.04)	0.61 (0.03)
Intracranial volume, ml	1125.3 (118.6)	1128.7 (121.3)
White matter lesion volume, ml*	2.5 (3.4)	4.9 (9.3)
Lacunar infarcts	195 (5.4)	141 (16.1)
History of symptomatic stroke	39 (1.1)	32 (3.7)
History of coronary heart disease	67 (1.9)	81 (9.3)
APOE ε4 carriers	940 (31.9)	251 (34.9)
Systolic blood pressure, mmHg	136.9 (20.8)	144.3 (21.8)
Diastolic blood pressure, mmHg	82.4 (10.8)	82.8 (11.2)
Total cholesterol	5.6 (2.2)	5.4 (1.1)
Smoking (ever in life)	289 (8.1)	92 (10.6)
Diabetes	289 (8.1)	92 (10.6)
Lipid lowering medication	783 (21.8)	267 (30.7)
Antihypertensive medication	759 (21.1)	180 (20.7)

Data are presented as mean (standard deviation) for continuous variables, and number (%) for categorical variables. The following variables had missing data: blood pressure (n=38), total cholesterol (n=67), smoking (n=14), diabetes (n=60), lipid lowering medication (n=24), antihypertensive medication (n=26), APOE ε4 genotype (n=294).
** White matter lesion volume presented as median (interquartile range).*

Table 4.2.2
Microbleeds (yes vs. no) and white-matter microstructural integrity

	FA		MD		AxD		RD	
	z Difference	p Value	z Difference	p Value	z Difference	p Value	z Difference	p Value
Presence of CMBs								
Model 1	-0.27 (-0.33, -0.21)	<0.001	0.25 (0.19, 0.30)	<0.001	0.17 (0.11, 0.23)	<0.001	0.26 (0.21, 0.32)	<0.001
Model 2	-0.25 (-0.32, -0.19)	<0.001	0.24 (0.19, 0.30)	<0.001	0.18 (0.11, 0.24)	<0.001	0.26 (0.20, 0.31)	<0.001
Model 3	-0.15 (-0.21, -0.10)	<0.001	0.15 (0.10, 0.20)	<0.001	0.10 (0.05, 0.16)	0.001	0.16 (0.11, 0.21)	<0.001
Model 4	-0.15 (-0.20, -0.09)	<0.001	0.15 (0.10, 0.20)	<0.001	0.11 (0.05, 0.17)	0.001	0.16 (0.10, 0.21)	<0.001

Model 1= adjusted for age and sex. Model 2= as Model 1, additionally adjusted for systolic and diastolic blood pressure, total cholesterol, smoking, diabetes lipid lowering medication, and antihypertensive medication. Model 3= adjusted for age, sex, lacunes, normal appearing white-matter volume, white matter lesion volume (log transformed), and intracranial volume. Model 4= adjusted for age, sex, cardiovascular risk as in Model 2, and imaging markers as in Model 3. Abbreviations: CMBs= cerebral microbleeds. Values represent difference in z score of mean fractional anisotropy and mean diffusivity parameters in normal appearing white-matter for presence of any microbleeds compared to no microbleeds. Bonferroni-corrected threshold for significance: p-value=0.0028.

Table 4.2.3 shows the association between microbleed location and integrity of brain white matter. Persons with microbleeds in either deep or infratentorial, or strictly lobar locations had lower mean FA and higher mean MD in the brain white matter compared with those who did not have CMBs. Again, these associations survived multiple comparison correction. Associations were stronger for microbleeds situated in the deep or infratentorial regions. Also, axial and radial diffusivity were highest in subjects with deep or infratentorial microbleeds. After additional stratification by *APOE* ε4 carriership, we found that only persons carrying an *APOE* ε4 allele showed a clear association between lobar microbleeds and loss of brain white matter microstructural integrity, whereas such an association was not present for noncarriers (*p* interaction FA = 0.022, MD = 0.002) (Table 4.2.4). Effect modification by *APOE* ε4 carriership was not present for deep or infratentorial microbleeds.

Additional exclusion of persons with a history of symptomatic stroke or those with MRI-defined lacunes and/or subcortical infarcts did not change any of the above-mentioned results.

Discussion

We found that the presence of microbleeds was associated with a poorer global microstructural integrity of brain white matter, even when only a single microbleed was present. Associations were present after adjusting for important cardiovascular

risk factors and other MRI markers of CSVD. When investigating directional diffusivity, we observed that both axial and radial diffusivity were higher in subjects with CMBs.

The large sample size and population-based setting increase generalizability of our results and are major strengths of our study. We used sensitive MRI sequences to detect microbleeds[23] and to measure microstructural integrity of brain white matter.[24] Also, because of availability of a wide range of other subject characteristics, we were able to investigate the association between CMBs and white matter integrity after adjusting for important cardiovascular risk factors and other macroscopic imaging markers of CSVD, i.e., WMLs and lacunes. Some limitations of our study need to be mentioned. Because of the cross-sectional design of our study, we were not able to assess temporality of associations. Also, we should note that microbleed detection strongly depends on MRI acquisition parameters and field strength used.[23,25] Although our scan protocol was optimized for the detection of CMBs on a 1.5T scanner,[23] we may have missed small bleeds that would have become apparent when, for example, using higher field strengths. Furthermore, registrations of DTIs are to some extent susceptible to artifacts and distortions and may therefore have small registration inaccuracies. All registration results were, however, visually inspected and no registration errors caused by distortions or susceptibility artifacts were observed. Finally, although we aimed to address all potential important confounders,

Table 4.2.3
Microbleeds by location and white-matter microstructural integrity

	FA		MD		AxD		RD	
	z Difference	p Value	z Difference	p Value	z Difference	p Value	z Difference	p Value
Deep / infratentorial								
Model 1	-0.49 (-0.59, -0.39)	<0.001	0.46 (0.37, 0.55)	<0.001	0.33 (0.23, 0.43)	<0.001	0.49 (0.40, 0.58)	<0.001
Model 2	-0.48 (-0.58, -0.37)	<0.001	0.46 (0.37, 0.55)	<0.001	0.34 (0.24, 0.44)	<0.001	0.48 (0.40, 0.57)	<0.001
Model 3	-0.24 (-0.34, -0.15)	<0.001	0.25 (0.16, 0.33)	<0.001	0.18 (0.08, 0.28)	<0.001	0.26 (0.18, 0.34)	<0.001
Model 4	-0.24 (-0.34, -0.15)	<0.001	0.25 (0.17, 0.34)	<0.001	0.19 (0.09, 0.29)	<0.001	0.27 (0.18, 0.35)	<0.001
Strictly lobar								
Model 1	-0.17 (-0.24, -0.10)	<0.001	0.16 (0.09, 0.22)	<0.001	0.11 (0.04, 0.18)	0.008	0.17 (0.10, 0.23)	<0.001
Model 2	-0.15 (-0.22, -0.08)	<0.001	0.15 (0.08, 0.21)	<0.001	0.11 (0.04, 0.18)	0.010	0.16 (0.09, 0.22)	<0.001
Model 3	-0.12 (-0.19, -0.05)	0.001	0.11 (0.05, 0.17)	0.001	0.08 (0.01, 0.14)	0.030	0.12 (0.06, 0.18)	<0.001
Model 4	-0.11 (-0.17, -0.04)	0.002	0.11 (0.05, 0.17)	<0.001	0.08 (0.01, 0.15)	0.028	0.11 (0.06, 0.17)	<0.001

Model 1= adjusted for age and sex. Model 2= as Model 1, additionally adjusted for systolic and diastolic blood pressure, total cholesterol, smoking, diabetes, lipid lowering medication, and antihypertensive medication. Model 3= adjusted for age, sex, lacunes, normal appearing white-matter volume, white matter lesion volume (log transformed), and intracranial volume. Model 4= adjusted for age, sex, cardiovascular risk as in Model 2, and imaging markers as in Model 3. Abbreviations: CMBs= cerebral microbleeds. Values represent difference in z score of mean fractional anisotropy and mean diffusivity parameters in normal appearing white-matter for presence of any microbleeds by their location compared to no microbleeds. Bonferroni-corrected threshold for significance: p-value=0.0028.

residual confounding due to unmeasured confounders or measurement inaccuracy in variables may have affected our results to some extent. Specifically, residual confounding by age may have overestimated the association presented in our study.

Previously, pathology studies have suggested that the presence of microbleeds reflects a more diffuse pathologic process in the brain by showing that white matter changes surround the actual microbleeds. However, these studies were often limited by sample size and generalizability.[8–10] Moreover, it is difficult to draw conclusions on diffuse brain pathology from these studies because pathologic examinations were not performed on the entire brain. DTI-MRI allows us to study the entire cerebral white matter in vivo, and alterations in DTI parameters have previously been linked to both cognitive deterioration as well as neurodegenerative disease,[26–28] suggesting that clinically relevant white matter changes can be assessed with DTI. Our DTI study in the general population now provides evidence to support the hypothesis that microbleeds are associated with subtle, but diffuse brain pathology in vivo, advocating the idea that presence of microbleeds on MRI may present merely a "tip of the iceberg" regarding the true extent of the underlying brain damage.

Several theories can be proposed when speculating about the underlying pathophysiologic mechanisms that link microbleeds and white matter integrity loss. First, CMBs may reflect vascular pathology that leads to white matter integrity loss via a pathway of shared risk factors, e.g., *APOE* genotype, cardiovascular risk, or inflammatory factors. Alternatively, CMBs may be linked to white matter integrity loss more directly through failure of the blood-brain barrier. For example, leakage of

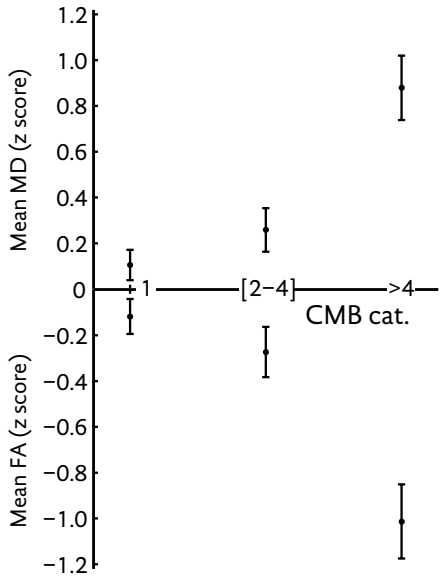

Figure 4.2. *Categories of CMB count and white-matter microstructural integrity. y-axis represents age- and sex-adjusted changes in z score in mean fractional anisotropy (FA) and mean diffusivity (MD) for each category of cerebral microbleed (CMB) count (x-axis), compared to reference group without microbleeds. Categories 0 CMBs n=3618; 1 CMB n=530; 2 to 4 CMBs n=242; ≥5 CMBs n=103.*

blood products due to blood-brain barrier dysfunction may result in microbleeds on one hand, and lead to subtle damage to the surrounding neuronal and white matter tissue on the other hand.[29,30]

We found that even the presence of a single microbleed related to a diffuse loss of white matter microstructure. This is particularly interesting because the presence of a single microbleed as isolated marker of CSVD remains an issue of debate.[31,32] Our results support the hypothesis that microbleed presence reflects damage to functional pathways more diffusively[33] rather than focally,[34] and thus that even a single microbleed marks relevant underlying vascular pathology. However, we should bear in mind that a single microbleed threshold should be interpreted within the context of MRI acquisition parameters and field strength used.[23,25]

Subjects with deep or infratentorial CMBs had poorer global white matter microstructure compared with subjects with strictly lobar microbleeds. One explanation could be that hypertensive vasculopathy may affect the brain microvasculature more diffusely, whereas CAA is primarily restricted to the cortical and meningeal

Table 4.2.4
Microbleeds and white matter microstructural integrity, by APOE ε4 status

	Carriers *APOE* ε4				Noncarriers *APOE* ε4			
	FA		MD		FA		MD	
	z Difference	p Value	z Difference	p Value	z Difference	p Value	z Difference	p Value
Presence of CMBs								
Model 1	-0.32 (-0.44, -0.20)	<0.001	0.31 (0.19, 0.43)	<0.001	-0.21 (-0.30, -0.13)	<0.001	0.19 (0.12, 0.26)	<0.001
Model 2	-0.30 (-0.42, 0.18)	<0.001	0.30 (0.18, 0.42)	<0.001	-0.19 (-0.28, -0.11)	<0.001	0.19 (0.11, 0.26)	<0.001
Model 3	-0.22 (-0.33, -0.11)	<0.001	0.21 (0.10, 0.32)	<0.001	-0.13 (-0.21, -0.05)	0.001	0.11 (0.04, 0.18)	0.001
Model 4	-0.20 (-0.31, -0.09)	<0.001	0.21 (0.10, 0.32)	<0.001	-0.12 (-0.20, -0.04)	0.004	0.11 (0.04, 0.18)	0.001
Deep / infratentorial								
Model 1	-0.44 (-0.63, -0.24)	<0.001	0.40 (0.22, 0.58)	<0.001	-0.46 (-0.60, -0.32)	<0.001	0.44 (0.32, 0.55)	<0.001
Model 2	-0.42 (-0.62, -0.22)	<0.001	0.40 (0.21, 0.59)	<0.001	-0.44 (-0.58, -0.30)	<0.001	0.44 (0.32, 0.55)	<0.001
Model 3	-0.20 (-0.38, -0.02)	0.027	0.19 (0.02, 0.37)	0.033	-0.26 (-0.39, -0.14)	<0.001	0.25 (0.15, 0.36)	<0.001
Model 4	-0.18 (-0.37, -0.001)	0.049	0.19 (0.01, 0.36)	0.043	-0.26 (-0.39, -0.14)	<0.001	0.26 (0.16, 0.37)	<0.001
Strictly lobar								
Model 1	-0.26 (-0.40, -0.13)	<0.001	0.28 (0.15, 0.41)	<0.001	-0.11 (-0.20, -0.01)	0.038	0.08 (0.002, 0.17)	0.044
Model 2	-0.24 (-0.38, -0.10)	0.001	0.26 (0.12, 0.39)	<0.001	-0.09 (-0.19, 0.01)	0.079	0.08 (-0.004, 0.16)	0.061
Model 3	-0.22 (-0.35, -0.10)	0.001	0.23 (0.11, 0.36)	<0.001	-0.08 (-0.17, 0.01)	0.096	0.06 (-0.02, 0.13)	0.151
Model 4	-0.21 (-0.34, -0.08)	0.001	0.22 (0.10, 0.35)	<0.001	-0.06 (-0.15, 0.03)	0.179	0.05 (-0.02, 0.13)	0.175

Model 1= adjusted for age and sex. Model 2= as Model 1, additionally adjusted for systolic and diastolic blood pressure, total cholesterol, smoking, diabetes, lipid lowering medication, and antihypertensive medication. Model 3= adjusted for age, sex, lacunes, normal appearing white-matter volume, white matter lesion volume (log transformed), and intracranial volume. Model 4= adjusted for age, sex, cardiovascular risk as in Model 2, and imaging markers as in Model 3. Abbreviations: CMBs= cerebral microbleeds. Values represent difference in z score of mean fractional anisotropy and mean diffusivity parameters in normal appearing white-matter for presence of any microbleeds, deep or infratentorial microbleeds, and strictly lobar microbleeds compared to no microbleeds. Bonferroni-corrected threshold for significance: p-value=0.0028.

vessels. Another consideration is that CAA pathology is known to cluster in occipital lobes,[35] and this may not be adequately reflected in a global brain white matter diffusion measurement. Future studies could use a lobar or regional approach to account for these specific focal changes.

For persons with strictly lobar microbleeds, poorer white matter integrity was confined to *APOE* ε4 allele carriers, although results were based on a smaller study sample. White matter pathology is a frequent finding in patients with CAA,[36] and the *APOE* ε4 allele is a well-known risk factor for CAA. It may be that subjects with strictly lobar CMBs who carry an *APOE* ε4 allele are more susceptible to diffuse white matter damage because both factors may act synergistically.

The association between CMBs and WMLs is well established, as is the association between WMLs and poorer white matter microstructural integrity. The novelty of our study is that we found a direct association between CMBs and white matter microstructure integrity loss. We showed that the relation between microbleeds and worse white matter microstructure remained after adjusting for burden of WMLs or presence of lacunes. A previous small study in patients with CAA did not find the same independency,[33] but differences in study population and sample size complicate comparison. Although the percentage of explained variance by microbleeds on DTI measurement in our study was only modest, the relation between microbleeds and white matter microstructural integrity provides important etiologic insights. Our finding suggests that microbleeds may reflect a more severe or unique form of vasculopathy that is not captured by other imaging markers of CSVD. This may implicate microbleeds as an important marker of risk stratification or therapy allocation in future studies.

Finally, we found that the presence of CMBs was associated with increased axial and radial diffusivity. Axial diffusivity describes water movement parallel to, and radial diffusivity perpendicular to, the main fiber orientation. From animal studies the hypothesis arose that an increase in axial diffusivity may correlate with axonal damage,[37] while increased radial diffusivity better reflects myelin damage.[17,38,39] This would suggest that the presence of CMBs may indicate both axonal and myelin damage. However, it is known from patient-based studies that demyelination and axonal damage often correlate and concordantly influence directional diffusivities. Also, the presence of both acute and chronic tissue damage may influence measures of axial diffusivity.[40,41] Thus, although it is tempting to extrapolate our understanding of directional diffusivity from animals to humans, interpretation of directional diffusivity measurements in observational studies is complex and warrants caution.

Overall, we found that CMBs may reflect a more severe or unique form of underlying vasculopathy because their presence associates with diffuse microstructural integrity loss of brain white matter even after adjusting for the presence of lacunes and WMLs. This subtle white matter pathology may be more severe in *APOE* ε4 allele carriers with lobar microbleeds.

References

1. Brumback-Peltz C, Balasubramanian AB, Corrada MM, Kawas CH. Diagnosing dementia in the oldest-old. *Maturitas*. 2011;70(2):164-8.
2. Le Bihan D, Mangin J-F, Poupon C, et al. Diffusion tensor imaging: concepts and applications. *J Magn Reson Imaging*. 2001;13(4):534-546.
3. O'Sullivan M, Morris RG, Huckstep B, Jones DK, Williams SC., Markus HS. Diffusion tensor MRI correlates with executive dysfunction in patients with ischaemic leukoaraiosis. *J Neurol Neurosurg Psychiatry*. 2004;75(3):441-447.
4. Patel B, Markus HS. Magnetic resonance imaging in cerebral small vessel disease and its use as a surrogate disease marker. *Int J Stroke*. 2011;6(1):47-59.
5. Moran C, Phan TG, Srikanth VK. Cerebral small vessel disease: a review of clinical, radiological, and histopathological phenotypes. *Int J Stroke*. 2012;7(1):36-46.
6. Greenberg SM, Vernooij MW, Cordonnier C, et al. Cerebral microbleeds: a guide to detection and interpretation. *Lancet Neurol*. 2009;8(2):165-74.
7. Gouw AA, Seewann A, van der Flier WM, et al. Heterogeneity of small vessel disease: a systematic review of MRI and histopathology correlations. *J Neurol Neurosurg Psychiatry*. 2011;82(2):126-35.
8. Fazekas F, Kleinert R, Roob G, et al. Histopathologic analysis of foci of signal loss on gradient-echo T2*-weighted MR images in patients with spontaneous intracerebral hemorrhage: evidence of microangiopathy-related microbleeds. *AJNR Am J Neuroradiol*. 1999;20(4):637-42.
9. Schrag M, McAuley G, Pomakian J, et al. Correlation of hypointensities in susceptibility-weighted images to tissue histology in dementia patients with cerebral amyloid angiopathy: a postmortem MRI study. *Acta Neuropathol*. 2010;119(3):291-302.
10. De Reuck J, Auger F, Cordonnier C, et al. Comparison of 7.0-T T_2*-magnetic resonance imaging of cerebral bleeds in post-mortem brain sections of Alzheimer patients with their neuropathological correlates. *Cerebrovasc Dis*. 2011;31(5):511-7.
11. Ikram MA, van der Lugt A, Niessen WJ, et al. The Rotterdam Scan Study: design and update up to 2012. *Eur J Epidemiol*. 2011;26(10):811-24.
12. Hofman A, van Duijn CM, Franco OH, et al. The Rotterdam Study: 2012 objectives and design update. *Eur J Epidemiol*. 2011;26(8):657-86.
13. Poels MMF, Vernooij MW, Ikram MA, et al. Prevalence and risk factors of cerebral microbleeds: an update of the Rotterdam scan study. *Stroke*. 2010;41(10 Suppl):S103-6.
14. Vernooij M, van der Lugt A, Ikram MA, et al. Prevalence and risk factors of cerebral microbleeds: the Rotterdam Scan Study. *Neurology*. 2008;70(14):1208-14.
15. Wardlaw JM, Smith EE, Biessels GJ, et al. Neuroimaging standards for research into small vessel disease and its contribution to ageing and neurodegeneration. *Lancet Neurol*. 2013;12(8):822-38.
16. De Boer R, Vrooman HA, van der Lijn F, et al. White matter lesion extension to automatic brain tissue segmentation on MRI. *Neuroimage*. 2009;45(4):1151-1161.
17. Song S-K, Sun S-W, Ramsbottom MJ, Chang C, Russell J, Cross AH. Dysmyelination Revealed through MRI as Increased Radial (but Unchanged Axial) Diffusion of Water. *Neuroimage*. 2002;17(3):1429-1436.
18. Koppelmans V, de Groot M, de Ruiter MB, et al. Global and focal white matter integrity in breast cancer survivors 20 years after adjuvant chemotherapy. *Hum Brain Mapp*. 2014;35(3):889-99.
19. Klein S, Staring M, Murphy K, Viergever MA, Pluim JPW. elastix: a toolbox for intensity-based medical image registration. *IEEE Trans Med Imaging*. 2010;29(1):196-205.

20. Leemans A, Jeurissen B, Sijbers J, Jones DK. ExploreDTI: a graphical toolbox for processing, analyzing, and visualizing diffusion MR data. In: *Proceedings 17th Scientific Meeting International Society for Magnetic Resonance in Medicine*.Vol 17.; 2009:3537.
21. Wenham PR, Price WH, Blandell G. Apolipoprotein E genotyping by one-stage PCR. *Lancet*. 1991;337(8750):1158-9.
22. Leening MJG, Kavousi M, Heeringa J, et al. Methods of data collection and definitions of cardiac outcomes in the Rotterdam Study. *Eur J Epidemiol*. 2012;27(3):173-85.
23. Vernooij M, Ikram M, Wielopolski P, Krestin GP, Breteler MMB, van der Lugt A. Cerebral Microbleeds: Accelerated 3D T2*-weighted GRE MR Imaging versus Conventional 2D T2*-weighted GRE MR Imaging for Detection. *Radiology*. 2008;248(1):3-8.
24. Vernooij MW, de Groot M, van der Lugt A, et al. White matter atrophy and lesion formation explain the loss of structural integrity of white matter in aging. *Neuroimage*. 2008;43(3):470-477.
25. Nandigam RNK, Viswanathan A, Delgado P, et al. MR imaging detection of cerebral microbleeds: effect of susceptibility-weighted imaging, section thickness, and field strength. *AJNR Am J Neuroradiol*. 2009;30(2):338-43.
26. Melzer TR, Watts R, MacAskill MR, et al. White matter microstructure deteriorates across cognitive stages in Parkinson disease. *Neurology*. 2013;80(20):1841-9.
27. Hulst HE, Steenwijk MD, Versteeg A, et al. Cognitive impairment in MS: impact of white matter integrity, gray matter volume, and lesions. *Neurology*. 2013;80(11):1025-32.
28. Lawrence AJ, Patel B, Morris RG, et al. Mechanisms of cognitive impairment in cerebral small vessel disease: multimodal MRI results from the St George's cognition and neuroimaging in stroke (SCANS) study. *PLoS One*. 2013;8(4):e61014.
29. Wardlaw JM, Sandercock PAG, Dennis MS, Starr J. Is breakdown of the blood-brain barrier responsible for lacunar stroke, leukoaraiosis, and dementia? *Stroke*. 2003;34(3):806-12.
30. Schreiber S, Bueche CZ, Garz C, Braun H. Blood brain barrier breakdown as the starting point of cerebral small vessel disease? - New insights from a rat model. *Exp Transl Stroke Med*. 2013;5(1):4.
31. Cordonnier C. Brain microbleeds: more evidence, but still a clinical dilemma. *Curr Opin Neurol*. 2011;24(1):69-74.
32. Goos JDC, van der Flier WM, Knol DL, et al. Clinical relevance of improved microbleed detection by susceptibility-weighted magnetic resonance imaging. *Stroke*. 2011;42(7):1894-900.
33. Viswanathan A, Patel P, Rahman R, et al. Tissue microstructural changes are independently associated with cognitive impairment in cerebral amyloid angiopathy. *Stroke*. 2008;39(7):1988-92.
34. Werring DJ, Frazer DW, Coward LJ, et al. Cognitive dysfunction in patients with cerebral microbleeds on T2*-weighted gradient-echo MRI. *Brain*. 2004;127(Pt 10):2265-75.
35. Rosand J, Muzikansky A, Kumar A, et al. Spatial clustering of hemorrhages in probable cerebral amyloid angiopathy. *Ann Neurol*. 2005;58(3):459-62.
36. Smith EE, Gurol ME, Eng JA, et al. White matter lesions, cognition, and recurrent hemorrhage in lobar intracerebral hemorrhage. *Neurology*. 2004;63(9):1606-12.
37. Budde MD, Xie M, Cross AH, Song S-K. Axial diffusivity is the primary correlate of axonal injury in the experimental autoimmune encephalomyelitis spinal cord: a quantitative pixelwise analysis. *J Neurosci*. 2009;29(9):2805-13.
38. Song S-K, Sun S-W, Ju W-K, Lin S-J, Cross AH, Neufeld AH. Diffusion tensor imaging detects and differentiates axon and myelin degeneration in mouse optic nerve after retinal ischemia. *Neuroimage*. 2003;20(3):1714-1722.
39. Song S-K, Yoshino J, Le TQ, et al. Demyelination increases radial diffusivity in corpus callosum of mouse brain. *Neuroimage*. 2005;26(1):132-40.
40. Naismith RT, Xu J, Tutlam NT, Trinkaus K, Cross a H, Song S-K. Radial diffusivity in remote optic neuritis discriminates visual outcomes. *Neurology*. 2010;74(21):1702-10.
41. Klawiter EC, Schmidt RE, Trinkaus K, et al. Radial diffusivity predicts demyelination in ex vivo multiple sclerosis spinal cords. *Neuroimage*. 2011;55(4):1454-60.

4.3

Cerebral small vessel disease affects white matter microstructure in mild cognitive impairment

Human Brain Mapping 2014

Janne M. Papma
Marius de Groot
Inge de Koning
Francesco U. Mattace-Raso
Aad van der Lugt
Meike W. Vernooij
Wiro J. Niessen
John C. van Swieten
Peter J. Koudstaal
Niels D. Prins
Marion Smits

Microstructural white matter deterioration is a frequent finding in mild cognitive impairment (MCI), potentially underlying default mode network (DMN) dysfunctioning. Thus far, microstructural damage in MCI has been attributed to Alzheimer's disease pathophysiology. A cerebrovascular role, in particular the role of cerebral small vessel disease (CSVD), received less interest. Here, we used diffusion tensor imaging (DTI) to examine the role of CSVD in microstructural deterioration within the normal appearing white matter (NAWM) in MCI. MCI patients were subdivided into those with (n = 20) and without (n = 31) macrostructural CSVD evidence on MRI. Using TBSS we performed microstructural integrity comparisons within the whole brain NAWM. Secondly, we segmented white matter tracts interconnecting DMN brain regions by means of automated tractography segmentation. We used NAWM DTI measures from these tracts as dependent variables in a stepwise-linear regression analysis, with structural and demographical predictors. Our results indicated microstructural deterioration within the anterior corpus callosum, internal and external capsule and periventricular white matter in MCI patients with CSVD, while in MCI patients without CSVD, deterioration was restricted to the right perforant path, a tract along the hippocampus. Within the full cohort of MCI patients, microstructure within the NAWM of the DMN fiber tracts was affected by the presence of CSVD. Within the cingulum along the hippocampal cortex we found a relationship between microstructure and ipsilateral hippocampal volume and the extent of white matter hyperintensity. In conclusion, we found evidence of CSVD-related microstructural damage in fiber tracts subserving the DMN in MCI.

Introduction

Mild cognitive impairment (MCI) is a clinical construct that identifies individuals with cognitive impairment at high risk of dementia, in most cases Alzheimer's disease (AD).[1–3] Within the past decades, structural MRI has been used extensively to study this prodromal dementia stage, as it offers the opportunity to identify early structural brain changes in vivo. Numerous studies have identified MCI and ultimately AD related atrophy within the medial temporal lobe, temporal and parietal association regions, the cingulate gyrus and prefrontal cortex.[4–6] Other commonly encountered MRI findings in MCI are white matter hyperintensities (WMH) and lacunar infarcts,[7,8] regarded as macrostructural MRI expressions of cerebral small vessel disease (CSVD). CSVD is a condition that affects

the microvessels supplying the white matter and subcortical brain regions.[9] There is increasing evidence that CSVD and AD pathophysiological changes on MRI do not just coincide but may be interrelated.[7,8,10–14]

Initially, MRI studies largely focused on region of interest analysis,[15,16] while the more current view is that widespread brain regions form interconnected neural networks encompassing multiple distinct brain regions. Research regarding neurodegeneration has therefore lately been more directed at these networks and network connectivity.[17,18] A neural network often studied in MCI and AD is the default mode network.[19–21] This network is known to be affected in several neurodegenerative conditions and thought to play a role in cognitive functions such as episodic memory.[18,22] Within functional networks, intact white matter representing structural connectivity, is very important for normal network functioning.[23,24] This implies that conditions affecting white matter structure can affect neural network functioning.[25,26]

While an assessment of macrostructural white matter deterioration can be obtained by means of T2 weighted Fluid Attenuated Inversion Recovery (T2-FLAIR) MRI, diffusion tensor imaging (DTI) can be used to non-invasively examine white matter damage on a microstructural level. DTI is an MRI technique based on the diffusion properties of unbound water molecules. In the presence of physical boundaries or restrictions diffusion becomes anisotropic, directionally dependent, as water diffuses more rapidly in the direction aligned with an internal structure (axial diffusivity), instead of perpendicular to it (radial diffusivity). DTI measures are considered sensitive markers for white matter microstructural damage, as degradation of axons or demyelination will result in reduced restrictions, increased free diffusion of water, and consequently a decrease in anisotropy. Numerous previous studies have reported decreased fractional anisotropy (FA) and increased random or mean diffusivity (MD) in MCI and AD patients within a diversity of white matter regions, including (para)hippocampal white matter,[27–29] posterior cingulate fasciculus/precuneus white matter,[28,30–32] the cingulum,[28,30,33–35] the corpus callosum,[30,34,36,37] the uncinate fasciculus[28,31,33] and the inferior and superior longitudinal fasciculus.[28,33] The nature of these microstructural white matter changes in MCI or AD patients is still a matter of debate. Some claim that microstructural deterioration is secondary to neuronal – grey matter – loss, so-called Wallerian degeneration.[38] But the frequent co-occurrence of CSVD in AD patients also points towards a role of vascular pathology.[37] Indeed, in MCI, microstructural white matter damage was found to correlate to macrostructural white matter changes such as WMH burden.[37] This relationship, however, was examined within the global white matter without controlling for WMH, like other DTI studies in MCI fail to control for the presence of

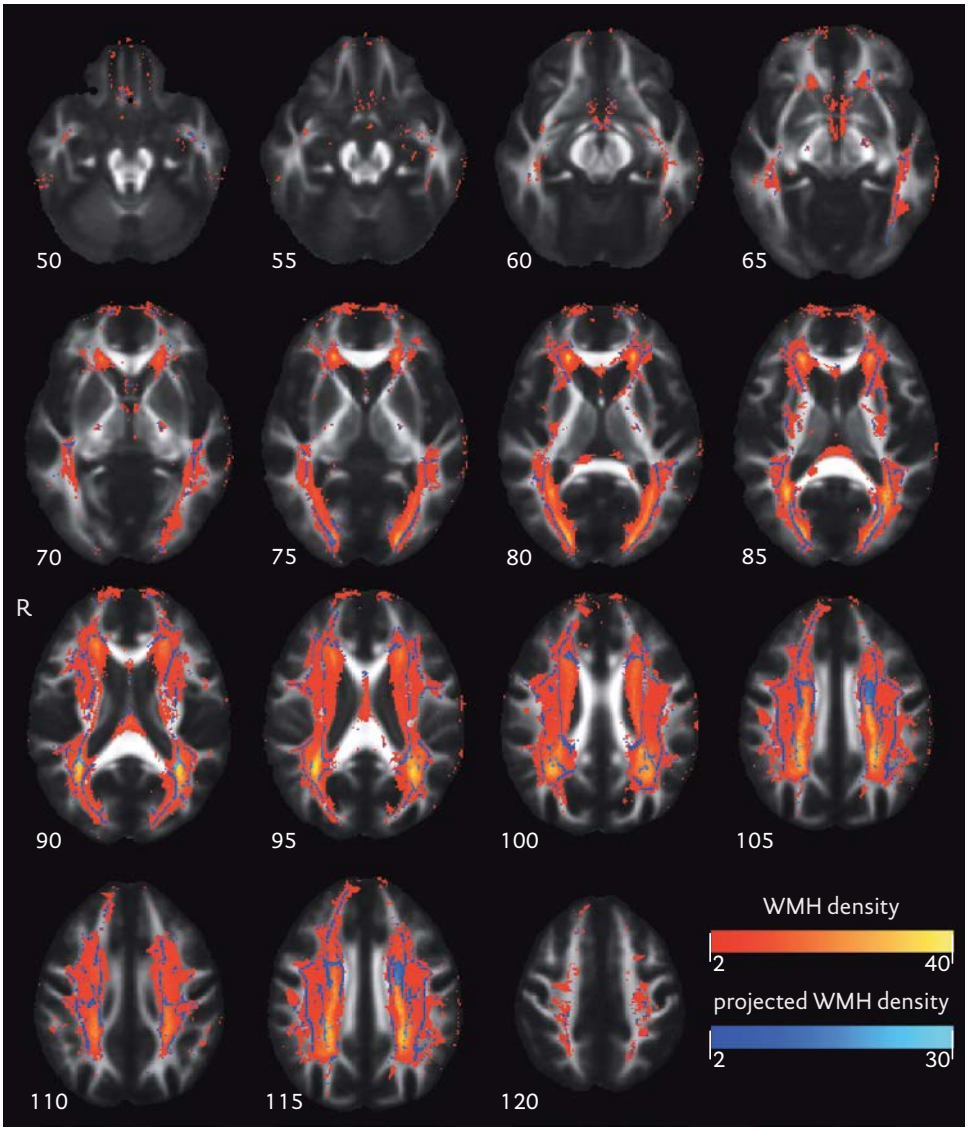

Figure 4.3.1. *TBSS skeleton projections on white mater hyperintensity map in axial planes at different MNI 152 Z-levels, overlaid on the mean FA image of the study participants. White matter hyperintensities range from red to yellow, indicating respectively voxelwise low to high prevalence of white matter hyperintensity. TBSS skeleton projections depicted in a range from dark blue to light blue, indicating respectively low to high prevalence of affected TBSS skeleton voxels.*

WMH as well.[28,30,32,37,39] This is an important issue, as we know that DTI measures differ within WMH regions,[40] and in the NAWM in relationship to the presence and vicinity of WMH.[41,42]

In the present study we aim to gain more insight into mechanisms affecting white matter microstructural integrity in MCI, in particular examining the role of CSVD. For this purpose we used DTI, and to avoid WMH influencing our results as much as possible, we restricted our analyses specifically to the normal appearing white matter (NAWM). We compared NAWM DTI measures in MCI patients with and without CSVD and healthy controls globally, and furthermore examined the role of CSVD as well as structural AD changes in specific white matter tracts known to be important in default mode network functioning.[23,30,43–45]

Methods

Participants

We recruited MCI patients aged 65 years or older, from 2008 onwards, from outpatient clinics of the Departments of Neurology and Geriatrics of the Erasmus MC, University Medical Center Rotterdam, and 7 surrounding hospitals, on the basis of criteria by Petersen.[3] These criteria include: 1) presence of cognitive complaint by patient or relatives; 2) impairment of one or more cognitive domains as determined by neuropsychological assessment; 3) preserved overall general functioning, with possible increased difficulty in the performance of activities of daily living; and 4) absence of dementia according to the DSM-IV or NINCDS-ADRDA criteria for dementia. In total 57 MCI patients were screened for study eligibility. We excluded patients with a previous neurological or psychiatric diagnosis negatively affecting cognition (e.g. major stroke, cerebral tumor or depression) or contraindications for MRI (e.g. pacemaker or claustrophobia). After initial screening, 55 MCI patients underwent a structured interview, physical examination and brain MRI, including 3D T1-weighted, T2-FLAIR MRI and DTI. After MRI examinations we excluded 4 patients, 2 due to physical inability or refusal to undergo MRI when confronted with the MRI scanner, 1 due to incomplete DTI data collection and 1 due to excessive head movement and consequently obvious blurring of the acquired data. Thus, for the present study, data of 51 MCI patients were available. Control subjects (n = 28), aged 65 years or older, were either relatives of MCI patients or were recruited by advertisement (e.g. posters and handouts) throughout the Erasmus MC. Controls did not meet any of the criteria for MCI, but were otherwise excluded on the basis of the same exclusion criteria as MCI patients. Controls underwent the exact same work up as MCI patients in this study. After MRI examinations we excluded 2 control partic-

Table 4.3.1
Characteristics and neuropsychological test results of controls and MCI patients with and without cerebral small vessel disease (N=74)

	Controls (n = 23)	Total MCI group (n = 51)	MCI without CSVD (n = 31)	MCI with CSVD (n = 20)
Age, y	70.9 (5.0)	74.1 (4.9)[a]	73.1 (4.3)	75.7 (5.4)[a]
Sex, women (%)	10 (43)	14 (27)	7 (23)	7 (35)
Education	5.4 (1.2)	5.2 (1.3)	5.0 (1.4)	5.4 (1.2)
MMSE	28.9 (1.1)	27.2 (1.9)[a]	27.0 (2.0)[a]	27.4 (1.8)[a]
Hypertension, prevalence (%)	15 (65)	30 (59)	13 (42)	17 (85)[b]
Smoking, prevalence (%)*	13 (57)	34 (67)	19 (61)	15 (75)
APOE -/ε4, prevalence (%)‡	5 (25)	27 (56)[a]	14 (47)	13 (72)[a]
APOE ε4/ε4, prevalence (%)‡	0 (0)	5 (10)	2 (7)	3 (17)
Memory	0.00 (0.72)	-1.73 (0.65)[a]	-1.70 (0.65)[a]	-1.76 (0.68)[a]
Processing speed	0.00 (0.90)	-0.41 (0.84)	-0.40 (0.84)	-0.43 (0.88)
Executive function	0.00 (0.92)	-0.92 (1.34)[a]	-0.83 (1.22)	-1.07 (1.55)[a]
Language	0.00 (0.75)	-0.98 (1.09)[a]	-1.11 (1.26)[a]	-0.78 (0.76)
Visuospatial ability	0.00 (1.00)	-0.68 (1.54)	-0.41 (1.03)	-0.28 (1.21)
Visuoconstructive ability	0.00 (1.00)	-0.36 (1.08)	-0.56 (1.77)	-0.87 (1.11)

*Values are unadjusted means (standard deviation), number of participants (percentages), or in case of neuropsychological data unadjusted z-score means (standard deviation). MCI: mild cognitive impairment. CSVD: cerebral small vessel disease. MMSE: mini mental state examination. APOE: apolipoprotein E * Prevalence current and former smoking. ‡ missing data for 2 MCI patients with CSVD, 1 MCI patient without CSVD and 3 healthy controls. Differences between groups analyzed by means of independent sample t-test, Chi-Square test, or in case of neuropsychological data ANCOVA corrected for age, sex and education: [a] p <0.05 compared with controls. [b] p <0.05 compared with MCI patients without CSVD.*

ipants on the basis of the quality of DTI imaging, caused by poor positioning of the head in the MRI head coil, and thus 26 controls were included in our study. All participants gave informed consent to the protocol of the study, which was approved by the medical ethics committee of the Erasmus MC.

Structured interview, physical examination

We collected data on demographics, medical history, and vascular risk factors during a structured interview. Level of education was assessed with a Dutch education scale, ranging from 1 (less than 6 years elementary school) to 7 (academic degree).[46] As measured twice during physical examination, we defined hypertension as systolic blood pressure ≥ 160 mm Hg or diastolic blood pressure ≥ 90 mm Hg, or

the use of antihypertensive medication. We determined *Apolipoprotein E* (*APOE*) genotype in all participants. The mini mental state examination (MMSE) was employed as a global cognitive screening method, and indicator for disease severity.[47]

Neuropsychological assessment

Extensive neuropsychological assessment was used both in the definition and diagnosis of MCI patients. Trained neuropsychologists administered tests covering cognitive domains including episodic memory functioning (15-word verbal learning test and the stories of the Rivermead Behavioural Memory Test), processing speed (Trail Making Test (TMT) part A and Stroop II), executive functioning (TMT part B and Stroop III), language (Boston Naming Test 60 items version and semantic fluency tasks, animals and occupations), visuospatial ability (Block Design of the Wechsler Adult Intelligence Scale III) and visuoconstructive ability (clock drawing, 14 points). For every neuropsychological test we calculated z-scores, using the mean and standard deviation of the control group (z-score = individual test score minus mean of controls, divided by standard deviation of controls), and subsequently constructed compound scores by averaging z-scores for all cognitive domains. Visuospatial and visuoconstructive ability were represented by a single neuropsyhological test. The Stroop and TMT are cognitive tests in which a higher score indicates worse performance; therefore we multiplied all individual z-scores for these tests with -1.

MRI acquisition

We performed MR imaging on a 3.0 T MRI scanner with an 8-channel head coil (HD platform, GE Healthcare, Milwaukee, WI, US). DTI data were acquired in the axial plane with a single shot echo-planar imaging (EPI) sequence with 25 non-collinear directions and the following parameters: repetition time (TR) = 14,200 ms, echo time (TE) = 73.3 ms, acquisition matrix 128 × 64 (phase encoding, A-P direction), field of view (FOV) 220 × 220 mm^2, flip angle = 90°. Maximum b-value was 1000 s/mm^2 and three volumes were acquired without diffusion weighting (b-value = 0 s/mm^2). We acquired 70 contiguous slices with a slice thickness of 2.0 mm in a total acquisition time of 7:06 min. High resolution 3D T1-weighted structural MRI was acquired in the axial plane with the following parameters: TR = 10.4 ms, TE = 2.1 ms, TI = 300 ms, flip angle = 18°, acquisition matrix = 416 × 256, FOV = 250 × 175 mm^2. In a total acquisition time of 4:57 min, we acquired 192 slices with a slice thickness of 1.6 mm and 0.8 mm overlap, resulting in an effective slice thickness of 0.8 mm. T2-FLAIR images were obtained with the following parameters: TR = 8,000 ms, TE

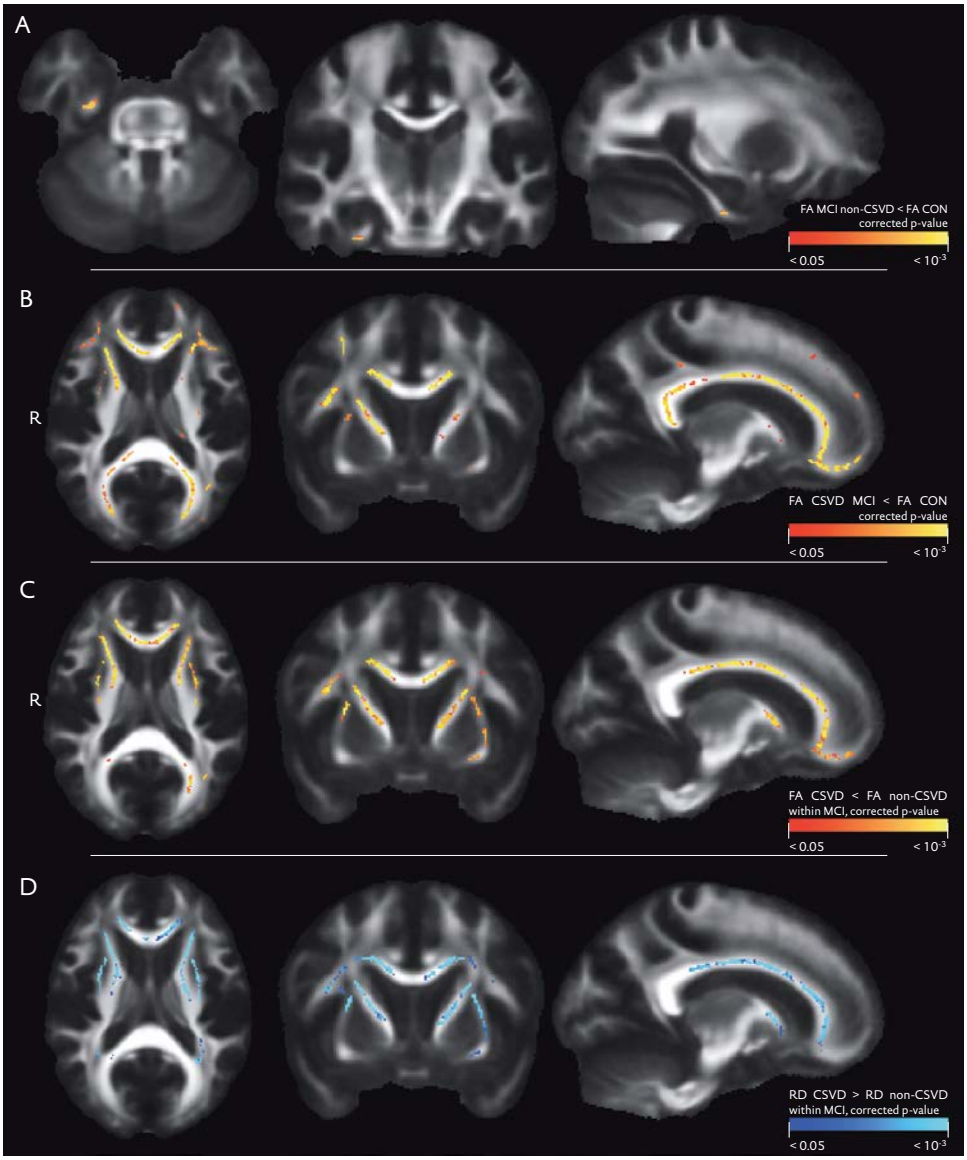

Figure 4.3.2. *A) Significantly lower FA in MCI patients without CSVD relative to controls. B) Significantly lower FA in MCI patients with CSVD relative to controls. C) Significantly lower FA in MCI patients with CSVD relative to MCI patients without CSVD. D) Significantly higher perpendicular diffusivity in MCI patients with CSVD relative to MCI patients without CSVD.*

= 120 ms, TI = 2000 ms, acquisition matrix = 256 × 128, FOV = 210 × 210 mm^2. We acquired 64 contiguous slices with a slice thickness of 2.5 mm in a total acquisition time of 3:13 min.

Visual assessment of WMH and lacunar infarcts

Blinded for all clinical information, a neurologist (NDP), experienced in the assessment of CSVD on MRI, examined 3D T1-weighted and T2-FLAIR MRI images for the presence of lacunar infarcts and WMH. The extent of WMH was assessed using the semi-quantitative rating scale of Fazekas.[48] This rating scale is used extensively in clinical practice. In line with the definition of CSVD on MRI used in previous studies,[49] we defined the presence of CSVD as the presence of substantial WMH (Fazekas score 2 or higher) affecting both the posterior and anterior white matter regions and/or the presence of two or more lacunar infarcts. Based on these ratings we classified MCI patients as MCI patients with CSVD (n = 20) and MCI patients without CSVD (n = 31). In addition, we excluded three control subjects, as they met the criteria for CSVD on MRI, eventually including 23 controls without CSVD on MRI in our analyses. Although available (see below), we did not make use of automated brain tissue segmentation and volumetric analysis of WMH for this subdivision, as these ratings are highly dependent upon the studied cohort and therefore difficult to translate to clinical practice or compare to previous studies.

Automated MRI brain tissue segmentation and volumetric analysis of WMH and hippocampi

Based on the intensities of the 3D T1-weighted and T2-FLAIR MRI scans we used a validated k-nearest neighbour classifier to automatically segment brain tissue into cerebrospinal fluid, grey matter, normal appearing white matter and WMH.[50,51] We refer to Figure 4.3.1 for the distribution of WMH in all participants. We segmented hippocampi on the basis of the 3D T1-weighted images by means of an automated method as described previously.[52,53] Briefly, the two most important components of this method are a statistical intensity model and a spatial probability map. The intensity model describes the typical intensities of the hippocampus and the background. The spatial probability map is derived from the registration of multiple atlases and contains the probability of being part of the hippocampus for every voxel. In a comparison with manually traced hippocampal volumes, this method produced accurate results with a mean Dice similarity index of 0.867.[54] Blinded for clinical

information, all automated segmentations were visually inspected and if necessary, we manually corrected the segmentations using FSLview, part of FSL.[55] Finally, we assessed total intracranial volume (TIV).

DTI data processing

As a first step in DTI processing, we corrected diffusion data for motion and Eddy currents by affine co-registration of the diffusion weighted volumes to the average b=0 s/mm^2 volume. These registrations were performed using Elastix, an open source ITK based registration package.[56] The rotation component of each transformation was used to realign the gradient vector for each diffusion-weighted volume to compensate for motion during the acquisition.[57] Then, resampling of the transformed diffusion weighted images was performed at an isotropic resolution of 1.0 mm for the tensor fit, and 2.0 mm for the probabilistic tractography. For masking out non-brain tissue, we used a multi-atlas approach, which showed increased robustness against masking errors. This approach consists of three steps. First, we used the Brain Extraction Tool (BET)[58] from FSL 4.1.9, to identify brain tissue in three random subjects, and manually corrected the resulting masks using FSLview. Second, the corrected masks were transformed to individual subject space using a nonlinear co-registration of the b=0 s/mm^2 volumes obtained with Elastix (three registrations per subject). Third, majority voting on the three transformed brain masks was used to obtain a final brain mask for each individual, which was then used to mask the diffusion data. We fitted diffusion tensors with a Levenberg-Marquard non-linear least squares optimization algorithm, available in ExploreDTI, on the 1.0 mm data. The eigenvalues of the fitted diffusion tensors were used to provide measures of FA, MD, axial diffusivity (AxD, or λ_1, the principal eigenvalue), and radial diffusivity (RD, the mean of the two smallest eigenvalues). The 2.0 mm data were used to fit a probabilistic model of fiber orientations for each voxel by means of Bedpostx.[59] Afterwards, data quality was examined through visual inspection of axial FA slices 4 mm apart, combined with two coronal and two sagittal slices around the center of the brain.

DTI data analysis

To examine the role of CSVD in white matter microstructural damage in MCI, we used several DTI analysis techniques. All analyses were restricted to the NAWM by mapping the individual WMH segmentation masks, as obtained from automated tissue segmentation, to the DTI data and thus excluding voxels originating from WMH.[42] The first analysis technique involved examining DTI measures within the

Table 4.3.2
MRI characteristics for controls and MCI patients with and without cerebral small vessel disease

	Controls (n = 23)	Total MCI group (n = 51)	MCI without CSVD (n = 31)	MCI with CSVD (n = 20)
WMH, Fazekas score*	1 (0; 1)	1 (1; 2)[a]	1 (0; 1)	2 (2; 2)[a,b]
Lacunar infarcts, presence (%)	2 (7.7)	12 (23.5)	3 (9.7)	9 (45.0)[a,b]
TIV, ml	1085.6 (88.4)	1123.7 (134.3)	1131.7 (122.2)	1111.3 (153.7)
Grey matter, ml	445.9 (56.9)	453.8 (69.2)	462.7 (60.8)	439.9 (80.5)
White matter, ml	415.9 (38.2)	402.8 (51.4)[a]	412.3 (49.2)	387.9 (52.4)[a]
WMH, ml*	13.1 (10.6, 21.4)	19.9 (14.1, 30.7)[a]	16.0 (10.5, 19.9)	33.8 (25.7, 50.4)[a,b]
Left hippocampus, ml	3.13 (0.40)	2.78 (0.53)[a]	2.76 (0.51)[a]	2.80 (0.57)
Right hippocampus, ml	3.05 (0.41)	2.80 (0.42)[a]	2.80 (0.43)[a]	2.81 (0.42)[a]
FA NAWM whole brain	0.39 (0.02)	0.38 (0.02)	0.38 (0.02)	0.37 (0.02)[a,b]
MD NAWM whole brain	0.95 (0.03)	0.99 (0.10)	0.99 (0.12)	0.99 (0.08)
AxD NAWM whole brain	1.37 (0.03)	1.41 (0.16)	1.42 (0.19)	1.38 (0.09)
RD NAWM whole brain	0.74 (0.04)	0.79 (0.08)	0.78 (0.09)	0.79 (0.07)

*Values are unadjusted means (standard deviation); or number of participants (percentages). * Median (interquartile range). MCI: mild cognitive impairment. CSVD: cerebral small vessel disease. TIV: total intracranial volume. WMH: white matter hyperintensities. NAWM: normal appearing white matter. NAWM whole brain measurements within the cerebral NAWM mask. WMH whole brain measurements within the cerebral WMH mask. MD, AxD and RD $\times 10^{-3}$ mm^2/s. Differences between groups analyzed by means of ANCOVA corrected for age and sex, Mann-Whitney U test or Chi Square tests: [a] $p < 0.05$ compared with controls. [b] $p < 0.05$ compared with MCI patients without CSVD.*

global NAWM (see 'DTI data analysis: global NAWM measurements'). The second analysis technique included a whole brain explorative framework of Tract Based Spatial Statistics (TBSS, see 'DTI data analysis: Tract Based Spatial Statistics'), to gain insight into the spatial distribution of white matter microstructural abnormalities related to CSVD in MCI patients. The third analysis technique we used was probabilistic tractography (see 'DTI data analysis: probabilistic tractography'), by which we considered specific white matter tracts which are found to subserve normal default mode network functioning, i.e. the cingulum in the cingulate cortex (CGC), the cingulum along the hippocampal cortex (CGH) and the superior longitudinal fasciculus (SLF).[23,43–45] In addition we included tracts that were found to be significantly affected in the whole brain TBSS analysis, as well as a control tract: the middle cerebellar peduncle (MCP). A control tract is a tract that remains unaffected by the disease process, in our case AD or CSVD.[31,60] We extracted all tracts for every individual, and performed between group comparisons of DTI measures as well as regression analysis with DTI measurements within the NAWM of tracts as dependent variable. All of the above described between group analyses were corrected for the effects of age and sex.

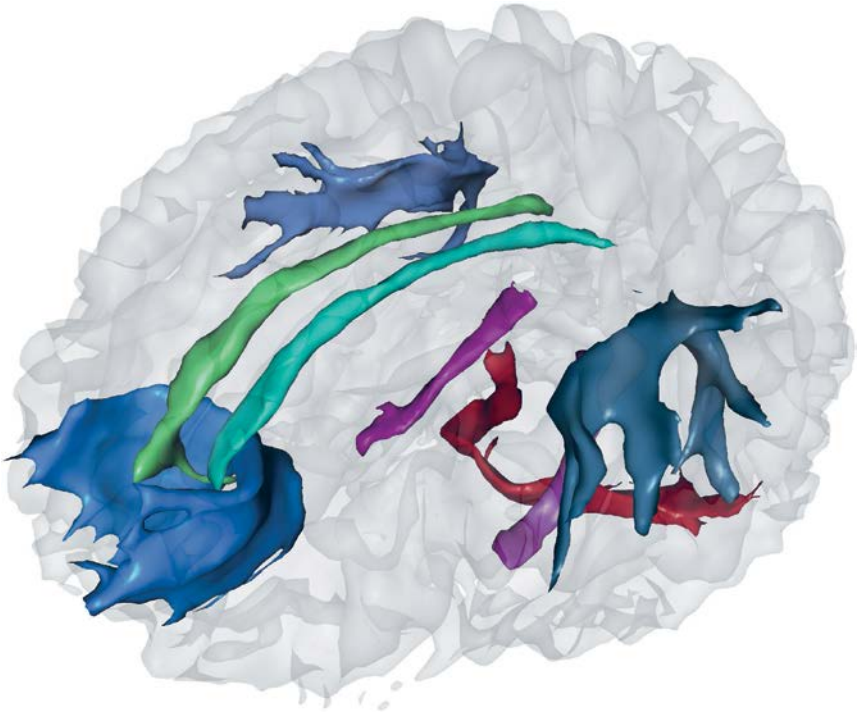

Figure 4.3.3. *Probabilistic tractography of tracts of interest and control tract in a single subject, blue: forceps minor; light and dark green: left and right cingulum cingulate part; light and dark purple: left and right cingulum hippocampus part; light and dark grey: left and right superior longitudinal fasciculus; red: middle cerebellar peduncle.*

DTI data analysis: global NAWM measurements

T1-weighted images were co-registered to the individuals' FA images using an affine registration with mutual information as similarity metric by means of FLIRT.[61] We averaged DTI measures, FA, MD, AxD and RD within the whole brain NAWM, using the tissue segmentation masks created in the automated MRI brain tissue segmentation in diffusion space, and subsequently compared these measures between groups.

DTI data analysis: Tract Based Spatial Statistics

For the TBSS analysis,[62] we followed the default pipeline. In short, individual subjects' FA images were co-registered to an FA template in standard MNI space. Next, a mean FA image was created and thinned to obtain a mean FA skeleton which rep-

resented the center of all tracts common to the entire group. We thresholded the white matter skeleton image at an FA value of 0.2 to constrain the analyses to those tracts that could reliably be identified. FA measurements were projected onto the white matter skeleton by searching the maximum FA value in a region perpendicular to the skeleton. This projection was performed in every skeleton voxel. MD, AxD and RD values and WMH status were then projected onto the white matter skeleton, using the same projection as for the FA. Hereafter, we performed voxelwise group comparisons while regressing out the linear effects of age and sex. All statistical analyses were corrected for multiple comparisons using 5,000 permutations in Randomise as available in FSL. We implemented the WMH exclusion by supplying voxelwise NAWM status masks per group to Randomise. Spatial clustering of results was performed with TCFE.[63]

DTI data analysis: probabilistic tractography

We performed automated probabilistic tractography in subject native space by means of Probtrackx, available in FSL. For these analyses we used standard space seed, target, stop and exclusion masks, which were based on protocols described by Mori et al.,[64] Stieltjes et al.,[65] Wakana et al.,[66] and Wakana et al.[67] The masks were transferred to subject-native space using a nonlinear registration obtained with default settings for FA images in FNIRT.[68] As mentioned before, tractography was performed for the CGC, CGH, SLF and MCP. As the TBSS group statistics indicated that the genu of the corpus callosum was particularly affected in MCI patients with CSVD, we also extracted the forceps minor (FMI), the most prominent white matter tract within the genu of the corpus callosum, as an additional tract of interest. The tract density image for each tract was normalized by division with the total number of fiber paths recorded in the tract density image. These images were then thresholded at 0.005 to yield binary segmentations. Tracts that could not be identified using the automated protocols were treated as missing values. Individual diffusion measurements were averaged within the NAWM, i.e. excluding voxels that were classified as WMH. Mean FA, MD, AxD and RD, resulting from the tractography-based segmentations were compared between groups.

Statistical analysis

We compared demographics, neuropsychological data and imaging measures between groups using the statistical package SPSS (version 17.0 for Windows, Chicago, IL, US). Imaging and neuropsychological data comparisons were corrected for age, sex, and in case of neuropsychological data, education. Differences between groups

on continuous variables were assessed with ANOVA or ANCOVA and post hoc two sample t-tests. We compared non-parametric data using Kruskal-Wallis, followed by Mann-Whitney *U* tests. Between group analyses of nominal variables were performed by means of Pearson Chi-square tests. To disentangle the role of CSVD in microstructural white matter damage in MCI, we performed a stepwise linear regression analysis within the full cohort of MCI patients, with DTI measures within the NAWM of 1) 'tracts of interest' as obtained with probabilistic tractography, and 2) within the whole brain, as dependent variables. 'Tracts of interest' were defined as the DTI measures within the segmented tracts that were found to show subtle differences between controls and the full cohort of MCI patients ($p<0.10$, without correction for multiple comparisons, represented as bold and italic numbers in Table 4.3.3). Independent variables in the stepwise linear regression analysis were: WMH volume in ml (log transformed), presence of lacunar infarcts, TIV in ml, grey matter volume in ml, white matter volume in ml, left and right hippocampal volume in ml, age, sex, education and the MMSE score as a measure of disease severity. We considered the model that predicted the most variance in the dependent variable. In all analyses a *p*-value <0.05 was considered statistically significant.

Results

Participant characteristics and neuropsychological data

Characteristics and neuropsychological data of MCI patients and controls are presented in Table 4.3.1. In comparison with controls, MCI patients with CSVD were on average 4.8 years older (age range controls: 65.4-83.8 years; age range MCI patients without CSVD: 65.9-81.0 years; age range MCI patients with CSVD: 68.4-88.1 years), and showed a higher prevalence of *APOE4* genotyping (prevalence in 72% of MCI with CSVD cases, and in 25% of control cases). MCI patients with CSVD more often had hypertension compared with MCI patients without CSVD (respectively, prevalence in 85% and 42%). Summarizing the neuropsychological data, MCI patients with and without CSVD showed a cognitive profile of prominent memory impairment, dysexecutive functioning and language problems, when compared to controls. In addition, MCI patients without CSVD showed impairment of processing speed. There were no differences in cognition between MCI patient groups.

Table 4.3.3

Tract volumes and DTI measures within tracts of interest as extracted by means of probabilistic tractography

Tracts	FA				MD				AxD				RD			
	Controls	Total MCI	MCI without CSVD	MCI with CSVD	Controls	Total MCI	MCI without CSVD	MCI with CSVD	Controls	Total MCI	MCI without CSVD	MCI with CSVD	Controls	Total MCI	MCI without CSVD	MCI with CSVD
CGC l	0.51 (0.03)	0.50 (0.04)	0.51 (0.04)	0.48 (0.03)	1.53 (0.06)	0.95 (0.06)	0.94 (0.06)	0.95 (0.06	1.53 (0.06)	1.54 (0.10)	1.55 (0.09)	1.52 (0.13)	0.63 (0.04)	0.65 (0.06)	0.64 (0.05)	0.67 (0.05)
CGC r	0.48 (0.04)	***0.47 (0.04)***[b]	0.48 (0.04)	0.46 (0.04)	1.51 (0.07)	0.95 (0.07)	0.96 (0.06)	0.95 (0.09	1.51 (0.07)	1.49 (0.11)	1.51 (0.09)	1.46 (0.13)	0.66 (0.05)	0.68 (0.06)	0.68 (0.06)	0.69 (0.07)
CGH l	0.38 (0.03)	***0.36 (0.03)***[b]	0.37 (0.03)	0.35 (0.03)	1.44 (0.06)	***1.06 (0.08)***[a]	1.06 (0.09)	1.07 (0.06	1.44 (0.06)	1.49 (0.11)	1.49 (0.12)	1.48 (0.10)	0.79 (0.06)	***0.85 (0.08)***[a]	0.84 (0.08)	0.86 (0.06)
CGH r	0.40 (0.03)	***0.38 (0.03)***[b]	0.38 (0.03)	0.38 (0.04)	1.46 (0.06)	***1.06 (0.08)***[a]	1.05 (0.08)	1.08 (0.09	1.46 (0.06)	1.51 (0.11)	1.50 (0.11)	1.53 (0.10)	0.77 (0.06)	***0.83 (0.08)***[a]	0.82 (0.07)	0.85 (0.09)
SLF l	0.49 (0.02)	0.48 (0.03)	0.49 (0.03)	0.47 (0.04)	1.43 (0.05)	0.92 (0.06)	0.90 (0.06)	0.95 (0.07	1.43 (0.05)	1.44 (0.09)	1.43 (0.08)	1.46 (0.10)	0.64 (0.03)	0.66 (0.06)	0.64 (0.05)	0.69 (0.06)
SLF r	0.48 (0.03)	0.47 (0.03)	0.48 (0.03)	0.46 (0.03)	1.44 (0.05)	0.93 (0.07)	0.92 (0.06)	0.95 (0.07	1.44 (0.05)	1.45 (0.10)	1.44 (0.09)	1.47 (0.11)	0.65 (0.04)	0.68 (0.06)	0.66 (0.06)	0.70 (0.05)
FMI	0.55 (0.03)	***0.51 (0.04)***[a]	0.53 (0.03)	0.49 (0.04)	1.65 (0.05)	1.01 (0.07)	0.99 (0.07)	1.02 (0.08	1.65 (0.05)	1.66 (0.10)	1.66 (0.10)	1.65 (0.11)	0.63 (0.05)	0.68 (0.07)	0.66 (0.06)	0.71 (0.08)
MCP	0.52 (0.04)	0.53 (0.04)	0.52 (0.05)	0.54 (0.04)	1.59 (0.11)	1.00 (0.12)	1.01 (0.13)	0.98 (0.09	1.59 (0.11)	1.63 (0.15)	1.64 (0.15)	1.61 (0.13)	0.68 (0.07)	0.69 (0.12)	0.70 (0.13)	0.66 (0.08)

Values are unadjusted means (standard deviation). MD, AxD, RD ×10^{-3} mm^2/s. Differences between the total MCI patient group and controls were analyzed by means of ANCOVA corrected for age and sex: [a] p <0.05 in comparison with controls. [b] p <0.10 in comparison with controls. Bold and italic numbers represent those tracts and DTI measures that were subsequently selected for stepwise regression analyses. CGC indicates cingulate gyrus part of cingulum, CGH parahippocampal part of cingulum, SLF superior longitudinal fasciculus, FMI forceps minor, MCP middle cerebellar peduncle.

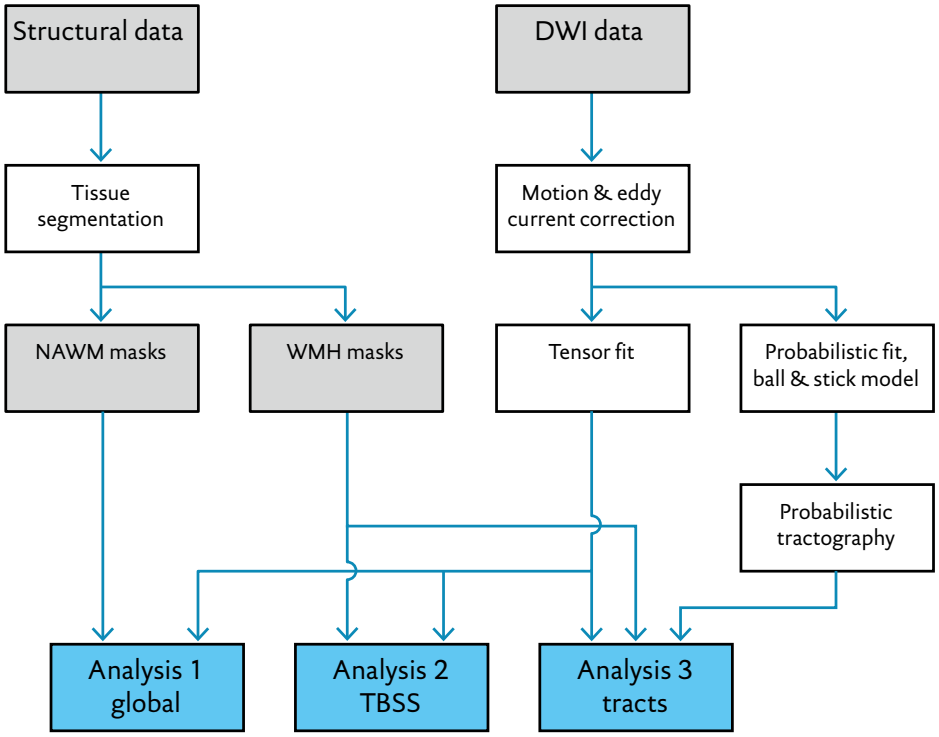

Figure 4.3.4. *Analysis steps of DTI data.*

MRI characteristics

After correction for age and sex, MCI patients with CSVD by definition more often had lacunar infarcts and more severe WMH burden, as reflected by higher Fazekas scores and higher WMH volume, compared with controls as well as MCI patients without CSVD (Table 4.3.2). Relative to controls, both MCI patient groups showed significant lower hippocampal volumes, with no differences between MCI patients with and without CSVD. MCI patients with CSVD showed significantly lower FA of the global NAWM compared with controls as well as MCI patients without CSVD (Table 4.3.2).

Tract-based spatial statistics

After correction for age and sex, analyses within the NAWM-skeleton showed no differences for MD, AxD or RD in MCI patients relative to controls, but decreased FA in the right perforant path. This difference was driven by MCI patients with-

out CSVD, as they showed a significant FA decrease in the same region in comparison with controls (Figure 4.3.2 A). Relative to controls, MCI patients with CSVD showed decreased FA and increased RD in the genu of the corpus callosum (CC), the bilateral internal and external capsule as well as periventricular white matter regions (Figure 4.3.2 B). Compared with MCI patients without CSVD, MCI patients with CSVD showed even more pronounced decreased FA (Figure 4.3.2 C) and increased RD (Figure 4.3.2 D) in these same regions.

Automated probabilistic tractography

The automated segmented tracts are shown in Figure 4.3.3. Not all selected white matter tracts could be identified with the automated probabilistic tractography approach, as the left and right CGC were identified in 60 out of 74 participants. All other tracts were identified in all subjects. Table 4.3.3 summarizes the DTI measures within the extracted tracts' NAWM. The primary goal of this table was to use it as a signal detection tool to select those tracts and DTI measures that showed subtle differences between the total MCI patient group and controls ($p<0.10$, without correction for multiple comparisons, represented as bold and italic numbers in Table 4.3.3). None of the comparisons between the control group and the total MCI group were significant using a Bonferroni multiple comparisons correction (32 comparisons for FA, MD, AxD and RD; controls vs. total MCI group).

Regression analyses of tracts of interest and whole brain NAWM

We analyzed the predictive value of several determinants on white matter microstructure within the full cohort of MCI patients. The analyses for the tracts of interest were restricted to tracts and DTI measures that differed ($p <0.10$) between the full cohort of MCI patients and controls (bold and italic numbers in Table 4.3.3). For the left and right CGH, left and right hippocampal volume respectively were the most important determinants for FA and RD, with WMH volume as second most important determinant in left CGH FA and RD (Table 4.3.5). In these tracts lower hippocampal volumes and higher WMH volume were associated with lower FA and higher RD values (Table 4.3.5). Within the FMI, WMH volume was the most important determinant for FA, followed by age. In this tract, higher WMH volume and higher age were associated with lower FA values. The stepwise regression analyses within the whole brain NAWM showed that WMH volume and left hippocampal volume were significant predictors of FA within whole brain NAWM, and age at scan for RD within whole brain NAWM.

Discussion

In the present study we examined the role of CSVD, represented by the extent of WMH and the presence of lacunar infarcts, in white matter microstructure deterioration in MCI. We found microstructural changes in several NAWM regions throughout the brain in MCI patients with CSVD as compared with controls and MCI patients without CSVD. Moreover, the presence of macrostructural manifestations of CSVD on MRI in patients with MCI was found to be one of the most important determinants of microstructural deterioration within the NAWM of fiber tracts interconnecting several brain regions involved in the default mode network, as well as within the whole brain NAWM.

Strengths of the present study are first, that all our analyses were restricted to the NAWM. As it is known that the white matter microstructure is affected in WMH regions,[40] global white matter analyses would be biased by WMH load. Second, the subdivision of MCI patients into MCI patients with and without CSVD was based on a semi-quantitative rating scale often used in clinical practice.[48] Therefore, our results can easily be translated to common clinical practice and other studies. While this is an important advantage of the use of this rating scale, it has to be noted that WMH on FLAIR MRI are recently found to represent the tail of a continuous distribution of white matter damage,[41,69] and dichotomization of CSVD on the basis of visually appreciable WMH can therefore be questionable. A final strength of this study was the fact that we used several advanced DTI post processing techniques as well as automated MRI tissue segmentation. By using an automated tractography procedure based on standard masks, we avoided the subjectivity and reproducibility issues of manually drawing and placing ROIs as a starting point for tractography. A limitation of our study is the lack of information on biomarkers reflecting amyloid β in our MCI population, as suggested by Albert et al.[1] While this information may have aided in our knowledge of etiology in our clinical cohort of MCI patients, the use of particularly amyloid positron emission tomography in a clinical setting is hampered by the fact that it still requires further longitudinal research, and is not widely available for clinical practice. The information we have on *APOE4* status in the MCI patient groups is difficult to interpret, as prevalence is higher in MCI patients with CSVD as compared with MCI patients without CSVD (respectively 72% and 47%). This can be explained by the fact that *APOE4* status is associated with AD pathophysiology as well as arteriosclerosis[70] and cerebral infarction.[71] The role of *APOE4* in vascular or mixed (AD and vascular) conditions however, has yet to be further elucidated. Another limitation is the age difference between controls and MCI patients, as a result of our inclusion method. Although control subjects had to be at least 65 years of age, they were not specifically age or sex matched with MCI patients. While we expect that we have dealt with this potential problem by

Table 4.3.4
Tract volumes and percentages of WMH per tract in controls and MCI patients

	Tract Volumes				% WMH per tract			
Tracts	Controls	Total MCI	MCI without CSVD	MCI with CSVD	Controls	Total MCI	MCI without CSVD	MCI with CSVD
CGC l	1490.3 (302.4)	1474.4 (230.3)	1465.6 (263.2)	1492.0 (152.2)	0.02 (0.06)	0.06 (0.20)	0.04 (0.18)	0.10 (0.24)
CGC r	1392.8 (228.1)	1404.1 (262.3)	1412.3 (274.8)	1388.9 (246.4)	0.01 (0.05)	0.20 (0.82)	0.01 (0.03)	0.56 (1.34)
CGH l	1362.9 (225.4)	1367.8 (268.0)	1349.8 (244.7)	1395.8 (305.0)	0.18 (0.27)	0.41 (0.92)	0.23 (0.48)	0.70 (1.32)
CGH r	1345.0 (190.0)	1344.4 (235.7)	1308.4 (243.7)	1400.3 (216.8)	0.09 (0.11)	0.39 (0.70)	0.22 (0.31)	0.66 (1.01)
SLF l	4416.4 (478.4)	4279.7 (815.0)	4512.2 (760.4)	3919.4 (781.3)	1.61 (1.95)	5.69 (10.50)	1.52 (1.67)	12.16 (14.6)
SLF r	4087.6 (533.6)	3986.0 (795.5)	4096.1 (731.4)	3815.5 (877.8)	1.68 (2.18)	6.02 (11.3)	1.41 (1.61)	13.15 (15.67)
FMI	6813.9 (948.1)	6040.9 (1184.8)	6235.3 (1005.1)	5739.5 (1393.5)	0.73 (0.87)	0.19 (0.40)	0.61 (0.56)	3.78 (5.84)
MCP	4102.9 (923.4)	3709.4 (1044.8)	3585.1 (1132.6)	3902.0 (885.0)	0.00 (0.00)	0.00 (0.00)	0.00 (0.00)	0.00 (0.00)

Values are unadjusted means of tract volumes in mm^3, or mean percentages (standard deviation); refer to Table 4.3.3 for tract abbreviations.

regressing out the effects of age and sex in all between group analyses, there is a possibility that there are still residual confounding effects of age. A final possible limitation is the use of relatively new analysis techniques like probabilistic tractography, as there are no gold standards yet for these advanced methods. For example, we made use of a threshold of 0.005 on the basis of apparent similarity between the resulting masks and delineations as obtained with deterministic tractography protocols of Mori et al.,[64] Stieltjes et al.,[65] Wakana et al.[66] and Wakana et al.[67] While we have to aknowledge that this may affect our segmentation results, it is important to note that probabilistic tractography is less constrained by thresholds on the diffusion measurements than deterministic tractography approaches, which adds to its robustness.

In MCI patients with CSVD we found damage of the NAWM microstructure in several WM regions throughout the brain, namely within the genu of the corpus callosum, the internal and external capsule bilaterally and periventricular white matter regions. These findings are in line with a recent DTI study of patients with subcortical ischemic vascular dementia, in which the same fiber tracts were found to be affected,[36] Our findings furthermore suggest that NAWM microstructural changes are associated with the presence of CSVD in MCI, which is in line with studies in healthy elderly,[42,72] and in diseased elderly.[41] Most previous DTI studies in MCI however failed to control for WMH load or any other expression of CSVD on MRI,[28,30,32,37,39] and subsequently attribute findings of widespread microstructural damage to AD-related neurodegeneration.[30,37,73] Even though it was shown that the widespread pattern of white matter deterioration cannot be explained by grey matter atrophy.[74] In line with a recent study of De Groot et al.,[69] we would suggest that

Table 4.3.5
Results of the stepwise regression model in tracts of interest and whole brain NAWM

Dependent variable	Predictors	β Value	p Value
FA CGC r	1. White matter volume	0.638	<0.001
FA CGH l	1. Left hippocampal volume	0.53	<0.001
	2. WMH volume	-0.327	0.012
FA CGH r	1. Right hippocampal volume	0.392	0.005
FA FMI	1. WMH volume	-0.492	<0.001
	2. Age at time of scan	-0.343	0.004
MD CGH l	1. Age at time of scan	0.385	0.006
MD CGH r	–	–	–
RD CGH l	1. Left hippocampal volume	-0.521	<0.001
	2. WMH volume	0.383	0.003
RD CGH r	1. White matter volume	-0.810	0.003
	2. TIV volume	0.597	0.035
FA whole brain NAWM	1. WMH volume	-0.493	<0.001
	2. Left hippocampal volume	0.260	0.049
MD whole brain NAWM	–	–	–
AxD Whole brain NAWM	–	–	–
RD whole brain NAWM	1. Age at time of scan	0.328	0.019

Significant predictors in a stepwise regression model. WMH: white matter hyperintensity. TIV: total intracranial volume; refer to Table 4.3.3 for tract abbreviations. Volumes in ml. Beta values are standardized coefficients.

the changes in the NAWM microstructure specifically found in MCI patients with CSVD and not in those without CSVD represent an early stage of vascular damage preceding the development of macrostructural lesions in the NAWM.[41,72,75,76]

Relative to controls, MCI patients without CSVD showed microstructural deterioration within the right perforant path, a fiber tract connecting the entorhinal cortex and the hippocampus,[77] thought to play an important role in the limbic system.[78] This finding within a group of MCI patients with a clinical, cognitive and pathophysiological profile of early AD without any macrostructural and clinical signs of vascular interference is in line with other DTI studies in MCI and AD, that reported either anterior temporal lobe microstructural damage, or specific perforant path deterioration.[29,79,80] Moreover, Damoiseaux et al.[79] found DTI changes in AD confined to the anterior temporal lobe in a whole brain TBSS analysis, when explicitly excluding subjects with macrostructural white matter abnormalities on MRI. Our results are furthermore consistent with current knowledge of neuropathological processes in AD,[81] in which the entorhinal cortex, hippocampus and other regions in the medial temporal lobe are known to be affected early in the disease process.

There is much debate concerning the pathophysiology underlying white matter abnormalities in MCI. One theory states that microstructural changes occur as a process secondary to grey matter atrophy, so-called Wallerian degeneration.[38,73] Changes in CGH microstructural integrity were for example found to be related to atrophy of the hippocampal formation.[82,83] Another theory focuses on the role of microvascular changes in white matter pathology, i.e. a process directly affecting the white matter.[73] Within the full cohort of MCI patients we found a relationship between CGH microstructure and ipsilateral hippocampal volume as well as the presence and extent of macrostructural manifestations of CSVD, in terms of WMH and lacunar infarcts. These results suggest that default mode network associated fiber tracts may be damaged in MCI as the consequence of both grey matter related Wallerian neurodegenerative and vascular effects. In the present study though, other fiber tracts thought to be important in default mode network functioning were found only to be affected in MCI patients with CSVD, even when compared with MCI patients without CSVD. Thus, although we did find evidence for grey matter related Wallerian related microstructure deterioration, vascular effects seem to be most prominent. The localization of a tract might be decisive here, as tracts nearby the ventricles are known and shown to be susceptible to vascular damage (the FMI),[84,85] while tracts connecting degenerating grey matter regions show influence of atrophy, i.e. Wallerian influence (the CGH, the perforant path), and white matter near the brain stem was not affected (the MCP). To examine the grey matter related Wallerian influence more closely, a voxel based morphometry analysis, in which VBM measures within distinct brain regions are related to DTI measures will be particularly interesting.

We measured white matter microstructure not only in terms of FA and MD, but also with respect to the directional properties of diffusion, i.e. axial and perpendicular diffusivity. Studies in mice suggest that a difference in the pathophysiology underlies axial and perpendicular diffusivity, as axial diffusivity was found to relate to axonal injury while perpendicular diffusivity was linked to myelin damage.[86,87] In the current study we found that axial diffusivity was less sensitive in distinguishing MCI patients from controls compared with the other DTI measures, suggesting little axonal injury in our MCI patient cohort. Perpendicular diffusivity increase was found primarily in MCI patients with CSVD compared to either controls or MCI patients without CSVD. This indicates that the underlying pathophysiology in our cohort of MCI patients with CSVD would primarily be myelin loss. Interestingly, myelin damage was found to be associated with transmission velocity reduction,[10] which might be the link between changes in myelin basic protein and the typical cognitive profile of decreased psychomotor speed in elderly with CSVD.[88,89]

The pathological mechanisms of Alzheimer's disease and cerebral vascular damage have traditionally been considered separate, sometimes even mutually exclusive.[49,90] The fact that in a large proportion of dementia cases underlying pathology was mixed, i.e. combined vascular and neurodegenerative pathology at autopsy, as well as on MRI,[7,11,91] contradicts this view. In the present study we show that grey matter atrophy related to AD and vascular damage both affect the white matter. Whether the different pathological processes influence each other, as suggested by studies reporting a reciprocal effect of vascular insufficiency promoting neurodegenerative changes and vice versa,[92] are synergistic or additive to the clinical and cognitive syndrome has yet to be further elucidated. We however think that where AD pathology affects mainly the grey matter, CSVD is responsible for the majority of white matter damage in MCI, thereby affecting the white matter interconnecting important grey matter regions, and interfering with neuronal network functioning.

Conclusion

This study indicates that in patients with MCI, CSVD affects the brain's white matter more extensively than the macrostructural findings visible on T2-FLAIR imaging. We found evidence of vascular disease related microstructural damage in important fiber tracts that subserve the default mode network. We postulate that such damage interferes with the normal functioning of the default mode network and consequently cognitive functioning. Our results also highlight a probable role for atrophy driven degeneration of white matter microstructure and therefore point towards a neuropathological white matter substrate in MCI in which both direct vascular damage and grey matter atrophy related Wallerian degeneration play a role.

References

1. Albert MS, DeKosky ST, Dickson D, et al. The diagnosis of mild cognitive impairment due to Alzheimer's disease: recommendations from the National Institute on Aging-Alzheimer's Association workgroups on diagnostic guidelines for Alzheimer's disease. *Alzheimers Dement.* 2011;7(3):270-9.
2. DeCarli C. Mild cognitive impairment: prevalence, prognosis, aetiology, and treatment. *Lancet Neurol.* 2003;2(January):15-21.
3. Petersen RC. Mild cognitive impairment as a diagnostic entity. *J Intern Med.* 2004;256(3):183-94.
4. Bozzali M, Filippi M, Magnani G, et al. The contribution of voxel-based morphometry in staging patients with mild cognitive impairment. *Neurology*. 2006;67(3):453-60.
5. Chételat G, Landeau B, Eustache F, et al. Using voxel-based morphometry to map the structural changes associated with rapid conversion in MCI: a longitudinal MRI study. *Neuroimage.* 2005;27(4):934-46.
6. Karas GB, Scheltens P, Rombouts SARB, et al. Global and local gray matter loss in mild cognitive impairment and Alzheimer's disease. *Neuroimage.* 2004;23(2):708-16.
7. Targosz-Gajniak M, Siuda J, Ochudło S, Opala G. Cerebral white matter lesions in patients with dementia - from MCI to severe Alzheimer's disease. *J Neurol Sci.* 2009;283(1-2):79-82.
8. Yoshita M, Fletcher E, Harvey D, et al. Extent and distribution of white matter hyperintensities in normal aging, MCI, and AD. *Neurology*. 2006;67(12):2192-8.
9. Pantoni L. Cerebral small vessel disease: from pathogenesis and clinical characteristics to therapeutic challenges. *Lancet Neurol.* 2010;9(7):689-701.
10. Bartzokis G, Sultzer D, Lu PH, Nuechterlein KH, Mintz J, Cummings JL. Heterogeneous age-related breakdown of white matter structural integrity: implications for cortical "disconnection" in aging and Alzheimer's disease. *Neurobiol Aging.* 2004;25(7):843-51.
11. Englund E, Brun A, Alling C. White Matter Changes In Dementia Of Alzheimer's Type. *Brain.* 1988;111:1425-1439.
12. Luchsinger JA, Brickman AM, Reitz C, et al. Subclinical cerebrovascular disease in mild cognitive impairment. *Neurology.* 2009;73(6):450-6.
13. Nordahl CW, Ranganath C, Yonelinas AP, DeCarli C, Reed BR, Jagust WJ. Different mechanisms of episodic memory failure in mild cognitive impairment. *Neuropsychologia.* 2005;43(11):1688-97.
14. Villeneuve S, Massoud F, Bocti C, Gauthier S, Belleville S. The nature of episodic memory deficits in MCI with and without vascular burden. *Neuropsychologia.* 2011;49(11):3027-35.
15. Dickerson BC, Goncharova I, Sullivan MP, et al. MRI-derived entorhinal and hippocampal atrophy in incipient and very mild Alzheimer's disease. *Neurobiol Aging.* 2001;22:747-754.
16. Jack CR, Petersen RC, Xu Y, et al. Rates of hippocampal atrophy correlate with change in clinical status in aging and AD. *Neurology.* 2000;55(4):484-89.
17. Bai F, Zhang Z, Yu H, et al. Default-mode network activity distinguishes amnestic type mild cognitive impairment from healthy aging: a combined structural and resting-state functional MRI study. *Neurosci Lett.* 2008;438(1):111-5.
18. Greicius MD, Srivastava G, Reiss AL, Menon V. Default-mode network activity distinguishes Alzheimer's disease from healthy aging: evidence from functional MRI. *Proc Natl Acad Sci U S A.* 2004;101(13):4637-42.
19. Buckner RL, Andrews-Hanna JR, Schacter DL. The brain's default network: anatomy, function, and relevance to disease. *Ann N Y Acad Sci.* 2008;1124:1-38.
20. Greicius MD, Krasnow B, Reiss AL, Menon V. Functional connectivity in the resting brain: a network analysis of the default mode hypothesis. *Proc Natl Acad Sci U S A.* 2003;100(1):253-8.
21. Raichle ME, MacLeod AM, Snyder AZ, Powers WJ, Gusnard DA, Shulman GL. A default mode of brain function. *Proc Natl Acad Sci U S A.* 2001;98(2):676-82.
22. Seeley WW, Crawford RK, Zhou J, Miller BL, Greicius MD. Neurodegenerative diseases target large-scale human brain networks. *Neuron.* 2009;62(1):42-52.

23. Damoiseaux JS, Greicius MD. Greater than the sum of its parts: a review of studies combining structural connectivity and resting-state functional connectivity. *Brain Struct Funct*. 2009;213(6):525-33.

24. Greicius MD, Supekar K, Menon V, Dougherty RF. Resting-state functional connectivity reflects structural connectivity in the default mode network. *Cereb Cortex*. 2009;19(1):72-8.

25. Mayda AB V, Westphal A, Carter CS, DeCarli C. Late life cognitive control deficits are accentuated by white matter disease burden. *Brain*. 2011;134(Pt 6):1673-83.

26. Rocca MA, Valsasina P, Absinta M, et al. Default-mode network dysfunction and cognitive impairment in progressive MS. *Neurology*. 2010;74(16):1252-9.

27. Cherubini A, Péran P, Spoletini I, et al. Combined volumetry and DTI in subcortical structures of mild cognitive impairment and Alzheimer's disease patients. *J Alzheimers Dis*. 2010;19(4):1273-82.

28. Liu Y, Spulber G, Lehtimäki KK, et al. Diffusion tensor imaging and Tract-Based Spatial Statistics in Alzheimer's disease and mild cognitive impairment. *Neurobiol Aging*. 2011;32(9):1558-71.

29. Rogalski EJ, Murphy CM, deToledo-Morrell L, et al. Changes in parahippocampal white matter integrity in amnestic mild cognitive impairment: a diffusion tensor imaging study. *Behav Neurol*. 2009;21(1):51-61.

30. Bai F, Zhang Z, Watson DR, et al. Abnormal integrity of association fiber tracts in amnestic mild cognitive impairment. *J Neurol Sci*. 2009;278(1-2):102-6.

31. Kiuchi K, Morikawa M, Taoka T, et al. Abnormalities of the uncinate fasciculus and posterior cingulate fasciculus in mild cognitive impairment and early Alzheimer's disease: a diffusion tensor tractography study. *Brain Res*. 2009;1287:184-91.

32. Zhou Y, Dougherty JH, Hubner KF, Bai B, Cannon RL, Hutson RK. Abnormal connectivity in the posterior cingulate and hippocampus in early Alzheimer's disease and mild cognitive impairment. *Alzheimers Dement*. 2008;4(4):265-70.

33. Bosch B, Arenaza-Urquijo EM, Rami L, et al. Multiple DTI index analysis in normal aging, amnestic MCI and AD. Relationship with neuropsychological performance. *Neurobiol Aging*. 2012;33(1):61-74.

34. Bozoki AC, Korolev IO, Davis NC, Hoisington LA, Berger KL. Disruption of limbic white matter pathways in mild cognitive impairment and Alzheimer's disease: a DTI/FDG-PET study. *Hum Brain Mapp*. 2012;33(8):1792-802.

35. Mielke MM, Kozauer NA, Chan KCG, et al. Regionally-specific diffusion tensor imaging in mild cognitive impairment and Alzheimer's disease. *Neuroimage*. 2009;46(1):47-55.

36. Chen T-F, Lin C-C, Chen Y-F, et al. Diffusion tensor changes in patients with amnesic mild cognitive impairment and various dementias. *Psychiatry Res*. 2009;173(1):15-21.

37. Zhuang L, Wen W, Zhu W, et al. White matter integrity in mild cognitive impairment: a tract-based spatial statistics study. *Neuroimage*. 2010;53(1):16-25.

38. Raff MC, Whitmore A V, Finn JT. Axonal self-destruction and neurodegeneration. *Science*. 2002;296(5569):868-71.

39. Chua TC, Wen W, Chen X, et al. Diffusion tensor imaging of the posterior cingulate is a useful biomarker of mild cognitive impairment. *Am J Geriatr Psychiatry*. 2009;17(7):602-13.

40. Horsfield MA, Jones DK. Applications of diffusion-weighted and diffusion tensor MRI to white matter diseases - a review. *NMR Biomed*. 2002;15(7-8):570-7.

41. Maillard P, Fletcher E, Harvey D, et al. White matter hyperintensity penumbra. *Stroke*. 2011;42(7):1917-1922.

42. Vernooij MW, de Groot M, van der Lugt A, et al. White matter atrophy and lesion formation explain the loss of structural integrity of white matter in aging. *Neuroimage*. 2008;43(3):470-477.

43. Teipel SJ, Bokde ALW, Meindl T, et al. White matter microstructure underlying default mode network connectivity in the human brain. *Neuroimage*. 2010;49(3):2021-32.

44. Van den Heuvel M, Mandl R, Luigjes J, Hulshoff Pol H. Microstructural organization of the cingulum tract and the level of default mode functional connectivity. *J Neurosci*. 2008;28(43):10844-51.

45. Van den Heuvel MP, Mandl RCW, Kahn RS, Hulshoff Pol HE. Functionally linked resting-state networks reflect the underlying structural connectivity architecture of the human brain. *Hum Brain Mapp*. 2009;30(10):3127-41.

46. Verhage F. *Intelligentie en leeftijd: onderzoek bij Nederlanders van twaalf tot zevenenzeventig jaar [Intelligence and age: Research on Dutch People Aged Twelve to Seventy-Seven Years Old]*. Assen: Van Gorcum; 1964.

47. Perneczky R, Wagenpfeil S, Komossa K, Grimmer T, Diehl J, Kurz A. Mapping scores onto stages: mini-mental state examination and clinical dementia rating. *Am J Geriatr Psychiatry*. 2006;14(2):139-44.

48. Fazekas F, Barkhof F, Wahlund LO, et al. CT and MRI rating of white matter lesions. *Cerebrovasc Dis*. 2002;13(suppl 2):31-36.

49. Frisoni GB, Galluzzi S, Bresciani L, Zanetti O, Geroldi C. Mild cognitive impairment with subcortical vascular features: clinical characteristics and outcome. *J Neurol*. 2002;249(10):1423-32.

50. De Boer R, Vrooman HA, van der Lijn F, et al. White matter lesion extension to automatic brain tissue segmentation on MRI. *Neuroimage*. 2009;45(4):1151-1161.

51. Vrooman HA, Cocosco CA, van der Lijn F, et al. Multi-spectral brain tissue segmentation using automatically trained k-Nearest-Neighbor classification. *Neuroimage*. 2007;37(1):71-81.

52. Den Heijer T, van der Lijn F, Koudstaal PJ, et al. A 10-year follow-up of hippocampal volume on magnetic resonance imaging in early dementia and cognitive decline. *Brain*. 2010;133(Pt 4):1163-72.

53. Van der Lijn F, den Heijer T, Breteler MMB, Niessen WJ. Hippocampus segmentation in MR images using atlas registration, voxel classification, and graph cuts. *Neuroimage*. 2008;43(4):708-20.

54. Van der Lijn F, de Bruijne M, Klein S, et al. Automated brain structure segmentation based on atlas registration and appearance models. *IEEE Trans Med Imaging*. 2012;31(2):276-86.

55. Woolrich MW, Jbabdi S, Patenaude B, et al. Bayesian analysis of neuroimaging data in FSL. *Neuroimage*. 2009;45(1 Suppl):S173-186.

56. Klein S, Staring M, Murphy K, Viergever MA, Pluim JPW. elastix: a toolbox for intensity-based medical image registration. *IEEE Trans Med Imaging*. 2010;29(1):196-205.

57. Leemans A, Jones DK. The B-matrix must be rotated when correcting for subject motion in DTI data. *Magn Reson Med*. 2009;61(6):1336-1349.

58. Smith SM. Fast robust automated brain extraction. *Hum Brain Mapp*. 2002;17(3):143-55.

59. Behrens TEJ, Johansen-Berg H, Jbabdi S, Rushworth MFS, Woolrich MW. Probabilistic diffusion tractography with multiple fibre orientations: What can we gain? *Neuroimage*. 2007;34(1):144-155.

60. Rose SE, Chen F, Chalk JB, et al. Loss of connectivity in Alzheimer's disease: an evaluation of white matter tract integrity with colour coded MR diffusion tensor imaging. *J Neurol Neurosurg Psychiatry*. 2000:528-530.

61. Jenkinson M, Smith SM. A global optimisation method for robust affine registration of brain images. *Med Image Anal*. 2001;5(2):143-56.

62. Smith SM, Jenkinson M, Johansen-Berg H, et al. Tract-based spatial statistics: voxelwise analysis of multi-subject diffusion data. *Neuroimage*. 2006;31(4):1487-1505.

63. Smith SM, Nichols TE. Threshold-free cluster enhancement: addressing problems of smoothing, threshold dependence and localisation in cluster inference. *Neuroimage*. 2009;44(1):83-98.

64. Mori S, Kaufmann WE, Davatzikos C, et al. Imaging cortical association tracts in the human brain using diffusion-tensor-based axonal tracking. *Magn Reson Med*. 2002;47(2):215-223.

65. Stieltjes B, Kaufmann WE, van Zijl PC, et al. Diffusion tensor imaging and axonal tracking in the human brainstem. *Neuroimage*. 2001;14(3):723-735.

66. Wakana S, Caprihan A, Panzenboeck MM, et al. Reproducibility of quantitative tractography methods applied to cerebral white matter. *Neuroimage*. 2007;36(3):630-644.

67. Wakana S, Jiang H, Nagae-Poetscher LM, van Zijl PCM, Mori S. Fiber Tract–based Atlas of human white matter anatomy. *Radiology*. 2004;230(1):77-87.

68. Andersson JL, Smith SM, Jenkinson M. FNIRT - FMRIB's Non-linear Image Registration Tool. In: *Fourteenth Annual Meeting of the Organization for Human Brain Mapping*. Melbourne; 2008.

69. De Groot M, Verhaaren BFJ, de Boer R, et al. Changes in normal-appearing white matter precede development of white matter lesions. *Stroke*. 2013;44(4):1037-42.

70. Yip AG, McKee AC, Green RC, et al. APOE, vascular pathology, and the AD brain. *Neurology*. 2005;65(2):259-65.

71. Schneider JA, Bienias JL, Wilson RS, Berry-Kravis E, Evans DA, Bennett DA. The apolipoprotein E epsilon4 allele increases the odds of chronic cerebral infarction [corrected] detected at autopsy in older persons. *Stroke*. 2005;36(5):954-9.

72. O'sullivan M, Summers PE, Jones DK, Jarosz JM, Williams SC., Markus H. Normal-appearing white matter in ischemic leukoaraiosis: A diffusion tensor MRI study. *Neurology*. 2001;57:2307-2310.

73. Sexton CE, Kalu UG, Filippini N, Mackay CE, Ebmeier KP. A meta-analysis of diffusion tensor imaging in mild cognitive impairment and Alzheimer's disease. *Neurobiol Aging*. 2011;32(12):2322.e5-18.

74. Xie S, Xiao JX, Gong GL, et al. Voxel-based detection of white matter abnormalities in mild Alzheimer disease. *Neurology*. 2006;66(12):1845-9.

75. Schmidtke K, Hüll M. Cerebral small vessel disease: how does it progress? *J Neurol Sci*. 2005;229-230:13-20.

76. Maillard P, Carmichael O, Harvey D, et al. FLAIR and Diffusion MRI Signals Are Independent Predictors of White Matter Hyperintensities. *AJNR*. 2012.

77. Witter MP, Wouterlood FG, Naber PA, van Haeften T. Anatomical organization of the parahippocampal-hippocampal network. *Ann N Y Acad Sci*. 2000;911:1-24.

78. Thal DR, Holzer M, Rüb U, et al. Alzheimer-related tau-pathology in the perforant path target zone and in the hippocampal stratum oriens and radiatum correlates with onset and degree of dementia. *Exp Neurol*. 2000;163(1):98-110.

79. Damoiseaux JS, Smith SM, Witter MP, et al. White matter tract integrity in aging and Alzheimer's disease. *Hum Brain Mapp*. 2009;30(4):1051-1059.

80. Kalus P, Slotboom J, Gallinat J, et al. Examining the gateway to the limbic system with diffusion tensor imaging: the perforant pathway in dementia. *Neuroimage*. 2006;30(3):713-20.

81. Braak H, Braak E. Neuropathological stageing of Alzheimer-related changes. *Acta Neuropathol*. 1991;82:239-259.

82. Sydykova D, Stahl R, Dietrich O, et al. Fiber connections between the cerebral cortex and the corpus callosum in Alzheimer's disease: a diffusion tensor imaging and voxel-based morphometry study. *Cereb Cortex*. 2007;17(10):2276-82.

83. Villain N, Desgranges B, Viader F, et al. Relationships between hippocampal atrophy, white matter disruption, and gray matter hypometabolism in Alzheimer's disease. *J Neurosci*. 2008;28(24):6174-81.

84. De Reuck J. The human periventricular arterial blood supply and the anatomy of cerebral infarctions. *Eur Neurol*. 1971;5(6):321-34.

85. Longstreth WT, Manolio TA, Arnold A, et al. Clinical correlates of white matter findings on cranial magnetic resonance imaging of 3301 elderly people. The Cardiovascular Health Study. *Stroke*. 1996;27(8):1274-82.

86. Song S-K, Yoshino J, Le TQ, et al. Demyelination increases radial diffusivity in corpus callosum of mouse brain. *Neuroimage*. 2005;26(1):132-40.

87. Sun S-W, Liang H-F, Le TQ, Armstrong RC, Cross AH, Song S-K. Differential sensitivity of in vivo and ex vivo diffusion tensor imaging to evolving optic nerve injury in mice with retinal ischemia. *Neuroimage*. 2006;32(3):1195-204.

88. Prins ND, van Dijk EJ, den Heijer T, et al. Cerebral small-vessel disease and decline in information processing speed, executive function and memory. *Brain*. 2005;128(Pt 9):2034-41.

89. Wang D-S, Bennett DA, Mufson EJ, Mattila P, Cochran E, Dickson DW. Contribution of changes in ubiquitin and myelin basic protein to age-related cognitive decline. *Neurosci Res*. 2004;48(1):93-100.

90. Erkinjuntti T, Gauthier S. The concept of vascular cognitive impairment. *Front Neurol Neurosci*. 2009;24:79-85.

91. Reed BR, Mungas DM, Kramer JH, et al. Profiles of neuropsychological impairment in autopsy-defined Alzheimer's disease and cerebrovascular disease. *Brain.* 2007;130(Pt 3):731-9.

92. Iadecola C. The overlap between neurodegenerative and vascular factors in the pathogenesis of dementia. *Acta Neuropathol.* 2010;120(3):287-96.

Chapter 5
General discussion

General Discussion

In this thesis, I have explored white matter microstructure using multi-subject diffusion MRI data in the context of aging, small vessel disease and cardiovascular risk. I have developed and evaluated automated approaches for the investigation of diffusion MRI data in large cohorts, and have applied these to participants of the Rotterdam Study. In the following chapter, I will first discuss my main findings and will place them in the context of existing research. I will then discuss some methodological considerations of my work, after which I will discuss future perspectives of the large-scale analysis of white matter microstructure in population-based cohorts.

Interpretation of main findings

The aims in this thesis were to develop new analysis approaches for the investigation of white matter microstructure in elderly subjects, and to apply these in the setting of large population-based cohorts. In this section I will discuss my main findings in the same order in which they were presented in this thesis: first methodological improvements, then their application in aging and finally the application in small vessel disease. In this last application, I separately discuss the impact of concomitant macrostructural white matter pathology, cerebral microbleeds and mild cognitive impairment with and without small vessel disease on white matter microstructure.

Improving cross subject diffusion analysis

The cingulum

The cingulum is part of the limbic system, connecting the thalamus to the hippocampus, and the hippocampus to multiple cortical regions along the cingulate bundle. With the hippocampus affected early on in Alzheimer's disease,[1] investigating its most important white matter connections is highly relevant.[2] The cingulum is a thin, wire-like structure which may be hard to identify,[3] but for which protocols for manual initialization of tractography have been published.[4,5] Different segments of the cingulum provide a slightly different set of connections as fibers branch off over most of its course. It is therefore too simplistic to assume constant microstructural appearance over its trajectory, leading many researchers to separate or parameterize the cingulum over multiple segments.[6–12] To take this approach one step further, we investigated feasibility of seeding tractography along the entire trajectory, while iteratively pruning fiber tracts that do not appear to be part of the structure. Using this approach, we were able to identify the cingulum continuously from its hippocampal connection to its anterior inflection point around the genu of the corpus callosum. Using this method, we could confirm asymmetry findings for the cingulate gyrus

part of the cingulum,[6–8] and newly identified an inverted (right higher than left) asymmetry in FA for the parahippocampal part of the cingulum.[7] However, we also ran into the limitations of deterministic tractography in the population-based DTI data used.

Deterministic tractography, elegant for its simplicity, and fast to perform, has trouble accounting for the uncertainty in the direction of single fiber populations, and cannot cope with crossing fibers.[13–16] A considerable prevalence of such complex fiber anatomies has been shown in several studies.[13,17] Additionally, the acquisition matrix of the Rotterdam Study diffusion data is relatively coarse, which further aggravates the problem. As a result, we especially experienced difficulty extracting the curved cingulum segments around the corpus callosum. We hypothesized that incorporating the uncertainty in the fiber direction, and modeling fiber populations individually, could improve results. Our next approach for automated tractography was therefore based on probabilistic tracking and modeling of the different fiber populations in each voxel. While for the cingulum this meant switching to individual definitions of the parahippocampal and cingulate gyrus parts, this resulted in a much more robust extraction of fiber tracts than with the deterministic tractography. In this next approach, we adopted protocols for deterministic tracking of white matter tracts[4,5,18,19] for automated probabilistic tracking,[12] to allow evaluation of image registration performance.

Improving diffusion image registration

To cope with change of a single subject's anatomy over time or across different participants' brains, image registration is commonly used to establish correspondence between images. Registration essentially is an optimization problem aimed at getting the best image similarity across images weighed against a cost-function penalizing deformations and displacements. As registration approaches perform an essential, non-trivial task in many neuro image analysis approaches, much effort has been invested in improving various aspects of this task.[20–28]

While these improvements aim to most effectively use all available image and anatomical information, this poses a fundamental problem with evaluation, as the criterion for assessing registration accuracy should be independent of the metric optimized in the registration. Evaluation of image registration needs to assess the level of correspondence obtained, which ultimately requires the use of the ground-truth correspondence that is generally not available.[29] This leaves data-driven evaluation as a viable alternative.[21] For diffusion MRI, this suggests a potential role for the anatomical information that can be extracted with tractography, provided the registration procedure did not use this information already. The feasibility of using tractography in registering diffusion datasets has been shown,[27,30–36] but mostly for *estimating* affine transformations as the information in tractography is relatively

sparse. Alternatively, tractography has also been used for *evaluating* the accuracy of registrations obtained using more conventional similarity metrics.[21,22,24,28,37,38] The latter strategy offers an evaluation that is not biased by the similarity metric optimized in the registration, and directly probes the accuracy of anatomical correspondence.[21,29]

In this thesis I have demonstrated that tract similarity is a highly reproducible metric, which is sufficiently robust to optimize parameter settings for registration algorithms. Using this evaluation framework, we were able to show that for two widely used image registration algorithms, FNIRT[39] and elastix,[40] high resolution registrations outperform the registration-projection cascade used in the popular tract-based spatial statistics (TBSS) approach.[41] This finding has since then been confirmed by another study.[42] Tract similarity evaluation showed some general trends for image registration in FA images, i.e.: 1) Over a population of 30 subjects, the average registration performance was highly reproducible. 2) The optimal registration parameters depended on the quality of the dataset in a graded and therefore controllable manner. 3) It was better to use regularization to control the dimensionality of the optimization problem, than to lower the resolution of the transformation.

While future studies are expected to benefit from the optimized registration parameters, and from the improved image alignment in TBSS, also the automated tractography protocols that resulted from our study could be useful. They allow fully automated, unsupervised probabilistic tractography for 27 white matter structures. For this reason, we decided to make these protocols publicly available* and have also applied them ourselves in the context of a large study on tract microstructure and age.

Longitudinal image analysis

White matter lesions (WML) are often seen on brain MRI in aging persons and are thought to reflect underlying small vessel disease. They are most commonly identified on FLAIR images, on which they appear as hyperintense signal areas. WML have been related to increased risk of stroke and dementia[43–45] but their development is still not fully understood. In a recent paper, Maillard et al.[46] investigated the idea of using the continuous FLAIR intensity[47] to study development of white matter lesions. Altered FLAIR and diffusion measurements, in both the penumbra around WML, as well as in the normal-appearing white matter that converted to WML corroborated the hypothesis of gradual lesion formation.[46,48] However, influence of partial volume effects and of spatial dependencies acting on WML formation *and* on diffusion measurements could not be ruled out. Therefore, we developed a longitudinal analysis approach that aimed to overcome these limitations. In the approach, we first symmetrically[49] established inter-subject correspondence, then intra-subject correspondence, and finally performed region-matching between cas-

* *http://fsl.fmrib.ox.ac.uk/fsl/fslwiki/AutoPtx*

es and controls. With this approach we investigated a population of nearly 700 participants (mean age 66.9 years), who were rescanned after 3.5 years. We were able to demonstrate that the normal-appearing white matter tissue that later converts to WML is already different before the conversion. This was true for both WML growth, as well as for WML that formed *de-novo* in the normal-appearing white matter. Furthermore, we showed that whereas FLAIR and diffusion measurements showed similar trends, there was also an independently informative component in each of the measurements. The core of the longitudinal registration framework used in this analysis was later in this thesis adopted to create a longitudinal version of TBSS for the investigation of change in microstructure in relation to age and cardiovascular risk factors.

Diffusion imaging in aging

With increasing myelination of axons in the developing brain, diffusion indices of white matter microstructure show increasing organization, peaking somewhere between the end of the second decade and the beginning of the fourth decade of life, depending on the region studied.[50–52] After plateauing, white matter diffusion indices rather start to reflect microstructural deterioration. Generally, cross-sectional research in aging subjects has shown a widespread reduction of white matter microstructure, reflected in decreased FA, and increased MD with higher age.[53–55] Few studies have however investigated microstructure in a longitudinal setting,[56–58]requiring that we should interpret these results with care. Also, to what extent these changes in diffusion properties were explained by concomitant macrostructural white matter pathology remained understudied.[59] Through our longitudinal investigation of change of microstructure in aging we could investigate whether changes found in a cross-sectional design are confirmed in a longitudinal study design. In addition, we were the first to show data that strongly suggest a relative sparing of the motor tracts, something that was previously described in patients with Williams Syndrome,[60] and with Alzheimer's disease.[61] Aging research has taught us that there are widespread associations with age in most of the white matter. Our longitudinal study in over 500 persons (mean age 69.9) over a scan interval of two years found significant change in 79.4% of the white matter skeleton, consistent with a linear decline with age. These findings were much more widespread than the loss of microstructure we previously observed with higher age in the cross-sectional analysis of microstructure in relation to small vessel disease. We additionally identified that white matter degeneration was more pronounced with higher age, which we were not able to identify cross-sectionally, and which has not been shown before in longitudinal investigations.

Investigating white matter microstructure in tracts with increasing age, we identified degeneration in association, commissural and limbic fibers. For all tracts, except for the cingulate bundle, we could attribute this loss partially to macroscopic white matter changes as expressed in white matter atrophy and WML load. Sensorimotor tracts were relatively spared with aging, as indicated by increased mode of anisotropy and FA, combined with increased diffusivities.[61,62] Independently from age and macroscopic white matter changes, we observed worse tract-specific microstructure in persons with severe hypertension, diabetes mellitus, and in current smokers. We also found increased rates of change with age for subjects with hypertension and carriers of the *Apolipoprotein E (APOE)*-ε4 risk allele. These findings further corroborate the impact of cardiovascular risk factors on brain health,[63–68] and translate into effective brain age differences of up to 8 years for smoking, 9 years for diabetes and 5 years for subjects with severe hypertension. That we did not find clear differences in white matter microstructure for *APOE* ε4 allele carriership, the strongest genetic risk factor for AD in the general population,[69] was however unexpected. While previous studies into the effect of *APOE* and white matter microstructure showed widespread changes in smaller cohorts,[63,70–72] there is increasing evidence for structural white matter differences in *APOE* ε4 carriers over the lifespan.[73]

Functional studies have illustrated potential compensational mechanisms in *APOE* ε4 allele carriers,[74,75] and as structure has been shown to follow function[76] the observed differences in microstructure may underestimate the true impact of the risk allele on cell membranes. While this does not explain the apparent disagreement of our observations and previous reports, it does indicate the complexity of the processes involved, and warrants future investigations in this matter.

Diffusion imaging in small vessel disease

Concomitant macrostructural white matter pathology

It is important to note that, over the lifespan, many processes simultaneously act on, and change the composition and structure of the white matter.[77] White matter atrophy and WML load have been linked to various (cardiovascular) risk factors and pathologies and the (non-trivial) relation between these macrostructural changes to changes in white matter microstructure is poorly understood.[44,77,78] In an attempt to disambiguate different aspects of tissue change, it is therefore essential to take macrostructural changes into account when investigating white matter microstructure. In our analyses, microstructural changes could always at least partially be explained by macrostructural changes.

While indeed some changes in microstructure might directly reflect changes in white matter macrostructure, our data on normal-appearing white matter converting to WML also corroborate that macrostructural manifestations of small vessel

disease are just the tip of the iceberg of white matter pathology.[46,79] Furthermore, the variance in diffusion measurements not explained by global indices of macrostructural white matter change indicate that there is either nonlinear development of this pathology, or additional pathophysiology detected with DTI. Also, we have reason to believe that more variance in tract microstructure is explained by tract-specific rather than global WML load. Therefore we argue that, even though there is a common trajectory of WML development,[80] there is spatial variation on this pattern that reflects local white matter changes.[81]

Cerebral microbleeds

Cerebral microbleeds (CMB) reflect small brain bleeds that can be observed on MRI, owing to the paramagnetic properties of the hemoglobin deposits.[82] While the etiology of microbleeds is still debated, they have been linked to arteriolosclerosis and cerebral amyloid angiopathy,[83] which are both small vessel diseases. There is preliminary evidence that CMBs in stroke patients relate to an increased risk of recurrent ischemic or hemorrhagic stroke.[84] However, in this debate, it is still unclear what CMBs in asymptomatic individuals reflect and whether in these subjects a single CMB has clinical relevance.[85] In that respect it is relevant that we identified a gradually worse systemic white matter microstructure with increasing numbers of CMB when investigating a population-based sample of almost 4,500 participants (mean age 63.9). We also showed that a single microbleed was already associated with worse white matter microstructure. These findings further support the notion that CMBs reflect underlying widespread small vessel disease, even in community-dwelling subjects.

Small vessel disease in mild cognitive impairment

Small vessel disease frequently occurs in patients at risk for, or diagnosed with Alzheimer's disease.[80,86] Besides this co-occurrence, there is also increasing evidence for a more involved role of small vessel disease in the pathophysiology of the neurodegenerative disease.[87,88] Altered microstructure was observed in patients with mild cognitive impairment (MCI), who are at high risk for developing Alzheimer's disease.[2] However, no studies have investigated how the presence of small vessel disease affects white matter microstructure in this risk group. By assessing the impact of small vessel disease on white matter diffusion in this population, we showed that these macrostructural changes also explain a large part of the microstructural changes observed with MCI. These findings suggest that future studies of white matter changes in MCI and Alzheimer's disease would benefit from incorporation of both markers for small vessel disease markers and macrostructural white matter changes into the analysis.

Methodological considerations

One characteristic aspect of the work presented in this thesis is that diffusion imaging is used to study white matter microstructure. Another characteristic is that both studies were conducted within the setting of a large population-based cohort. There are several methodological considerations that pertain to both of these characteristics and which are briefly discussed below. Firstly, to what extent diffusion data can be used to infer information on underlying white matter architecture is a point of discussion. Secondly, I discuss methodological considerations relating to the analytical methods used to study the diffusion data. Thirdly, I discuss considerations with respect to the study design and the processing of very large datasets, which includes considerations brought about by the longitudinal nature of a number of studies.

Diffusion imaging and white matter architecture

Characterizing white matter microstructure via the diffusion of water is rather indirect. As a result, there is no explicit model of how microstructure relates to measurements, and we are left with a conceptual model that relies on many assumptions. Early experiments using diffusion tensor imaging, showed that the major determinants for anisotropy measured with DTI are membranes of the axon and myelin, and that fast axonal transport and the axonal cytoskeleton are much less influential.[89] Among the many factors influencing the configuration of these membranes, are the axon packing density, the axon diameter and the distribution of axon diameters, which are all thought to vary with age and anatomical location.[90,91] While preliminary studies on animal models have suggested that the axial diffusivity is more related to axonal loss, and that radial diffusivity is more related to myelination, this relation is likely to be much more complex.[92]

In the interpretation of diffusion measurements it is generally assumed that the investigated anatomy is adequately sampled. With the Gaussian diffusion process modeled by the diffusion tensor this means that there should only be a single and mono-directional fiber population within each voxel. This assumption will practically only hold in a minority of the white matter voxels.[17,93,94] If a voxel contains multiple fibers or a complex anatomy, interpretation of associations on the tensor should be made with caution,[60,61,95–97] and, provided that sufficient directions and b-values can be measured, a higher order model might be considered.[16] For diffusion data that are acquired under constraints of time or – in a clinical setting – patient factors, it will often be difficult to unequivocally solve these issues. Nevertheless there are some approaches, also used in this thesis, which can prove effective to better understand pathological changes that underlie diffusion properties. The tensor-based

mode of anisotropy, for example, is mathematically independent from the FA and MD, and describes the needle-ness of the diffusion tensor.[62] Using this triplet of measurements has aided in the identification of selective degeneration in the superior longitudinal fasciculus in Alzheimer's disease, with relative sparing the crossing sensorimotor tracts.[61]

While the simpler tensor model requires less data than higher order diffusion models, this does allow for short acquisition times which are a necessity when multi-sequence MRI needs to acquired in elderly volunteers. With faster acquisition schemes and higher magnet strength, however, more advanced models are coming in reach for population studies and for potential clinical use, offering measurements of biophysical properties such as mean axon diameter or myelin water fraction that are less convoluted.[98]

Analytical approaches for diffusion MRI

Different from the signal intensity in most routinely acquired MR imaging data, diffusion measures can be interpreted quantitatively. In order to characterize tissue properties, many analytical approaches have been proposed, with varying degrees of complexity, both with respect to interpretation and implementation. In this thesis, we have adopted existing approaches and have expanded on some of them, all targeted to investigate different aspects of the white matter microstructure, especially in the context of large population studies.

We investigated 'systemic' normal-appearing white matter changes in relation to aging, vascular risk factors, the occurrence of cerebral microbleeds, and in the context of mild cognitive impairment and small vessel disease. By aggregation of diffusion measures over the entire normal-appearing white matter, changes in the bulk of the white matter tissue can be investigated. The approach is straightforward to apply and statistically powerful. However, systemic changes over the entire white matter volume are assumed, which may not be in line with the underlying biological process. Another disadvantage of the technique is that thinning of white matter tracts will increase partial voluming in the measurements[78] because the periphery of the white matter is explicitly included, making it hard to disambiguate macrostructural and microstructural changes. Correcting analyses for the white matter tissue volume may compensate for linear effects, but higher order effects might also be present. Solutions could be found in the voxelwise correction for partial volume effects e.g. by using a highly accurate tissue segmentation,[99,100] or in the incorporation of neighborhood information by means of the tensor covariance.[101]

Regional measurements are, by virtue of the matched filter theorem, most sensitive to change expressed in the entire region.[102] They are therefore best suited to investigate conditions in which a strong regional dependency is hypothesized, e.g. with cerebrovascular pathology[80] or Wallerian(-like) degeneration.[103] Whereas manually defined regions-of-interest (ROI) are practically unfeasible for large cohorts, automated ROI definition can be challenging. In our research, we have used tractography-based segmentation of 25 white matter tracts to (effectively) obtain ROIs of entire tracts to aggregate diffusion measurements per tract. While this reduces the complexity of the analysis considerably compared to voxel-based analysis, the multitude of tracts and models quickly leads to analyses that become difficult to interpret. For this reason, we have not yet ventured into comparing measurement distributions inside tracts, e.g. analyzing higher order descriptors like standard deviation, skewness and kurtosis, or even the full histogram of measurements within a tract.[104,105] Tract-based ROIs, like global measurements also contain tract periphery, making them also vulnerable to partial volume effects.

Aggregation over larger areas can be adopted if white matter changes of similar extent are hypothesized. Investigating white matter changes in a voxelwise manner relaxes the assumption of widespread involvement, but requires very accurate anatomical alignment of the region of change. Yet, voxelwise analysis is probably the most widely used approach for investigating diffusion data, especially since the introduction of the tract-based spatial statistics (TBSS) approach.[41] Initially we applied TBSS with the recommended registration to the (population specific) most representative brain. However, as registration algorithms improved, the approach was updated (version 1.1) to support registration to an FA template, thereby greatly reducing the computational load. We further improved the spatial alignment in TBSS by introducing an optimized, high-dimensional non-rigid registration in favor of the registration-projection cascade initially used in TBSS. We evaluated this improvement in an example experiment and finally applied it in a large longitudinal analysis. TBSS is (relatively) insensitive to potentially interesting effects in the tract periphery, it might not extract an anatomically perfect skeleton and may hide important details from the end user,[95] but it has empowered neuroscientists and clinical investigators with a versatile approach that is straightforward to apply. In that sense, it serves as an example for algorithm developers looking to contribute more broadly to the neuroimaging field.

TBSS however, lacks the incorporation of anatomical information that many tractography approaches offer. The two paradigms can be seen as complimentary, with tractography-based analyses offering much greater power in exploring effects on the whole tract or effects along the tract using a parameterization similar to our approach in the cingulum, or much more detailed.[8,11,106–109] Ideally, the approaches should be integrated, e.g. by building an analysis space in which tracts and regions of crossing fibers are modeled explicitly. Approaches that integrate information along the

tract,[110,111] in such a way as to identify the 'weakest link' do not even require damage to the tract to occur at the same site. These approaches do however also implicitly assume a uniformity of connections for all fibers within a tract, i.e. a single function for the entire tract, which for e.g. the cingulum may be hard to justify.

Study population

The research described in this thesis was predominantly performed in the context of the population based Rotterdam Study, a study aimed to investigate diseases of the elderly. All participants were free from clinical dementia at time of MRI, and represent a sample from the general aging population. Yet, the long prodromal phase of many neurodegenerative diseases undoubtedly means that also in our population, neurodegenerative pathology was present. For Alzheimer's disease, population based studies in slightly older populations estimate the prevalence of pre-clinical pathology in the order of 30%.[112,113] Not all participants with amyloid pathology will eventually develop Alzheimer's disease, but combined with other incipient (e.g. vascular) diseases, this does illustrate the high prevalence of pathology in this sample of presumed 'normal' aging. It might even be postulated that all changes to white matter microstructure found on imaging in aging subjects could be attributed to varying degrees of underlying brain pathology. Regardless of the exact pathological underpinning of these imaging findings, describing observations in 'normal' aging contributes to the establishment of reference values and adds understanding to investigation of specific pathologies.

The age range of the investigated population, 45 years and over, is just outside the period of neurodevelopment as observed by lifespan studies of diffusion.[50,52,59,114–116] This has some consequences for the modeling of associations with age,[117] as we may expect some influence of the proximity of the inflection point between net development and net degeneration identified in these lifespan studies. With higher age, interaction effects between risk factors might also contribute to accelerate microstructural deterioration. This means higher order models should always considered when investigating changes in this age range. In the work presented in this thesis, however, we only identified non-linear associations with age in our longitudinal analysis of microstructure.

Automated analysis of large datasets

Whenever the volume of image data outgrows the size of what is feasible to inspect and handle visually and/or manually, there is a need for (semi) automated analysis tools. Above all, these tools need to be robust, but they can be so at the expense of computational cost and or generalizability with respect to heterogeneity of the type of input data.

Robust, automated methods require less supervision, but unless properly managed, increase the risk of being used without any supervision. As population imaging data, acquired using strict routines will also yield incidental findings[118] and imaging artifacts, no pipeline should be run without inspection[95,119] or at the very least some exception detection. An approach that worked well in our research has been to render compilations of views to reduced resolution previews, enabling quick review of processing steps with minimal data-handling overhead.

With large cohorts comes increased statistical power to detect differences. With that, estimates for effect sizes become more interesting, while raw significance becomes less meaningful. Especially in voxelwise statistics this issue has not yet been widely addressed, but this might change as more and more population imaging studies are being performed.

Longitudinal data analysis
Imaging data acquired at different time points in a longitudinal study offer a much closer assessment on causal relationships than do cross-sectional studies, by virtue of much fewer assumptions on the source of explained variance. Also, investigating change over repeated visits effectively regards subjects as their own control, taking away the inter-subject variation encountered in cross-sectional analyses, thereby increasing the statistical power of longitudinal study designs. Intra-subject fluctuation, noise in data and measurement errors are however present, which might give rise to implausible observations such as loss of white matter lesions. These observations can be confusing, while understandable from a technical point of view.

Longitudinal analyses do, however, make strong assumptions on the consistency of the data acquisition over time. While scanners that are fully dedicated to research applications can be excluded from routine updates that might affect data continuity, hardware replacements and drift in scanner component specifications are harder to control. Phantom based quality control could help, but requires consistency of the phantoms. Also, this approach might not be able to identify all sources of change, and identified changes may not always be correctable. While acquisitions should ideally be truly quantitative and calibrated, this would still leave ambiguity in interpreting results as long as the measured physical quantity is influenced by many

tissue properties. In that sense, striving for maximum SNR over acquisition time, while compensating scanner effects using image based corrections[77,78] might offer a reasonable compromise, with a potential role for transfer learning techniques that are being developed to overcome scanner differences.[120]

Future perspectives

Analytical approaches

Methods for analyzing cross-subject diffusion data increasingly integrate multiple imaging modalities (e.g. structural and functional imaging[121,122]) and prior knowledge.[123] Improved image registration techniques for example, unlock the potential of resources ranging from atlas based structure segmentations to gene expression brain maps.[124,125] Atlas based tractography is available for many white matter tracts,[12,126] but further integration of anatomical prior knowledge has been limited. The goal of further incorporating prior knowledge would be to reduce the dimensionality of the analysis in a sensible way. This involves finding sensible support regions for associations in tracts,[33,127,128] as well as simultaneously investigating changes in different tensor metrics.[111,129] Methods analyzing multidimensional information could even integrate other image modalities such as the continuous FLAIR intensity or voxelwise partial volume estimates of white matter tissue. The multidimensional aspect might aid in better discrimination between macrostructural changes and microstructural changes.

Tractography has often been seeded from regions identified in voxel-based analyses. In this hybrid approach, strengths from tractography and voxel-based analyses are combined. This concept facilitates multiple novel analysis approaches. First, voxel-based studies could draw tract-continuity information from tractography, e.g. by introducing a (non-euclidean) distance in the clustering approach that has greater proximity for voxels inside the same tract, thereby promoting associations inside tracts, or even breaking clusters that run over separate tracts. This would improve the specificity of associations found in voxel-based analyses such as with TBSS. Another hybrid approach would be to incorporate spatial relations between tracts to identify regions of tract-overlap, and to explicitly incorporate the different patterns of change affecting the different fiber populations observed in these regions. Even if tracts are analyzed as functional entities, this might help us to better understand the changes occurring in these mixed fiber regions and better identify persistence of white matter microstructure. Thirdly, combining the deterministic tract-pruning approach presented in this thesis for the cingulum with atlas based probabilistic tractography could further enhance the automated delineation of white matter tracts. As the use of a large number of anatomical definitions for identifying single

tracts has been beneficial for probabilistic tractography,[12] seeding and trimming over the entire structure could be especially helpful to deal with complex geometry such as sharply bending tracts. Lastly, while (advanced) segmentation approaches e.g. using region growing or graph-cuts have widely been used in medical image analysis, little has been done on advanced segmentation of white matter fiber bundles using tractography. [130–132] In this work, a hard threshold on the normalized tract-density maps was used, but it would be relatively straightforward to incorporate additional knowledge and to segment tracts using graph-cuts. The threshold-based segmentation could be used as initialization on a graph of the white matter tissue segmentation and/or atlas based prior knowledge of the tract-anatomy. Such an approach is expected to produce a much more accurate tract-segmentation.

Contamination of diffusion measurements by neighboring CSF is a well known phenomenon,[133–135] limiting the analysis of the (CSF surrounded) fornix especially.[136,137] Changes in fornix microstructure have however been shown to predict cognitive decline and progression to Alzheimer's disease,[138,139] which warrants inclusion of the fornix in future studies of age related changes. With active development of new models that correct for CSF contamination, this should soon enable investigation of fornix microstructure in the Rotterdam Study.

Multidisciplinary collaboration

The analysis of advanced imaging data in clinical or population-based cohorts almost always requires multi-disciplinary teams to cover the relevant theoretical and practical grounds. As research interests and incentives across technical and clinical disciplines are not always aligned, ineffective collaborations may occur and the information in the data may not be fully exploited. While this touches on the fundamental difficulties of multidisciplinary collaborations, some recommendations could be made. First, a better focus on the final development stages of new analytical approaches would unlock these approaches to a wider audience of clinical researchers. To drive this development, the secondary (external) application of techniques should be incentivized. This could be achieved by introducing grants to specifically fund the last stage of development required for widespread application of methods, or by attributing more scientific impact to the adoption of techniques.[140] Secondly, specifically for existing data that are not publically available, an analysis-hackathon, which compels researchers from both domains to jointly work on new analyses, could provide new investigations with a head start. In this context, which is especially relevant in large epidemiologic studies, an integrated analysis team could form naturally after an initial round of pitches. A welcome side-effect of this approach

would be the direct feedback of clinical researchers on pitched analytical approaches. This interaction will likely promote the development of better interpretable and more clinically applicable measures.

Data and computational aspects

Confronted with the large number of datasets in the Rotterdam Study, I have invested much time in streamlining and handling of data. However, with growing scientific interaction at both the level of the data, as well as at the level of tools, new approaches are necessary.

In the domain of data-sharing, the extensible neuroimaging archive toolkit (XNAT) is effectively transforming the way researchers can interact with large datasets, even remotely.[141,142] By enabling data access over open application programming interfaces (APIs), much of the *technical* limitations in data sharing can thereby be overcome. Combined with far reaching anonimization of image datasets, e.g. including defacing of structural images,[143] *privacy concerns* can also be overcome. Enabling access to research data has thereby mostly become a *political* issue. With funding bodies and journals increasingly demanding open access to raw research data, access to much larger volumes of image data will thereby mostly be a matter of time. For research groups developing analysis algorithms, this means there will be much more data for development and (independent) testing, but there will also increasingly be a demand for tools that were developed on the data. The popular analogy with genetic research, in which consortia include many thousands of participants, might suggest that adding participants automatically leads to novel insights. This analogy is however broken by the intrinsic limitations in establishing anatomical correspondence across subjects, and the absence of a brain-structure equivalent to a genetic mutation. Larger datasets will however considerably aid in our understanding of 'normal' change with age, and thereby ultimately provide reference for investigations of (neurodegenerative) diseases.

Besides access to datasets and tools, also results might be released more widely. Functional MRI experiments often report their findings to brainmap, an online database for storing functional and structural associations. For associations with microstructural change this way of reporting has not yet been popularized. While it may be hard to overcome differences in e.g. skeletons used for analysis, such a resource could enable direct meta-analysis of microstructural changes with increasing age. A brainmap database of microstructure would therefore be very relevant.

Concluding remarks

I have introduced new analytical approaches for diffusion and structural MRI that improve the correspondence that can be established across subjects. This improved correspondence enables detection of microstructural changes that are more subtle than the macrostructural pathologies on which previous studies have focused. The methods contributed to research in the Rotterdam Study by enabling novel, large-scale analyses, but should also be useful and beneficial to other researchers.

I have shown widespread reduction in the microstructural organization of brain white matter with increasing age and with various cardiovascular risk factors. The extent to which these changes are associated to macrostructural changes lead to two important notions. Firstly, it strengthens the hypothesis that white matter is highly susceptible to vascular pathology in general, and small vessel disease in particular. Secondly, it suggests that studies using diffusion MRI to investigate white matter changes should incorporate these macrostructural markers of disease progression in order to identify the microstructural aspects of tissue change.

The use of diffusion imaging to support clinical decision-making is still far away. However, clinically relevant microstructural parameters are coming within reach.[138] A process aided by the accessibility of diffusion MRI and the increasing availability of integrated analysis approaches. While there certainly is heated debate on various aspects of the technique, more and more established approaches are being introduced. With this coming of age, diffusion MRI may be nearing the end of adolescence making it an extremely exciting field to work in.

References

1. Sperling RA, Aisen PS, Beckett LA, et al. Toward defining the preclinical stages of Alzheimer's disease: recommendations from the National Institute on Aging-Alzheimer's Association workgroups on diagnostic guidelines for Alzheimer's disease. *Alzheimers Dement*. 2011;7(3):280-92.
2. Mielke MM, Kozauer NA, Chan KCG, et al. Regionally-specific diffusion tensor imaging in mild cognitive impairment and Alzheimer's disease. *Neuroimage*. 2009;46(1):47-55.
3. Concha L, Gross DW, Beaulieu C. Diffusion tensor tractography of the limbic system. *AJNR Am J Neuroradiol*. 2005;26(9):2267-74.
4. Wakana S, Jiang H, Nagae-Poetscher LM, van Zijl PCM, Mori S. Fiber Tract–based Atlas of human white matter anatomy. *Radiology*. 2004;230(1):77-87.
5. Wakana S, Caprihan A, Panzenboeck MM, et al. Reproducibility of quantitative tractography methods applied to cerebral white matter. *Neuroimage*. 2007;36(3):630-644.
6. Gong G, Jiang T, Zhu C, et al. Asymmetry analysis of cingulum based on scale-invariant parameterization by diffusion tensor imaging. *Hum Brain Mapp*. 2005;24(2):92-98.

7. Malykhin N, Concha L, Seres P, Beaulieu C, Coupland NJ. Diffusion tensor imaging tractography and reliability analysis for limbic and paralimbic white matter tracts. *Psychiatry Res*. 2008;164(2):132-142.

8. O'Donnell LJ, Westin C-F, Golby AJ. Tract-based morphometry for white matter group analysis. *Neuroimage*. 2009;45(3):832-844.

9. Hua K, Zhang J, Wakana S, et al. Tract probability maps in stereotaxic spaces: analyses of white matter anatomy and tract-specific quantification. *Neuroimage*. 2008;39(1):336-47.

10. Zhang Y, Zhang J, Oishi K, et al. Atlas-guided tract reconstruction for automated and comprehensive examination of the white matter anatomy. *Neuroimage*. 2010;52(4):1289-1301.

11. Colby JB, Soderberg L, Lebel C, Dinov ID, Thompson PM, Sowell ER. Along-tract statistics allow for enhanced tractography analysis. *Neuroimage*. 2012;59(4):3227-42.

12. Yendiki A, Panneck P, Srinivasan P, et al. Automated probabilistic reconstruction of white-matter pathways in health and disease using an atlas of the underlying anatomy. *Front Neuroinform*. 2011;5(October):23.

13. Behrens TEJ, Johansen-Berg H, Jbabdi S, Rushworth MFS, Woolrich MW. Probabilistic diffusion tractography with multiple fibre orientations: What can we gain? *Neuroimage*. 2007;34(1):144-155.

14. Qazi AA, Radmanesh A, O'Donnell L, et al. Resolving crossings in the corticospinal tract by two-tensor streamline tractography: Method and clinical assessment using fMRI. *Neuroimage*. 2009;47 Suppl 2:T98-106.

15. Tournier J-D, Mori S, Leemans A. Diffusion tensor imaging and beyond. *Magn Reson Med*. 2011;65(6):1532-56.

16. Farquharson S, Tournier J-D, Calamante F, et al. White matter fiber tractography: why we need to move beyond DTI. *J Neurosurg*. 2013;118(6):1367-77.

17. Jeurissen B, Leemans A, Tournier J-D, Jones DK, Sijbers J. Investigating the prevalence of complex fiber configurations in white matter tissue with diffusion magnetic resonance imaging. *Hum Brain Mapp*. 2013;34(11):2747-66.

18. Stieltjes B, Kaufmann WE, van Zijl PC, et al. Diffusion tensor imaging and axonal tracking in the human brainstem. *Neuroimage*. 2001;14(3):723-735.

19. Mori S, Kaufmann WE, Davatzikos C, et al. Imaging cortical association tracts in the human brain using diffusion-tensor-based axonal tracking. *Magn Reson Med*. 2002;47(2):215-223.

20. Jones DK, Griffin LD, Alexander DC, et al. Spatial normalization and averaging of diffusion tensor MRI data sets. *Neuroimage*. 2002;17(2):592-617.

21. Park H-J, Kubicki M, Shenton ME, et al. Spatial normalization of diffusion tensor MRI using multiple channels. *Neuroimage*. 2003;20(4):1995-2009.

22. Zhang H, Yushkevich PA, Alexander DC, Gee JC. Deformable registration of diffusion tensor MR images with explicit orientation optimization. *Med Image Anal*. 2006;10(5):764-785.

23. Van Hecke W, Leemans A, D'Agostino E, et al. Nonrigid coregistration of diffusion tensor images using a viscous fluid model and mutual information. *IEEE Trans Med Imaging*. 2007;26(11):1598-1612.

24. Yap P-T, Wu G, Zhu H, Lin W, Shen D. TIMER: Tensor Image Morphing for Elastic Registration. *Neuroimage*. 2009;47(2):549-563.

25. Yeo BTT, Vercauteren T, Fillard P, et al. DT-REFinD: diffusion tensor registration with exact finite-strain differential. *IEEE Trans Med Imaging*. 2009;28(12):1914-1928.

26. Klein S, Pluim JPW, Staring M, Viergever MA. Adaptive Stochastic Gradient Descent Optimisation for Image Registration. *Int J Comput Vis*. 2009;81(3):227-239.

27. Zvitia O, Mayer A, Shadmi R, Miron S, Greenspan HK. Co-registration of white matter tractographies by adaptive-mean-shift and Gaussian mixture modeling. *IEEE Trans Med Imaging*. 2010;29(1):132-145.

28. Zöllei L, Stevens A, Huber K, Kakunoori S, Fischl B. Improved tractography alignment using combined volumetric and surface registration. *Neuroimage*. 2010;51(1):206-213.

29. Crum WR, Griffin LD, Hill DLG, Hawkes DJ. Zen and the art of medical image registration: correspondence, homology, and quality. *Neuroimage*. 2003;20(3):1425-1437.

30. Leemans A, Sijbers J, de Backer S, Vandervliet E, Parizel P. Multiscale white matter fiber tract coregistration: a new feature-based approach to align diffusion tensor data. *Magn Reson Med*. 2006;55(6):1414-1423.

31. Ziyan U, Sabuncu MR, Grimson WEL, Westin C-F. Consistency Clustering: A Robust Algorithm for Group-wise Registration, Segmentation and Automatic Atlas Construction in Diffusion MRI. *Int J Comput Vis*. 2009;85(3):279-290.

32. Shadmi R, Mayer A, Sochen N, Greenspan H, Fiber-data TODB, Model O. Piecewise smooth affine registration of point-sets with application to DT-MRI brain fiber-data. In: *ISBI 2010: IEEE International Symposium on Biomedical Imaging*. IEEE; 2010:528-531.

33. Caan MWA, van Vliet LJ, Majoie CBLM, van der Graaff MM, Grimbergen CA, Vos FM. Nonrigid point set matching of white matter tracts for diffusion tensor image analysis. *IEEE Trans Biomed Eng*. 2011;58(9):2431-40.

34. Durrleman S, Fillard P, Pennec X, Trouvé A, Ayache N. Registration, atlas estimation and variability analysis of white matter fiber bundles modeled as currents. *Neuroimage*. 2011;55(3):1073-90.

35. Mayer A, Zimmerman-Moreno G, Shadmi R, Batikoff A, Greenspan H. A supervised framework for the registration and segmentation of white matter fiber tracts. *IEEE Trans Med Imaging*. 2011;30(1):131-45.

36. O'Donnell L, Wells III WM, Golby AJ, Westin C-F. Unbiased groupwise registration of white matter tractography. *Med image Comput Comput Interv MICCAI*. 2012:1-9.

37. Xue Z, Li H, Guo L, Wong STC. A local fast marching-based diffusion tensor image registration algorithm by simultaneously considering spatial deformation and tensor orientation. *Neuroimage*. 2010;52(1):119-130.

38. Jia H, Yap P-T, Wu G, Wang Q, Shen D. Intermediate templates guided groupwise registration of diffusion tensor images. *Neuroimage*. 2011;54(2):928-39.

39. Andersson JL, Smith SM, Jenkinson M. FNIRT - FMRIB's Non-linear Image Registration Tool. In: *Fourteenth Annual Meeting of the Organization for Human Brain Mapping*. Melbourne; 2008.

40. Klein S, Staring M, Murphy K, Viergever MA, Pluim JPW. elastix: a toolbox for intensity-based medical image registration. *IEEE Trans Med Imaging*. 2010;29(1):196-205.

41. Smith SM, Jenkinson M, Johansen-Berg H, et al. Tract-based spatial statistics: voxelwise analysis of multi-subject diffusion data. *Neuroimage*. 2006;31(4):1487-1505.

42. Schwarz CG, Reid RI, Gunter JL, et al. Improved DTI registration allows voxel-based analysis that outperforms Tract-Based Spatial Statistics. *Neuroimage*. 2014;94:65-78.

43. Pantoni L. Pathophysiology of age-related cerebral white matter changes. *Cerebrovasc Dis*. 2002;13 Suppl 2:7-10.

44. Debette S, Markus HS. The clinical importance of white matter hyperintensities on brain magnetic resonance imaging: systematic review and meta-analysis. *BMJ*. 2010;341:c3666.

45. Pantoni L. Cerebral small vessel disease: from pathogenesis and clinical characteristics to therapeutic challenges. *Lancet Neurol*. 2010;9(7):689-701.

46. Maillard P, Fletcher E, Harvey D, et al. White matter hyperintensity penumbra. *Stroke*. 2011;42(7):1917-1922.

47. Yoshita M, Fletcher E, DeCarli C. Current concepts of analysis of cerebral white matter hyperintensities on magnetic resonance imaging. *Top Magn Reson Imaging*. 2005;16(6):399-407.

48. Maillard P, Carmichael O, Harvey D, et al. FLAIR and Diffusion MRI Signals Are Independent Predictors of White Matter Hyperintensities. *AJNR*. 2012.

49. Reuter M, Fischl B. Avoiding asymmetry-induced bias in longitudinal image processing. *Neuroimage*. 2011;57(1):19-21.

50. Westlye LT, Walhovd KB, Dale AM, et al. Life-span changes of the human brain white matter: diffusion tensor imaging (DTI) and volumetry. *Cereb Cortex*. 2010;20(9):2055-68.

51. Hsu J-L, van Hecke W, Bai C-H, et al. Microstructural white matter changes in normal aging: a diffusion tensor imaging study with higher-order polynomial regression models. *Neuroimage*. 2010;49(1):32-43.

52. Lebel C, Gee M, Camicioli R, Wieler M, Martin W, Beaulieu C. Diffusion tensor imaging of white matter tract evolution over the lifespan. *Neuroimage*. 2012;60(1):340-52.

53. Abe O, Aoki S, Hayashi N, et al. Normal aging in the central nervous system: quantitative MR diffusion-tensor analysis. *Neurobiol Aging*. 2002;23(3):433-441.

54. Sullivan EV., Pfefferbaum A. Diffusion tensor imaging and aging. *Neurosci Biobehav Rev*. 2006;30(6):749-761.

55. Bastin ME, Muñoz Maniega S, Ferguson KJ, et al. Quantifying the effects of normal ageing on white matter structure using unsupervised tract shape modelling. *Neuroimage*. 2010;51(1):1-10.

56. Barrick TR, Charlton RA, Clark CA, Markus HS. White matter structural decline in normal ageing; a prospective longitudinal study using tract based spatial statistics. *Neuroimage*. 2010;51(2):565-77.

57. Sullivan EV., Rohlfing T, Pfefferbaum A. Longitudinal study of callosal microstructure in the normal adult aging brain using quantitative DTI fiber tracking. *Dev Neuropsychol*. 2010;35(3):233-56.

58. Nowrangi MA, Lyketsos CG, Leoutsakos J-MS, et al. Longitudinal, region-specific course of diffusion tensor imaging measures in mild cognitive impairment and Alzheimer's disease. *Alzheimers Dement*. 2013;9(5):519-28.

59. Kennedy KM, Raz N. Pattern of normal age-related regional differences in white matter microstructure is modified by vascular risk. *Brain Res*. 2009;1297:41-56.

60. Hoeft F, Barnea-Goraly N, Haas BW, et al. More is not always better: increased fractional anisotropy of superior longitudinal fasciculus associated with poor visuospatial abilities in Williams syndrome. *J Neurosci*. 2007;27(44):11960-11965.

61. Douaud G, Jbabdi S, Behrens TEJ, et al. DTI measures in crossing-fibre areas: increased diffusion anisotropy reveals early white matter alteration in MCI and mild Alzheimer's disease. *Neuroimage*. 2011;55(3):880-90.

62. Ennis DB, Kindlmann G. Orthogonal tensor invariants and the analysis of diffusion tensor magnetic resonance images. *Magn Reson Med*. 2006;55(1):136-146.

63. Persson J, Lind J, Larsson A, et al. Altered brain white matter integrity in healthy carriers of the APOE epsilon4 allele: a risk for AD? *Neurology*. 2006;66(7):1029-33.

64. Gons RAR, van Norden AGW, de Laat KF, et al. Cigarette smoking is associated with reduced microstructural integrity of cerebral white matter. *Brain*. 2011;134(Pt 7):2116-24.

65. Salat DH, Williams VJ, Leritz EC, et al. Inter-individual variation in blood pressure is associated with regional white matter integrity in generally healthy older adults. *Neuroimage*. 2012;59(1):181-92.

66. Gons RAR, van Oudheusden LJB, de Laat KF, et al. Hypertension is related to the microstructure of the corpus callosum: the RUN DMC study. *J Alzheimers Dis*. 2012;32(3):623-31.

67. Reijmer YD, Brundel M, de Bresser J, et al. Microstructural white matter abnormalities and cognitive functioning in type 2 diabetes: a diffusion tensor imaging study. *Diabetes Care*. 2013;36(1):137-44.

68. Mayor S. Time to add prevention of brain complications to heart and kidneys in diabetes? *Lancet Diabetes Endocrinol*. 2013;1(3):180-181.

69. Mahley RW, Rall SCJ. Apolipoprotein E: Far More Than a Lipid Transport Protein. *Annu Rev genomics Hum Genet*. 2000;(59).

70. Nierenberg J, Pomara N, Hoptman MJ, Sidtis JJ, Ardekani B a, Lim KO. Abnormal white matter integrity in healthy apolipoprotein E epsilon4 carriers. *Neuroreport*. 2005;16(12):1369-72.

71. Honea RA, Vidoni E, Harsha A, Burns JM. Impact of APOE on the healthy aging brain: a voxel-based MRI and DTI study. *J Alzheimers Dis*. 2009;18(3):553-64.

72. Westlye LT, Reinvang I, Rootwelt H, Espeseth T. Effects of APOE on brain white matter microstructure in healthy adults. *Neurology*. 2012;79(19):1961-9.

73. Dean DC, Jerskey BA, Chen K, et al. Brain differences in infants at differential genetic risk for late-onset Alzheimer disease: a cross-sectional imaging study. *JAMA Neurol*. 2014;71(1):11-22.

74. Bondi MW, Houston WS, Eyler LT, Brown GG. fMRI evidence of compensatory mechanisms in older adults at genetic risk for Alzheimer disease. *Neurology*. 2005;64(3):501-8.

75. Machulda MM, Jones DT, Vemuri P, et al. Effect of APOE ε4 status on intrinsic network connectivity in cognitively normal elderly subjects. *Arch Neurol*. 2011;68(9):1131-6.

76. Scholz J, Klein MC, Behrens TEJ, Johansen-Berg H. Training induces changes in white-matter architecture. *Nat Neurosci*. 2009;12(11):1370-1.

77. Fjell AM, Westlye LT, Greve DN, et al. The relationship between diffusion tensor imaging and volumetry as measures of white matter properties. *Neuroimage*. 2008;42(4):1654-68.

78. Vos SB, Jones DK, Viergever MA, Leemans A. Partial volume effect as a hidden covariate in DTI analyses. *Neuroimage.* 2011;55(4):1566-76.

79. Simpson JE, Ince PG, Higham CE, et al. Microglial activation in white matter lesions and nonlesional white matter of ageing brains. *Neuropathol Appl Neurobiol.* 2007;33(6):670-683.

80. Holland CM, Smith EE, Csapo I, et al. Spatial distribution of white-matter hyperintensities in Alzheimer disease, cerebral amyloid angiopathy, and healthy aging. *Stroke.* 2008;39(4):1127-33.

81. Van der Lijn F, Verhaaren BFJ, Ikram MA, et al. Automated measurement of local white matter lesion volume. *Neuroimage.* 2012;59(4):3901-8.

82. Greenberg SM, Vernooij MW, Cordonnier C, et al. Cerebral microbleeds: a guide to detection and interpretation. *Lancet Neurol.* 2009;8(2):165-74.

83. Vernooij M, van der Lugt A, Ikram MA, et al. Prevalence and risk factors of cerebral microbleeds: the Rotterdam Scan Study. *Neurology*. 2008;70(14):1208-14.

84. Nighoghossian N, Hermier M, Adeleine P, et al. Old Microbleeds Are a Potential Risk Factor for Cerebral Bleeding After Ischemic Stroke: A Gradient-Echo T2*-Weighted Brain MRI Study. *Stroke.* 2002;33(3):735-742.

85. Goos JDC, van der Flier WM, Knol DL, et al. Clinical relevance of improved microbleed detection by susceptibility-weighted magnetic resonance imaging. *Stroke.* 2011;42(7):1894-900.

86. Yoshita M, Fletcher E, Harvey D, et al. Extent and distribution of white matter hyperintensities in normal aging, MCI, and AD. *Neurology*. 2006;67(12):2192-8.

87. DeCarli C. Vascular factors in dementia: an overview. *J Neurol Sci.* 2004;226(1-2):19-23.

88. Gorelick PB, Scuteri A, Black SE, et al. Vascular Contributions to Cognitive Impairment and Dementia: A Statement for Healthcare Professionals From the American Heart Association/American Stroke Association. *Stroke.* 2011;42(9):2672-2713.

89. Beaulieu C. The basis of anisotropic water diffusion in the nervous system - a technical review. *NMR Biomed.* 2002;15(7-8):435-455.

90. Assaf Y, Blumenfeld-Katzir T, Yovel Y, Basser PJ. AxCaliber: a method for measuring axon diameter distribution from diffusion MRI. *Magn Reson Med.* 2008;59(6):1347-54.

91. Alexander DC, Hubbard PL, Hall MG, et al. Orientationally invariant indices of axon diameter and density from diffusion MRI. *Neuroimage.* 2010;52(4):1374-89.

92. Wheeler-Kingshott CAM, Cercignani M. About "axial" and "radial" diffusivities. *Magn Reson Med.* 2009;61(5):1255-60.

93. Behrens TEJ, Woolrich MW, Jenkinson M, et al. Characterization and propagation of uncertainty in diffusion-weighted MR imaging. *Magn Reson Med.* 2003;50(5):1077-1088.

94. Vos SB, Jones DK, Jeurissen B, Viergever MA, Leemans A. The influence of complex white matter architecture on the mean diffusivity in diffusion tensor MRI of the human brain. *Neuroimage.* 2012;59(3):2208-16.

95. Jones DK, Cercignani M. Twenty-five pitfalls in the analysis of diffusion MRI data. *NMR Biomed.* 2010;23(7):803-20.

96. Lazar M, Lee JH, Alexander AL. Axial asymmetry of water diffusion in brain white matter. *Magn Reson Med.* 2005;54(4):860-867.

97. Assaf Y, Pasternak O. Diffusion tensor imaging (DTI)-based white matter mapping in brain research: a review. *J Mol Neurosci.* 2008;34(1):51-61.

98. Assaf Y, Alexander DC, Jones DK, et al. The CONNECT project: Combining macro- and micro-structure. *Neuroimage.* 2013;80:273-82.

99. Skimminge A, Sidaros K, Liptrot M, Sidaros A. Partial volume effects in DTI. *ISMRM 2007.* 2007;15:2007.

100. Rousset OG, Ma Y, Evans AC. Correction for partial volume effects in PET: principle and validation. *J Nucl Med.* 1998;39(5):904-11.

101. Kindlmann G, Ennis DB, Whitaker RT, Westin C-F. Diffusion tensor analysis with invariant gradients and rotation tangents. *IEEE Trans Med Imaging.* 2007;26(11):1483-99.

102. Rosenfeld A, Kak AC. *Digital picture processing, Volume 1.*; 1982.

103. Coleman MP, Freeman MR. Wallerian degeneration, wld(s), and nmnat. *Annu Rev Neurosci.* 2010;33:245-67.

104. Mascalchi M, Tessa C, Moretti M, et al. Whole brain apparent diffusion coefficient histogram: a new tool for evaluation of leukoaraiosis. *J Magn Reson Imaging.* 2002;15:144-148.

105. Della Nave R, Foresti S, Pratesi A, et al. Whole-brain histogram and voxel-based analyses of diffusion tensor imaging in patients with leukoaraiosis: correlation with motor and cognitive impairment. *AJNR Am J Neuroradiol*. 2007;28(7):1313-9.

106. Zhu H, Styner M, Tang N, Liu Z, Lin W, Gilmore J. FRATS: Functional Regression Analysis of DTI Tract Statistics. *IEEE Trans Med Imaging*. 2010.

107. Corouge I, Fletcher PT, Joshi S, Gouttard S, Gerig G. Fiber tract-oriented statistics for quantitative diffusion tensor MRI analysis. *Med Image Anal*. 2006;10(5):786-798.

108. Goodlett CB, Fletcher PT, Gilmore JH, Gerig G. Group statistics of DTI fiber bundles using spatial functions of tensor measures. *Med Image Comput Comput Assist Interv Int Conf Med Image Comput Comput Assist Interv*. 2008;11(Pt 1):1068-1075.

109. Gouttard S, Prastawa M, Bullitt E, Lin W, Goodlett C, Gerig G. Constrained data decomposition and regression for analyzing healthy aging from fiber tract diffusion properties. *Med Image Comput Comput Assist Interv*. 2009;12(Pt 1):321-8.

110. White T, Schmidt M, Karatekin C. White matter "potholes" in early-onset schizophrenia: a new approach to evaluate white matter microstructure using diffusion tensor imaging. *Psychiatry Res*. 2009;174(2):110-5.

111. Hua Z, Dunson DB, Gilmore JH, Styner MA, Zhu H. Semiparametric Bayesian local functional models for diffusion tensor tract statistics. *Neuroimage*. 2012;63(1):460-74.

112. Jack CR, Knopman DS, Weigand SD, et al. An operational approach to National Institute on Aging-Alzheimer's Association criteria for preclinical Alzheimer disease. *Ann Neurol*. 2012;71(6):765-75.

113. Vos SJ, Xiong C, Visser PJ, et al. Preclinical Alzheimer's disease and its outcome: a longitudinal cohort study. *Lancet Neurol*. 2013;12(10):957-65.

114. Salat DH, Tuch DS, Greve DN, et al. Age-related alterations in white matter microstructure measured by diffusion tensor imaging. *Neurobiol Aging*. 2005;26(8):1215-27.

115. Michielse S, Coupland N, Camicioli R, et al. Selective effects of aging on brain white matter microstructure: a diffusion tensor imaging tractography study. *Neuroimage*. 2010;52(4):1190-201.

116. Lebel C, Walker L, Leemans A, Phillips L, Beaulieu C. Microstructural maturation of the human brain from childhood to adulthood. *Neuroimage*. 2008;40(3):1044-1055.

117. Fjell AM, Walhovd KB, Westlye LT, et al. When does brain aging accelerate? Dangers of quadratic fits in cross-sectional studies. *Neuroimage*. 2010;50(4):1376-83.

118. Vernooij MW, Ikram MA, Tanghe HL, et al. Incidental findings on brain MRI in the general population. *N Engl J Med*. 2007;357(18):1821-1828.

119. Jenkinson M, Beckmann CF, Behrens TEJ, Woolrich MW, Smith SM. FSL. *Neuroimage*. 2012;62(2):782-90.

120. Van Opbroek A, Ikram MA, Vernooij MW, de Bruijne M. A Transfer-Learning Approach to Image Segmentation Across Scanners by Maximizing Distribution Similarity. *MICCAI 2013 Work Mach Learn Med imaging*. 2013.

121. Kochunov P, Thompson PM, Lancaster JL, et al. Relationship between white matter fractional anisotropy and other indices of cerebral health in normal aging: tract-based spatial statistics study of aging. *Neuroimage*. 2007;35(2):478-487.

122. Groves AR, Smith SM, Fjell AM, et al. Benefits of multi-modal fusion analysis on a large-scale dataset: life-span patterns of inter-subject variability in cortical morphometry and white matter microstructure. *Neuroimage*. 2012;63(1):365-80.

123. Eckstein I, Shattuck DW, Stein JL, et al. Active fibers: matching deformable tract templates to diffusion tensor images. *Neuroimage*. 2009;47 Suppl 2:T82-T89.

124. Toga A, Thompson P, Mori S, Amunts K, Zilles K. Towards multimodal atlases of the human brain. *Nat Rev Neurosci*. 2006;7(12):952-966.

125. Ball S, Gilbert TL, Overly CC. The human brain online: an open resource for advancing brain research. *PLoS Biol*. 2012;10(12):e1001453.

126. Yeatman JD, Dougherty RF, Myall NJ, Wandell BA, Feldman HM. Tract Profiles of White Matter Properties: Automating Fiber-Tract Quantification. Beaulieu C, ed. *PLoS One*. 2012;7(11):e49790.

127. Maddah M, Wells WM, Warfield SK, Westin C-F, Grimson WEL. Probabilistic clustering and quantitative analysis of white matter fiber tracts. *Inf Process Med Imaging*. 2007;20:372-383.

128. O'Muircheartaigh J, Vollmar C, Traynor C, et al. Clustering probabilistic tractograms using independent component analysis applied to the thalamus. *Neuroimage*. 2011;54(3):2020-32.

129. Zhu H, Kong L, Li R, et al. FADTTS: functional analysis of diffusion tensor tract statistics. *Neuroimage*. 2011;56(3):1412-25.

130. Niethammer M, Zach C, Melonakos J, Tannenbaum A. Near-tubular fiber bundle segmentation for diffusion weighted imaging: segmentation through frame reorientation. *Neuroimage*. 2009;45(1 Suppl):S123-S132.

131. Barbieri S, Bauer MHA, Klein J, Nimsky C, Hahn HK. Segmentation of fiber tracts based on an accuracy analysis on diffusion tensor software phantoms. *Neuroimage*. 2011;55(2):532-44.

132. Barbieri S, Bauer MHA, Klein J, Moltz J, Nimsky C, Hahn HK. DTI segmentation via the combined analysis of connectivity maps and tensor distances. *Neuroimage*. 2012;60(2):1025-35.

133. Alexander AL, Hasan K, Kindlmann G, Parker DL, Tsuruda JS. A geometric analysis of diffusion tensor measurements of the human brain. *Magn Reson Med*. 2000;44(2):283-291.

134. Latour LL, Warach S. Cerebral spinal fluid contamination of the measurement of the apparent diffusion coefficient of water in acute stroke. *Magn Reson Med*. 2002;48(3):478-86.

135. Pfefferbaum A, Sullivan EV. Increased brain white matter diffusivity in normal adult aging: relationship to anisotropy and partial voluming. *Magn Reson Med*. 2003;49(5):953-961.

136. Metzler-Baddeley C, O'Sullivan MJ, Bells S, Pasternak O, Jones DK. How and how not to correct for CSF-contamination in diffusion MRI. *Neuroimage*. 2012.

137. Berlot R, Metzler-Baddeley C, Jones DK, O'Sullivan MJ. CSF contamination contributes to apparent microstructural alterations in mild cognitive impairment. *Neuroimage*. 2014;92C:27-35.

138. Mielke MM, Okonkwo OC, Oishi K, et al. Fornix integrity and hippocampal volume predict memory decline and progression to Alzheimer's disease. *Alzheimers Dement*. 2012;8(2):105-13.

139. Fletcher E, Raman M, Huebner P, et al. Loss of Fornix White Matter Volume as a Predictor of Cognitive Impairment in Cognitively Normal Elderly Individuals. *JAMA Neurol*. 2013;95616:1-7.

140. Prawiroatmodjo G. *TEDxDELFT Salon: Redefining High-impact Science*. Delft; 2012:http://youtu.be/zJwOKMHOlwI.

141. Marcus DS, Olsen TR, Ramaratnam M, Buckner RL. The Extensible Neuroimaging Archive Toolkit: an informatics platform for managing, exploring, and sharing neuroimaging data. *Neuroinformatics*. 2007;5(1):11-34.

142. Marcus DS, Harms MP, Snyder AZ, et al. Human Connectome Project informatics: quality control, database services, and data visualization. *Neuroimage*. 2013;80:202-19.

143. Bischoff-Grethe A, Ozyurt IB, Busa E, et al. A technique for the deidentification of structural brain MR images. *Hum Brain Mapp*. 2007;28(9):892-903.

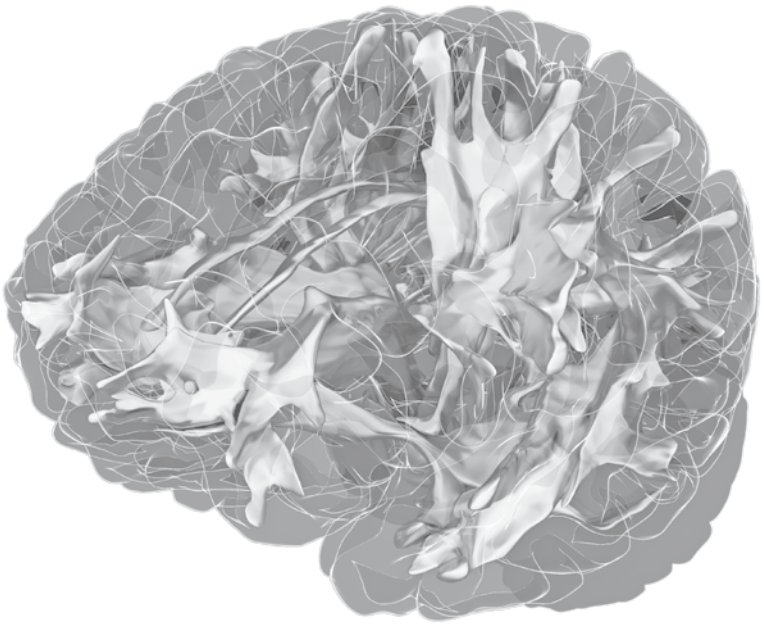

6.1
English Summary

English summary

As our life expectancy continues to rise, the prevalence of diseases associated with aging increases correspondingly. For Alzheimer's disease, this implies that the number of persons affected, directly or indirectly, will rise dramatically. Early diagnosis, intervention, and ultimately prevention of Alzheimer's disease are therefore ever more urgent research aims. Advanced neuroimaging techniques such as diffusion MRI, which provides non-invasive insight into brain changes at the microstructural level, are promising for the identification of changes that relate to the early stages of the disease. Disentangling these early pathological changes from those in 'normal' brain aging however requires more insight in the broad spectrum of brain changes that commonly accompany advancing age. Investigating these changes in a population-based context poses novel challenges by demanding new and advanced methods for analyzing the large number of subjects effectively.

In this thesis, I therefore presented novel methodology for cross subject image analysis in diffusion brain MRI. Subsequently, I presented investigations of brain white matter microstructure in relation to age, cardiovascular risk factors and macrostructural white matter changes. Studies focusing on changes in brain white matter microstructure in the context of small vessel disease were presented last.

Improving cross subject diffusion analysis

The rich characterization of the white matter that is encoded in a diffusion MRI acquisition allows for a wide variety of methods to be applied on the data. Tractography methods integrate as much of the local diffusion information as possible with the aim of identifying and segmenting entire white matter tracts. To identify the cingulum and at the same time parameterize this tube-like white matter structure for analysis, an iterative tract selection and pruning strategy was devised (in Chapter 2.1). With this approach, left-right asymmetry in the cingulum was investigated in a group of 500 participants from the Rotterdam Study. The analysis revealed left higher than right microstructural organization in the anterior part of the cingulum, and a reverse contrast in the parahippocampal part of the cingulum. The limitations of the deterministic tractography used in this approach did however also become apparent, as the cingulum could often not be identified in its entirety. For the next approach that relied on extracting white matter structures (Chapter 2.2), a more robust strategy based on probabilistic tractography was therefore adopted. This chapter focused on the quantitative evaluation of registration accuracy, which is relevant as neuroimaging research often relies on image registration for establishing correspondence across subjects. In this work, registration accuracy was defined

as the similarity, after registration, of white matter tracts across subjects. We used native space tractography that was initialized by anatomic definitions in standard space to extract 23 white matter tracts that covered the whole brain. The (highly reproducible) registration accuracy measurement was then used to optimize registration parameters for two widely used registration algorithms, FNIRT and elastix. Ultimately we showed that both high degree-of-freedom registration algorithms outperformed the registration accuracy of the popular tract-based spatial statistics (TBSS) method. This result demonstrates the feasibility of adopting an optimized registration approach instead of the registration-projection cascade that is currently used in TBSS.

Establishing anatomical correspondence was also the aim in Chapter 2.3, in which we focused on the development of white matter lesions. For this approach, we aimed to establish correspondence over multiple (longitudinal) imaging sessions, but also across participants in standard space, using a population of just under 700 participants and a follow-up interval of 3.5 years. By investigating tissue that at follow-up had converted from normal appearing white matter to a white matter lesion, we were able to show that this seemingly normal white matter was already different before the visually appreciable white matter lesions developed. This difference was, furthermore, evident regardless of whether the lesion was growing or newly appearing. These observations support the hypothesis that white matter lesions develop gradually, and that they are just the tip of the iceberg of white matter pathology.

Diffusion imaging in aging

A better understanding of changes in tissue microstructure with age provides the necessary context for the interpretation of changes observed with neurodegenerative diseases. Within the Rotterdam Study, we therefore investigated multiple features of microstructural change with age. First, in Chapter 3.1, we focused on change in structural connections with aging in a cross-sectional design. By choosing entire white matter tracts as regions of interest, we investigated tract microstructure in relation to age, macrostructural white matter changes and cardiovascular risk factors. In a population of over 4,500 participants, we measured diffusion characteristics in 25 white matter tracts. With increasing age, we observed loss of microstructural organization in association, commissural and limbic tracts. These changes could partly be explained by macrostructural white matter changes. Additional loss of microstructural organization was observed with severe hypertension, current smoking and with diabetes mellitus. While these changes may more sensitively mark neurodegenerative pathology than macrostructural white matter changes can, the design of the study was cross-sectional. Very few studies have actually investigated change in diffusion characteristics over time. In order to investigate changes in tis-

sue microstructure with increasing age, we therefore performed a longitudinal analysis, which is described in Chapter 3.2. This analysis was performed in a group of 501 participants with a follow-up interval of 2.0 years, using the improved version of TBSS developed in Chapter 2.2, and using the longitudinal registration framework developed in Chapter 2.3. We investigated changes in diffusion measurements over time and in relation to cardiovascular risk factors, while constraining the analysis to the normal appearing white matter. Over time, we observed reduced fractional anisotropy (FA) and increased mean diffusivity (MD) in the majority of brain white matter, consistent with reductions in microstructural organization. In the majority of the sensorimotor pathways however, we observed an *increase* in FA combined with an increase in MD. These are changes that may reflect relative sparing of the sensorimotor pathways in crossing fiber configurations with fibers that follow the more general trend of reduced microstructural organization.

Diffusion imaging in small vessel disease

Cerebral small vessel disease is a condition which affects the smallest blood vessels in the brain and which is associated with an increased risk of stroke and dementia. Subclinical manifestations of the disease can be seen on imaging as macrostructural white matter changes (e.g. white matter lesions and white matter atrophy) and e.g. cerebral microbleeds. Assuming that microstructural changes accumulate over time into macrostructural changes, and keeping in mind that visible white matter lesions appear to indicate only a fraction of the total white matter pathology, it is relevant to further investigate how small vessel disease affects tissue microstructure. In an initial analysis (Chapter 4.1), we investigated white matter microstructure in relation to age and macrostructural white matter changes in a population of over 800 participants using TBSS. We identified widespread loss of microstructural organization, reflected in reduced FA and increased axial and radial diffusivities with increasing age. This loss could however be primarily explained by macrostructural white matter changes, i.e. either by white matter atrophy, or by white matter lesion load. In a subsequent analysis (Chapter 4.2), we focused on cerebral microbleeds and white matter microstructure. We measured diffusion measurements in the entire normal appearing white matter of almost 4,500 participants, and visually assessed their microbleed status. We identified progressively worse white matter microstructural organization associated with both presence and number of microbleeds. Interestingly, worse microstructure was related to presence of even a single microbleed, suggesting that also microbleeds reflect diffuse white matter pathology beyond the focal lesions themselves.

Microstructural changes associated with mild cognitive impairment have often been attributed to Alzheimer's disease pathologic changes. The relatively high prevalence of small vessel disease amongst patients with mild cognitive impairment

could however also allow for a vascular etiological pathway. In order to investigate this hypothesis, in Chapter 4.3 we compared diffusion characteristics between patients with mild cognitive impairment and controls, while subdividing the patient group into those with and those without evidence of small vessel disease as revealed by white matter lesions on MRI. Using TBSS and analyzing tracts that are part of the default mode network, we found reduced microstructural organization mainly associated with small vessel disease, and only minor differences between patients with mild cognitive impairment without small vessel disease and controls. Additionally, we found evidence of small vessel disease related changes in microstructural organization in tracts that subserve the default mode network. These findings indicate the importance of taking small vessel disease into account when investigating patients with mild cognitive impairment.

Concluding

In this thesis I have introduced analytical approaches that enable novel analyses of brain diffusion MRI data. The improved anatomical correspondence, both over time and across subjects, enable more sensitive analyses. The automated tractography unlocks a number of advanced analysis approaches for population imaging studies, and holds promise for clinical applications. With increasing age and with vascular risk factors, we identified loss of microstructural organization in large parts of the brain white matter. These changes could only partially be explained by macrostructural white matter changes, and more sensitively reflect subtle white matter pathologies. Our findings highlight the sensitivity of the white matter to vascular pathology in general, and small vessel disease in particular. Future investigations can benefit from this work by adopting or building on the presented methods, and also by further investigating the identified microstructural changes with age and vascular risk factors.

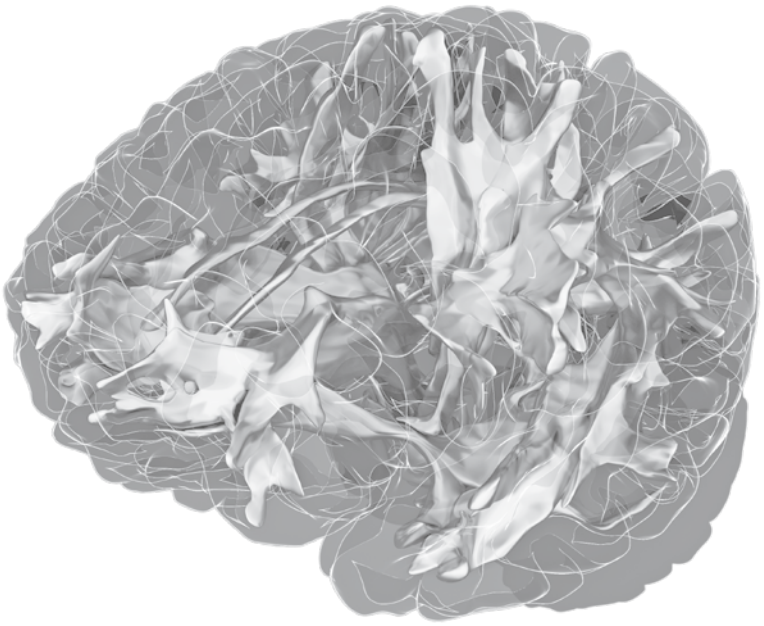

6.2
Nederlandse Samenvatting

Nederlandse samenvatting

Omdat we steeds ouder worden komen ouderdomsziektes vaker en vaker voor. Zo wordt een dramatische toename verwacht van patiënten met de ziekte van Alzheimer. Met almaar groeiende inzet zoekt de wetenschap dan ook naar manieren om het ziekteproces van Alzheimer dementie te vertragen en eventueel zelfs te voorkomen. Voorwaarde hiervoor is echter wel dat de ziekte al in een vroeg stadium herkend moet kunnen worden. Met name nieuwe beeldvormende technieken zijn hierbij veelbelovend. Diffusie MRI geeft bijvoorbeeld zonder gebruik van ioniserende straling of contrastmiddel inzicht in de veranderende microstructuur van de hersenen. Beter begrip van de vroege veranderingen die samenhangen met neurodegeneratieve ziekten begint echter bij een goed begrip van de veranderingen die samenhangen met 'normale' veroudering. Begrip waarvoor bevolkingsstudies, waarin grote groepen vrijwilligers langere tijd gevolgd kunnen worden, cruciale inzichten kunnen verschaffen. Om diffusie MRI beelden in zulke studies op een effectieve manier te kunnen analyseren, zijn echter nieuwe, geavanceerde methodes vereist.

In dit proefschrift heb ik meerdere nieuwe methodes beschreven om de analyse van diffusie MRI beelden over grote groepen mensen mogelijk te maken. Aansluitend heb ik gekeken naar de relatie tussen leeftijd en microstructuur van de witte stof van de hersenen. Hierbij heb ik ook de invloed van risicofactoren voor hart en vaatziekten, én de invloed van macroscopische veranderingen in de witte stof meegenomen. Macroscopische veranderingen in de witte stof zijn hierbij veel voorkomende veranderingen die op structurele MRI scans zichtbaar zijn, waarbij ik onderscheid heb gemaakt tussen atrofie (weefselverlies) en het optreden van witte stof lesies. Als laatste heb ik de microstructuur van de witte stof onderzocht in relatie tot schade aan de zeer kleine hersenvaten, ook wel cerebrale microangiopathie genoemd. Deze aandoening komt veel voor, en omvat een scala aan presymptomatische veranderingen in de hersenen die samen hangen met beschadigingen aan de kleinste bloedvaten van het brein. De Rotterdam Studie, de bevolkingsstudie waar het grootste deel van dit proefschrift op is gebaseerd, volgt nauwgezet de gezondheidstoestand van de duizenden deelnemers. Sinds 2005 beschikt de studie ook over een eigen MRI scanner waarmee deelnemers volgens gestandaardiseerde protocollen worden gescand. Inmiddels zijn er zodoende al meer dan tienduizend hersenscans gemaakt.

Verbeteringen in de analyse van diffusie beelden over meerdere personen

Omdat het diffusie signaal zoals we dat kunnen meten met diffusie MRI zo'n rijke beschrijving geeft van de onderzochte witte stof, is er een waar arsenaal aan analysemethoden beschikbaar voor deze data. Tractografie combineert zo veel mogelijk van de informatie die op iedere anatomische plek in het brein gemeten is, met het doel om hele witte stof banen, in feite de verbindingskabels in de hersenen, te kunnen onderzoeken. Hoofdstuk 2.1 presenteert een nieuwe methode om het cingulum, een draadvormige verbinding die onder meer belangrijk is voor het geheugen, te vinden en gelijktijdig te bemeten. Vernieuwend in deze aanpak was het almaar verfijnen van de gevonden bundel door het toevoegen en wegknippen van (delen van) vezels die al dan niet onderdeel van de gezochte structuur leken uit te maken. Met deze aanpak hebben wij links-rechts asymmetrie onderzocht in een groep van 500 deelnemers aan de Rotterdam Studie. Hierbij vonden we dat de microstructuur in het voorste deel van het cingulum meer georganiseerd was aan de linkerzijde, en een omgekeerd verschil vonden wij voor het cingulum ter hoogte van de hippocampus. In Hoofdstuk 2.2 heb ik opnieuw tractografie gebruikt om witte stof banen automatisch te vinden. Van de gevonden banen konden er 23 worden gebruikt om de kwaliteit van het registreren van diffusie beelden te kunnen meten en verbeteren. Dit is belangrijk, omdat door deze registratie anatomisch corresponderende gebieden vergeleken kunnen worden tussen verschillende personen: hoe beter de registratie, des te nauwkeuriger de analyse. Door het nauwkeurig kunnen vergelijken van verschillende registraties, was het mogelijk om de instellingen van twee veelgebruikte registratiealgoritmes (FNIRT en elastix) te optimaliseren. Nog belangrijker echter, was de bevinding dat de registratiekwaliteit van beide algoritmes hoger was dan die van de veelgebruikte 'tract-based spatial statistics' (TBSS) aanpak, en dat deze analysemethode dus verbeterd kan worden door het gebruik van de meer verfijnde registraties.

Ook in Hoofdstuk 2.3 richtte ik mij op het verbeteren van de registratie, maar nu met het doel om meer inzicht te verkrijgen in de ontstaansgeschiedenis van witte stof lesies. Met een nieuwe methode vonden wij anatomische correspondentie tussen opvolgende scans van de deelnemers (correspondentie over tijd), maar ook tussen de bijna 700 deelnemers onderling (correspondentie tussen personen). Analyse van de witte stof die tussen de eerste en de tweede scan, een periode van gemiddeld 3.5 jaar, veranderde in een witte stof lesie, toonde dat deze witte stof al aan structuurverlies lijdt voordat de lesies zichtbaar worden. Dit verschil was zowel zichtbaar voor de aangroei aan bestaande lesies, als voor lesies die zich nieuw ontwikkelden. Deze observaties versterken de gedachte dat we met witte stof lesies eigenlijk slechts naar het topje van de ijsberg van totale witte stof schade kijken.

Diffusie MRI in veroudering

Een beter begrip van de microstructurele veranderingen die het brein ondergaat bij veroudering, biedt een kader voor het bestuderen van veranderingen die optreden bij neurodegeneratieve ziekten. Binnen de Rotterdam Studie heb ik dan ook meerdere aspecten van de veroudering van witte stof van het brein onderzocht. In Hoofdstuk 3.1 onderzocht ik microstructuur in verbindingsbanen als functie van leeftijd, vasculaire risicofactoren en macroscopische veranderingen. Voor 25 verbindingen analyseerden wij diffusie karakteristieken in een populatie van ruim 4,500 deelnemers. Met toenemende leeftijd vonden wij een verlies van microstructurele organisatie in witte stof banen met verschillende functies, te weten: associatieve, commissurele en limbische banen. Deze veranderingen werden deels verklaard door macrostructurele veranderingen, dus door de gelijktijdige aanwezigheid van atrofie en witte stof lesies. Tevens vonden wij additionele schade die samenhing met een sterk verhoogde bloeddruk, roken en diabetes mellitus. Deze veranderingen maken wellicht een gevoeliger identificatie van neurodegeneratieve processen mogelijk dan dat macroscopische veranderingen dit kunnen, maar de cross-sectionele studieopzet blijft een beperking om causale verbanden te kunnen identificeren. Omdat er tot nu toe maar weinig bekend was over microstructuur bij veroudering in een longitudinaal verband, heb ik een dergelijke analyse beschreven in Hoofdstuk 3.2. Voor deze analyse onderzocht ik 501 deelnemers over een tijdsbestek van twee jaar met de verbeterde versie van TBSS zoals beschreven in Hoofdstuk 2.2, en met gebruikmaking van de longitudinale registratie zoals beschreven in Hoofdstuk 2.3. Hiermee werd gekeken naar veranderingen in diffusie karakteristieken over tijd en in relatie tot vasculaire risicofactoren. In het grootste deel van het brein nam de fractionele anisotropie (FA) af, en nam de gemiddelde diffusiviteit (D) toe, hetgeen overeenkomt met een afname van de gestructureerdheid van de witte stof. Echter, in het grootste deel van de sensorimotor banen nam de FA juist *toe* in combinatie met een toename in D. Dit zou kunnen wijzen op een relatief behoud van deze banen, die betrokken zijn bij de belangrijkste bewegings- en gevoelsfuncties, bij veroudering.

Analyse van diffusie MRI in cerebrale microangiopathie

Cerebrale microangiopathie is een aandoening waarbij de kleinste bloedvaten in de hersenen worden aangetast en die samenhangt met een verhoogd risico op beroerte en dementie. Geavanceerde beeldvormingstechnieken maken verschillende preklinische verschijnselen van de aandoening zichtbaar, zoals de eerder genoemde macroscopische witte stof veranderingen maar ook microbloedingen. Wij observeerden eerder al een onderschatting van de totale witte stof pathologie bij bestu-

dering van alleen witte stof lesies. Daarnaast mogen we aannemen dat opstapelende microstructurele veranderingen over tijd leiden tot macrostructurele veranderingen. Het is dan ook van groot belang om meer inzicht te verkrijgen in de relatie tussen cerebrale microangiopathie en de microstructuur van de witte stof. In een eerste analyse (Hoofdstuk 4.1) onderzocht ik, met TBSS de witte stof microstructuur in relatie tot leeftijd en de macroscopische witte stof veranderingen in een populatie van ruim 800 deelnemers aan de Rotterdam Studie. Wij vonden dat verlies van microstructuur, gereflecteerd in een verlaagde FA en verhoogde diffusiviteit, samenhing met een hogere leeftijd. Deze veranderingen werden echter vrijwel volledig verklaard door macroscopische witte stof veranderingen, dus ofwel door witte stof atrofie, ofwel door witte stof lesies. In een volgende analyse (Hoofdstuk 4.2) onderzochten we de relatie tussen zichtbare microbloedingen en witte stof microstructuur, gemeten over de totale witte stof van het brein. In de bijna 4,500 deelnemers vonden wij een sterker verlies van microstructurele organisatie bij een toenemend aantal microbloedingen. Opvallend genoeg was zelfs bij deelnemers met slechts één microbloeding al sprake van een minder georganiseerde microstructuur, hetgeen suggereert dat ook microbloedingen een reflectie zijn van meer uitgebreide hersenschade dan uitsluitend de plek van de kleine lesie zelf.

Veranderingen van de microstructuur die gevonden worden bij patiënten met een geringe cognitieve stoornis, ook wel mild cognitive impairment (MCI) genoemd, worden vaak toegeschreven aan pathologische processen van de ziekte van Alzheimer. Omdat cerebrale microangiopathie bij deze patiëntengroep echter ook vaak voorkomt, zou een vasculaire oorzaak echter ook een mogelijke verklaring kunnen bieden. Om deze hypothese te onderzoeken vergeleken we in Hoofdstuk 4.3 diffusie karakteristieken tussen patiënten met MCI en gezonde deelnemers, waarbij binnen de MCI groep onderscheid werd gemaakt tussen patiënten met, en patiënten zonder tekenen van cerebrale microangiopathie op MRI. Middels TBSS en een analyse van witte stof banen die onderdeel uit maken van het zogenaamde 'functionele default-netwerk' van het brein, vonden wij verminderde microstructuur die voornamelijk samenhing met de aanwezigheid van cerebrale microangiopathie. Slechts in beperkte mate werd er verschil gevonden tussen patiënten mét MCI maar zonder cerebrale microangiopathie en de controle groep. Tevens vonden wij aanwijzingen voor microstructurele veranderingen in witte stof banen van het defaultnetwerk samenhangend met cerebrale microangiopathie. Deze bevindingen onderschrijven het belang van het betrekken van cerebrale microangiopathie in hersenonderzoek bij patiënten met MCI.

Concluderend

In dit proefschrift beschreef ik verschillende methoden om vernieuwende analyses van diffusie MRI beelden mogelijk te maken. De verbeterde correspondentie, zowel over tijd als tussen personen, maakt gevoeliger analyses mogelijk. De automatische tractografie brengt een aantal geavanceerde analyses binnen bereik van grote bevolkingsstudies, en zal in de toekomst ook voor klinische toepassingen relevant zijn. Bij veroudering van het brein, en met vasculaire risicofactoren, toonden deze technieken verlies van microstructuur in de witte stof. Deze veranderingen hingen deels samen met macroscopische veranderingen in de witte stof, maar niet volledig, hetgeen bevestigt dat deze metingen gevoeliger zijn voor pathologie. Deze bevindingen onderschrijven verder dat de witte stof zeer gevoelig is voor vasculaire pathologie in het algemeen, en cerebrale microangiopathie in het bijzonder. Toekomstige studies zullen kunnen voortbouwen op de analyse methoden enerzijds, en op de gevonden relaties met microstructuur bij veroudering anderzijds.

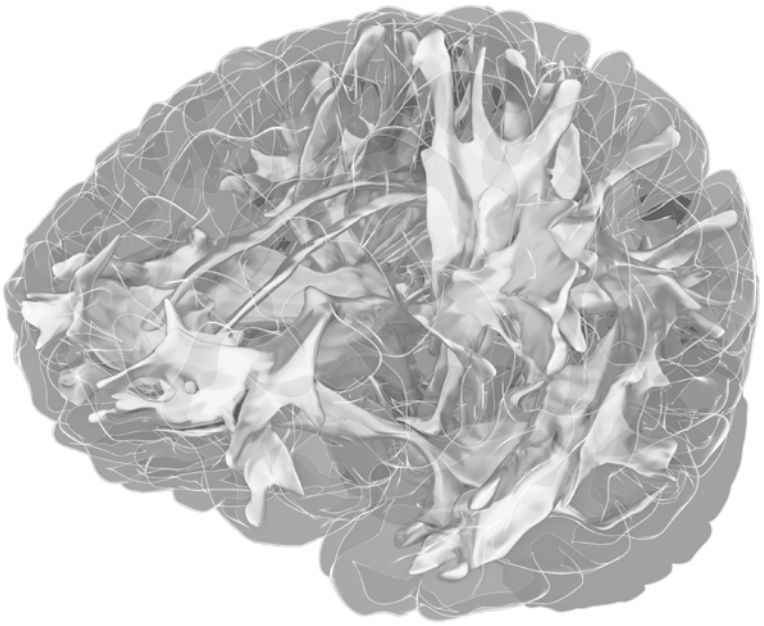

Dankwoord

Dankwoord

Een promotie is een bijzonder traject, je kunt zovéél verantwoordelijkheid naar je toehalen als je wilt, hebt jaren de tijd om iets moois op te bouwen, en kunt met gelijkgestemden van over de hele wereld sparren en lol maken op conferenties. Voor mij was het een geweldige tijd waar ik me volledig voor heb ingezet. Zoiets kan echter alleen in een omgeving waar vertrouwen heerst en waar men er naar streeft het beste in iedereen naar boven te halen. De onderzoeksomgevingen binnen de Biomedical Imaging Group Rotterdam en de afdeling Neuro Epidemiologie van het Erasmus MC waren wat dat betreft essentieel en boden kennis, kansen en ontspanning. Deze omgevingen ontstaan niet vanzelf en aan iedereen die zich over de jaren heeft ingezet voor deze warme omgevingen ben ik dan ook grote dank verschuldigd. Toch wil ik ook een aantal mensen in het bijzonder bedanken voor alles wat de afgelopen jaren zo interessant en fijn heeft gemaakt.

Ten eerste wil ik Wiro Niessen bedanken voor het vertrouwen. Wiro, dankzij jouw betoverende mix van vertrouwen in de mensen om je heen, een helder punt op de horizon en een enthousiasme voor het nieuwe, voelde ik me direct verbonden. Je creëerde in Rotterdam een bijzondere omgeving waarbinnen zo ongeveer alles mogelijk is, met veel connecties, weinig politiek en een mentaliteit van opgestroopte mouwen. Dank voor de vele openhartige gesprekken, vaak ook niet over het onderzoek, en voor de spannende buitenlandse avonturen.

Ook Meike Vernooij wil ik hartgronding bedanken. Lieve Meike, een diepe bewondering heb ik voor je inzicht en persoonlijke effectiviteit. In jouw rol als co-promotor heb ik onnoemelijk veel van je kunnen leren, ben je een mentor en een inspirator. Dankzij jou geen grenzen tussen de epidemiologie en de beeldanalyse. Bedankt voor het uitdagen, de kansen, de lol in het werk en het vertrouwen. Ik had me geen betere co-promotor kunnen wensen! Belangrijker voor onze klik is echter de houding die wij denk ik delen, dat je ergens volledig voor gaat, en anders niet. Via die verwantschap leerden we elkaar kennen en ontwikkelden we onze hechte vriendschap. Een vriendschap die voortleeft, waar de toekomst ons ook mag brengen.

I would like to thank the committee members to whom I will be defending my thesis to in October. A special thanks to professors Frederik Barkhof, Peter Koudstaal and Steve Smith for their additional efforts in taking part in the inner committee; and the plenary members, professors Christian Beckmann, Arfan Ikram and Aad van der Lugt, thank you all for your time and your willingness to take part in my defense.

Hanneke Pieters, dank je voor al je geduld en je tomeloze energie om de wereld om je heen een mooiere plek te maken. Lieve mattie, aan een half woord heb je genoeg, je bent een ontzettend fijn en bijzonder mens. Het was heerlijk om af en toe een avond met jou uit het onderzoek te stappen voor een echt gesprek of een prachtig concert. Ik ben erg gelukkig en trots dat jij naast me staat in Oktober, matties forever!

Lieve Jory, dank voor je onvoorwaardelijke steun en voor je onvermoeibare vechtlust voor het goede. In de moeilijke momenten waren we er voor elkaar door dik en dun. De mooie momenten waren daardoor des te briljanter. Ik heb ontzettend genoten van alle borrels, dansjes, etentjes, het klussen, je Delftse humor, de popconcertjes (en de meet en greet achteraf), het wii-en en je genadeloze grappen. Bedankt voor alle onvoorstelbare avonturen. Je bent een intens persoon, een soulmate, en de ongekroonde borrelkoningin van Rotterdam eo.

When spending so much time at work, you better make sure that your co-workers are your friends. In that respect, I could not have been luckier. To all at BIGR, Medical Informatics and Radiology, I would like to express my gratitude for the perfect atmosphere. Renske en Fedde bedankt voor het kameraadschap vanaf mijn allereerste dag. Dankzij het enthousiasme en de inzet van jullie, Coert, Michiel en Reinhard kon de vakgroep de groei aan. Dank voor alle gezelligheid en het voorbeeld dat jullie neergezet hebben. Also Annegreet, Esben, Esther, Gennady, Gerardo, Ghassan, Gijs, Hakim, Henri, Hortense, Marcel, Mart, Nora, Petra, Rahil, Stefan, Wyke and Yuan, thank you for all your warm contributions to all the side projects, borrels, barbecues, and the small moments with a discussion over a cup of coffee or just joining me in looking out of the widow. This is what makes BIGR feel like a family. Coert bedankt voor de (nachtelijke) step wedstrijdjes door het ziekenhuis. Hakim en Marcel bedankt voor de hilarische acroniemen, de hartelijkheid, het op peil brengen/houden van mijn nerdgehalte en ons gezamelijke toezicht op de bouwplaats. Marcel bedankt dat je mijn paranimf wil zijn. Marleen ik vond het erg leuk om met jou samen te werken, dank voor je openheid en je toewijding. Dear Yuan, you were the perfect student I could ever wish for, thanks for your patience, wit and commitment. Vera bedankt voor onze gesprekken en je hartelijkheid. Mart en Henri, dank voor het altijd oplossen van de puzzels op IT en opslaggebied. Desiree en Petra, dank voor al jullie organisatorische oplossingen, het meedenken en het regelen, jullie zijn geweldig.

Aad van der Lugt ik ben blij dat ik heb mogen leren van jouw kennis, realisme en tact. Onze population imaging discussies waren enerverend en spannend, over 5 jaar is het daar, daar twijfel ik niet aan, ik ben vooral benieuwd naar alle avonturen die je op weg daar naartoe nog gaat beleven.

To Steve and Karla, thank you both so much for being so generous and warm in making me feel part of FMRIB during my visit. You have set the best example I have ever seen for caring for a visitor. Also Gwen, Eugene, Lisa, Adrian, Saad, Jingie, Jesper and Katie, you guys made sure that every day was worth remembering. We had just so much fun, good dinners and the occasional bender, thank you all for the blast and the positivity.

Alle lieve mensen van de epidemiologie wil ik ook graag bedanken: Arfan, Ben, Elisabeth, Hazel, Hieab, Jory, Liz, Lotte, Mariëlle, Mendel, Monique, Ryan, Saloua, Vincent en Vincent. Bedankt voor de gezelligheid en het geduld als jullie weer langer op datasets moesten wachten. Veel dank ook voor de inspiratie en de epidemiolgische inzichten, dankzij jullie had ik het idee dat ik af en toe nog iets nuttigs deed. Daarbij zijn jullie een ontzettend leuke en gezellige groep waar ik me altijd zeer welkom heb gevoeld. Saloua onze papers samen waren een feestje, gedegen maar soepel. Dank voor je grote jouw inzet en superpositieve instelling. Ben, bedankt voor ons mooie paper samen, een prachtig voorbeeld van een Epi-BIGR samenwerking waarbij de revisies over en weer het paper elke keer weer leesbaarder maakten. Hieab, dank voor je ongebreidelde enthousiasme, het is inspirerend om te zien hoe veel lol je in het onderzoek hebt en brengt.

Alle fijne mensen die ik verder nog heb leren kennen in het Erasmus MC wil ik ook bedanken voor de mooie gesprekken en de gezellige borrels. Bedankt Carolina, Christianne, Janneke, Martine, Rebecca en Rozanna. Ton, dank voor de supergrappige, spitsvondige momenten tussendoor. Veel dank ook voor de bezielende hulp bij allerhande grafische stress. Janne dank je wel voor je lieve aandacht, je humor en de afleiding op een moment dat er geen land met mij te bezeilen was.

All people that I, over the years, spent time with at conferences I would like to thank for the amazing nighttime adventures. Nothing beats celebrating a successful presentation with a night on the dance floor. I have learned that broken knees and torn pants are acceptable collateral damage. A special thanks in this regard to Marion, Liz, Saloua, Janne, Elise, Hanan, Gerbrich, Alexander and Wiro.

Renske, heel erg bedankt voor de fijne tijd die we samen hebben gehad, de avonturen die we hebben beleefd, van woestijn tot bayou; hoe we samen gegroeid zijn, dat gaat niet voorbij.

Ook alle Delftse vrienden bedankt. Bedankt Jansbrug. Bedankt Paardemarkt: Ali, Gydo, Hester, Jagers, Manon en Noor voor de gezellige borrels en breedsprakige whatsapp discussies. Gijs-Jan en Caat voor het gezellige koken, de mooie feestjes en de geweldige weekendjes in Ranzières. A big special thanks to the ski tourers: Franz, Friso, Gerhard, Gijs-Jan, Hein, Kim, Nick, Paul and Wiet. Our tours have

grown into an amazing tradition and I'm looking forward to next year from the day we come home. Thanks for the pow-pow, the exhaustion, the kwalitätsmusik and the topfenstrudel.

Dear Katja, you give me wings and make everything leuk en lekker. The sun never rose prettier than it did those early mornings with you, and it never seemed to have set since. You make me silent and happy, you are incredible.

Als laatste wil ik mijn lieve ouders bedanken. Die er altijd waren en zijn, lieve Anneke en Herman, bedankt. Bij alles wat ik van jullie in mezelf herken voel ik trots. Bedankt voor alle zorg en liefde.

Marius de Groot, Augustus 2014

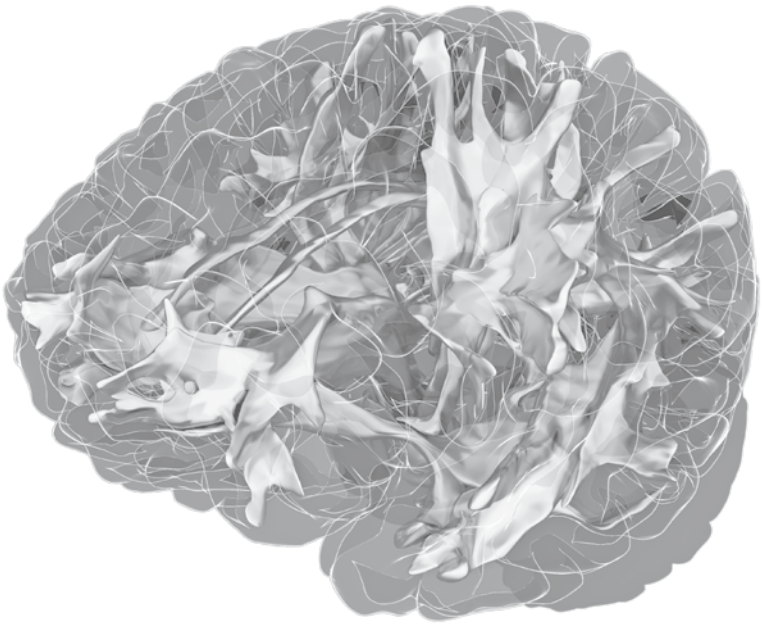

List of publications

Journal papers

- **M. de Groot**, L. Cremers, M. A. Ikram, A Hofman, G. P. Krestin, A. van der Lugt, W. J. Niessen and M. W. Vernooij. "White matter degeneration in aging, a longitudinal diffusion MRI analysis," submitted.

- **M. de Groot**, M. A. Ikram, S. Akoudad, G. P. Krestin, A. Hofman, A. van der Lugt, W. J. Niessen and M. W. Vernooij, "Tract-specific white matter degeneration in aging. The Rotterdam Study," *Alzheimer's & Dementia*, in press.

- V. J. A. Verlinden, J. N. van der Geest, **M. de Groot**, A. Hofman, W. J. Niessen, A. van der Lugt, M. W. Vernooij and M. A. Ikram, "Structural and microstructural brain changes predict impairment in daily functioning," *American Journal of Medicine*, in press.

- J. M. Papma, **M. de Groot**, I. de Koning, F. U. Mattace-Raso, A. van der Lugt, M. W. Vernooij, W. J. Niessen, J. C. van Swieten, P. J. Koudstaal, N. D. Prins and M. Smits, "Cerebral small vessel disease affects white matter microstructure in mild cognitive impairment," *Human Brain Mapping*, vol. 35, no. 6, pp. 2836–51, 2014.

- V. Koppelmans, **M. de Groot**, M. B. de Ruiter, W. Boogerd, C. Seynaeve, M. W. Vernooij, W. J. Niessen, S. B. Schagen, M. M. B. Breteler, "Global and focal white matter integrity in breast cancer survivors 20 years after adjuvant chemotherapy," *Human Brain Mapping*, vol. 35, no. 3, pp. 889–99, 2014.

- S. Akoudad, **M. de Groot**, P. J. Koudstaal, A. van der Lugt, W. J. Niessen, A. Hofman, M. A. Ikram and M. W. Vernooij, "Cerebral microbleeds are related to loss of white matter structural integrity," *Neurology*, vol. 81, no. 22, pp. 1930–7, 2013.

- **M. de Groot**, M. W. Vernooij, S. Klein, M. A. Ikram, F. M. Vos, S. M. Smith, W. J. Niessen and J. L. R. Andersson, "Improving alignment in Tract-based spatial statistics: evaluation and optimization of image registration," *NeuroImage*, vol. 76, pp. 400–11, 2013.

- **M. de Groot***, B. F. J. Verhaaren*, R. de Boer, S. Klein, A. Hofman, A. van der Lugt, M. A. Ikram, W. J. Niessen and M. W. Vernooij, "Changes in normal-appearing white matter precede development of white matter lesions," *Stroke*, vol. 44, no. 4, pp. 1037–42, 2013.

- T. den Heijer, F. Van der Lijn, M. W. Vernooij, **M. de Groot**, P. J. Koudstaal, A. van der Lugt, G. P. Krestin, A. Hofman, W. J. Niessen and M. M. B. Breteler, "Structural and diffusion MRI measures of the hippocampus and memory performance," *NeuroImage*, vol. 63, no. 4, pp. 1782–9, 2012.

- R. de Boer, M. Schaap, F. van der Lijn, H. A. Vrooman, **M. de Groot**, A. van der Lugt, M. A. Ikram, M. W. Vernooij, M. M. B. Breteler and W. J. Niessen, "Statistical analysis of minimum cost path based structural brain connectivity," *NeuroImage*, vol. 55, no. 2, pp. 557–65, 2011.

- M. W. Vernooij*, **M. de Groot***, A. van der Lugt, M. A. Ikram, G. P. Krestin, A. Hofman, W. J. Niessen and M. M. B. Breteler, "White matter atrophy and lesion formation explain the loss of structural integrity of white matter in aging," *NeuroImage*, vol. 43, no. 3, pp. 470–7, 2008.

Conference papers

- R. de Boer, M. Schaap, F. van der Lijn, H. A. Vrooman, **M. de Groot**, M. W. Vernooij, M. A. Ikram, E. F. S. van Velsen, A. van der Lugt, M. M. B. Breteler and W. J. Niessen, "Statistical Analysis of Structural Brain Connectivity," *Medical Image Computing and Computer-Assisted Intervention 2010 (MICCAI),* Part II, LNCS 6362, 2010.

- **M. de Groot**, M. W. Vernooij, S. Klein, A. Leemans, R. de Boer, A. van der Lugt, M. M. B. Breteler and W. J. Niessen, "Iterative Co-Linearity Filtering and Parameterization of Fiber Tracts in the Entire Cingulum," *Medical Image Computing and Computer-Assisted Intervention 2009 (MICCAI)*, Part I, LNCS 5761, 2009.

Conference abstracts

- **M. de Groot**, M.A. Ikram, W.J. Niessen and M.W. Vernooij, "White matter tract diffusion measurements in the general population," *AAIC 2013: Alzheimer's Association International Conference*, 2013.

- **M. de Groot**, B. F. J. Verhaaren, R. de Boer, S. Klein, A. Hofman, A. van der Lugt, M. A. Ikram, W. J. Niessen and M. W. Vernooij, "Development of white matter lesions is preceded by changes in normal-appearing white matter," *AAIC 2013: Alzheimer's Association International Conference*, 2013.

- **M. de Groot**, M. W. Vernooij, S. M. Smith, M. A. Ikram, W. J. Niessen and J. Andersson, "Evaluation of registration performance with probabilistic tractography," *HBM 2011: 17th Annual Meeting of the Organization for Human Brain Mapping*, 2011.

- **M. de Groot**, M. W. Vernooij, P. A. Wielopolski, M. M. B. Breteler, A. van der Lugt and W. J. Niessen, "Influence of Parallel Imaging on Regional Fractional Anisotropy Measurements in a Large Population," *RSNA 2009: Radiological Society of North America, 95th Annual Meeting*, 2009.

- **M. de Groot**, M. W. Vernooij, H. A. Vrooman, A. van der Lugt, M. M. B. Breteler and W. J. Niessen, "Repairing Missing or Distorted Slices in a Diffusion Tensor Image Acquisition," *RSNA 2009: Radiological Society of North America, 95th Annual Meeting*, 2009.

- **M. de Groot**, M. W. Vernooij, S. Klein, A. Leemans, R. de Boer, A. van der Lugt, M. M. B. Breteler and W. J. Niessen, "Asymmetry analysis along the entire cingulum in the general population," *HBM 2009: 15th Annual Meeting of the Organization for Human Brain Mapping*, 2009.

- **M. de Groot**, M. W. Vernooij, A. van der Lugt, M. A. Ikram, G. P. Krestin, A. Hofman, M. M. B. Breteler and W. J. Niessen, "White matter atrophy and lesion formation explain the loss of structural integrity of white matter in aging," *NVPHBV Fall 2008, BioMedical Image Analysis*, 2008.

Workshop proceedings

- W. Huizinga, C. T. Metz, D. H. J. Poot, **M. de Groot**, A. Leemans, W. J. Niessen and S. Klein, "Groupwise registration for correcting subject motion and eddy current distortions in diffusion MRI using a PCA based dissimilarity metric," *MICCAI 2013 Workshop on Computational Diffusion MRI and Brain Connectivity*, 2013.

- V. Terzopoulos, H. C. Achterberg, A. Plaisier, A. M. Heemskerk, **M. de Groot**, D. H. J. Poot, W. J. Niessen, J. Dudink and S. Klein, "A 3D atlas of MR diffusion parameters in the neonatal brain," *MICCAI 2012 Workshop on Perinatal and Paediatric Imaging*, 2012.

* denotes equal contribution

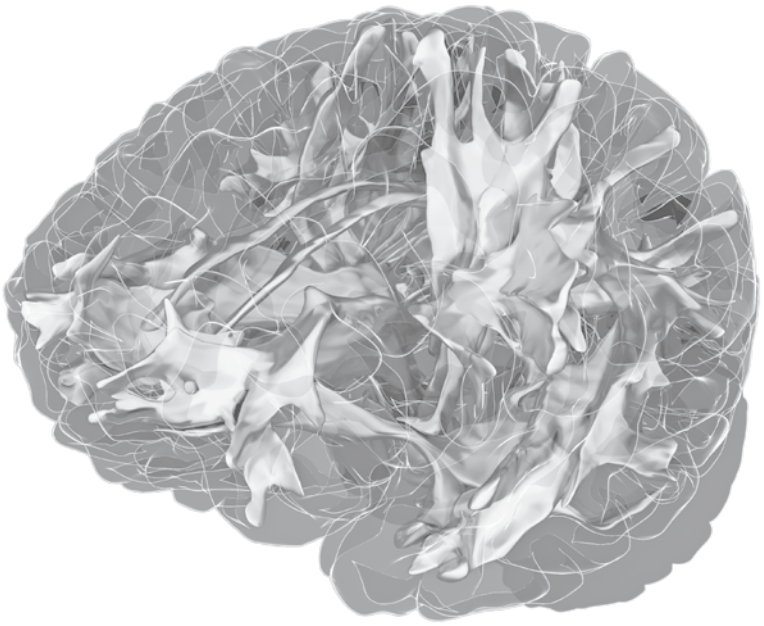

PhD portfolio

PhD Portfolio

PhD period 2008-2014
Departments Radiology, Medical Informatics & Epidemiology
Research School ASCI

In-depth courses

Principles of Research in Medicine and Epidemiology (NIHES)	2008
Introduction to data analysis (NIHES)	2008
Regression analysis (NIHES)	2008
Measuring features (ASCI)	2008
R course (Biostatistics Erasmus MC)	2008
Genetic Analysis in Clinical Research (NIHES)	2009
Bayesian Methods and Bias Analysis (Erasmus MC)	2010
Integrity in medical research (Erasmus MC)	2010
Biomedical English writing and communication (Erasmus MC)	2010

International conferences

European Congress of Radiology - ECR, Vienna Austria (attendance)	2008
Human Brain Mapping - HBM, San Francisco USA, (poster)	2009
Medical Image Computing and Computer-Assisted Intervention - MICCAI, London UK (poster)	2009
Annual meeting of the Radiological Society of North America - RSNA, Chicago USA, (oral presentation and electronic poster)	2009
IEEE Internation Symposium on Biomedical Imaging - ISBI, Rotterdam the Netherlands (attendance)	2010
Human Brain Mapping - HBM, Quebec Canada (poster)	2011
International Society for Magnetic Resonance Imaging White Matter Study Group - ISMRM WMSG, Reykjavik Iceland (attendance)	2011
Alzheimer's Association Internation Conference - AAIC, Boston USA (oral presentation and 2 posters)	2013
International Stroke Conference - ISC, San Diego USA (prize)	2014
SPIE Medical Imaging, San Diego USA (attendance)	2014

Seminars and workshops

Netherlands Forum for Biomedical Imaging, Delft / Leiden	2008, 2009
Dutch Bio-Medical Engineering - Dutch BME, Egmond aan Zee the Netherlands (poster)	2009
Anatomy sessions in dissecting room, Erasmus MC	2009, 2013
Nederlandse Vereniging voor Patroon Herkennen en Beeldverwerken - NVPHBV, Eindhoven the Netherlands	2008
Structural and Diffusion MRI, workshop at HBM, San Francisco USA	2009

Trends in HARDI and Brain Tissue Modelling, workshop at MICCAI, London UK 2009
Diffusion Modelling & the Fibre Cup, workshop at MICCAI, London UK 2009
Neuroscience for physicists, FMRIB seminar series, Oxford UK 2009
UK diffusion meeting: Tract-based Analyses and Group studies, Manchester UK (oral presentation) 2010
Neuroanatomy educational course at HBM, Quebec Canada 2011
Cluster sysadmin training, Clustervision, Rotterdam the Netherlands 2011
Population NeuroImaging Workshop, Utrecht the Netherlands 2013
Seminar De uitdaging van het delen van medische onderzoeksdata, SURFacademy, Utrecht the Netherlands 2013
Alzheimer's Imaging Consortium meeting at AAIC, Boston USA (oral presentation) 2013
Rotterdam and Groningen meeting on IBM center for exascale technology, Zurich, Switzerland 2014
Imaging Genetics, workshop at MICCAI, Boston USA 2014

Presentations in research seminar series

Medical Informatics lunch seminars, biweekly (4 talks) 2008 - 2014
Biomedical Imaging Group Rotterdam Seminars, monthly (5 talks) 2008 - 2014
Department of Radiology (1 talk) 2008 - 2012
FMRIB centre themes meeting (1 talk) 2009

Invited lectures

Brain white matter microstructure in the Rotterdam Scan Study, DZNE, Bonn Germany 2013
Microstructure of white matter tracts in the Rotterdam Scan Study, iDEA lab, Davis USA 2014

Teaching experience

Teaching assistant: Introduction to Image Processing, lecture for Medical Students once every 6 weeks Rotterdam, 2008 - 2011
Teaching assistant: Clinical Image Processing, lecture for MSc students from TUDelft 2010, 2011
Practical assistant: ESMRMB Hands on MRI course, fMRI & DTI Rotterdam the Netherlands 2009

Reviewing experience

American Journal of Neuroradiology, Biological Psychiatry, Brain, Human Brain Mapping, IEEE International Conference on Image Processing, Magnetic Resonance in Medicine, NeuroBiology of Aging, NeuroImage, IEEE Transactions on Medical Imaging.

About the author

Marius de Groot was born in Delft, on October 29 in 1979. After attending a Steiner school for elementary education, he attended secondary education at the Grotius College in Delft from which he graduated in 1998. He stayed in Delft to study Mechanical Engineering at the Delft University of Technology, and at the same time worked as a lighting engineer for Improve in Delft. Marius temporarily suspended his studies to help found the Lijm & Cultuur event facilities in Delft, after which he enrolled in the Medical Imaging track of the Biomedical Engineering master programme at the TU Delft. He conducted an internship on the detection of microcalcifications in digital breast tomosynthesis images with Siemens in Israel. Subsequently he joined the Biomedical Imaging Group Rotterdam of Prof. Wiro Niessen. Here he started to work on the analysis of diffusion data in the Rotterdam Scan Study, together with dr. Meike Vernooij, as part of his master thesis project. He graduated cum laude from the TU Delft in 2008, and was awarded a prize for best master project by the University Fund. After co-authoring a successful grant application with prof. Niessen, Marius continued his research as a PhD project which ultimately led to this thesis.

Between 2009 and 2011, Marius spent 8 months at FMRIB Centre in Oxford to work with prof. Steve Smith and dr. Jesper Andersson on improving the alignment of cross-subject diffusion data in the popular TBSS approach.

In early 2014, Marius received the Stroke Progress and Innovation Award for the 2013 paper by him and dr. Ben Verhaaren on the development of white matter lesions.

Marius has always had an interest in streamlining the exchange of data and measurements between different research groups and is currently working on the development of large-scale infrastructure for population imaging studies in Rotterdam.

ISBN 978-90-6464-814-4